(4)

AD-A196 563

Technical Report 1018

Control of Vibration in Mechanical Systems Using Shaped Reference Inputs

Peter Heinrich Meckl

MIT Artificial Intelligence Laboratory

REPORT DOCUMENTATION PAGE		READ INSTRUCTIONS BEFORE COMPLETING FORM
1. REPORT NUMBER AI-TR 1018	2. GOVT ACCESSION NO.	3. RECIPIENT'S CATALOG NUMBER
4. TITLE (and Subtitle) Control of Vibration in Mechanical Systems Using Shaped Reference Inputs		5. TYPE OF REPORT & PERIOD COVERED technical report
		6. PERFORMING ORG. REPORT NUMBER
7. AUTHOR(s) Peter Heinrich Meckl		8. CONTRACT OR GRANT NUMBER(s) N00014-86-K-0685 N00014-85-K-0124
9. PERFORMING ORGANIZATION NAME AND ADDRESS Artificial Inteligence Laboratory 545 Technology Square Cambridge, MA 02139		10. PROGRAM ELEMENT, PROJECT, TASK AREA & WORK UNIT NUMBERS
11. CONTROLLING OFFICE NAME AND ADDRESS Advanced Research Projects Agency 1400 Wilson Blvd. Arlington, VA 22209		12. REPORT DATE January 1988
		13. NUMBER OF PAGES 216
14. MONITORING AGENCY NAME & ADDRESS(If different from Controlling Office) Office of Naval Research Information Systems Arlington, VA 22217		15. SECURITY CLASS. (of this report)
		15a. DECLASSIFICATION/DOWNGRADING SCHEDULE

16. DISTRIBUTION STATEMENT (of this Report)

Distribution is unlimited.

17. DISTRIBUTION STATEMENT (of the abstract entered in Block 39, If different from Report)

18. SUPPLEMENTARY NOTES

None

19. KEY WORDS (Continue on reverse side if necessary and identify by block number)

control
vibration
robotics,

20. ABSTRACT (Continue on reverse side if necessary and identify by block number)

Dynamic systems which undergo rapid motion can excite natural frequencies that lead to residual vibration at the end of the motion. This work presents a method to shape force profiles that reduce excitation energy at the natural frequencies in order to reduce residual vibration for fast moves. Such profiles are developed using a ramped sinusoid function and its harmonics, choosing coefficients to reduce spectral energy at the natural frequencies of the system. To improve robustness with respect

DD FORM 1473 EDITION OF 1 NOV 65 IS OBSOLETE
1 JAN 73
S/N 0102-014-6601 |

to parameter uncertainty, spectral energy is reduced for a range of frequencies surrounding the nominal natural frequency. An additional set of versine profiles are also constructed to permit motion at constant speed for velocity-limited systems.

These shaped force profiles are incorporated into a simple closed-loop system with position and velocity feedback. The force input is doubly integrated to generate a shaped position reference for the controller to follow. This control scheme is evaluated on the MIT Cartesian Robot. The shaped inputs generate motions with minimum residual vibration when actuator saturation is avoided. Feedback control compensates for the effect of friction. Using only a knowledge of the natural frequencies of the system to shape the force inputs, vibration can also be attenuated in modes which vibrate in directions other than the motion direction. When moving several axes, the use of shaped inputs allows minimum residual vibration even when the natural frequencies are dynamically changing by a limited amount.

Control of Vibration in Mechanical Systems Using Shaped Reference Inputs

Peter H. Meckl

Control of Vibration in Mechanical Systems
Using Shaped Reference Inputs

by

Peter Heinrich Meckl

Abstract

Dynamic systems which undergo rapid motion can excite natural frequencies that lead to residual vibration at the end of the motion. This work presents a method to shape force profiles that reduce excitation energy at the natural frequencies in order to reduce residual vibration for fast moves. Such profiles are developed using a ramped sinusoid function and its harmonics, choosing coefficients to reduce spectral energy at the natural frequencies of the system. To improve robustness with respect to parameter uncertainty, spectral energy is reduced for a range of frequencies surrounding the nominal natural frequency. An additional set of versine profiles are also constructed to permit motion at constant speed for velocity-limited systems.

These shaped force profiles are incorporated into a simple closed-loop system with position and velocity feedback. The force input is doubly integrated to generate a shaped position reference for the controller to follow. This control scheme is evaluated on the MIT Cartesian Robot. The shaped inputs generate motions with minimum residual vibration when actuator saturation is avoided. Feedback control compensates for the effect of friction. Using only a knowledge of the natural frequencies of the system to shape the force inputs, vibration can also be attenuated in modes which vibrate in directions other than the motion direction. When moving several axes, the use of shaped inputs allows minimum residual vibration even when the natural frequencies are dynamically changing by a limited amount.

Thesis Committee:
Prof. Warren Seering, Chairperson
Prof. Steven Dubowsky
Prof. Karl Hedrick
Mr. Nicholas Mango

2

Transformation of positive predicates into their negative duals can introduce universal quantification in the body of the defining clause, so Walinsky had to attack this difficult problem as well. Constructive implementation of universal quantifiers in general requires unbounded searches, but in an important subcase implementation is practical. Frequently, the universally quantified formula is an implication, allowing the antecedent to "filter" instantiations of the consequent. He modified the SLD resolution procedure to handle this situation, and explored circumstances under which the resulting executions are practical.

3. Specific Accomplishments

Cliff Walinsky's thesis lays solid groundwork for systematic study of negation in logic programming that preserves the declarative nature of the languages like pure PROLOG, can be efficiently executed without major changes to present interpreters, and allows programs to retain their constructive solutions. The work is a model of defining a significant research topic, exploring and changing it as more information is gathered, and successfully obtaining results of the kind sought.

AFOSR support not only made possible the research described above, but also provided for extra opportunities for Walinsky. He was invited to attend a Washington, DC workshop as student observer. He was able to attend two major conferences (one an international gathering in Australia which otherwise would have been beyond possibility), to meet and interact with other researchers (and to thereby interest others in his ideas), and ultimately to obtain employment in a prestigious institution where he will continue to be a productive researcher. Several important logic-programming theoreticians visited OGC and provided contact with the broader research community. J-L. Lassez and J. Jaffar are at the core of the logic-programming group at IBM (Yorktown); Lassez invited Cliff to join that group as a visitor in the near future. R. Topor (Melbourne) provided some invaluable early direction for Cliff's work.

The one area in which Cliff was not as successful as we had hoped was in publishing his ideas. He submitted papers to both logic-programming conferences, but they were not accepted. The field is new, not always well defined, and very competitive. There is a measure of politics in writing acceptable papers, particularly for conferences with a high rejection rate. (We were able to learn that the difficulty is not in the ideas, which should find acceptance in the more controlled arena of professional journals.)

The technical reports being submitted under separate cover give a complete description of constructive negation:

Walinsky, C., "Constructive Semantics for Negation", Report CS/E 87-008, Oregon Graduate Center, September, 1987.

Walinsky, C., "Constructive Negation in Logic Programs", Report CS/E 87-009, Oregon Graduate Center, September, 1987 (PhD thesis).

Dedicated to my family...

my parents Tony and Doris Meckl

who lovingly made me what I am,

my wife Marie

who patiently accepts who I am,

and our awaited baby

who will begin a new generation.

Contents

Introduction

1.1   Motivation:

The advent of microprocessor technology has brought about an entirely new way to control production machinery. No longer do control engineers have to rely on analog circuits for controlling dynamic systems. Now, computers can be programmed and reprogrammed to produce a wide range of control actions in real time. Microprocessor technology has enabled the power of computers to be cheaply installed in many dynamic systems. These capabilities have made the newly-developing field of robotics possible. Robots and other computer-controlled machines have become the dominant components in automating production processes.

Along with the opportunities that these microprocessor-controlled machines bring has come a new set of challenges. For robots to perform assembly tasks economically they must be able to move from place to place very quickly. Such fast motions will excite vibrations in the moving elements. Since robot structures are typically only lightly damped, these oscillations require additional time to settle and hence delay the start of the next task. Since each relative motion excites a different set of frequencies, the only way to avoid exciting any structural modes using existing controllers is to move sufficiently slowly. To achieve fast motions, an effective motion

control scheme is necessary that will not excite the system natural frequencies.

The goal of this research is to develop methods to reduce motion-induced vibration during fast moves. The assumption is that the motion itself is the main source of system vibration. Thus, force profiles which do not contain energy at the system natural frequencies produce motions which do not excite structural vibration and hence do not require any additional settling time. The approach adopted here is to remove the task of reducing vibration from the controller which ensures accurate positions in the presence of disturbances. In this way, a simple control loop can accomplish accurate positioning without the complexity required to suppress vibration. Structural oscillations are not damped out but avoided by judicious choice of force inputs. This approach works as long as the motion itself is the only source of vibration, which is usually the case in typical positioning systems. Thus, this work develops shaped input functions that can reduce residual vibration regardless of which controller has been selected. In those cases in which even optimal regulators fail to adequately suppress vibration, these inputs can significantly improve performance.

1.2 Literature Review:

Many researchers have addressed the problem of controlling vibrating systems such as robots and space structures. An excellent review of current theory and practice in dynamics and control of large space structures has been presented by Nurre, et al. [1]. A review of general control strategies is given by Bryson [2], with discussion of specific control techniques applied to flexible systems given by Seltzer [3], Croopnick, et al. [4], Joshi and Groom [5], Meirovitch and Öz [6].

These control strategies can be loosely organized into two main classifications: terminal controllers and regulators. Terminal controllers take the system from an initial state to a final state while satisfying some optimization criterion. This is

also known as slewing when applied to space structures. Open-loop slewing is accomplished using a control input that is strictly a function of time, not explicitly of the system states. To accomplish slewing maneuvers, control inputs are specified as smooth time functions to minimize excitation of system resonances. Aspinwall [7] shaped such a profile using a finite Fourier series expansion that minimizes frequency content over a wide range of frequencies, but these functions take twice as long as the corresponding time-optimal function to complete the motion. Other researchers have used performance indices in combination with Pontryagin's principle to generate "optimal" control functions for performing open-loop slewing maneuvers. Various performance indices and system models have been used by researchers including Swigert [8], Farrenkopf [9], Turner and Junkins [10], Turner and Chun [11], and Alfriend and Longman [12]. Swigert also included a penalty on residual amplitude due to natural frequency changes to allow limited variations in frequency. Lisowski and Hale [13] included the control input and its derivative as additional states and imposed smooth start and stop transitions on the control input function to minimize excitation of higher resonant frequencies.

Additional open-loop functions have been developed by making use of cam profile shapes. Such a forcing function was developed by Makino [14] to drive the SCARA robot arm. Sehitoglu and Aristizabal [15] used a cycloidal motion profile to generate smooth motions. However, no attempt was made to tune these functions to the dynamics of the system to minimize both move time and residual vibration.

Another open-loop approach has been to use a series of appropriately-timed step inputs to eliminate residual vibration upon completion of the move. This technique has come to be known as posicast control. A detailed presentation of this approach is given in Smith [16]. An extension of this concept, incorporating robustness to parameter uncertainties, is under development by Singer [17].

In addition to these open-loop slewing functions, researchers have also developed closed-loop slewing strategies that utilize time-varying gains on feedback states.

Breakwell [18] determined these gains as a function of remaining time to maneuver. Juang, Turner, and Chun [19,20] determined time-varying gains using a terminal constraint on the performance index that penalizes residual vibration. Experimental results using this approach are presented by Juang, Horta, and Robertshaw [21].

Classical proportional-plus-integral-plus-derivative (PID) control has been utilized on the Space Telescope Pointing Control System, as presented by Dougherty, et al. [22,23]. The stability properties of such a control scheme as applied to flexible systems is discussed by Hughes and Abdel-Rahman [24].

A majority of control techniques applied to vibrating systems utilize regulator or tracking control theory. Basically, the controller is designed to maintain a set-point or to track a reference input. The terminal states are not incorporated into the determination of constant feedback gains. The coupling between vibration regulation and large-angle slewing is discussed by Baruh and Silverberg [25]. The design of modal controllers to control several dominant modes of distributed flexible systems has been suggested by Meirovitch, et al. [26] and Balas [27]. Other researchers, such as Henrichfreise, Moritz, and Siemensmeyer [28], have developed a detailed system model that includes the vibrating states. An observer is constructed to estimate the unmeasured states. This technique works well if the model accurately represents the actual system. Stability problems can arise if system parameters change significantly. Another approach has been to utilize measurements at the tip of the flexible member to generate control signals. Such an approach has been used by Cannon and Rosenthal [29], Cannon and Schmitz [30], and Hollars and Cannon [31] to actively control both the rigid-body angle and the vibration of a flexible system. Stability problems again may arise, however, when modeling errors exist because actuator and sensor are not colocated.

An alternative to actively suppressing the vibration is to alter the damping characteristics of the structure. Both passive and active methods have been proposed. Alberts, et al. [32] added layers of viscoelastic material to a beam in order to add

passive damping. This reduced vibration and enhanced stability in the presence of higher unmodeled modes. Active damping techniques have also been proposed, which add distributed damping to beam-like structures. Silverberg [33] has developed a discrete implementation which approximates uniform distributed damping with several discrete actuators. Burke and Hubbard [34] generated a distributed control law by applying a piezoelectric film to the beam that alters its resistance to bending when given a voltage signal. An extension of active damping is presented by Finzi, Lanz, and Mantegazza [35], who developed a control law that adds both mass and damping at discrete locations to reduce residual vibration.

All of these techniques have shortcomings when applied to physical systems. Problems arise because of unmodeled modes, parameter variations, and nonlinearities. Robustness of the control methods in light of these modeling errors is discussed by Nesline and Zarchan [36], Kosut, et al. [37], and Arbel and Gupta [38]. Balas [39] points out that the presence of unmodeled modes can cause undesirable excitation and potential instability. Radcliffe and Mote [40] discovered such an instability when they tried to control the vibration of a rotating saw blade.

Some solutions to these problems have been proposed. Gupta [41] and Gupta, et al. [42] have suggested a "frequency-shaped cost functional" that allows the feedback control to be tailored to have less energy at frequencies corresponding to unmodeled system resonances. "Innovations feedthrough" and output feedback control have been proposed by Balas [43] and Lin, et al. [44] to introduce terms in the control law which can prevent instability due to unmodeled modes. Sesak, et al. [45] have proposed a modified performance index which suppresses excitation of unmodeled modes in a technique known as Model Error Sensitivity Suppression.

A review of robust control techniques that ensure stability in the presence of parameter errors is given by Dorato [46]. Yamada and Nakagawa [47] have developed a technique for designing a state feedback controller with constant gains which works over a limited range of parameter variations. The effect of parameter uncertainties

on a controller designed for modal suppression is described by Calico and Moore [48].

Some researchers have proposed adaptive control methods to compensate for parameter variations. Several different approaches have been presented by Ih and Leondes [49], Bar-Kana, et al. [50], Dubowsky and DesForges [51], Johnson [52], Benhabib, et al. [53] and Potter and Ginter [54].

1.3   Overview of Thesis:

The approach taken here, as described in several previous papers [55,56,57,58,59], is to generate smooth force profiles that have been shaped to reduce excitation energy at the system natural frequencies. These profiles are constructed by summing harmonics of the ramped sinusoid function using an appropriate choice of coefficients. They result in fast motions while minimizing the residual vibration which occurs at the end of the move. By minimizing energy in a band of frequency components surrounding the nominal natural frequency, some variation in system parameters can be tolerated without affecting vibration attenuation. A detailed development of these force profiles is given in Chapter 2.

To put this approach in perspective, some results using alternative filtering techniques are presented in Chapter 3. The use of filters removes energy from the input at certain frequencies instead of building up a function with specified frequency content. These two different approaches are compared.

Since the force inputs generated in Chapter 2 can only be directly implemented in open-loop systems, Chapter 4 discusses closed-loop implementations. In any closed-loop system, the actual force input is determined by a combination of reference and feedback signals and hence cannot be prespecified. One approach to incorporate these shaped inputs into closed-loop systems is to use a reference system model to generate the reference trajectory. Results for this approach are presented along

with a discussion of the problems that arise when the reference model significantly differs from the actual system dynamics. Another implementation is then developed that generates an appropriate position reference by doubly-integrating the shaped force inputs. Because this approach treats the closed-loop system as an equivalent open-loop system, these shaped inputs must be tuned to the closed-loop natural frequencies. Finally, the optimal regulator state feedback approach is studied in some detail to point out several cases in which it fails to give adequate performance. When used in conjunction with shaped reference inputs, however, residual vibration can be significantly reduced.

The force profiles discussed so far assume that the actuators which drive the system can generate peak force regardless of the velocity. But since the force that real actuators can provide decreases with speed, the system will eventually saturate at some peak velocity. This has motivated the development of velocity profiles which accelerate to peak velocity, travel at peak velocity for some time, and then decelerate to final position. The shaped inputs developed in Chapter 2 do not allow for any motion at constant velocity. This limits system performance by requiring that the peak force be kept sufficiently small. Thus in Chapter 5 a new set of force profiles are developed using versine functions that allow motion at constant velocity.

To evaluate the practical implementation of these shaped inputs in actual systems, experiments were performed on the MIT Cartesian Robot. Chapter 6 discusses the simulation model of the experimental hardware that helped determine appropriate inputs. Chapter 7 presents details of the microprocessor implementation and a set of response data indicating the usefulness of shaped inputs in reducing system vibration. Chapter 8 presents a number of conclusions and recommendations for future work.

Development of Shaped Inputs

2.1 Review of Previous Work:

In work done for my Master's thesis [55], I developed input functions constructed from a ramped sinusoid and its harmonics. This function was the solution to a boundary-value problem imposing zero magnitude and slope on the desired wave-form. Harmonics are given by characteristic numbers that satisfy the boundary values. The fundamental ramped sinusoid function alone requires nearly 50% longer than the time-optimal input to move a given distance with a given peak force. To reduce this move time, harmonics of the ramped sinusoid were added to the fundamental. The coefficients of the harmonic terms were chosen so the resulting function gives a least-squares fit to a single cycle of a square wave. A typical input function consisting of five ramped sinusoid terms is shown in Figure 2.1. Its frequency spectrum, shown in Figure 2.2, has troughs at certain frequencies. The location of these frequency troughs depends on the total number of terms used to construct the input function. If the system natural frequencies correspond to the trough frequencies of a particular function, then that function generates much smaller residual vibration. So the idea is to pick the input function with the appropriate number of terms. Unfortunately, the troughs in the input spectrum are very narrow. If the actual
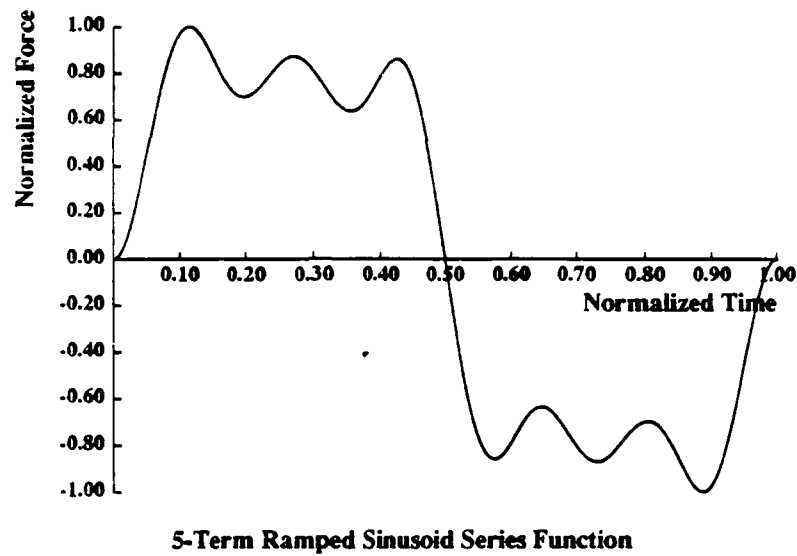
15

5-Term Ramped Sinusoid Series Function

Figure 2.1: Ramped Sinusoid Series Function Composed of Five Terms.

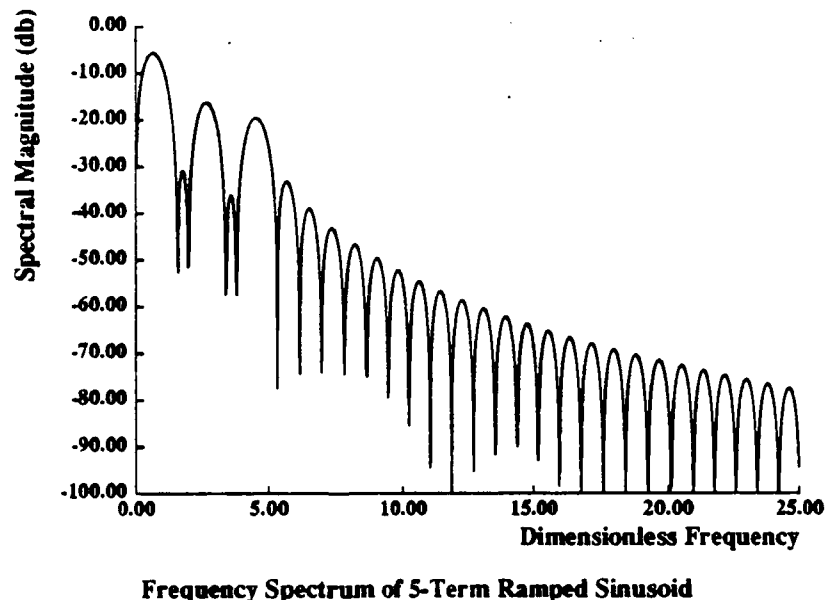**Frequency Spectrum of 5-Term Ramped Sinusoid**

Figure 2.2: Frequency Spectrum of Five-Term Ramped Sinusoid Series.

natural frequency is sufficiently different from the nominal frequency for which the function was developed, a considerable amount of residual vibration may still occur.

For this reason, a new method will be developed for determining the harmonic coefficients of the ramped sinusoid functions. Functions will be generated having a sufficiently wide trough in the frequency spectrum to accommodate errors in nominal natural frequencies. The hope is that these functions will work not only for systems having a static error in natural frequency but also for systems in which natural frequency changes dynamically with time.

2.2 Relationship Between Input Spectrum and Residual Acceleration Amplitude:

Before actually formulating the desired input functions, it seems useful to determine the relationship between the input function spectrum and the residual acceleration amplitude. The work presented here will restrict attention to a two-mass system model (Fig. 2.3) which has one rigid body mode and one resonant mode. Mass m_1 represents motor inertia, mass m_2 represents endpoint inertia, and k represents transmission and structural stiffness. This is a good model to represent the first mode of a single Cartesian robot axis, in which the endpoint position y_e oscillates relative to the motor position y_m where the force f is applied. Other axes can be similarly represented, treating any cross-coupling between axes as disturbances. Damping is neglected in this model since it serves to reduce vibration amplitudes. All system parameters are treated in dimensionless groups (Table 2.1), leading to the dimensionless transfer function shown in Figure 2.3. All positions are nondimensionalized with respect to final position y_f, and T_s represents the time to move the equivalent rigid-body mass the same distance y_f using a square wave input having peak force F. Errors in system natural frequency are represented by the ratio ω_A/ω_N, where ω_A is the actual natural frequency and ω_N is the nominal natural
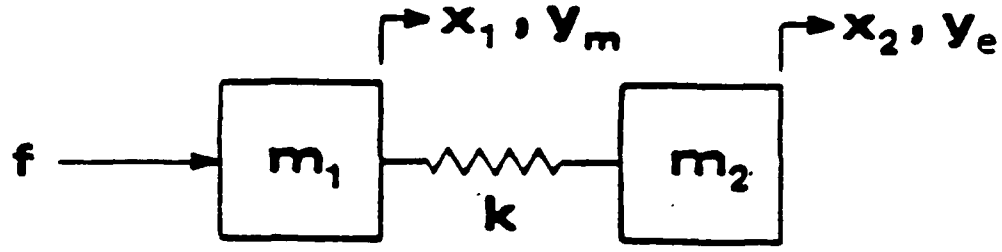
$$\frac{y_e^*}{f^*} = \frac{\left(\frac{\omega_A}{\omega_N}\right)^2}{s^2 \left[s^2 + \left(\frac{\omega_A}{\omega_N}\right)^2\right]}$$

Figure 2.3: Two-Mass System Model.

frequency.

For this system model with a single natural frequency, a direct relationship can be derived between the magnitude of the input spectrum at the natural frequency and the amplitude of the residual acceleration. The amplitude of the acceleration of mass m_2 (the unforced mass) <u>after</u> the input force f is turned off at time T_f is given by

$$A = \sqrt{a_o^2 + \left(\frac{J_o}{\omega_n}\right)^2} \tag{2.1}$$

where

$a_o = \frac{d^2}{dt^2} y(T_f)$ is the acceleration of m_2 <u>at</u> time T_f,

$J_o = \frac{d^3}{dt^3} y(T_f)$ is the jerk of m_2 <u>at</u> time T_f, and

$\omega_n = \sqrt{\frac{k}{m_1}(1 + \frac{m_1}{m_2})}$ is the natural frequency of the two-mass system.

Note that A in expression (2.1) represents the amplitude of free undamped vibration.

In order to determine expressions for a_o and J_o, it is necessary to use Fourier transforms. The general expressions for a_o and J_o are given by

$$a_o = \frac{1}{\pi} \int_{-\infty}^{\infty} \text{Re}[F(\omega)H_a(\omega)] \cos \omega T_f \, d\omega \tag{2.2}$$

Table 2.1

Definition of Dimensionless Parameters

$$t^* = \omega_N t / 2\pi$$

$$y_e^* = \frac{y_e}{y_f}$$

$$\ddot{y}_e^* = \frac{\ddot{y}_e}{\omega_N^2 y_f}$$

$$F^* = \frac{F}{(m_1 + m_2) y_f \omega_N^2} = \left(\frac{2}{\omega_N T_s} \right)^2$$

$$J_o = \frac{1}{\pi} \int_{-\infty}^{\infty} \text{Re}[F(\omega) H_J(\omega)] \cos \omega T_f \, d\omega \qquad (2.3)$$

where $F(\omega)$ is the Fourier transform of the input function, $H_a(\omega)$ is the Fourier integral representation of the transfer function relating the input force f to $\frac{d^2}{dt^2} y$, and $H_J(\omega)$ is the Fourier integral representation of the transfer function relating f and $\frac{d^3}{dt^3} y$.

Any function $f(t)$ which starts at time $t = 0$ and ends at time $t = T_f$ will have a Fourier transform of the form

$$F(\omega) = \int_0^{T_f} f(t) e^{-j\omega t} \, dt = [F_R(\omega) + j F_I(\omega)] e^{-j \frac{\omega T_f}{2}}, \qquad (2.4)$$

where $F_R(\omega)$ and $F_I(\omega)$ are the real and imaginary parts, respectively. Deriving the Fourier integral representations of the appropriate transfer functions requires the use of singularity functions as described by Papoulis [60]. This leads to the following expressions:

$$H_a(\omega) = \frac{\omega_n^2}{m_1 + m_2} \left\{ \frac{1}{\omega_n^2 - \omega^2} - \frac{\pi}{2j\omega_n} [\delta(\omega - \omega_n) - \delta(\omega + \omega_n)] \right\} \qquad (2.5)$$

$$H_J(\omega) = \frac{\omega_n^2}{m_1 + m_2} \left\{ \frac{j\omega}{\omega_n^2 - \omega^2} + \frac{\pi}{2} [\delta(\omega - \omega_n) + \delta(\omega + \omega_n)] \right\} \qquad (2.6)$$

where $\delta(\omega)$ is the delta function defined by

$$\int_{-\infty}^{\infty} \delta(\omega - \omega_o)\phi(\omega)d\omega = \phi(\omega_o) \tag{2.7}$$

for an arbitrary function $\phi(\omega)$.

Using these Fourier integral representations in the expressions for a_o and J_o gives the following results:

$$a_o = \frac{\omega_n}{m_1 + m_2} \left[F_R(\omega_n) \sin \frac{\omega_n T_f}{2} + F_I(\omega_n) \cos \frac{\omega_n T_f}{2} \right] \tag{2.8}$$

$$\frac{J_o}{\omega_n} = \frac{\omega_n}{m_1 + m_2} \left[F_R(\omega_n) \cos \frac{\omega_n T_f}{2} - F_I(\omega_n) \sin \frac{\omega_n T_f}{2} \right]. \tag{2.9}$$

Inserting these expressions into (2.1) gives

$$A = \frac{\omega_n}{m_1 + m_2} |F(\omega_n)| \tag{2.10}$$

where

$$|F(\omega_n)| = \sqrt{F_R^2(\omega_n) + F_I^2(\omega_n)}. \tag{2.11}$$

With the following definition of the dimensionless frequency spectrum,

$$F^*(\omega_n T_f) = \frac{|F(\omega_n)|}{F T_f} \tag{2.12}$$

where F is the peak force amplitude and T_f is the move time, the expression for residual acceleration amplitude can be rewritten in dimensionless form as

$$A^* = \frac{A}{F/(m_1 + m_2)} = \omega_n T_f |F^*(\omega_n T_f)|. \tag{2.13}$$

These results show that only the frequency component corresponding to the system resonant frequency ω_n contributes to residual acceleration amplitude. Of course, the actual frequency spectrum of any given input function also depends on its time duration T_f. The relationship (2.13) then establishes an upper bound on the input spectral magnitude at the system natural frequency in order to achieve acceptable residual acceleration amplitude.

It is interesting to apply this relationship to the bang-bang function developed in my Master's thesis [55]. This forcing function generates only peak force and switches between positive and negative force levels to produce time-optimal response. As Appendix A shows, this function leaves the system with zero residual vibration only because vibration excited in the first half of the move is removed in the second half. Thus, spectral energy for the entire function is zero at the natural frequency and (2.13) is satisfied. However, if the actual system differs from the nominal system, spectral energy at resonance will not completely cancel and residual vibration results. Therefore, we will develop another input function that tolerates uncertainty in natural frequency.

2.3 Development of Shaped Functions:

We are now in a position to derive forcing functions that reduce residual vibration when the system natural frequency is uncertain. We choose the ramped sinusoid function and its harmonics to construct a series representation of the input, analogous to a Fourier series representation. The coefficients of each harmonic in this series will be chosen so that the spectral magnitude constraint is satisfied. Ramped sinusoid functions were selected as basis functions because of their odd symmetry about $t = T_f/2$ (Fig. 2.4) and their smooth transitions in slope, which result in the narrow frequency spectra of Figure 2.5.

In order to allow for changes in system parameters, one goal in picking coefficients in this series will be to reduce spectral magnitude in a sufficiently wide band of frequencies surrounding the nominal natural frequency. The system natural frequency is assumed to vary by $\pm 10\%$. This variation was chosen based on a detailed dynamic analysis of the MIT Cartesian Robot. Garcia Reynoso [61] determined that for two extreme locations of the moving axes, the maximum change in the first three natural frequencies due to the change in geometric configuration is within $\pm 10\%$ of
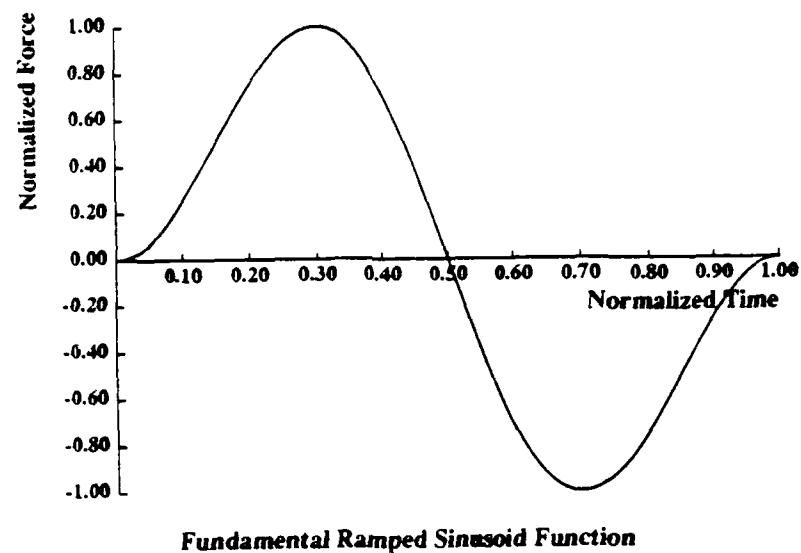
Fundamental Ramped Sinusoid Function

Figure 2.4: Fundamental Ramped Sinusoid Function.

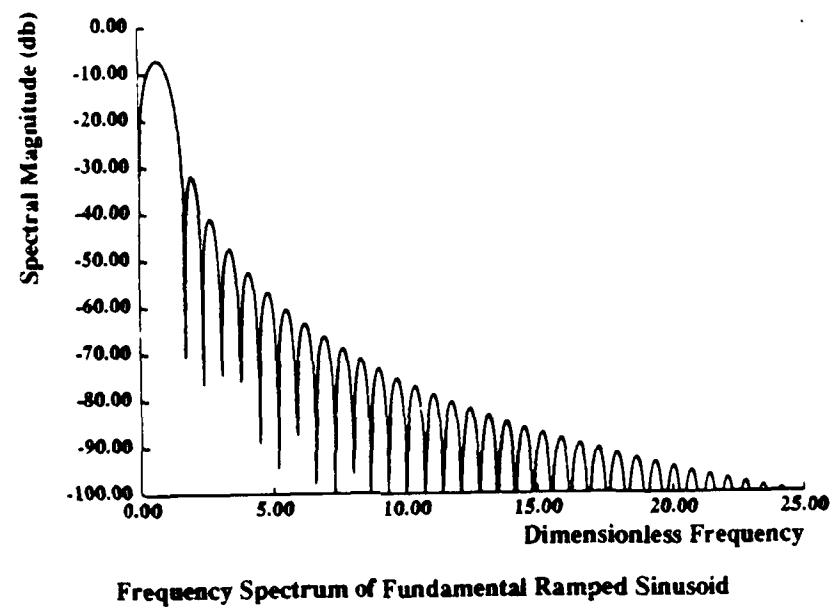
Frequency Spectrum of Fundamental Ramped Sinusoid

Figure 2.5: Frequency Spectrum of Fundamental Ramped Sinusoid Function.

the nominal natural frequency. Thus, functions which have low spectral magnitudes in a band of $\pm 10\%$ surrounding the resonant frequency would represent practical inputs for such a robot system.

In general, the input functions can be represented by the following series expansion, where $\Phi_\ell^*(t)$ represents a particular harmonic of the ramped sinusoid function, α_ℓ is the characteristic number associated with each harmonic (defined in [55]). B_ℓ is the coefficient for each harmonic, T_f represents the time to reach a desired position, and τ is normalized time:

$$f(t) = \sum_{\ell=1}^{L} \frac{B_\ell}{\alpha_\ell^2} \, \Phi_\ell^*(t) \tag{2.14}$$

$$\Phi_\ell^*(t) = \alpha_\ell \left(\frac{1}{2} - \tau \right) - \sin \alpha_\ell \tau - \frac{\alpha_\ell}{2} \cos \alpha_\ell \tau \tag{2.15}$$

$$\tau = t/T_f \tag{2.16}$$

The goal is to pick appropriate values for B_ℓ that will minimize move time T_f and minimize spectral magnitudes over a range of frequencies surrounding the system natural frequency ω_n.

To achieve this, we will combine these objectives into a single minimization problem to pick the coefficients B_ℓ. To minimize move time, we minimize the square of the difference between the ramped sinusoid series and a single cycle of a square wave. This gives a least-squares fit to a square wave. A square wave is chosen since it is known to give optimal move time for a rigid body. This alone determined the harmonic coefficients in my Master's thesis [55]. To explicitly incorporate the constraint in the frequency spectrum, a second expression will be added to minimize the squared magnitude of the frequency spectrum F^* at several frequencies ω, surrounding system resonance. A weighting factor o determines relative weighting between these objectives. The overall objective function J represents the quantity to be minimized:

$$J = \frac{1}{T_f} \left\{ \int_0^{T_f/2} [1 - f(t)]^2 \, dt + \int_{T_f/2}^{T_f} [-1 - f(t)]^2 \, dt \right\}$$

$$- \rho \sum_{i=1}^{11} (\omega_i T_s)^2 |F^*(\omega_i T_f)|^2 \qquad (2.17)$$

In this formulation, we have arbitrarily chosen 11 frequencies surrounding resonance to satisfy the spectral magnitude constraint. This provides enough frequencies to keep spectral magnitudes small throughout the entire frequency band without the need to integrate over all frequencies in this band. The upper and lower limits on frequency can be adjusted to give any desired frequency band. For a $\pm 10\%$ frequency range, the bounds on the frequency ω_i are $0.9\omega_n < \omega_i < 1.1\omega_n$.

The coefficients of the harmonics B_ℓ can be calculated by differentiating the objective function J with respect to B_r, where r represents a particular value of the index ℓ, and setting the result to zero.

$$\partial J / \partial B_r = 0 \qquad (2.18)$$

This gives an expression explicitly in terms of B_ℓ, and $I'_{r\ell}$ and I^*_r, which are known functions of α_r and α_ℓ:

$$\sum_{\ell=1}^{L} B_\ell I'_{r\ell} = I^*_r \qquad (2.19)$$

$$I'_{r\ell} = \left[I^*_{r\ell} - \rho \sum_{i=1}^{11} (\omega_i T_s)^2 \frac{\alpha_\ell}{\alpha_\ell^2 - (\omega_i T_f)^2} \frac{\alpha_r}{\alpha_r^2 - (\omega_i T_f)^2} \right.$$

$$\left. \bullet \left(\frac{2 \sin \frac{\omega_i T_f}{2} - \omega_i T_f \cos \frac{\omega_i T_f}{2}}{(\omega_i T_f)^2} \right)^2 \right] \qquad (2.20)$$

$$I^*_{r\ell} = \begin{cases} -\frac{1}{\alpha_\ell^2 - \alpha_r^2} \left\{ \frac{\alpha_r}{\alpha_\ell^4} \left[\frac{\alpha_\ell^3}{12} + \left(\frac{\alpha_\ell^2}{2} - 1 \right) \sin \alpha_\ell \right. \right. \\ \qquad \left. - \alpha_\ell \cos \alpha_\ell + \frac{\alpha_\ell}{2} (\cos \alpha_\ell - 1) \right] \\ \qquad - \frac{\alpha_\ell}{\alpha_r^4} \left[\frac{\alpha_r^3}{12} + \left(\frac{\alpha_r^2}{2} - 1 \right) \sin \alpha_r \right. \\ \qquad \left. \left. - \alpha_r \cos \alpha_r + \frac{\alpha_r}{2} (\cos \alpha_r - 1) \right] \right\} \qquad (r \neq \ell) \\ \\ \frac{1}{\alpha_\ell^5} \left\{ \frac{\alpha_\ell}{4} + \frac{5}{24} \alpha_\ell^3 + \frac{1}{4} \left[\left(\frac{\alpha_\ell}{2} \right)^2 - 1 \right] \sin 2\alpha_\ell \right. \\ \qquad \left. + \left(\frac{\alpha_\ell^2}{2} - 2 \right) \sin \alpha_\ell + \frac{\alpha_\ell}{4} \cos 2\alpha_\ell + 2\alpha_\ell \cos \alpha_\ell \right\} \qquad (r = \ell) \end{cases} \qquad (2.21)$$

$$I_r^\bullet = \frac{1}{\alpha_r^3}\left[\left(\frac{\alpha_r}{2}\right)^2 - 2\cos\left(\frac{\alpha_r}{2}\right) - \alpha_r\sin\left(\frac{\alpha_r}{2}\right)\right.$$
$$\left. - \cos\alpha_r + \frac{\alpha_r}{2}\sin\alpha_r + 1\right]. \tag{2.22}$$

If the final move time T_f is known, then $I'_{r\ell}$ is known, and the coefficients B_ℓ can be determined by simply solving the following set of linear equations, expressed in matrix form:

$$[I'_{r\ell}][B_\ell] = [I_r^\bullet] \tag{2.23}$$

Unfortunately, T_f is not known until the coefficients B_ℓ are known. The dependence of T_f on B_ℓ can be expressed in terms of the square wave move time T_s and a scale function Γ:

$$T_f = \Gamma T_s \tag{2.24}$$

where

$$\Gamma = \sqrt{\frac{3}{\frac{1}{SF}\sum_{\ell=1}^{L}\frac{B_\ell}{\alpha_\ell}}} \tag{2.25}$$

$$T_s = 2\sqrt{\frac{(m_1 + m_2)y_f}{F}} \tag{2.26}$$

SF is a scale factor which normalizes the peak of the function to 1. T_s represents the move time to cover a distance y_f when the input is a single cycle of a square wave of amplitude F. Γ is a function of α_ℓ and B_ℓ which ensures that the resulting input signal brings the system to the desired final position. Since the ramped sinusoid functions cannot supply as much energy for the same peak force as the corresponding square wave, they will take somewhat longer to complete the same move. This time penalty is represented by Γ. Due to the inherent coupling of B_ℓ and Γ, an iteration scheme is necessary to correctly compute values for the coefficients B_ℓ. This iteration procedure can be outlined as follows:

1. Determine $\omega_n T_s$ for desired move distance and system parameters.

2. Guess a value of Γ. (Note that Γ is slightly greater than 1.)

3. Solve for B_ℓ by solving the matrix equation (2.23).

4. Normalize ramped sinusoid series expansion by determining the value for the scale factor SF.

5. Calculate Γ using expression (2.25).

6. Use the new value of Γ to update B_ℓ.

7. Repeat until Γ converges to acceptable accuracy (error with respect to previous value is less than 10^{-5}).

To improve convergence, every fourth value of Γ is updated using Aitken acceleration:

$$\Gamma_{i+3} = \frac{\Gamma_i \Gamma_{i+2} - \Gamma_{i+1}^2}{\Gamma_{i+2} - 2\Gamma_{i+1} + \Gamma_i} \tag{2.27}$$

Using the procedure outlined above, we can derive functions which satisfy our objectives. We used a total of $L = 15$ terms for computational efficiency while retaining enough mathematical degrees of freedom to achieve acceptable minimization. A good compromise between minimizing move time and minimizing spectral magnitude near the system natural frequency is achieved for a value of $\rho = 10$. Note that larger values of ρ will give lower spectral magnitudes and slightly higher move times. Functions were developed which minimize the frequency content at dimensionless frequencies $\omega_n T_s / 2\pi$ of 5, 10, and 15, respectively. Each of these functions minimizes spectral magnitude at 11 frequencies extending $\pm 10\%$ around resonance. These inputs are shown in Figures 2.6 to 2.8. The time function is shown in (a) and the frequency spectrum is shown in (b). Notice that the spectral magnitudes for the entire range of frequencies extending $\pm 10\%$ about $\omega_n T_s$ have been significantly attenuated. In comparison with the five-term ramped sinusoid function of Figures 2.1 and 2.2, the spectral magnitude near the nominal natural frequency has been attenuated by more than an order of magnitude (20 db).
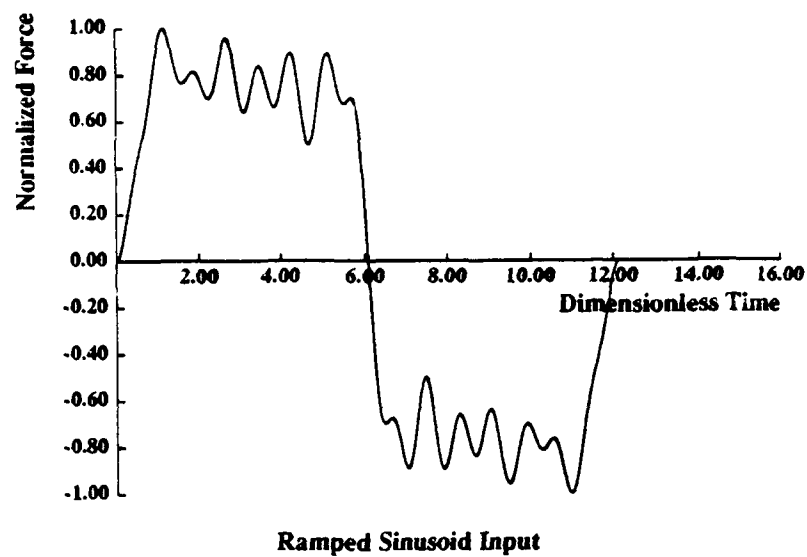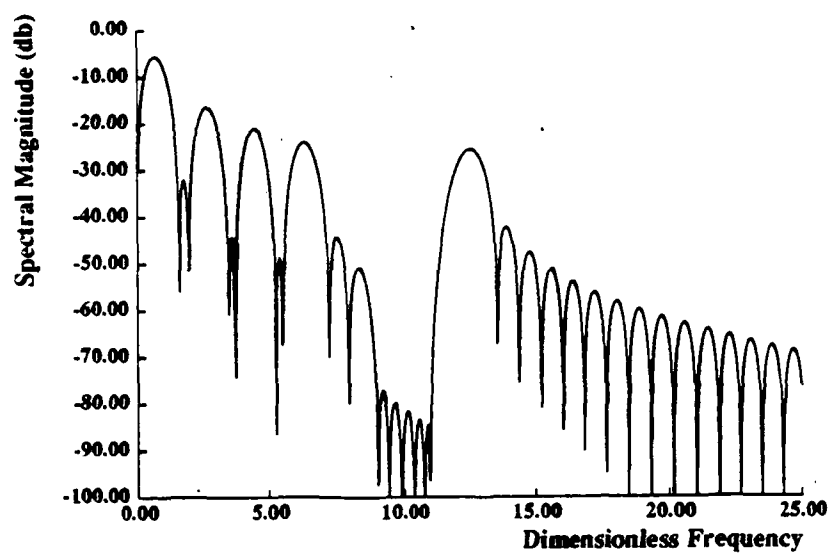
Ramped Sinusoid Input

(a)

Frequency Spectrum of Ramped Sinusoid
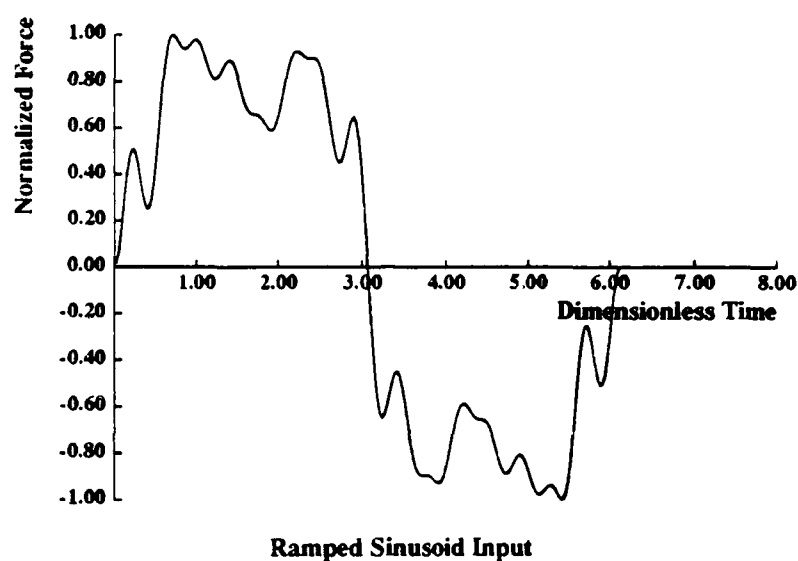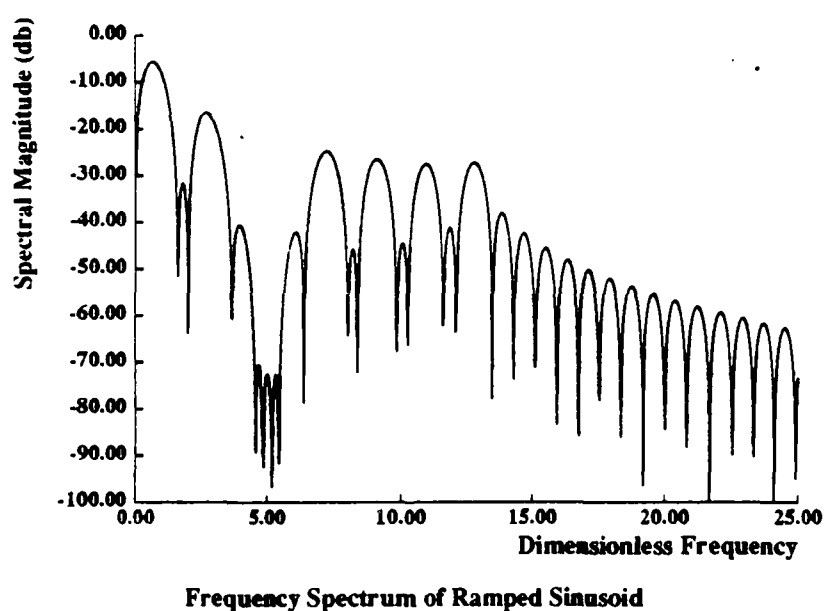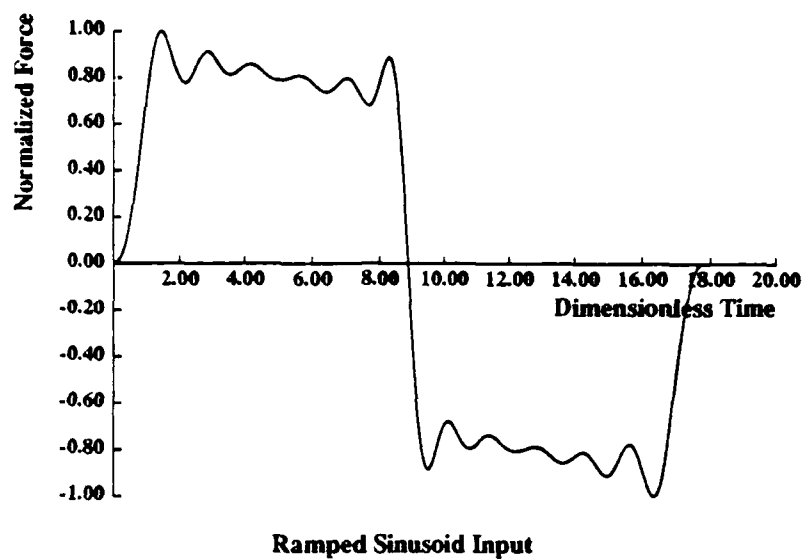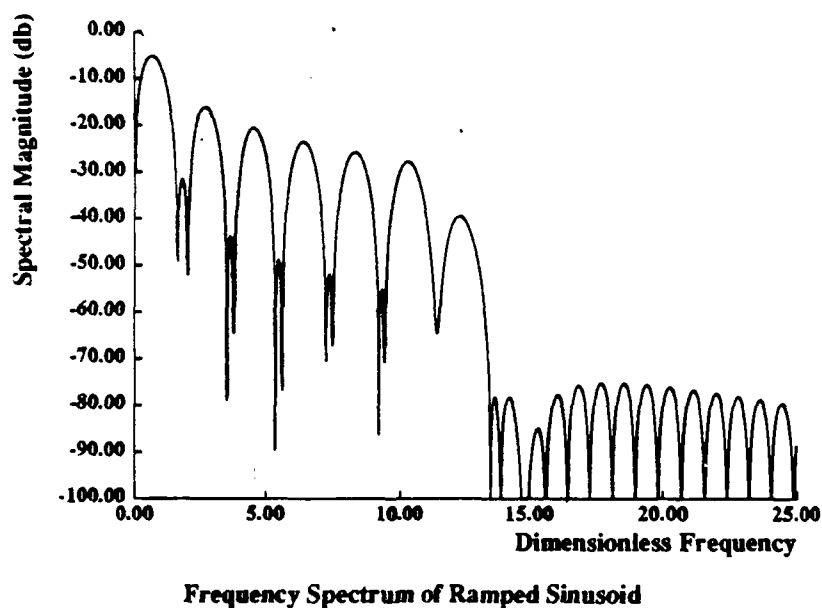
(b)

Figure 2.6: Ramped Sinusoid Input Tuned to $\omega_n T_s/2\pi = 5 \pm 10\%$: (a) Time Function (b) Frequency Spectrum.

Figure 2.7: Ramped Sinusoid Input Tuned to $\omega_n T_s / 2\pi = 10 \pm 10\%$: (a) Time Function (b) Frequency Spectrum.

Ramped Sinusoid Input

(a)

Frequency Spectrum of Ramped Sinusoid

(b)

Figure 2.8: Ramped Sinusoid Input Tuned to $\omega_n T_s/2\pi = 15 \pm 10\%$: (a) Time Function (b) Frequency Spectrum.
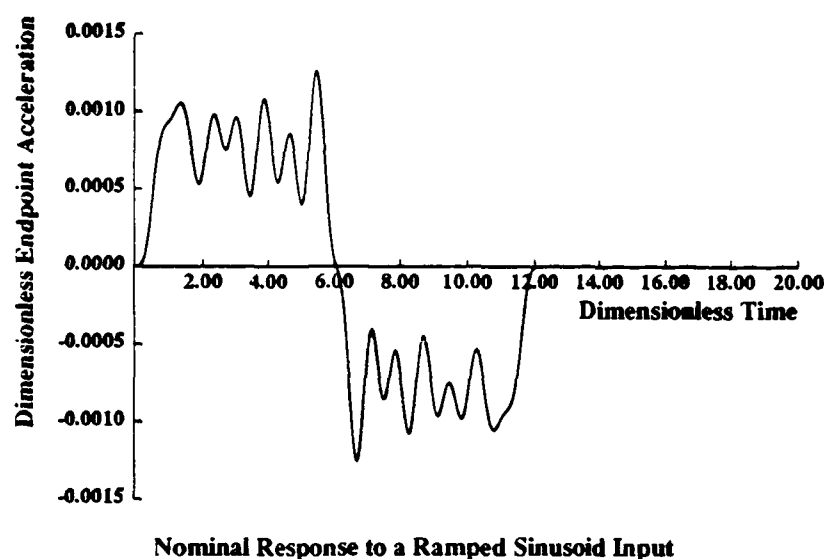
Nominal Response to a Ramped Sinusoid Input

Figure 2.9: Simulated Acceleration Response for Nominal System With Ramped Sinusoid Input; $\omega_N T_s/2\pi = 10$.

2.4 Open-Loop Simulation Results:

To determine the effectiveness of these shaped functions in meeting our goal. we evaluated the response of the two-mass system to these inputs using computer simulations. These simulations were performed using a Runge-Kutta-Merson integration routine. A nominal value of $\omega_n T_s/2\pi = 10$ was assumed in order to construct the input function. This gives the final dimensionless move time as $\omega_n T_f/2\pi = 12$. The response of the nominal system to this input is shown in Figure 2.9 as the dimensionless acceleration of mass m_2. The acceleration response is shown rather than the position response because double differentiation accentuates the vibration signal. Notice that under nominal conditions, residual acceleration amplitude is nearly eliminated when the input has finished.

A more challenging test, however, is when the actual resonant frequency is different from the nominal frequency. If we assume that the actual frequency is only
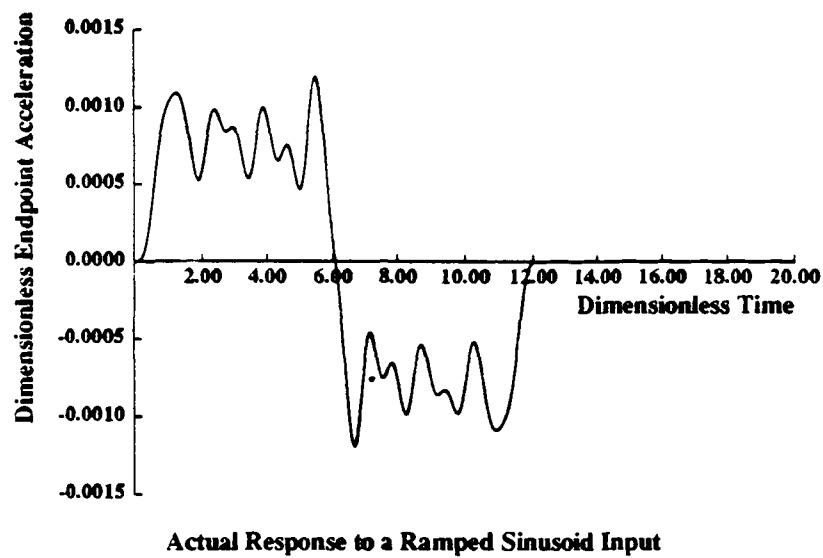
Actual Response to a Ramped Sinusoid Input

Figure 2.10: Simulated Acceleration Response for Actual System With Ramped Sinusoid Input; $\omega_N T_s/2\pi = 10$, $\omega_A/\omega_N = 0.9$.

90% of the nominal frequency and use the same input function derived in the nominal case, the response in Figure 2.10 results. Notice that even with a 10% error in resonant frequency, the input function still achieves nearly zero residual acceleration amplitude.

These results can be compared with the square wave response to determine the effect of shaped inputs on residual vibration. Square wave response is shown in Figure 2.11. The square wave input generates considerably more residual vibration than the ramped sinusoid input.

If only move time is compared, ignoring settling time needed to damp out residual vibration, the move time ratio T_f/T_s has a value of 1.2 for the ramped sinusoid function. Thus, we can achieve the desired vibration attenuation with a move time only 20% longer than that required for a square wave. Since the optimal time to complete the move without vibration is nearly the same as the square wave time, these functions only take 20% longer than time-optimal inputs. Because the ramped
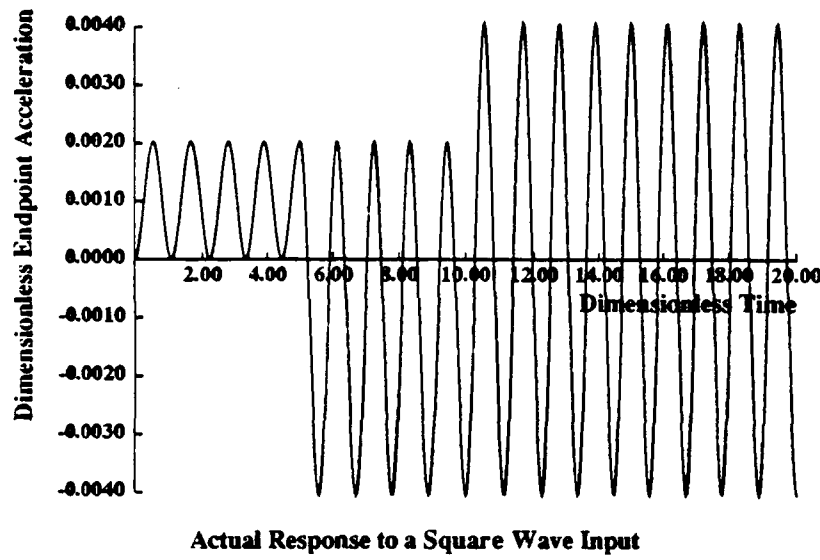
Actual Response to a Square Wave Input

Figure 2.11: Simulated Acceleration Response for Actual System With Square Wave Input; $\omega_N T_s / 2\pi = 10$, $\omega_A / \omega_N = 0.9$.

sinusoid inputs nearly eliminate residual vibration, this extra time is more than compensated for by the reduction in settling time.

2.5 Shaped Inputs for Several Natural Frequencies:

The approach outlined in Section 2.3 can be extended to minimize excitation energy at several natural frequencies. The new objective function can be expressed as

$$J = \frac{1}{T_f} \left\{ \int_0^{T_f/2} \left[1 - f(t) \right]^2 \, dt + \int_{T_f/2}^{T_f} \left[-1 - f(t) \right]^2 \, dt \right\}$$
$$+ \rho \sum_{i=1}^{11M} (\omega_i T_s)^2 |F^*(\omega_i T_f)|^2 \tag{2.28}$$

where M is the total number of modes (natural frequencies) to attenuate, and ω_i is given by

$$(1 - p_m)\omega_m < \omega_i < (1 + p_m)\omega_m, \qquad i = m, \ldots, 11m \tag{2.29}$$

where p_m represents the fraction of nominal frequency that determines the upper and lower bounds of the frequency band surrounding the nominal natural frequency ω_m for the mth mode.

The remaining development follows exactly as before. A function that attenuates three natural frequencies was constructed in this way. For the dimensionless frequencies $\omega_m T_s/2\pi = 1.5$, 5, and 10, with $\pm 10\%$ frequency bands, the resulting shaped input function is shown in Figure 2.12(a), with the corresponding frequency spectrum shown in (b). Notice that all three frequency bands have been attenuated as specified.

2.6   Shaped Inputs for Lightly Damped Systems:

The development so far has assumed that the system to be controlled has no inherent damping. Damping has the effect of spreading out the resonant peak over a broader range of frequencies. It will therefore also affect the vibration attenuation of inputs that have been shaped for an undamped system. The following analysis is intended to quantify the effect of damping on residual vibration. We will derive the residual acceleration amplitude for a damped system in terms of characteristics of the shaped input functions.
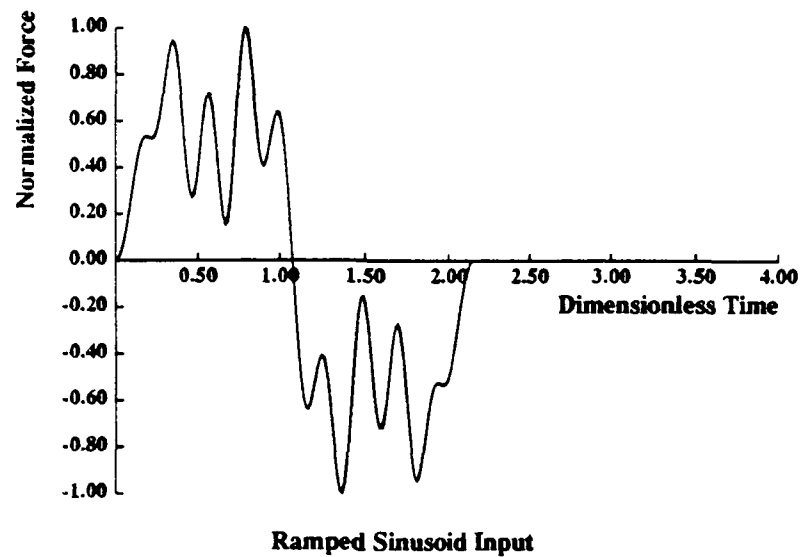
The model used to derive this relationship is similar to the undamped model of Figure 2.3 with an additional viscous damping element b, as shown in Figure 2.13. For this system, the peak residual acceleration amplitude of mass m_2 after the input force f is turned off at time T_f is given by

$$A = \sqrt{a_o^2 + \left(\frac{J_o + \zeta\omega_n a_o}{\omega_n\sqrt{1-\zeta^2}}\right)^2} \qquad (2.30)$$

where

a_o is the acceleration of m_2 <u>at</u> time T_f,

$J_o =$ is the jerk of m_2 <u>at</u> time T_f,

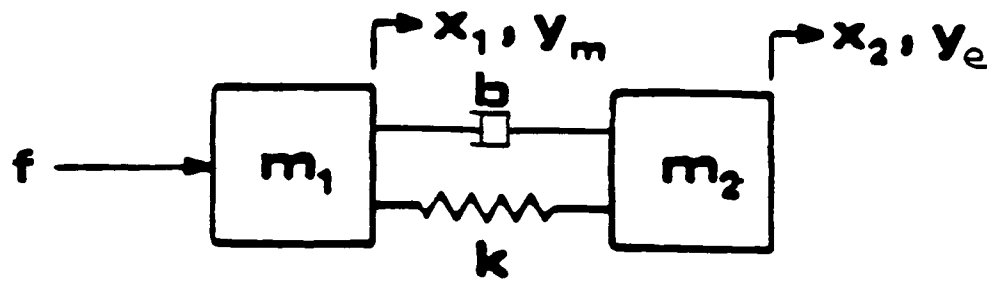Ramped Sinusoid Input

(a)

Frequency Spectrum of Ramped Sinusoid
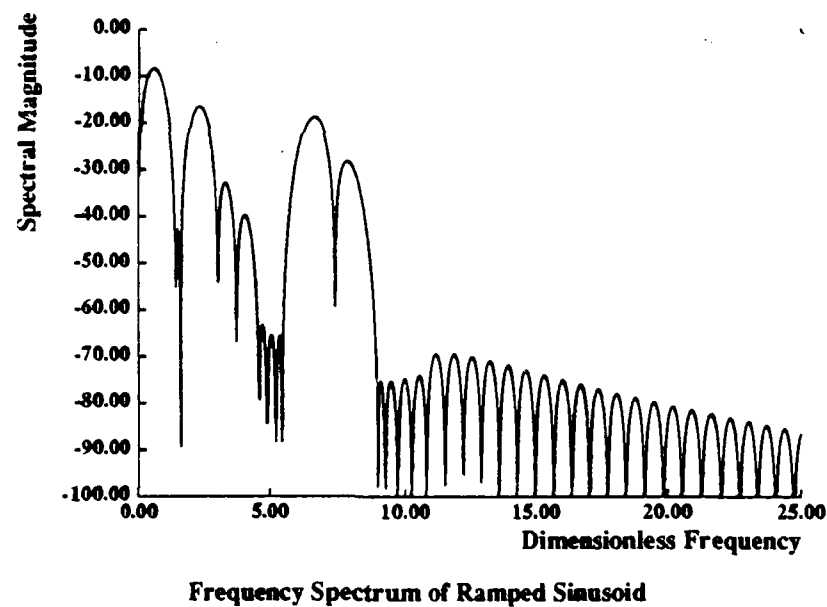
(b)

Figure 2.12: Ramped Sinusoid Input Tuned to $\omega_m T_s/2\pi = 1.5, 5,$ and $10 \pm 10\%$: (a) Time Function (b) Frequency Spectrum.

$$\frac{y_e^*}{f^*} = \frac{\left(\frac{\omega_A}{\omega_N}\right)^2}{s^2 \left[s^2 + 2\zeta \left(\frac{\omega_A}{\omega_N}\right) s + \left(\frac{\omega_A}{\omega_N}\right)^2\right]}$$

Figure 2.13: Damped Two-Mass System Model.

ω_n is the undamped natural frequency, given by

$$\omega_n = \sqrt{\frac{k}{m_1}\left(1 + \frac{m_1}{m_2}\right)} \tag{2.31}$$

ζ is the damping ratio, given by

$$\zeta = \frac{b}{2}\sqrt{\frac{1}{km_1}\left(1 + \frac{m_1}{m_2}\right)}. \tag{2.32}$$

Using the same technique as before, a_o and J_o can be represented in terms of system parameters and input characteristics as follows:

$$a_o = \frac{1}{2\pi} \int_{-\infty}^{\infty} F(\omega) H_a(\omega) e^{j\omega T_f} d\omega \tag{2.33}$$

$$J_o = \frac{1}{2\pi} \int_{-\infty}^{\infty} F(\omega) H_J(\omega) e^{j\omega T_f} d\omega \tag{2.34}$$

where $F(\omega)$ is the Fourier transform of the input function, $H_a(\omega)$ is the Fourier integral representation of the transfer function relating f to $\frac{d^2}{dt^2}y$, and $H_J(\omega)$ is the Fourier integral representation of the transfer function relating f and $\frac{d^3}{dt^3}y$.

The ramped sinusoid functions under consideration have a Fourier transform which can be written as

$$F(\omega) = jF_I(\omega)e^{-j\omega\frac{T_f}{2}} \tag{2.35}$$

This is a more specific form of equation (2.4) in which $F_R(\omega) = 0$. The Fourier integral representations of the transfer functions are given by:

$$H_a(\omega) = \frac{1}{m_1 + m_2} \frac{\omega_n^2 + j2\zeta\omega_n\omega}{(\omega_n^2 - \omega^2) + j2\zeta\omega_n\omega} \qquad (2.36)$$

$$H_J(\omega) = \frac{1}{m_1 + m_2} \frac{-2\zeta\omega_n\omega^2 + j\omega_n^2\omega}{(\omega_n^2 - \omega^2) + j2\zeta\omega_n\omega}. \qquad (2.37)$$

After performing the required residue calculus to obtain the integrals, the square of the residual acceleration amplitude can be expressed as

$$A^2 = -\left(\frac{\omega_n}{m_1 + m_2}\right)^2 \frac{e^{-\zeta\omega_n T_f}}{1 - \zeta^2} F_I(-\omega_n\sqrt{1 - \zeta^2} + j\zeta\omega_n)F_I(\omega_n\sqrt{1 - \zeta^2} + j\zeta\omega_n). \quad (2.38)$$

This gives residual amplitude in terms of the input Fourier transforms of complex frequencies. These can no longer be expressed simply in terms of the input frequency spectrum as was the case for an undamped system (equation 2.10). However they can be evaluated for the shaped ramped sinusoid function. In terms of real frequency ω, the function $F_I(\omega)$ can be expressed as

$$F_I(\omega) = \frac{FT_f}{SF}\left|\sum_{\ell=1}^{L} \frac{B_\ell\alpha_\ell}{\alpha_\ell^2 - (\omega T_f)^2}\left(\frac{2\sin\frac{\omega T_f}{2} - \omega T_f\cos\frac{\omega T_f}{2}}{(\omega T_f)^2}\right)\right|, \qquad (2.39)$$

where F is the peak force and SF is a normalizing scale factor. In order to evaluate sines and cosines of complex arguments, the following identities are useful:

$$\sin(X + jY) = \sin X \cosh Y + j\cos X \sinh Y \qquad (2.40)$$

$$\cos(X + jY) = \cos X \cosh Y - j\sin X \sinh Y \qquad (2.41)$$

After considerably more algebra, the final expression for the dimensionless squared residual acceleration amplitude is given by

$$(A^*)^2 = \left(\frac{A}{F/(m_1 + m_2)}\right)^2 = \left(\frac{\omega_n T_f}{SF}\right)^2 \frac{e^{-\zeta\omega_n T_f}}{1 - \zeta^2}$$

$$\cdot\left[\frac{4s^2ch^2 + 4c^2sh^2 - 4\omega_n\sqrt{1 - \zeta^2}T_f sc - 4\zeta\omega_n T_f shch + \omega_n^2 T_f^2(c^2ch^2 + s^2sh^2)}{(\omega_n T_f)^4}\right.$$

$$\left.\cdot\sum_{\ell=1}^{L}\sum_{r=1}^{L}\frac{B_\ell B_r\alpha_\ell\alpha_r\left[\phi(\alpha_\ell)\phi(\alpha_r) + 4\zeta^2(1 - \zeta^2)\omega_n^4 T_f^4\right]}{\left[\phi(\alpha_\ell)^2 + 4\zeta^2(1 - \zeta^2)\omega_n^4 T_f^4\right]\left[\phi(\alpha_r)^2 + 4\zeta^2(1 - \zeta^2)\omega_n^4 T_f^4\right]}\right] \qquad (2.42)$$

where s, c, sh, and ch are defined as

$$s = \sin \omega_n \sqrt{1 - \zeta^2} \frac{T_f}{2} \qquad (2.43)$$

$$c = \cos \omega_n \sqrt{1 - \zeta^2} \frac{T_f}{2} \qquad (2.44)$$

$$sh = \sinh \zeta \frac{\omega_n T_f}{2} \qquad (2.45)$$

$$ch = \cosh \zeta \frac{\omega_n T_f}{2} \qquad (2.46)$$

and the functions $\phi(\alpha)$ are defined as

$$\phi(\alpha) = \alpha^2 - (1 - \zeta^2)\omega_n^2 T_f^2. \qquad (2.47)$$

This expression (2.42) gives the dimensionless peak residual amplitude for a particular ramped sinusoid input as a function of the dimensionless frequency ωT_f. This functional dependence can also be expressed in terms of ωT, using the known value of Γ given by expression (2.25) for the particular input. When $\zeta = 0$, the resulting function gives simply a scaled frequency spectrum of the input, as given by (2.13). There is a direct relationship between residual amplitude and input frequency spectrum for an undamped system. For $\zeta \neq 0$, this functional dependence on frequency is no longer proportional to the input frequency spectrum.

For the ramped sinusoid input tuned to the undamped natural frequency $\omega_n T_f / 2\pi = 10$, constructed using the technique of Section 2.3, we can now investigate the effects of system damping on the residual response. Note that for lightly damped systems, the resonant frequency where response amplitude peaks is very nearly the same as the undamped natural frequency. Figure 2.14 shows the frequency dependence of the residual amplitude for $\zeta = 0$. As expected, this looks similar to the Fourier spectrum of Figure 2.7. When $\zeta = 0.1$, the lobes which occur for $\zeta = 0$ disappear and the curve becomes smoother, as shown in Figure 2.15. For $\zeta = 0.3$ more smoothing takes place, as shown in Figure 2.16. Notice that the peaks which appear in Figure 2.14 become lower and the troughs become more shallow as damping increases (Fig-
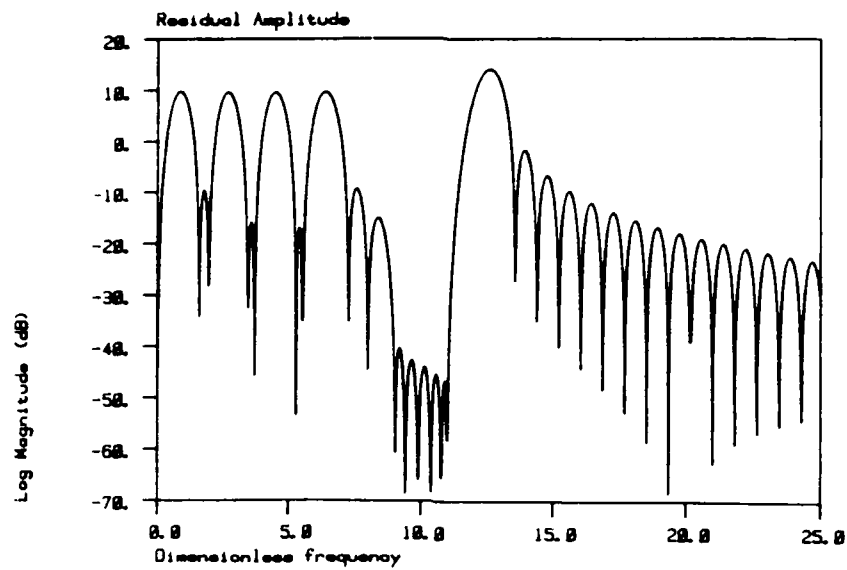
Figure 2.14: Residual Acceleration Amplitude as a Function of $\omega T_s/2\pi$ for Ramped Sinusoid Input Tuned to $\omega_n T_s/2\pi = 10 \pm 10\%$; $\zeta = 0.0$.

Figure 2.15: Residual Acceleration Amplitude as a Function of $\omega T_s/2\pi$ for Ramped Sinusoid Input Tuned to $\omega_n T_s/2\pi = 10 \pm 10\%$; $\zeta = 0.1$.
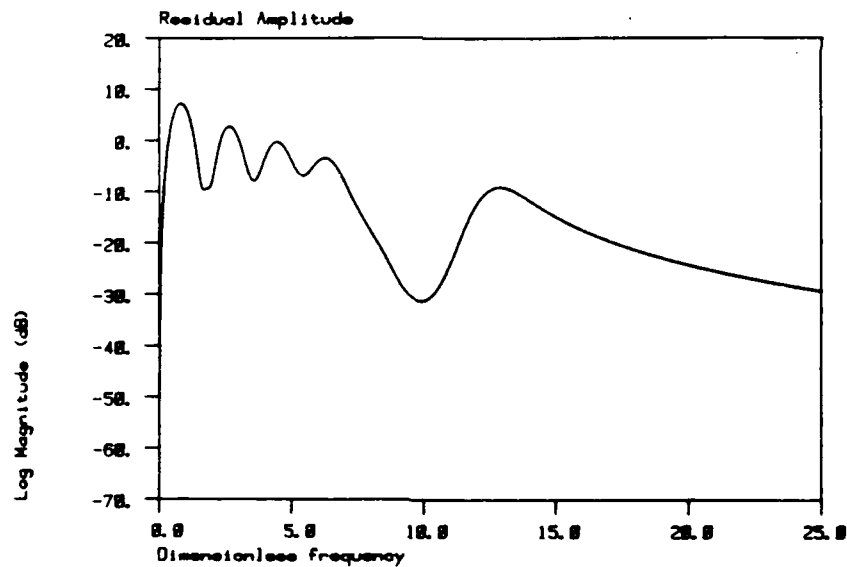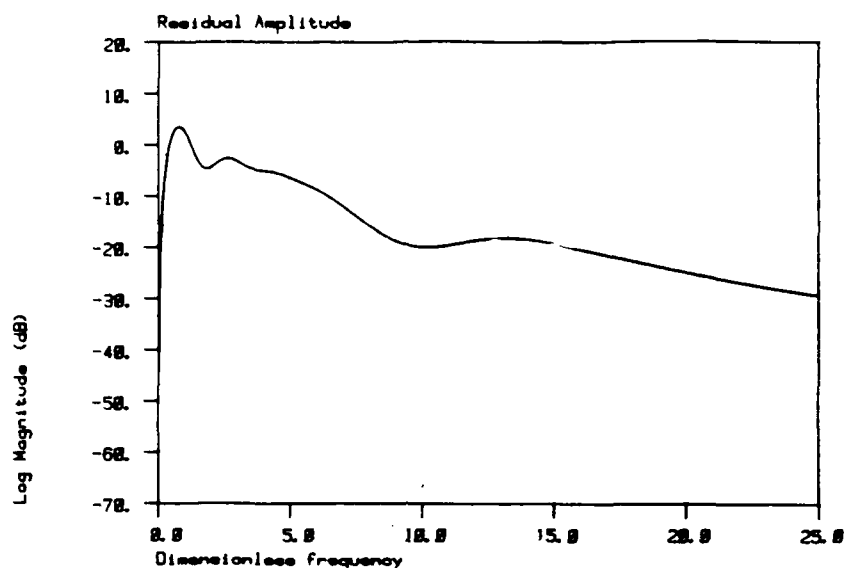
Residual Amplitude

Figure 2.16: Residual Acceleration Amplitude as a Function of $\omega T_s/2\pi$ for Ramped Sinusoid Input Tuned to $\omega_n T_s/2\pi = 10 \pm 10\%$; $\zeta = 0.3$.

ures 2.15 and 2.16). This implies that slightly higher residual amplitude will exist for a lightly damped system than for an undamped one. In addition, because the troughs bow up at their edges, the effective range of frequencies for which residual amplitudes are small becomes narrower.

Simulation results using this ramped sinusoid input for a lightly damped system ($\zeta = 0.1$) are shown in Figures 2.17 and 2.18. Again, we plot the dimensionless acceleration of mass m_2. Figure 2.17 shows the case when the dimensionless system undamped natural frequency $\omega_n T_f$ coincides with the frequency for which the ramped sinusoid has been tuned. Figure 2.18 shows the case when the system undamped natural frequency is only 90% of the nominal tuned frequency. Notice that for light damping, the residual amplitude is higher than for the undamped case. The effect of damping is to raise the residual amplitude for frequencies near the limits of the notch in the frequency spectrum. Since the natural frequency of the actual system coincides with the lowest frequency which has been filtered from the input spectrum, damped response gives higher initial residual amplitude. However, this

Nominal Damped Response to a Ramped Sinusoid Input
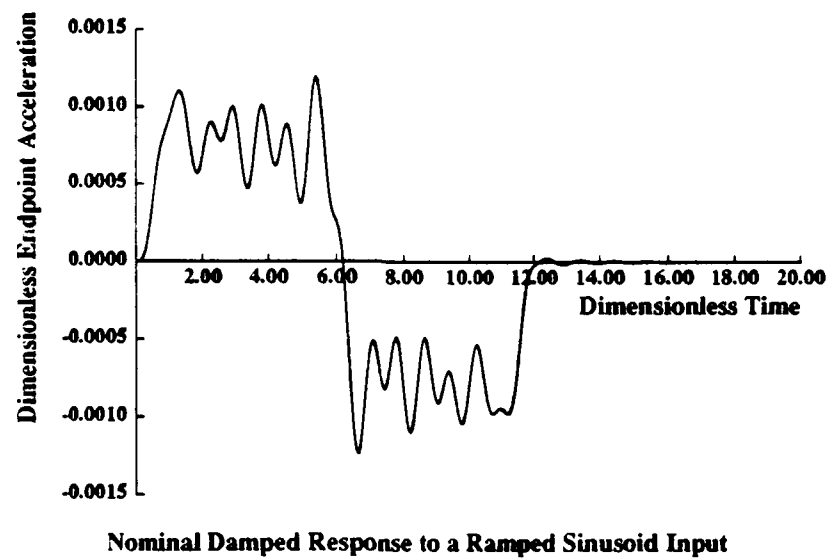
Figure 2.17: Simulated Acceleration Response for Nominal Damped System with Ramped Sinusoid Input; $\omega_N T_s/2\pi = 10$, $\zeta = 0.1$.
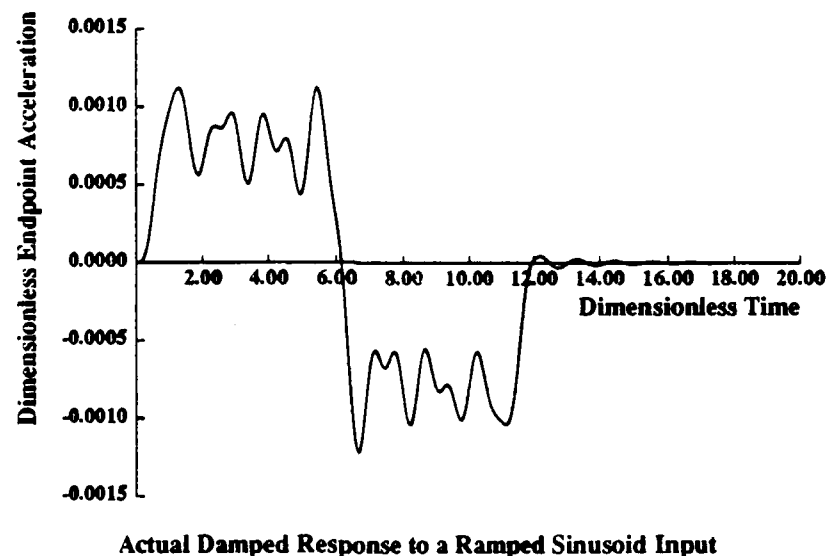

Actual Damped Response to a Ramped Sinusoid Input

Figure 2.18: Simulated Acceleration Response for Actual Damped System with Ramped Sinusoid Input; $\omega_N T_s/2\pi = 10$, $\zeta = 0.1$, $\omega_A/\omega_N = 0.9$.

amplitude decays because of the presence of damping. Therefore, damped response to the ramped sinusoid input for this lightly damped system is satisfactory. The settling time for the damped system response to a square wave input is considerably longer.

If the actual system has considerable inherent damping, then an alternative is to incorporate the more complex damped expression (2.42) into the minimization for determining the harmonic coefficients. Because of the complexity involved in doing this, the simpler development assuming no damping is preferable since it gives good attenuation over the frequency range of interest for lightly damped systems. Since most practical systems tend to be only lightly damped, the inputs developed assuming no damping are appropriate.

2.7 Closure:

This chapter has described a method of constructing force profiles for moving a dynamic system while keeping excitation energy near the natural frequencies as small as desired. A useful feature is that the depth and width of the notch in the frequency spectrum can be adjusted to allow for variation in the natural frequency. Force profiles can be constructed for any number of natural frequencies occurring in the physical system. As long as system damping is relatively small, these inputs generate motions with small residual vibration, even when natural frequencies are uncertain

Alternative Filtering Techniques

Chapter 3

3.1 Introduction:

In the previous chapter, a set of input functions were developed to produce relatively fast motions for a vibrating system. These inputs were built up from a ramped sinusoid and its harmonics in an effort to increase the energy available for motion while minimizing spectral energy near the natural frequency of the system. An alternative strategy would be to start with a single cycle of a square wave, which is known to give time-optimal response, and filter out any spectral energy near the natural frequency.

Several methods for accomplishing this filtering are available. Two of these techniques are discussed in the following sections and evaluated analytically. One method is simply to use an analog low-pass filter to pre-shape the square wave before sending it on to the vibrating system. This requires that the filter cut-off frequency be sufficiently below the lowest natural frequency to provide acceptable attenuation.

Another method is to use a notch filter to filter out only those frequencies that correspond to the system natural frequencies. Such a filter is hard to implement in real time since an effective notch filter requires many poles which introduce large phase lag at higher frequencies. This tends to delay the system response

42

and lengthen the time needed to complete the move. So instead we will synthesize a new time function that will serve as the notch-filtered input to the system. This allows us to have the entire input waveform available for filtering, including future values which would not be available to a filter in real time.

The square wave input can be filtered by removing frequency bands in its frequency spectrum and then regenerating the time function by using the inverse Fourier transform. This approach gives time functions described by sine integrals. These functions must start earlier and end later than the square wave from which they were derived in order to achieve the notched spectrum. This leads to unacceptably long move times.

3.2   Analog Low-Pass Filter:

The simplest method to remove energy at system natural frequencies is to pass the square wave through a low-pass filter. This attenuates all frequencies above the filter cut-off frequency. The most important consideration is achieving a steep roll-off rate at the cut-off frequency so that energy can be passed for frequencies nearly up to the lowest natural frequency of the system.

A particularly useful filter to accomplish this is a Butterworth filter, which has the desired low-pass frequency response in magnitude, allows for any desired roll-off rate, and is physically realizable. A fourth-order Butterworth filter was selected for analysis here.

The magnitude of the frequency response for an nth order Butterworth filter is given by (see Papoulis [60], p. 105)
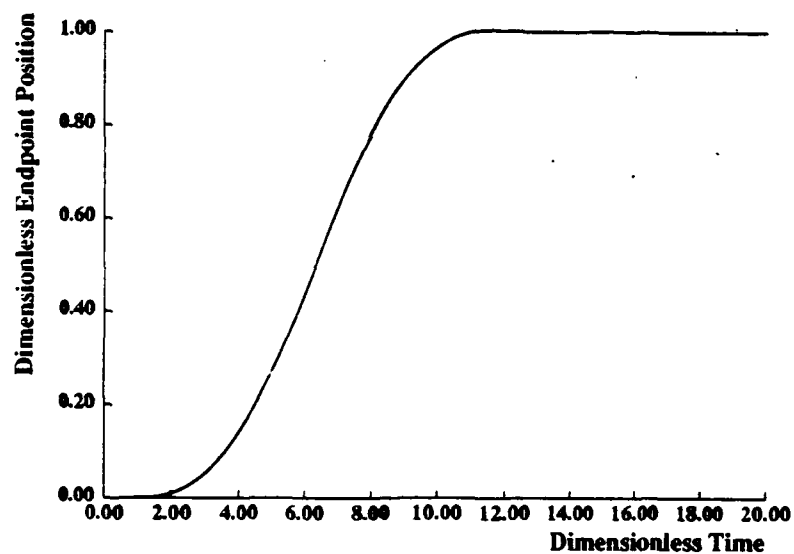
$$|H_F(\omega)| = \frac{1}{\sqrt{1 + \left(\frac{\omega}{\omega_c}\right)^{2n}}} \tag{3.1}$$

where ω_c is the filter cut-off frequency and n is the order of the filter. Thus, for a
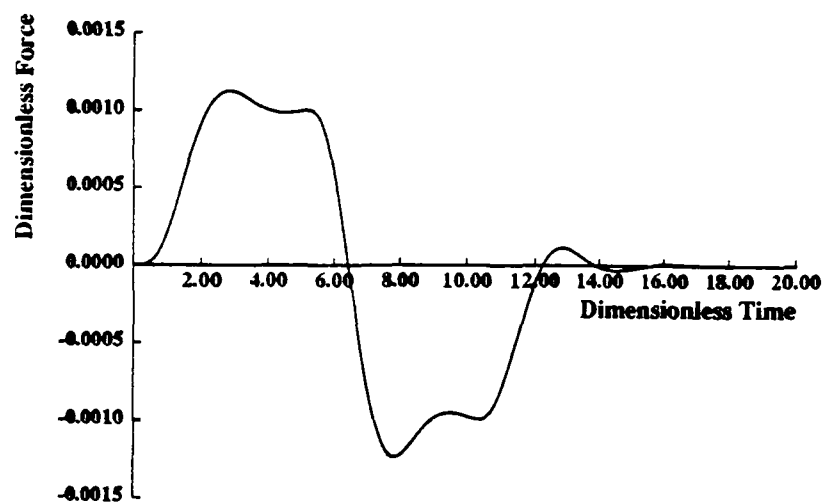
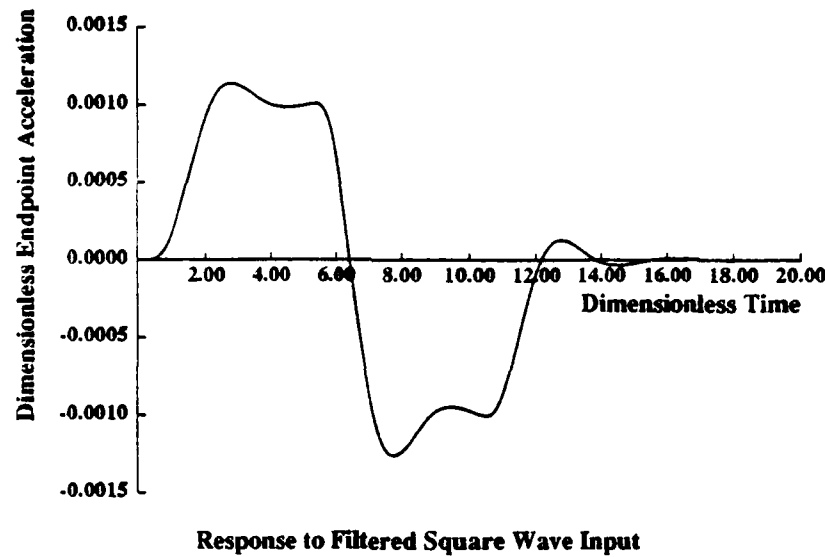Filtered Square Wave Input

(a)

Response to Filtered Square Wave Input

(b)

Figure 3.3: System Response using Butterworth Filtered Input: (a) Filtered Square Wave (b) Position Response.

Response to Filtered Square Wave Input

(c)

Figure 3.3: System Response using Butterworth Filtered Input: (c) Acceleration Response.

3.3 Notch-Filtered Square Wave:

Excitation energy can be introduced above the lowest natural frequency by notching out only the frequencies in the square wave frequency spectrum that correspond to system natural frequencies. Such a notch filter will be implemented by generating new filtered time functions from the square wave input. A similar approach has been presented by Singer [62], who also has pointed out some of the drawbacks.

For the sake of clarity, we will again restrict attention to a system model having only a single natural frequency, as shown in Figure 2.13. Thus, only a single frequency will be filtered from the spectrum of the square wave. To generate the filtered time function, we will analytically remove a band of frequency components from the Fourier spectrum of the square wave. We will then produce a time function corresponding to this filtered spectrum by taking the inverse Fourier transform.
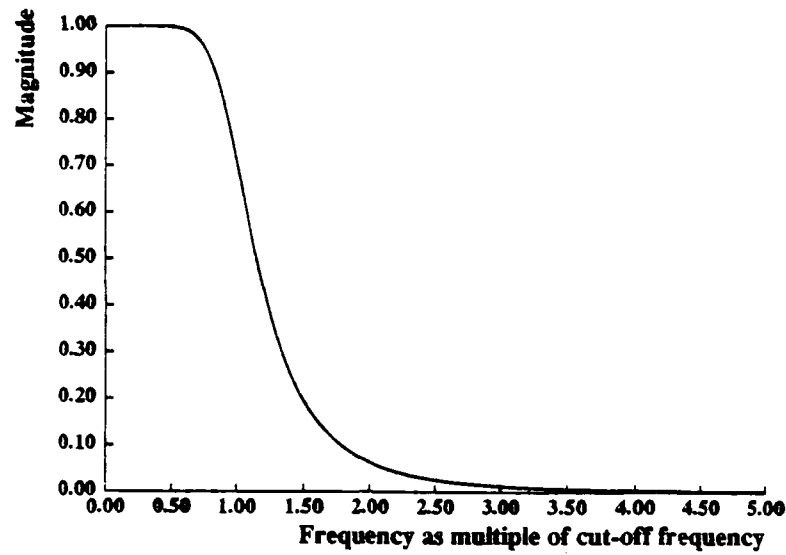
Frequency Response of Butterworth Filter

Figure 3.1: Magnitude of Frequency Response for Fourth-order Butterworth Filter.

fourth-order filter, the magnitude is given by

$$|H_F(\omega)| = \frac{1}{\sqrt{1 + \left(\frac{\omega}{\omega_c}\right)^8}}. \tag{3.2}$$

A plot of this frequency response as a function of the parameter ω/ω_c is given in Figure 3.1. Note the steep fall-off as ω/ω_c becomes greater than 1. In order to attenuate the frequency content at the natural frequency by a factor of 100 ($|H_F(\omega_n)| = 1/100$), the ratio ω_n/ω_c must be equal to 3.16, as can be verified by the magnitude expression (3.2). A Butterworth filter with this cut-off frequency was used to pre-shape a square wave before sending it on to the vibrating system. A block diagram representation of this scheme is shown in Figure 3.2. The filter transfer function $H_F(s)$ and the vibrating system transfer function $H(s)$ are given in terms of dimensionless parameters as follows:

$$H_F(s) = \frac{1}{\left(\frac{\omega_n}{\omega_c}\right)^4 s^4 + 2.613 \left(\frac{\omega_n}{\omega_c}\right)^3 s^3 + 3.414 \left(\frac{\omega_n}{\omega_c}\right)^2 s^2 + 2.613 \left(\frac{\omega_n}{\omega_c}\right) s + 1} \tag{3.3}$$
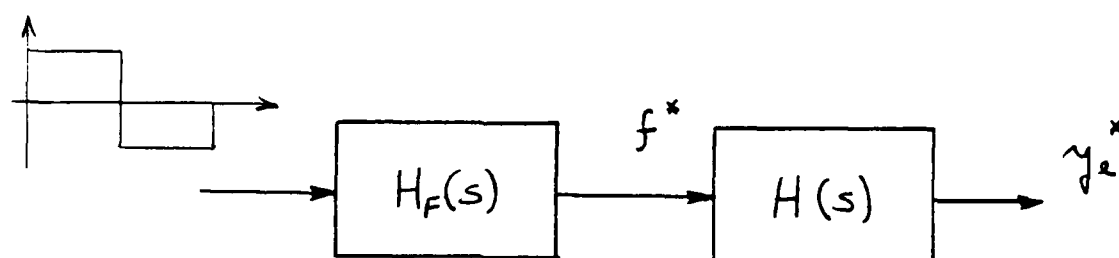
Figure 3.2: Block Diagram of Filtering Scheme.

and

$$H(s) = \frac{2\zeta s + 1}{s^2(s^2 + 2\zeta s + 1)}. \tag{3.4}$$

When we use the filtered square wave as input to this system, with $\omega_n T_s/2\pi = 10$, $\zeta = 0.1$, and $\omega_n/\omega_c = 3.16$, we achieve the response shown in Figure 3.3. Figure 3.3(a) shows the filtered input waveform, (b) shows the position response of the end mass m_2, and (c) shows the acceleration of mass m_2, all in dimensionless units. Notice that the system does not settle down until $\omega_n t/2\pi$ is nearly 16. Since the time-optimal response would have finished in time $\omega_n t/2\pi = 10$, this filtered input takes 60% longer than the time-optimal one. This is also 30% longer than the ramped sinusoid input presented in Chapter 2, which only takes 20% longer than the time-optimal function.

Analog low-pass filters work, but they require considerably longer to complete the move. In the example above, the situation is especially favorable for the filter since the natural frequency is relatively high, permitting a reasonably wide bandwidth for the filtered input. However, in fast systems the parameter $\omega_n T_s/2\pi$ for the lowest mode and for a typical move is closer to 1. To avoid vibration, the filtered signal bandwidth in these systems must be reduced considerably, which increases move time even more. The conclusion is that move time can be significantly reduced if some excitation energy is permitted in the input function above the lowest system natural frequency.

The Fourier transform of a square wave of height F and time duration T_s is given by the expression:

$$F(\omega) = \frac{F}{j\omega}\left(1 - 2e^{-j\omega\frac{T_s}{2}} + e^{-j\omega T_s}\right) \qquad (3.5)$$

Since this expression applies for both positive and negative frequencies ω, removing spectral energy at the natural frequency ω_n requires notching both $-\omega_n$ and $+\omega_n$. The filtered Fourier transform is given by

$$F'(\omega) = \frac{F}{j\omega}\left(1 - 2e^{-j\omega\frac{T_s}{2}} + e^{-j\omega T_s}\right)\left(1 - p_{\Delta\omega}(\omega + \omega_n) - p_{\Delta\omega}(\omega - \omega_n)\right) \qquad (3.6)$$

where $p_{\Delta\omega}(\omega - \omega_n)$ represents a rectangular pulse of height 1 and width $\Delta\omega$ centered at $\omega = \omega_n$. Notice that all frequency components in the two frequency bands about $\omega = \pm\omega_n$ have been removed by essentially subtracting the original spectrum in the two regions specified by the pulses.

The inverse Fourier transform of the sum of these two rectangular pulses is given by

$$f_p(t) = \frac{1}{2\pi}\int_{-\infty}^{\infty}\left[p_{\Delta\omega}(\omega + \omega_n) + p_{\Delta\omega}(\omega - \omega_n)\right]e^{j\omega t}d\omega = \frac{2\sin\Delta\omega t}{\pi t}\cos\omega_n t. \qquad (3.7)$$

The filtered time function can be completely represented in terms of the unit step function $u(t)$ and its time convolutions (represented by the symbol $*$) with the sinusoidal function $f_p(t)$ of equation (3.7):

$$f'(t) = F\left[u(t) - 2u(t - T_s/2) + u(t - T_s)\right]$$

$$- F\left[f_p(t) * u(t) - 2f_p(t - T_s/2) * u(t - T_s/2) + f_p(t - T_s) * u(t - T_s)\right] \qquad (3.8)$$

These time convolutions can be evaluated as

$$f_p(t) * u(t) = \frac{1}{\pi}\int_{(\omega_n - \Delta\omega)t}^{(\omega_n + \Delta\omega)t}\frac{\sin\tau}{\tau}d\tau. \qquad (3.9)$$

The integral on the right-hand-side is known as the sine integral, which is a tabulated function. Thus, the above expression can be rewritten as

$$f_p(t) * u(t) = \frac{1}{\pi}\left[\text{si}\left((\omega_n + \Delta\omega)t\right) - \text{si}\left((\omega_n - \Delta\omega)t\right)\right] \qquad (3.10)$$
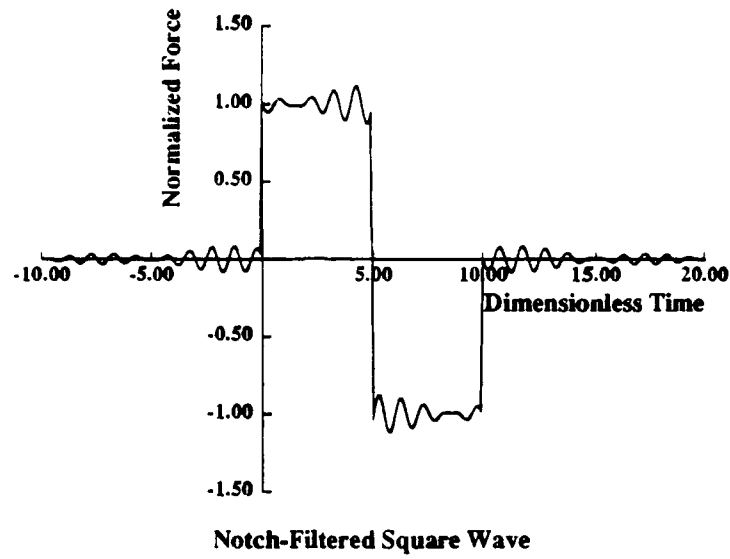
Notch-Filtered Square Wave

Figure 3.4: Notch-Filtered Square Wave Time Function.

where the sine integral si is defined by

$$\text{si}(t) = -\int_t^\infty \frac{\sin \tau}{\tau} d\tau = -\frac{\pi}{2} + \int_0^t \frac{\sin \tau}{\tau} d\tau. \qquad (3.11)$$

Using these sine integral expressions, the time function $f'(t)$ can be rewritten in terms of dimensionless parameters as

$$
\begin{aligned}
f'(\omega_n t) =\ & F\left[u(\omega_n t) - 2u\left(\omega_n(t - T_s/2)\right) + u\left(\omega_n(t - T_s)\right)\right] \\
& - F\left[\frac{1}{\pi}\left[\text{si}\left((\omega_n + \Delta\omega)t\right) - \text{si}\left((\omega_n - \Delta\omega)t\right)\right]\right. \\
& - \frac{2}{\pi}\left[\text{si}\left((\omega_n + \Delta\omega)(t - T_s/2)\right) - \text{si}\left((\omega_n - \Delta\omega)(t - T_s/2)\right)\right] \quad (3.12) \\
& \left. + \frac{1}{\pi}\left[\text{si}\left((\omega_n + \Delta\omega)(t - T_s)\right) - \text{si}\left((\omega_n - \Delta\omega)(t - T_s)\right)\right]\right].
\end{aligned}
$$

A plot of this filtered square wave input computed as a function of time is shown in Figure 3.4, for values of $\omega_n T_s/2\pi = 10$ and $\Delta\omega/\omega_n = 0.1$ (a $\pm 10\%$ frequency band).

To strictly maintain zero magnitude in the filtered frequency spectrum requires that the input start before $t = 0$ and end after $t = T_s$. This can readily be seen in Figure 3.4. In fact, the input function would need to occur for all time. If this

input function is truncated by a window of half-width T_t centered at $t = T_s/2$, then the input is active in the range $T_s/2 - T_t < t < T_s/2 + T_t$. Truncation of the time function will give a nonzero frequency spectrum in the specified frequency band. The Fourier transform of this truncated time function gives the dimensionless frequency spectrum as

$$F^*(\omega T_s)| = \frac{1}{FT_s} \left| \int_{T_s/2 - T_t}^{T_s/2 + T_t} f'(t) e^{-j\omega t} dt \right| \tag{3.13}$$

When this integral is evaluated, the following expression results:

$$F^*(\omega T_s)| = \frac{1}{\omega T_s} \left| 2(\cos \frac{\omega T_s}{2} - 1) \right.$$
$$\left. - \frac{1}{\pi} \left[\cos \frac{\omega T_s}{2} F_1(\omega T_s) + \sin \frac{\omega T_s}{2} F_2(\omega T_s) - 2F_3(\omega T_s) - 2\cos\beta_1\omega T, F_4 \right] \right| \tag{3.14}$$

where F_1, F_2, and F_3 are functions of ωT_s and F_4 is a constant. To simplify the representation of these functions, we define the following frequencies and coefficients:

$$\omega_1 T = (1 + \Delta\omega/\omega_n)(\omega_n T_t + \omega_n T_s/2) \tag{3.15}$$

$$\omega_2 T = (1 - \Delta\omega/\omega_n)(\omega_n T_t + \omega_n T_s/2) \tag{3.16}$$

$$\omega_3 T = (1 + \Delta\omega/\omega_n)(\omega_n T_t - \omega_n T_s/2) \tag{3.17}$$

$$\omega_4 T = (1 - \Delta\omega/\omega_n)(\omega_n T_t - \omega_n T_s/2) \tag{3.18}$$

$$\omega_5 T = (1 + \Delta\omega/\omega_n)\omega_n T_t \tag{3.19}$$

$$\omega_6 T = (1 - \Delta\omega/\omega_n)\omega_n T_t \tag{3.20}$$

$$\beta_1 = \frac{\omega_n T_t}{\omega_n T_s} \tag{3.21}$$

$$\beta_2 = \left(\beta_1 + \frac{1}{2} \right) \tag{3.22}$$

$$\beta_3 = \left(\beta_1 - \frac{1}{2} \right) \tag{3.23}$$

Using these parameters, the functions F_1 through F_4 can be written in terms of the sine integral si, defined by (3.11), and the cosine integral ci, defined by

$$\text{ci}(t) = -\int_t^\infty \frac{\cos \tau}{\tau} d\tau = \ln|t| + \int_0^t \frac{\cos \tau - 1}{\tau} d\tau. \tag{3.24}$$

The functions can then be expressed as follows:

$$\begin{aligned}
F_1(\omega T_s) &= \operatorname{si}(\omega_1 T + \beta_2 \omega T_s) - \operatorname{si}(\omega_2 T + \beta_2 \omega T_s) + \operatorname{si}(\omega_3 T + \beta_3 \omega T_s) \\
&\quad - \operatorname{si}(\omega_4 T + \beta_3 \omega T_s) + \operatorname{si}(\omega_1 T - \beta_2 \omega T_s) - \operatorname{si}(\omega_2 T - \beta_2 \omega T_s) \quad (3.25) \\
&\quad + \operatorname{si}(\omega_3 T - \beta_3 \omega T_s) - \operatorname{si}(\omega_4 T - \beta_3 \omega T_s)
\end{aligned}$$

$$\begin{aligned}
F_2(\omega T_s) &= -\operatorname{ci}(\omega_1 T + \beta_2 \omega T_s) + \operatorname{ci}(\omega_2 T + \beta_2 \omega T_s) + \operatorname{ci}(\omega_3 T + \beta_3 \omega T_s) \\
&\quad - \operatorname{ci}(\omega_4 T + \beta_3 \omega T_s) + \operatorname{ci}(\omega_1 T - \beta_2 \omega T_s) - \operatorname{ci}(\omega_2 T - \beta_2 \omega T_s) \quad (3.26) \\
&\quad - \operatorname{ci}(\omega_3 T - \beta_3 \omega T_s) + \operatorname{ci}(\omega_4 T - \beta_3 \omega T_s)
\end{aligned}$$

If $\omega_n T_t = \omega_n T_s/2$, then

$$\begin{aligned}
F_2(\omega T_s) &= -\operatorname{ci}(\omega_1 T + \beta_2 \omega T_s) + \operatorname{ci}(\omega_2 T + \beta_2 \omega T_s) + \operatorname{ci}(\omega_1 T - \beta_2 \omega T_s) \\
&\quad - \operatorname{ci}(\omega_2 T - \beta_2 \omega T_s) - \ln|\omega_2 T + \beta_2 \omega T_s| + \ln|\omega_1 T + \beta_2 \omega T_s| \quad (3.27) \\
&\quad - \ln|\omega_1 T - \beta_2 \omega T_s| + \ln|\omega_2 T - \beta_2 \omega T_s|
\end{aligned}$$

$$\begin{aligned}
F_3(\omega T_s) &= \operatorname{si}(\omega_5 T + \beta_1 \omega T_s) - \operatorname{si}(\omega_6 T + \beta_1 \omega T_s) + \operatorname{si}(\omega_5 T - \beta_1 \omega T_s) \\
&\quad - \operatorname{si}(\omega_6 T - \beta_1 \omega T_s) \qquad (3.28)
\end{aligned}$$

$$F_4 = \operatorname{si}(\omega_1 T) - \operatorname{si}(\omega_2 T) + \operatorname{si}(\omega_3 T) - \operatorname{si}(\omega_4 T) - 2\operatorname{si}(\omega_5 T) + 2\operatorname{si}(\omega_6 T) \qquad (3.29)$$

A plot of this frequency spectrum, with values of $\omega_n T_s/2\pi = 10$, $\Delta\omega/\omega_n = 0.1$, and $\omega_n T_t/2\pi = 5$ is shown in Figure 3.5(a). In this case, the input function has been truncated so that only the portion for $0 < t < T_s$ remains. The frequency spectrum shows considerable spectral magnitude at the dimensionless frequency $\omega_n T_s/2\pi = 10$, where the input should have been filtered. The considerable energy which this input function contains at the natural frequency is a direct result of the truncation in time.

If a longer portion of the input function is used, then the spectral magnitude near the natural frequency will decrease. This is illustrated in Figure 3.5(b) and (c).
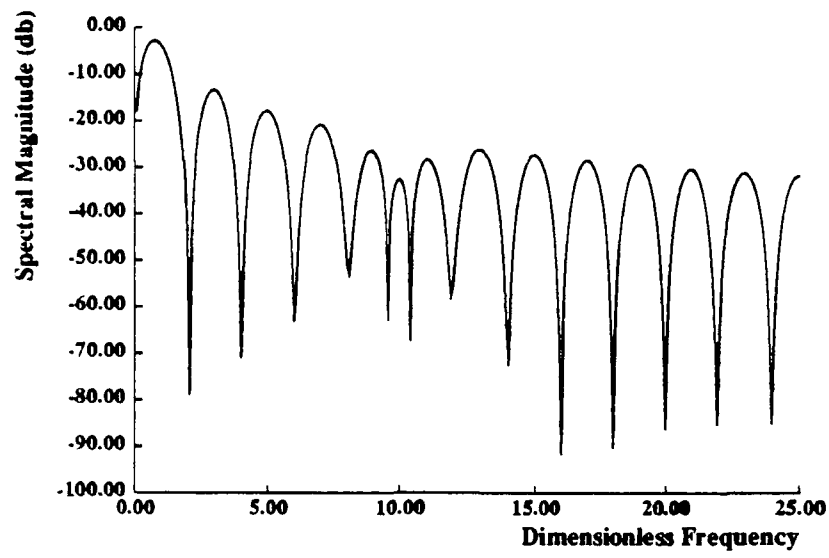
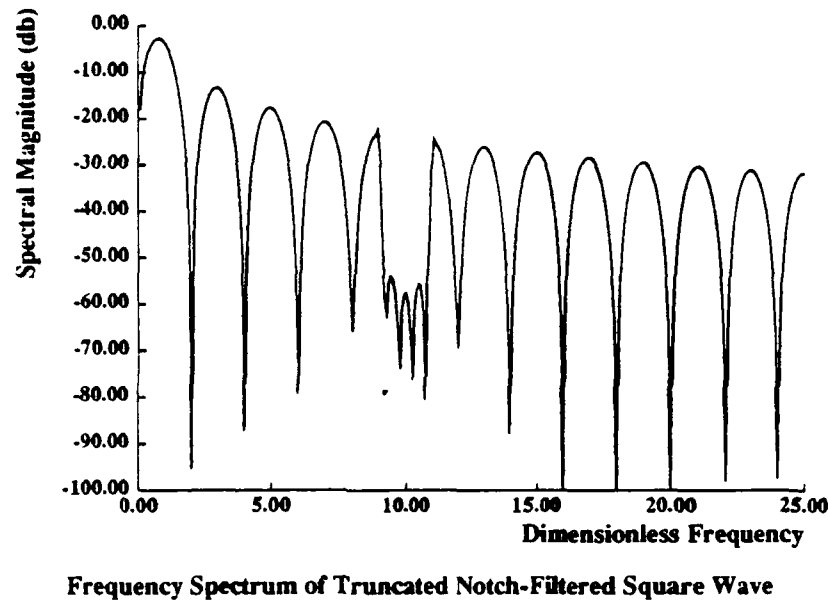Frequency Spectrum of Truncated Notch-Filtered Square Wave

(a)
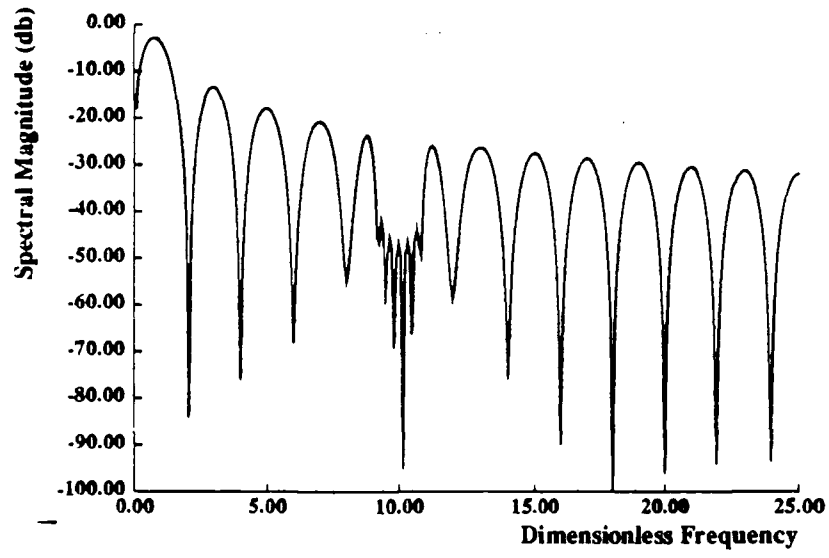
— Frequency Spectrum of Truncated Notch-Filtered Square Wave

(b)

Figure 3.5: Frequency Spectra of Truncated Notch-Filtered Square Wave: (a) $\omega_n T_t / 2\pi = 5$ (b) $\omega_n T_t / 2\pi = 15$.

Frequency Spectrum of Truncated Notch-Filtered Square Wave

(c)

Figure 3.5: Frequency Spectra of Truncated Notch-Filtered Square Wave: (c) $\omega_n T_t / 2\pi = 50$.

In Figure 3.5(b), the input is truncated with a window of half-width $\omega_n T_t / 2\pi = 15$. This corresponds to the function as shown in its entirety in Figure 3.4. In figure 3.5(c), the truncation window has half-width $\omega_n T_t / 2\pi = 50$. This corresponds to an input which lasts for a total dimensionless time of 100 multiples of 2π. This is an order of magnitude longer to cover the same distance than the original square wave. Yet the spectral magnitude near resonance is still more than an order of magnitude larger than that of the corresponding ramped sinusoid function shown in Figure 2.7, which only takes 25% longer than the square wave input.

In summary, the time function produced by completely removing the frequency components in a notch near resonance has infinite duration. When this input is truncated in time, considerable energy still remains near resonance. As spectral energy is reduced, the input function takes longer to complete. To achieve sufficient

filtering at resonance, so much of the input must be retained that the move takes much longer than necessary. The ramped sinusoid functions, in contrast, have lower spectral magnitude at resonance with a much smaller time penalty.

Before closing this chapter, it is worthwhile to comment on the use of continuous Fourier transforms in the development of the preceding functions. It would have been easier to take discrete Fourier transforms (FFT's). However, the resolution of these Fourier transforms is limited by the duration of the time function. With a square wave input of duration $t = T_s$, the discrete frequency components in the FFT occur only at multiples of $2\pi/T_s$. Everywhere in between, the FFT claims to be zero when in fact the continuous Fourier transform has discernible amplitude. This is a result of the fact that the FFT assumes that the input function is periodic with period T_s when in reality it only occurs for time $0 < t < T_s$. Should the actual natural frequency lie between these discrete frequency points, even zeroing out the adjacent components will not zero the frequency component at the actual frequency in the continuous Fourier transform of the filtered input. Increased frequency resolution can be obtained by adding zeros to the time function from $t = T_s$ to $t = T_{max} > T_s$, thus giving frequency components at multiples of $2\pi/T_{max}$. However, this does not alter the original problem. Therefore, even though the computation of continuous Fourier transforms is more complex, it ensures that all frequency components are at least ideally reduced to zero.

3.4 Closure:

We have presented two alternative filtering techniques in this chapter to put the work of Chapter 2 into perspective. Instead of constructing a function to look like a square wave while maintaining some specified bounds in the frequency spectrum, we tried here to filter out the specified frequency components of a square wave. A simple low-pass filter can be used to remove all frequency components of the input

above the filter cut-off frequency, which is chosen to be somewhat less than the lowest system natural frequency. A fourth-order Butterworth filter works quite well in reducing residual vibration, but response time is relatively long because no input energy is passed above the lowest natural frequency of the vibrating system.

Another alternative is to generate time functions from a square wave spectrum that has had all frequency components removed in a band surrounding the natural frequency. This produces alternative time functions to those specified by the ramped sinusoid series, which are given in terms of sine integrals. These functions must start considerably earlier and end considerably later than the corresponding square wave in order to achieve sufficient filtering. Thus, move time is unacceptably long.

Therefore, although these filtering techniques present viable alternatives, both the low-pass filter and the notch filter lead to considerably longer move time. The ramped sinusoid functions, however, permit a simpler implementation of filtered inputs without excessively increasing move time.

Closed-Loop Implementation of Shaped Inputs

Chapter 4

4.1 Introduction:

The shaped inputs developed in Chapter 2 are given strictly as functions of time. This means that they can only directly be used in systems where the force can be specified as a function of time. Since closed-loop systems with feedback determine control force as a function of system states rather than as a function of time, these shaped inputs can be specified directly only in open-loop systems. Because most physical systems experience disturbances, nonlinearities, and parameter uncertainty, accurate performance cannot be guaranteed for open-loop control. Thus, we need some way of incorporating these shaped inputs into a closed-loop control system.

In this chapter, we will present several methods for incorporating shaped inputs into closed-loop systems. The first scheme directly sends the shaped force into the vibrating system. This represents the feedforward portion of the control force. This same input also goes into a reference model of the vibrating system to generate an ideal response. This response is compared with feedback states and the error is used as an additional control input to help generate the desired ideal response even when

56

the actual system differs from the ideal system.

Some of the drawbacks of this method are then discussed, keeping in mind the limitations which actual systems impose on the controller. These observations serve to motivate a different closed-loop implementation. In this new formulation, only motor states are measured and a simple PD loop is used to achieve accurate positions in the presence of disturbances. The shaped force input is converted into an equivalent position reference trajectory and the motor feedback allows the closed-loop system to follow this time-varying reference signal.

Once an appropriate closed-loop implementation has been developed, we look more carefully at the optimal regulator formulation and indicate several cases in which it fails to give adequate performance. Shaped reference inputs then serve to augment the optimal regulator and minimize residual vibration.

4.2 Model-Reference-Based Control Scheme:

4.2.1 Overview of Concept:

The first closed-loop implementation to be studied involves the use of a reference system model. This control scheme is not to be confused with Model Reference Adaptive Control. State feedback is used to impose on the actual system the ideal behavior of the reference system. The shaped force input is directly applied to both systems. The error between the actual response and the ideal model response serves to correct the control input to maintain the desired response.

A key feature of this control implementation is the use of the shaped force as a direct feedforward input to the controlled system. The control input is thus specified as a function of time as well as a function of the error states. The main advantage of introducing a feedforward signal is the ability to deal with unwanted resonant vibrations before they occur by proper frequency-shaping of the feedforward functions. An outline of this approach was presented in an earlier paper [63].
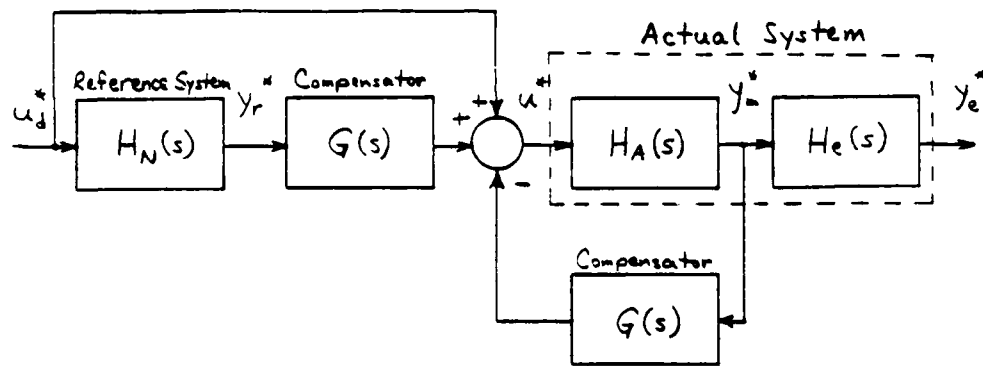
Figure 4.1: Block Diagram of Model-Reference-Based Control Scheme.

The use of additional feedforward signals to reduce system tracking error is quite common. Dougherty, et al. [22] suggest the use of acceleration feedforward in the pointing control of the Space Telescope. A similar technique has been used to compute joint torques of serial-link robot arms. The acceleration of the reference trajectory is used to reduce tracking errors, as described by An, Atkeson, and Hollerbach [64]. In each case, a feedforward signal derived from the reference is directly fed to the system to reduce tracking error. However, no frequency-shaping is done on the feedforward functions to reduce vibration.

4.2.2 Controller Specifications:

A block diagram of the proposal control scheme is shown in Figure 4.1. Since in typical systems the motor position is usually measured instead of the absolute endpoint position, we will do likewise here. Thus, an additional transfer function $H_e(s)$ is necessary to obtain the endpoint position y_e^* as a function of motor position y_m^*. The compensator $G(s)$ represents the combination of a state feedback control law and a state estimator. State feedback ensures that all the actual system states approach the ideal reference states. Since only motor position is measured, the remaining states are estimated using a steady-state Kalman filter.

To evaluate this control scheme, very simple models were used to represent the
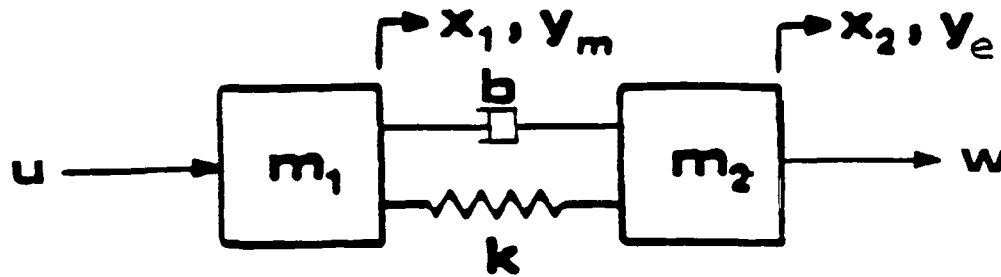
Figure 4.2: Damped Two-Mass System Model.

Table 4.1

Definition of Dimensionless Parameters

$t^* = \omega_N t / 2\pi$	$u^* = \dfrac{u}{(m_1 + m_2)y_f\omega_N^2}$
$y_m^* = \dfrac{y_m}{y_f}$	$v^* = \dfrac{v}{y_f}$
$y_e^* = \dfrac{y_e}{y_f}$	$w^* = \dfrac{w}{(m_1 + m_2)y_f\omega_N^2}$
$\ddot{y}_e^* = \dfrac{\ddot{y}_e}{\omega_N^2 y_f}$	

ideal plant and the actual plant. A simple damped two mass, one spring model, shown in Fig 4.2 represents a system with one resonant mode and one rigid body mode. The control force u acts on mass m_1, while a disturbance force w acts on m_2, the mass we wish to control. For the sake of generality, all parameters have been nondimensionalized, as shown in Table 4.1, where y_f is the final position of the controlled mass, v is the measurement noise, and ω_N is the nominal undamped natural frequency, given by

$$\omega_N = \sqrt{\frac{k}{m_1}\left(1 + \frac{m_1}{m_2}\right)} \qquad (4.1)$$

and ζ is the damping ratio, given by

$$\zeta = \frac{b}{2}\sqrt{\frac{1}{km_1}\left(1 + \frac{m_1}{m_2}\right)}. \tag{4.2}$$

The ideal plant is assumed to vibrate at the nominal natural frequency ω_N and to have no disturbance force acting on it. Its transfer function relating the control input u^* to the motor position y_m^* is given by:

$$H_N(s) = \frac{y_m^*(s)}{u^*(s)} = \frac{(1 + \frac{m_2}{m_1})s^2 + 2\zeta s + 1}{s^2(s^2 + 2\zeta s + 1)} \tag{4.3}$$

This ideal plant is used to generate the motor position reference y_r^* for the feedback loop.

The actual plant is assumed to vibrate at a natural frequency denoted by ω_A, which may be different from the nominal frequency ω_N. It also has a disturbance force w^* acting on mass m_2. Therefore, it has two transfer functions associated with the measurement y_m^*:

$$H_A(s) = \frac{y_m^*(s)}{u^*(s)} = \frac{(1 + \frac{m_2}{m_1})s^2 + 2\zeta\left(\frac{\omega_A}{\omega_N}\right)s + \left(\frac{\omega_A}{\omega_N}\right)^2}{s^2[s^2 + 2\zeta\left(\frac{\omega_A}{\omega_N}\right)s + \left(\frac{\omega_A}{\omega_N}\right)^2]} \tag{4.4}$$

$$\frac{y_m^*(s)}{w^*(s)} = \frac{2\zeta\left(\frac{\omega_A}{\omega_N}\right)s + \left(\frac{\omega_A}{\omega_N}\right)^2}{s^2[s^2 + 2\zeta\left(\frac{\omega_A}{\omega_N}\right)s + \left(\frac{\omega_A}{\omega_N}\right)^2]} \tag{4.5}$$

In addition, the endpoint position is given in terms of the motor position by

$$H_e(s) = \frac{y_e^*(s)}{y_m^*(s)} = \frac{2\zeta\left(\frac{\omega_A}{\omega_N}\right)s + \left(\frac{\omega_A}{\omega_N}\right)^2}{\left(1 + \frac{m_2}{m_1}\right)s^2 + 2\zeta\left(\frac{\omega_A}{\omega_N}\right)s + \left(\frac{\omega_A}{\omega_N}\right)^2}. \tag{4.6}$$

This plant represents the idealized model of the actual system and is used to derive the optimal feedback compensator for $\omega_A/\omega_N = 1$. It could also have included additional nonideal characteristics, such as nonlinearities and unmodeled modes, but for simplicity these were neglected in this analysis.

The state-space formulation of the actual plant model is given by:

$$\begin{aligned}
\dot{\mathbf{x}} &= A\mathbf{x} + bu^* + \gamma w^* \\
y_m^* &= c^T\mathbf{x} \\
z^* &= c^T\mathbf{x} + v^*
\end{aligned} \tag{4.7}$$

where **x** is the state vector consisting of endpoint position y_e^* and its three derivatives, A is the dynamics matrix, b is the control input vector, γ is the disturbance input vector, w^* is the dimensionless disturbance force acting on m_2, c is the output vector, z^* is the noisy measurement of y^*, and v^* is the nondimensionalized noise that corrupts the measurement of y_m^*.

The feedback compensator shown in Fig. 4.1 represents the transfer function equivalent of an optimal state feedback controller and a steady-state Kalman filter applied to the plant model given by Equation (4.7). This approach was motivated by an article by Bryson [65] that discusses a classical interpretation of optimal control theory. Basically, quadratic performance index weightings are adjusted to achieve desirable filtering properties in the compensator. The plant model used to construct the compensator was assumed to have $\omega_A/\omega_N = 1$, $m_1/m_2 = 1$, and $\zeta = 0.1$.

In conventional Kalman filter design, white noise processes are assumed for w^* and v^*. In designing this compensator, the spectral densities for w^* and v^* were treated as parameters that were selected to achieve good filtering of the endpoint position measurement at higher frequencies. Thus, the Kalman filter accommodates disturbances and measurement noise as well as estimating unmeasured system states.

The feedback compensator was designed in two parts, as suggested by the separation principle. In this development, u^* is assumed to consist only of the feedback component, i.e. no feedforward function is applied. The state feedback gains were determined by minimizing the following quadratic performance index:

$$J = \frac{1}{2} \int_0^\infty (y_e^{*2} + \rho u^{*2})\, dt \qquad (4.8)$$

The value of ρ was selected to be $1/49$ so as to weight the penalty on endpoint position error more heavily than control input. This leads to a set of constant feedback gains on the system states.

The steady-state Kalman filter gains were determined so as to minimize the expected value of

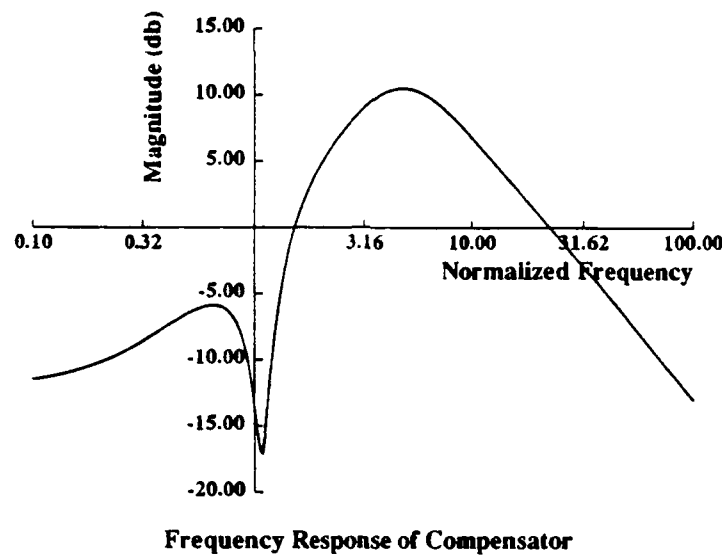$$\int_0^\infty (z^* - c^T \mathbf{x})^2\, dt \qquad (4.9)$$

Frequency Response of Compensator

Figure 4.3: Magnitude of Frequency Response of Optimal Compensator.

given the spectral densities q and r for w^* and v^*, respectively. In analogy with the optimal regulator problem, this minimum variance observer leads to a steady-state Riccati equation which depends on the ratio r/q. A value of 1 was used here for r/q to give a compensator capable of accommodating both plant disturbances and measurement noise.

The final compensator transfer function for these weightings is given by:

$$G(s) = \frac{u^*(s)}{y_m^*(s)} = -\frac{22(s + 0.27)(s^2 + 0.12s + 1.5)}{(s^2 - 0.94s + 1.3)(s^2 + 6.6s + 22)} \qquad (4.10)$$

This transfer function can be represented in a frequency response plot. Such a depiction emphasizes the filtering properties of the compensator, which depend on the number of controlled states, a fact pointed out by Larson and Likins [66]. A plot of the magnitude of the frequency response for our compensator is shown in Fig. 4.3. Here the frequency is normalized to the resonant frequency of the system. Near resonance, the compensator acts as a notch filter. Beyond resonance, higher frequency components are at first amplified by the full state feedback controller, then attenuated by the Kalman filter.

This compensator has a pair of poles in the right-half-plane. These poles will not appear in the closed-loop transfer function, but they could appear as closed-loop zeros if a different compensator is used in the feedforward path. This can potentially lead to poor transient response.

If the original plant for which the compensator is developed is more lightly damped than $\zeta = 0.1$, then the characteristics of the compensator change. If the open-loop damping ratio is assumed to be $\zeta = 0.02$, the compensator for the same weightings as before has the transfer function given by

$$G(s) = \frac{u^*(s)}{y_m^*(s)} = -\frac{22(s + 0.25)(s^2 - 0.025s + 1.3)}{(s^2 - 0.89s + 1.6)(s^2 + 6.6s + 22)}. \tag{4.11}$$

Notice that this compensator has a pair of zeros in the right-half-plane in addition to a pair of poles. This is common in optimal controllers for systems with lightly damped poles, as pointed out by Martin and Bryson [67]. In the feedback loop, this is of no concern. However, if this same compensator is used in a tracking controller to act on the reference signal, then the nonminimum phase zeros occur in the closed-loop system and can cause poor transient performance. This is a result of the fact that this compensator was derived for a regulator control. Typically, a new compensator would be derived for a tracking controller that would have no right-half-plane zeros.

The closed-loop transfer function between y_r^* and y_m^* for $\zeta = 0.1$ is given by

$$\frac{y_m^*(s)}{y_r^*(s)} = \frac{44(s + 0.27)(s^2 + 0.1s + 0.5)(s^2 + 0.12s + 1.5)}{(s^2 + 1.4s + 0.69)(s^2 + 0.56s + 1.4)(s^2 + 2.7s + 2.3)(s^2 + 1.2s - 3.1)} \tag{4.12}$$

The right-half-plane poles of the compensator do not appear as right-half-plane zeros because the same compensator is used in the feedforward path. The dominant closed-loop poles (with the lowest natural frequencies) have damping ratios of 0.84 and 0.24. Thus, the optimal regulator has replaced the lightly-damped open-loop poles with more heavily damped closed-loop poles. The dominant closed-loop damping ratio achievable with an optimal regulator depends on the control weight ρ, as
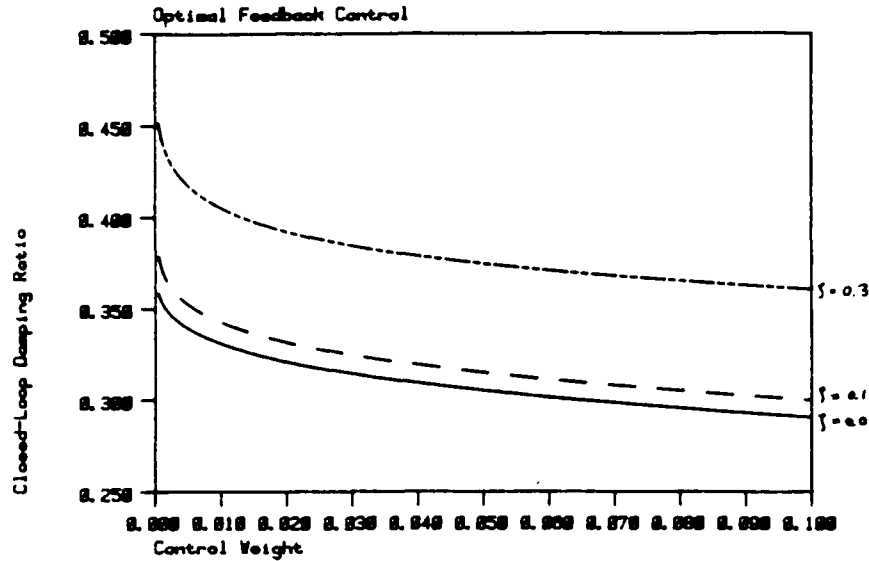
Figure 4.4: Closed-Loop Damping Ratios as a Function of Control Weight for Several Open-Loop Damping Ratios.

shown in Figure 4.4 for several open-loop damping ratios. As control weight decreases, the damping ratio of the dominant closed-loop poles increases. Systems having higher inherent open-loop damping can achieve larger closed-loop damping. But even with an optimal controller, the maximum achievable closed-loop damping ratio is limited.

4.2.3 Closed-Loop Simulation Results:

The control scheme suggested in Fig. 4.1 was used to determine closed-loop responses using the shaped functions of Chapter 2 as the feedforward inputs u_d^*. A dimensionless time $\omega_N T_s$ was used to specify move time relative to the resonant period. The time T_s represents the time to move the center of mass of the two-mass system a distance y_f when driven by an input force which is $+F$ for the first half of the move and $-F$ for the second half. Therefore, $\omega_N T_s$ is given by:

$$\omega_N T_s = \omega_N \sqrt{4(m_1 + m_2)y_f/F} \qquad (4.13)$$

The actual dimensionless move time is somewhat longer than $\omega_N T_s$ since the shaped forcing functions do not provide as much energy for a given peak force F.
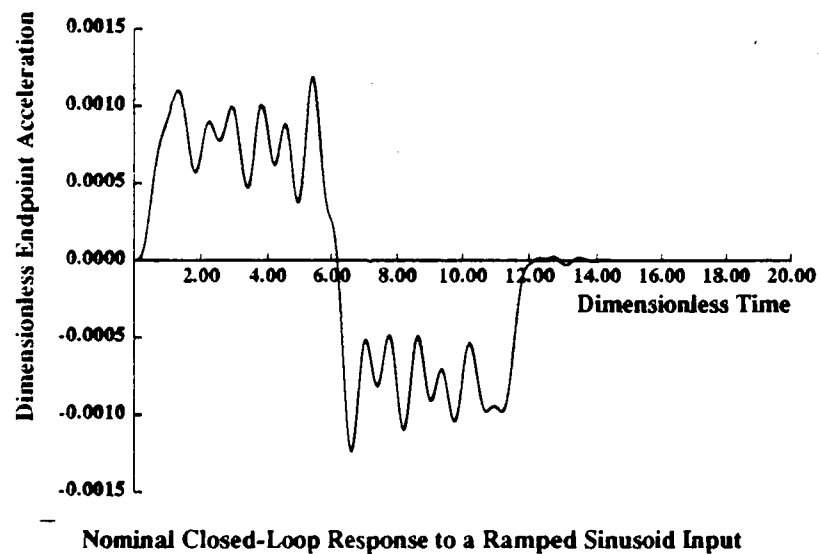
For this series of simulations, a value of 10 was used for the parameter $\omega_N T_s/2\pi$. damping ratio was assumed to be 0.1, and mass ratio m_1/m_2 was taken to be 1. Three sets of simulations were performed. In the first, the actual plant was taken to be identical to the ideal model, with $\omega_A/\omega_N = 1$. The control system generates the required control input to produce the output that is called for by the forcing function. Of course, when the controlled system is ideal, as we assume here, the output exactly follows the reference input and no feedback correction is generated. However, the feedforward function applied here leads to some residual vibration even in the ideal system. Therefore, the reference input imposed on the feedback loop was set to y_f after the feedforward function ended in order to bring the system to rest. This response is shown in Figure 4.5, with total control input in (a) and acceleration response $(\ddot{y}_e^*)$ of m_2 in (b). Notice that the feedforward function alone brings the system to final position with very little vibration for the feedback loop to damp out. This gives negligible settling time with residual vibration nearly eliminated beyond $\omega_N t/2\pi = 13$.

In the second simulation, the actual system was assumed to have a natural frequency different from the nominal frequency, with $\omega_A/\omega_N = 0.9$. The response under these conditions is shown in Figure 4.6. In this case, residual vibration takes until $\omega_N t/2\pi = 14$ before it settles. This is longer than the nominal system response of Figure 4.5 because the initial residual amplitude is higher for damped systems with an error in natural frequency.

When a disturbance is added to the model for the actual system with $\omega_A/\omega_N = 1$. the advantages of combining feedforward and feedback control become apparent. Figure 4.7 shows the response when a constant opposing disturbance force acts on the end mass. A force of dimensionless amplitude 0.0003 was used. This represents a disturbance having 30% of the peak force level of the input functions. Notice that
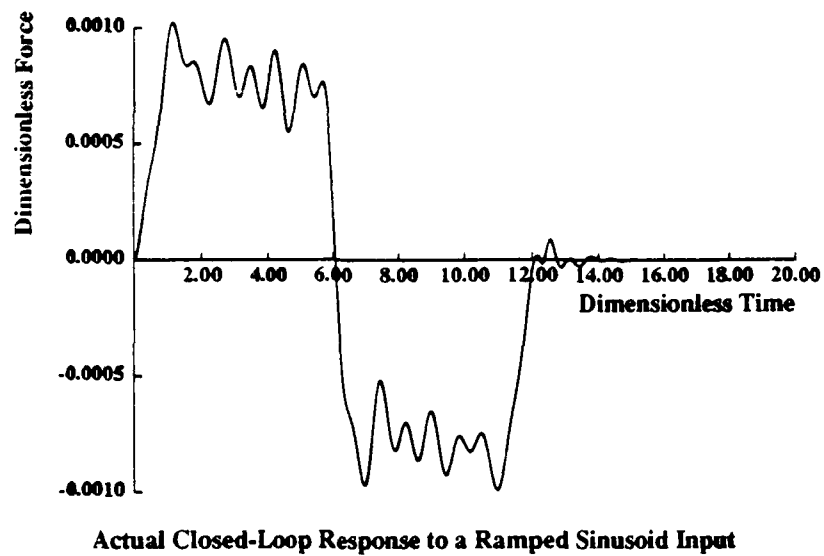
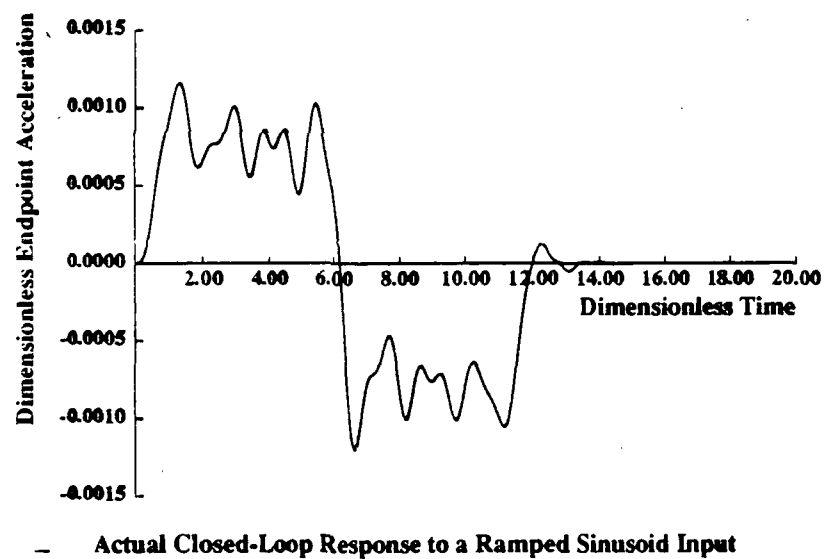Nominal Closed-Loop Response to a Ramped Sinusoid Input

(a)

Nominal Closed-Loop Response to a Ramped Sinusoid Input
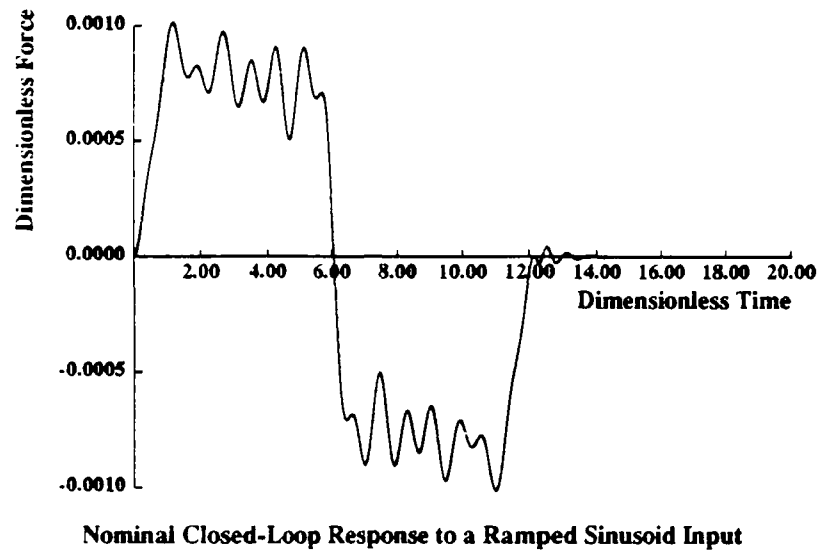
(b)

Figure 4.5: Simulated Response for Nominal System using Model-Reference-Based Controller: $\omega_N T_s/2\pi = 10$, $\zeta = 0.1$: (a) Control Force (b) Acceleration Response.

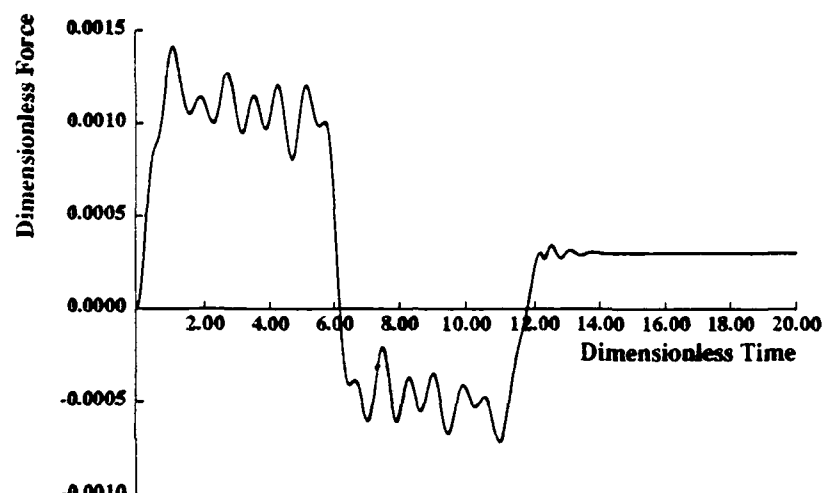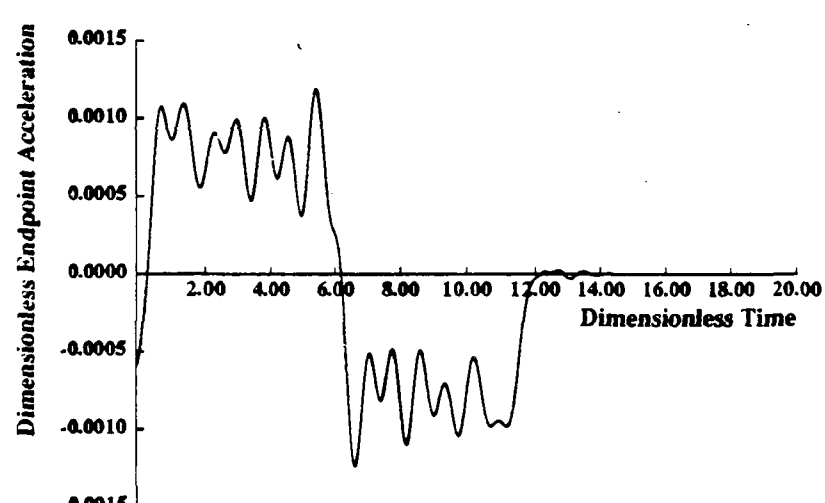Actual Closed-Loop Response to a Ramped Sinusoid Input

(a)

Actual Closed-Loop Response to a Ramped Sinusoid Input

(b)

Figure 4.6: Simulated Response for Actual System using Model-Reference-Based Controller; $\omega_N T_s/2\pi = 10$, $\zeta = 0.1$, $\omega_A/\omega_N = 0.9$: (a) Control Force (b) Acceleration Response.

Closed-Loop Response to a Ramped Sinusoid Input with Disturbance

(a)

Closed-Loop Response to a Ramped Sinusoid Input with Disturbance

(b)

Figure 4.7: Simulated Response for Nominal System using Model-Reference-Based Controller with 0.0003 Disturbance Force: $\omega_N T_s / 2\pi = 10$, $\zeta = 0.1$: (a) Control Force (b) Acceleration Response.

the total control input differs from the feedforward function at the start because the feedback loop has recognized that output motion is lagging behind the reference input. Beyond this initial transient, the control input is just as before except it includes a constant force offset to oppose the disturbance. Settling time remains essentially the same as without the disturbance. Thus, the model-reference-based control scheme achieves response comparable to that for an open-loop system, even in the presence of a disturbance force.

4.2.4 Discussion:

Although this feedforward/feedback control scheme seems to work quite nicely, it has a number of drawbacks. First, derivatives of the reference position y_r^* undergo a sudden jump to zero when the feedforward input ends in order to ensure that any residual vibration remaining in the ideal system is damped out. This reference discontinuity could lead to a control input that excites vibration if the actual system differs significantly from the nominal system.

Second, the feedforward inputs have been constructed on the assumption that the only dynamics of interest are the reference model dynamics. However, if the actual system is sufficiently different from the reference model, additional dynamics will exist. This can be illustrated by determining the transfer function between y_m^* and u_d^* in terms of the compensator $G(s)$, reference system model $H_N(s)$, and actual system $H_A(s)$:

$$\frac{y_m^*(s)}{u_d^*(s)} = \frac{H_A(s)}{1 + G(s)H_A(s)} \left(1 + G(s)H_N(s)\right) \tag{4.14}$$

As long as $H_A(s) = H_N(s)$, only the dynamics of $H_N(s)$ occur. But if $H_A(s) \neq H_N(s)$, then more complicated dynamics exist which have been ignored in the design of the feedforward inputs. More specifically, the natural frequencies of the closed-loop system will appear, although these have been neglected in the design of the feedforward inputs. These additional dynamics could potentially reintroduce energy into the system at the natural frequencies to cause undesirable vibration. Because
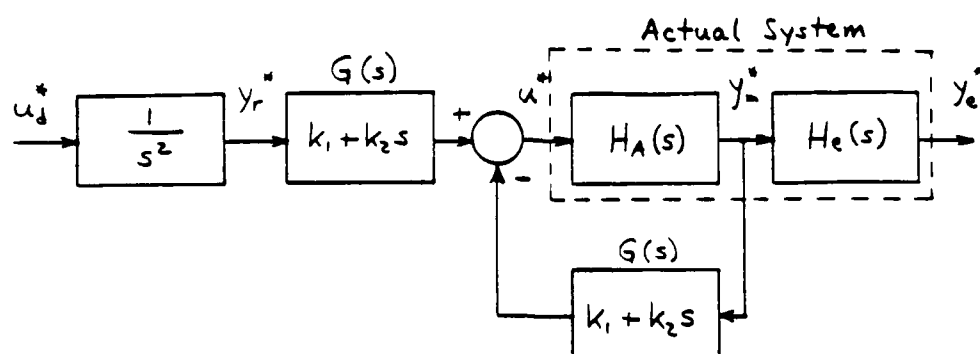
Figure 4.8: Block Diagram of PD Controller with Shaped Reference Input.

of these potential difficulties, we looked for an alternative method of incorporating shaped input functions into a closed-loop system.

4.3 Proportional-Derivative Control with Shaped Reference Input:

4.3.1 Introduction:

The model-reference-based control scheme presented earlier was based on the premise that a feedforward function could be tuned to a nominal system whose response could then be imposed on the actual system. An alternative formulation would use whatever closed-loop system has been configured as the basis for tuning the shaped input functions. Such an idea has already been proposed in connection with the posicast control concept developed by Smith [16, page 338]. In this section, the frequency-shaped inputs will be tuned to the closed-loop natural frequencies.

In many respects, the new closed-loop system model of Figure 4.8 resembles that of Figure 4.1. But there are important differences. First of all, the shaped force input no longer acts as a direct feedforward input to the control force. For sufficiently stiff systems, this extra input has little effect on the response and was left out for simplicity. (Further discussion of the effect of a feedforward input is

presented in Section 4.3.5.)

Another important difference is the use of a simple proportional-derivative (PD) compensator instead of the optimal compensator presented earlier. There were a number of reasons for doing this. Motor position and velocity are readily available for measurement in most practical systems. Thus, no estimator with its inherent sensitivity to parameter errors and unmodeled modes is required to obtain additional unmeasured states. Since actuator and sensor are colocated, the system is much more robust to modeling errors which otherwise could lead to instability.

The full-state optimal compensator is designed to remove the resonant characteristics of the vibrating system by replacing them with its own set of dynamics. In this way, the compensator is trying to suppress the resonant vibration, whether it be excited by the motion or by a disturbance. However, the assumption underlying the present work is that the motion itself causes the vibration and that a judicious choice of input should be able to prevent the resonant vibration from occurring at all. To fully test this hypothesis, a simple compensator was used that does not try to suppress the resonant vibration. Such a compensator also keeps the controller simple to make it easy to implement on existing servo systems.

When a simple controller gives adequate positioning accuracy and disturbance rejection, development of shaped inputs to reduce residual vibration is easier than development of an optimal regulator to suppress vibration. An optimal regulator requires a system model with reasonably accurate values of the system poles and zeros. Since the zeros are difficult to determine and are likely to vary, system performance will suffer. Developing shaped inputs, on the other hand, requires only a knowledge of the poles (natural frequencies), which can be determined to reasonable accuracy.

In more complicated systems in which an optimal regulator is necessary to ensure stability and disturbance rejection, the use of shaped inputs can still give beneficial results. Conditions for which shaped reference inputs are useful in conjunction

with optimal regulators are described in Section 4.4. Thus, the use of a simple PD controller in the following discussion is not intended to preclude more complex compensators. but rather to highlight the advantages of shaped inputs.

A final difference in the new control scheme of Figure 4.8 is that the reference system model has been replaced by a double-integrator. This system element generates the position reference from the shaped force profile. Its use is further clarified in Section 4.3.3. The compensator used on the reference y_r^* is the same as the PD compensator to ensure good tracking.

4.3.2   Tuning Shaped Inputs to Closed-Loop Systems:

Since the effect of feedback is to alter the dynamics of the open-loop system, the shaped inputs should be tuned to the closed-loop system, rather than the open-loop system. In this way, the controller can operate as designed to ensure accurate motion in the presence of disturbances, while the force inputs can be shaped to avoid exciting any closed-loop resonances that occur.

To implement this strategy. the closed-loop system is treated as an equivalent open-loop system. Figure 4.9 shows this equivalence in block diagram form. Note that at this stage, the input to the equivalent open-loop system is treated as a force input u_d^* which can be prespecified.

Once the equivalent open-loop system has been characterized using the given functions for $G(s)$ and $H(s)$, its natural frequencies can be identified and the shaped force input can be derived as detailed in Chapter 2. Note that the frequencies which are to be filtered from the input spectrum are the closed-loop natural frequencies.

Consider the ideal system model presented in Figure 4.2 with transfer function relating motor position y_m^* to control force u^* given by equation (4.3). The effect of closing the loop around this system using the PD controller can be seen in a root locus plot as a function of feedback gains (Figure 4.10). The damping value is assumed to be 0.1, with $m_1/m_2 = 1$. For simplicity in seeing the trend, we have
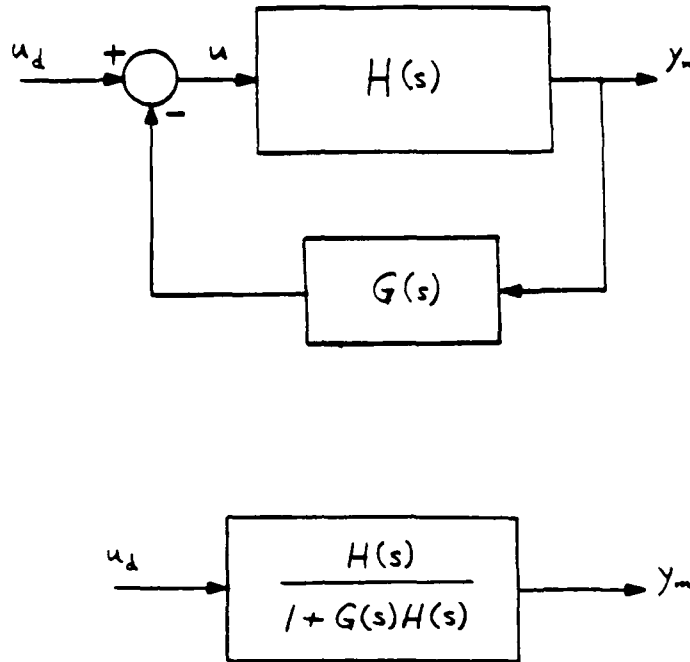
Figure 4.9: Equivalent Open-Loop System.

set $k_1 = k_2$. Notice that the open-loop poles very rapidly approach the open-loop zeros, even for moderate values of gain. Thus, we can safely use the open-loop zeros to determine the closed-loop natural frequency ω_C, which occurs at a dimensionless frequency (relative to the open-loop natural frequency ω_N) of $\omega_C/\omega_N = 0.7$. For a value of $\omega_N T_s/2\pi = 10$ as used in Chapter 2, the shaped input tuned to the closed-loop natural frequency $\omega_C T_s/2\pi = 7$ is shown in Figure 4.11(a), with its spectrum shown in (b).

4.3.3 Generating a Shaped Reference Input:

The shaped input constructed above is only a force profile that must now be incorporated into a closed-loop controller. Using this profile u_d^* as a direct input to the closed-loop system, as shown in Figure 4.9, will not work. Since the closed-loop controller attempts to follow the specified input. in this case the shaped force profile, the
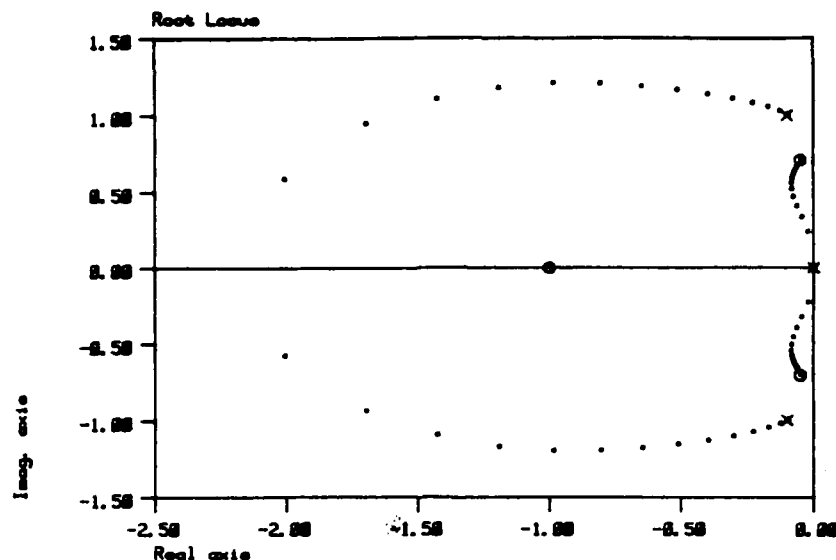
Figure 4.10: Root Locus of Closed-Loop Poles with PD Controller as Function of Feedback Gains $k_1 = k_2$; $\zeta = 0.1$.

system would merely move away from and ultimately return to its starting position. Instead of specifying a force profile, we need to specify a position trajectory.

One way to do this would be to use the nominal open-loop reference system or even the nominal closed-loop system to generate a position profile from the system response to the shaped input. As pointed out in the discussion on the model-reference-based control scheme, this element in the block diagram will introduce its own dynamics into the closed-loop transfer function. Since the shaped inputs are tuned to the closed-loop natural frequencies, it makes no sense to introduce the open-loop natural frequencies which have not been attenuated in the force profiles. Using the nominal closed-loop system to generate a position trajectory simply reintroduces the closed-loop natural frequencies.

Perhaps the easiest way to generate the position trajectory is to use a simple rigid-body mass having the combined value $m_1 + m_2$. This is equivalent to retaining only the double-integrator in the dimensionless transfer function of equation (4.3), eliminating the additional resonant frequencies. This generates a position trajectory

Ramped Sinusoid Input

(a)

Frequency Spectrum of Ramped Sinusoid
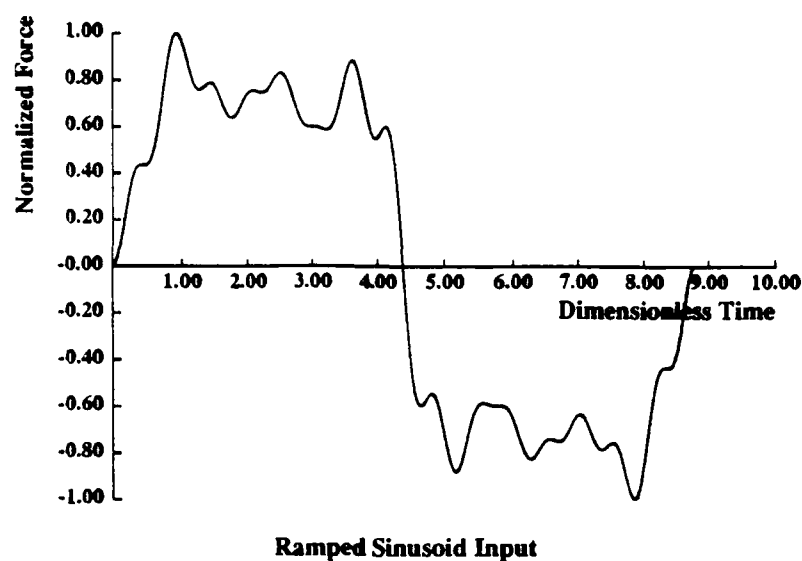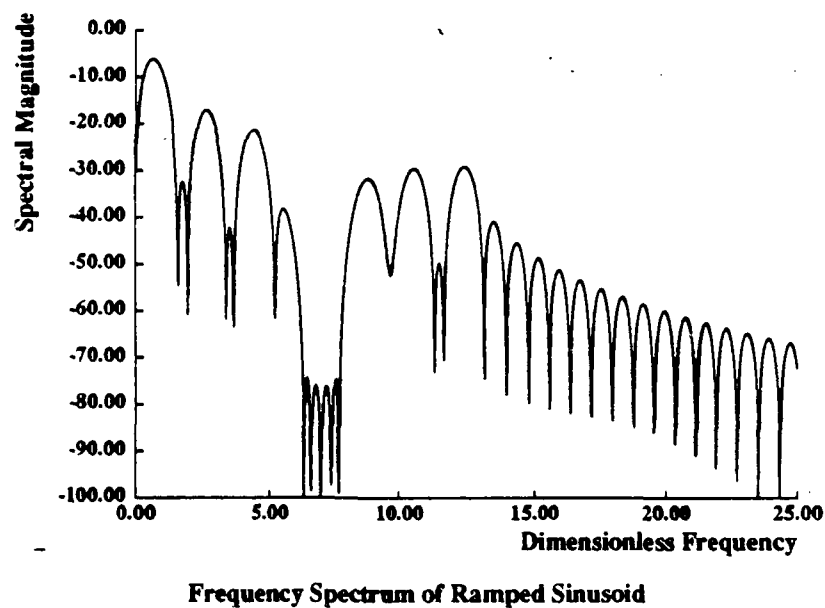
(b)

Figure 4.11: Ramped Sinusoid Input Tuned to $\omega_n T_s/2\pi = 7 \pm 10\%$: (a) Time Function (b) Frequency Spectrum.

that can be directly followed by the PD controller, while retaining the frequency-shaping characteristics of the original force profile.

It is worth noting that the double-integrator is not intended to act as a filter. In fact, as simulations will show, a doubly-integrated square wave used as position trajectory still generates considerable residual vibration.

4.3.4   Closed-Loop Simulation Results:

Using the damped system model of Figure 4.2 with parameters $\omega_N T_s/2\pi = 10$, $\zeta = 0.1$, $m_1/m_2 = 1$, $k_1 = k_2 = 4$, and the force profile of Figure 4.11, we obtained three sets of simulation results. The feedback gains k_1 and k_2 were chosen to give critically damped response for the equivalent rigid-body system with closed-loop bandwidth twice the natural frequency. In the first simulation, the nominal system with $\omega_A/\omega_N = 1$ was used. This response is shown in Figure 4.12. The actual control force is shown in (a), while the acceleration of mass m_2 is shown in (b). The residual vibration has indeed been eliminated. Notice also that the control force differs from the shaped force profile because of the feedback control action. Residual amplitude is very nearly the same as that of the open-loop response of Figure 2.17.

The second set of results were obtained from an actual system model having $\omega_A/\omega_N = 0.9$; that is, the actual open-loop natural frequency was assumed to be 10% less than the nominal natural frequency. Since this error puts the actual natural frequency at the extreme low end of the spectral notch, the damped response is expected to give some initial residual amplitude. Because the PD controller gives very lightly damped closed-loop poles, the actual response shown in Fig. 4.13 takes longer to decay than that with the optimal compensator (Fig. 4.6). However, the initial residual amplitude is smaller for the PD controller because the input has been tuned to the actual closed-loop dynamics. The model-reference-based controller introduces additional dynamics when modeling errors are present which increase the initial residual amplitude.
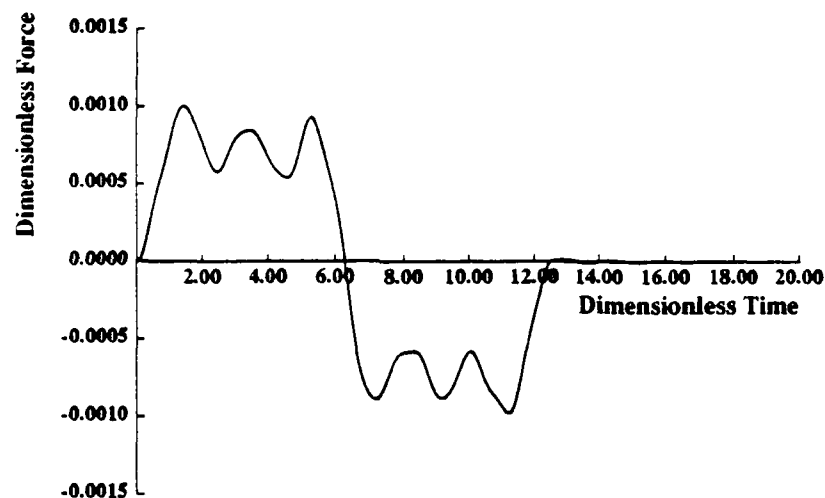
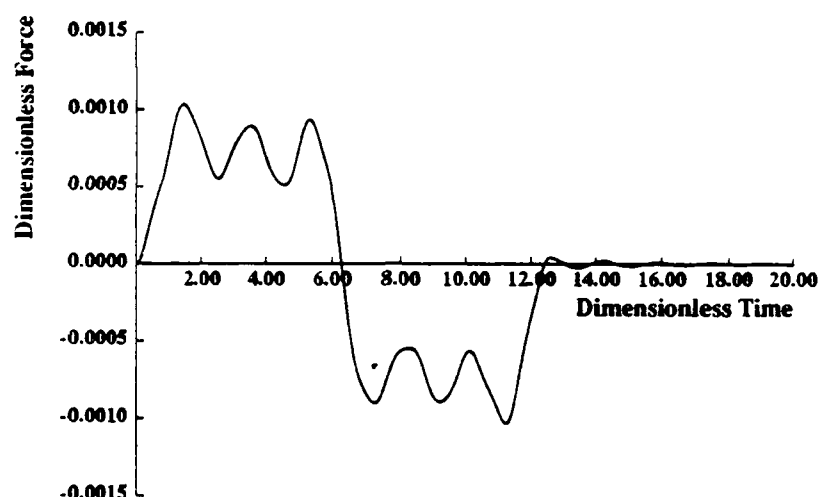Nominal Closed-Loop Response to a Ramped Sinusoid Input

(a)
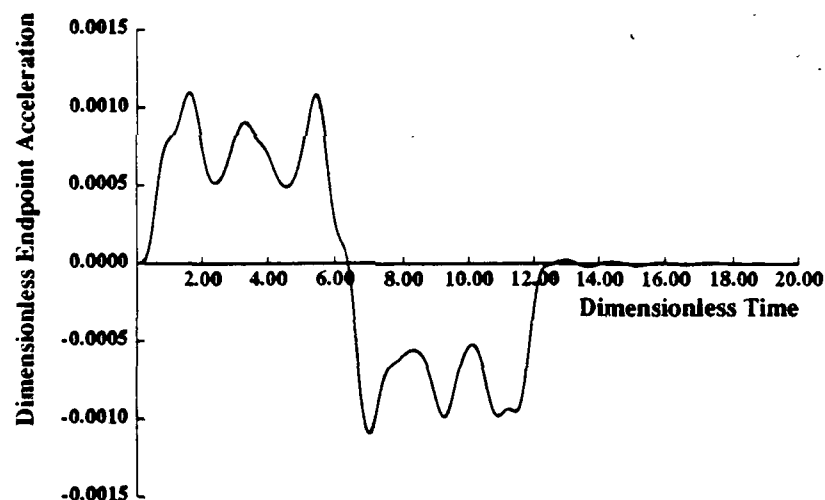
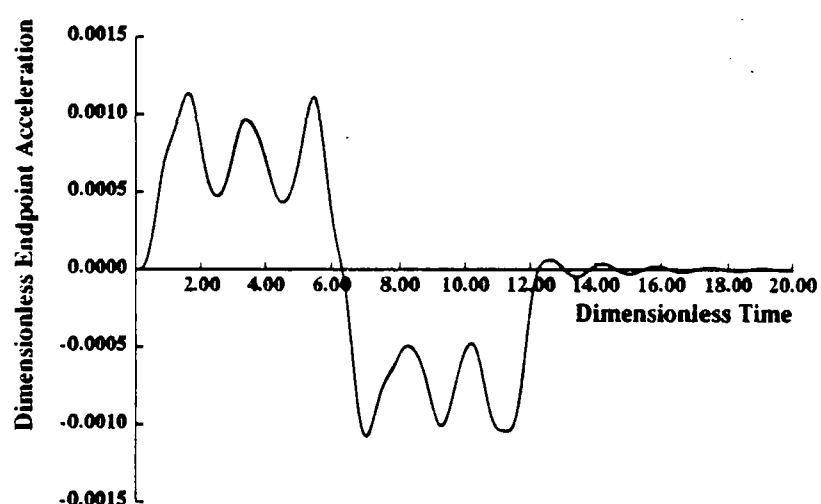Nominal Closed-Loop Response to a Ramped Sinusoid Input

(b)

Figure 4.12: Simulated Response for Nominal System Using PD Controller with Ramped Sinusoid Input; $\omega_N T_s/2\pi = 10$, $\omega_C T_s/2\pi = 7$, $\zeta = 0.1$: (a) Control Force (b) Acceleration Response.

Actual Closed-Loop Response to a Ramped Sinusoid Input

(a)

Actual Closed-Loop Response to a Ramped Sinusoid Input

(b)

Figure 4.13: Simulated Response for Actual System Using PD Controller with Ramped Sinusoid Input; $\omega_N T_s/2\pi = 10$, $\omega_C T_s/2\pi = 7$, $\zeta = 0.1$, $\omega_A/\omega_N = 0.9$: (a) Control Force (b) Acceleration Force.

A third simulation gives the results when a constant opposing force of dimensionless amplitude 0.0003 acts on mass m_2. This represents a disturbance which is 30% of the peak input force. The ratio ω_A/ω_N is again assumed to be 1. This response is shown in Figure 4.14. Notice how the closed-loop feedback compensates for the disturbing force, while the shaped input reduces residual vibration.

To point out the advantages of using the frequency-shaped profiles, we also simulated the response to a square wave force input u_d^*. These results are shown in Figure 4.15. At the end of the move, considerable amplitude of residual acceleration remains that must be damped out by the relatively lightly damped closed-loop controller.

4.3.5 Effect of a Direct Feedforward Input:

If the shaped force input, u_d^* of Figure 4.8, is fed directly into the controlled system, the new block diagram will look like Figure 4.16. The transfer function between y_m^* and u_d^* when this feedforward input is included is given by

$$\frac{y_m^*(s)}{u_d^*(s)} = \frac{H_A(s)}{s^2[1 + (k_1 + k_2 s)H_A(s)]}\left(s^2 + k_2 s + k_1\right) \tag{4.15}$$

This compares with the transfer function when feedforward is absent:

$$\frac{y_m^*(s)}{u_d^*(s)} = \frac{H_A(s)}{s^2[1 + (k_1 + k_2 s)H_A(s)]}\left(k_2 s + k_1\right) \tag{4.16}$$

Basically, then, the feedforward input generates an additional acceleration reference signal. This will tend to improve tracking performance by enhancing the higher-frequency components of the input function u_d^*.

As the transfer function (4.15) makes clear, the use of a direct feedforward signal will enhance frequencies of the input function u_d^* above the break frequency given by $\sqrt{k_1}$. For a system which is relatively stiff, with large k_1, this effect is insignificant. In our simulations, we used a value $k_1 = 4$. This suggests that adding the direct feedforward connection only serves to enhance frequencies which are twice the
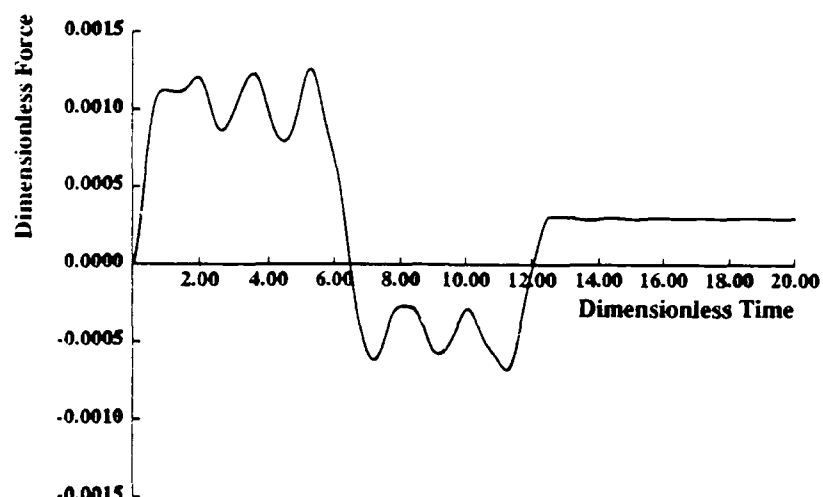
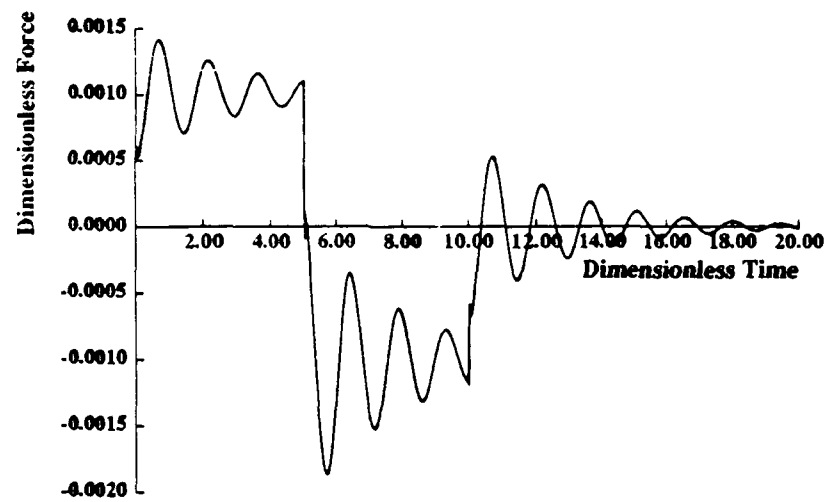Closed-Loop Response to a Ramped Sinusoid Input with Disturbance

(a)
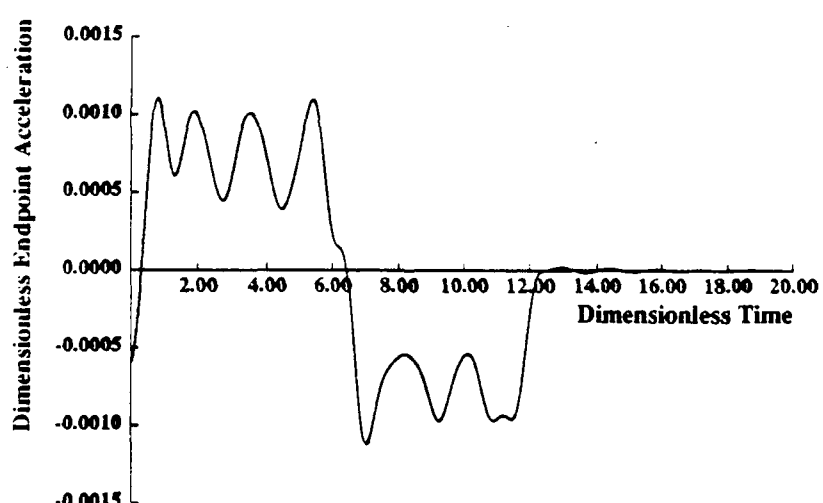
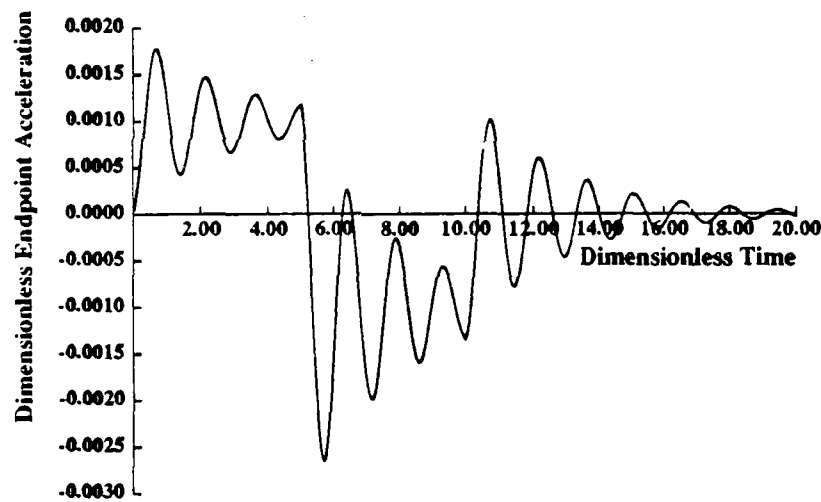Closed-Loop Response to a Ramped Sinusoid Input with Disturbance

(b)

Figure 4.14: Simulated Response for Nominal System Using PD Controller with Ramped Sinusoid Input, with 0.0003 Disturbance Force: $\omega_N T_s/2\pi = 10$, $\omega_C T_s/2\pi = 7$, $\zeta = 0.1$: (a) Control Force (b) Acceleration Response.

Nominal Closed-Loop Response to a Square Wave Input

(a)

Nominal Closed-Loop Response to a Square Wave Input

(b)

Figure 4.15: Simulated Response for Nominal System Using PD Controller with Square Wave Input; $\omega_N T_s/2\pi = 10$, $\omega_C T_s/2\pi = 7$, $\zeta = 0.1$: (a) Control Force (b) Acceleration Response.
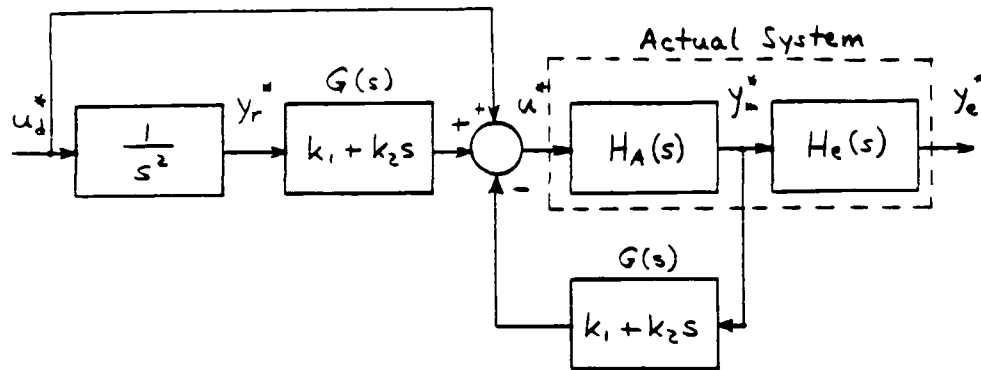
Figure 4.16: Block Diagram of PD Controller with Shaped Reference Input Including a Direct Feedforward Input.

natural frequency of the system and higher. When the dimensionless closed-loop natural frequency $\omega_C T_s / 2\pi$ is 7, this suggests that only dimensionless frequencies of 14 and greater will be enhanced by feedforward. As the frequency spectrum of Figure 4.11(b) shows, there is very little energy in the shaped ramped sinusoid inputs above $\omega T_s / 2\pi = 14$. Thus, we would not expect feedforward to markedly affect the response in this case.

However, for systems which are relatively compliant, the additional feedforward input can make a difference. For the sake of argument, assume that for a particular move distance, force level, and inertia value, the dimensionless closed-loop frequency $\omega_C T_s / 2\pi$ is 2. Also, assume that the position loop is relatively compliant, with a value $k_1 = 0.25$. This suggests that a direct feedforward input will amplify the frequency components of the shaped input above $\omega T_s / 2\pi = 1$. This represents a significant part of the input spectrum, as shown in Figure 4.17(b).

Simulation results comparing responses with and without feedforward are shown in Figures 4.18 and 4.19, respectively. The total control input u^* is shown in (a), with the acceleration of mass m_2 shown in (b). The response does lag behind a small amount when the direct feedforward signal is left out. But even under these conditions, the advantage in using feedforward is minimal.

Thus, the effectiveness of a direct feedforward signal contributing to the control
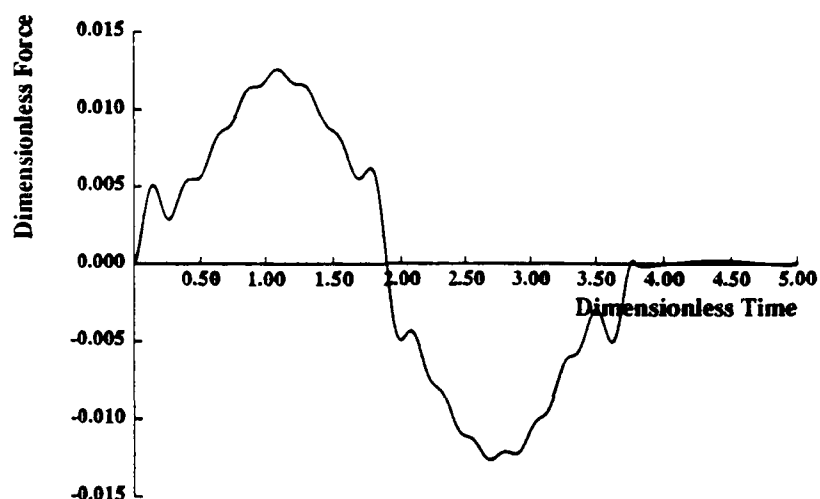
Ramped Sinusoid Input
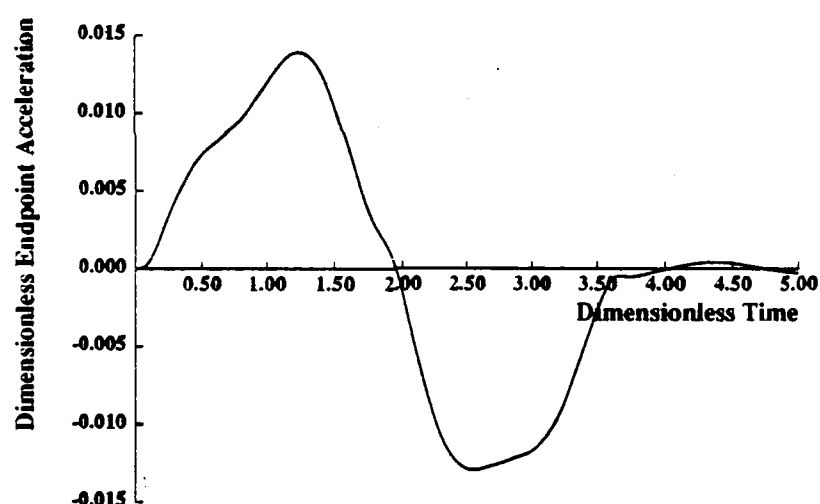
(a)

Frequency Spectrum of Ramped Sinusoid
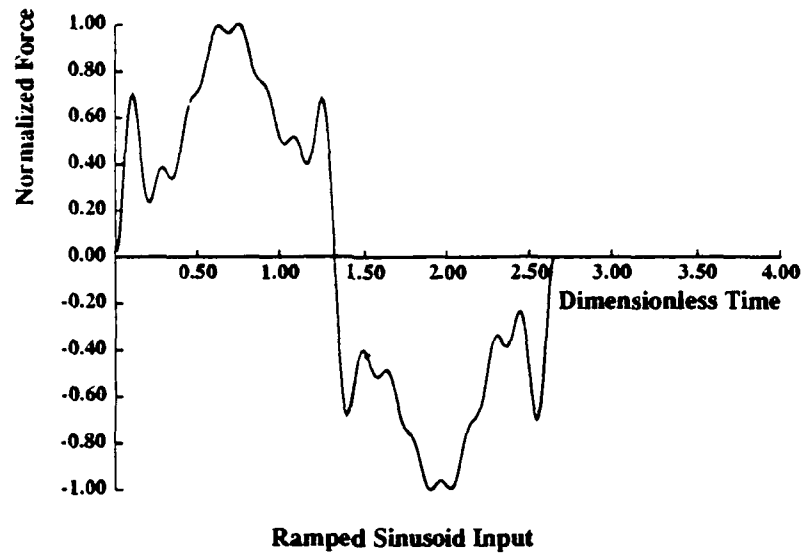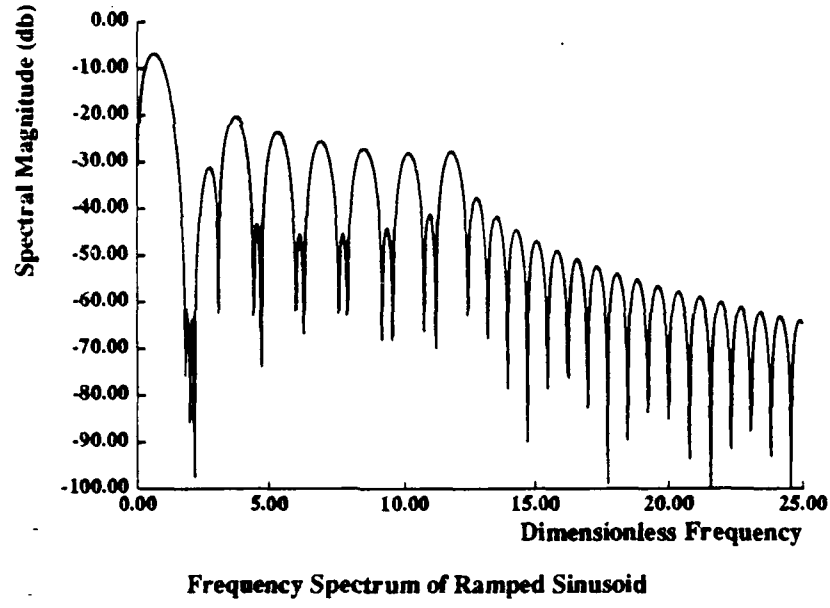
(b)

Figure 4.17: Ramped Sinusoid Input Tuned to $\omega_n T_s/2\pi = 2 \pm 10\%$: (a) Time Function (b) Frequency Spectrum.

Closed-Loop Response to a Ramped Sinusoid Input with Feedforward

(a)

Closed-Loop Response to a Ramped Sinusoid Input with Feedforward

(b)

Figure 4.18: Simulated Response to Nominal System using PD Controller with Ramped Sinusoid Input and with Direct Feedforward; $\omega_N T_s/2\pi = 2.86$, $\omega_C T_s/2\pi = 2$, $\zeta = 0.1$: (a) Control Force (b) Acceleration Response.

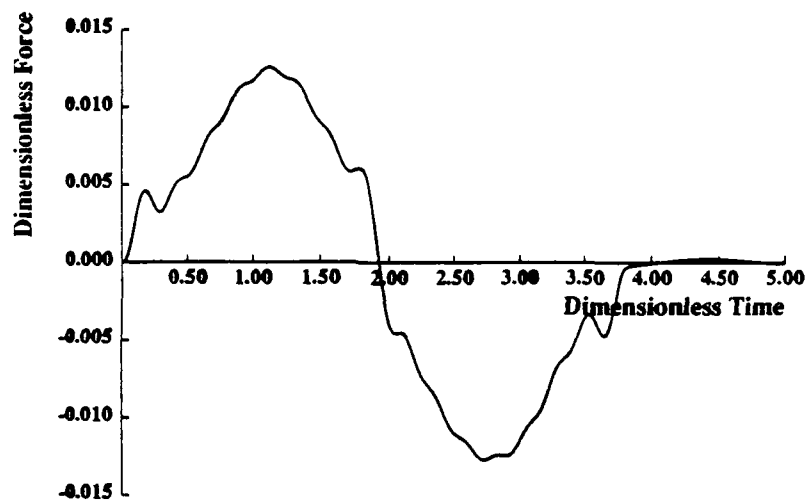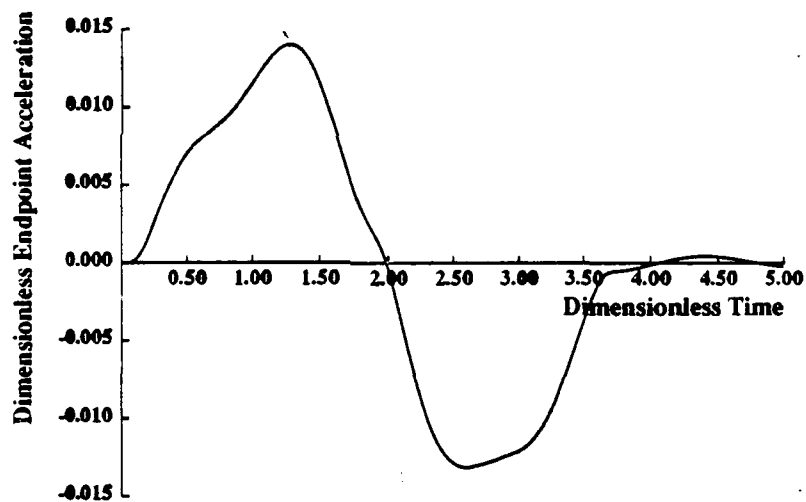Closed-Loop Response to a Ramped Sinusoid Input without Feedforward

(a)

Closed-Loop Response to a Ramped Sinusoid Input without Feedforward

(b)

Figure 4.19: Simulated Response to Nominal System using PD Controller with Ramped Sinusoid Input and without Direct Feedforward; $\omega_N T_s/2\pi = 2.86$, $\omega_C T_s/2\pi = 2$, $\zeta = 0.1$: (a) Control Force (b) Acceleration Response.

effort is related to the stiffness of the position loop. For a relatively stiff control loop, feedforward can be left out with very little effect on performance. For compliant systems, the use of a feedforward input may speed up the response. This would be especially useful for improving the performance of feedback loops which require small position gains for stability.

4.4 Suppressing Vibration Using Optimal Regulators:

4.4.1 Introduction:

The preceding section has emphasized the use of shaped reference inputs to reduce residual vibration. The PD compensator that was used to achieve accurate positions does not actively suppress vibration. Instead, excitation of system natural frequencies is minimized by using appropriately shaped reference inputs. This approach highlights the effectiveness of shaped inputs but ignores vibration suppression that can be achieved by more sophisticated compensators. Optimal regulators can serve as effective controllers to actively suppress vibration for systems having several natural frequencies. This section discusses optimal regulators and identifies several conditions for which they do not sufficiently reduce residual vibration without the use of shaped inputs.

Two different cases for which optimal regulators cannot adequately suppress vibration will be investigated. First, we will show that optimal regulators can only achieve limited closed-loop damping ratios for the higher frequency modes. Second, we will describe a system having a mode which is nearly unobservable and therefore cannot be adequately compensated.

In both of the examples used to illustrate these conditions, we will apply linear-quadratic-regulator (LQR) theory to develop a state feedback controller. Feedback
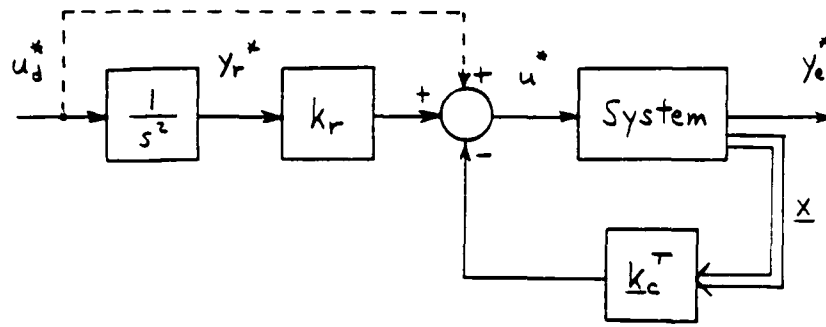
Figure 4.20: Block Diagram of Optimal Regulator State Feedback Controller.

gains were determined by minimizing the following performance index,

$$J = \frac{1}{2} \int_0^\infty (y_e^{*2} + \rho u^{*2})\, dt, \tag{4.17}$$

where y_e^* represents the dimensionless endpoint position whose deviation from a desired trajectory we wish to minimize, and u^* is the dimensionless control effort of the actuator. We will assume that all system states are available for measurement to simplify the analysis.

State feedback derived from the optimal regulator formulation is augmented by a reference input to bring the system to the desired position. The complete closed-loop system is shown in Figure 4.20. The system state vector x is multiplied by the state feedback gain vector k_c^T. The reference position y_r^* is multiplied by a position gain k_r that causes endpoint position y_e^* to follow the reference.

Finally, the reference is generated by doubly integrating a square wave force profile u_d^*. Typically a simple step reference would be used to achieve the desired position. But since we recognize that real actuators are force-limited, we will follow a realistic position trajectory which achieves time-optimal motion for the equivalent rigid-body. The task of the state feedback regulator is to maintain this trajectory by minimizing vibration in the actual system.

Results using this control scheme with the integrated square wave input will be compared with results using the ramped sinusoid force input to generate the

Table 4.2

Definition of Dimensionless Parameters

$$t^* = \omega_1 t / 2\pi$$

$$y_e^* = \frac{y_e}{y_f}$$

$$\ddot{y}_e^{*\,*} = \frac{\ddot{y}_e}{\omega_1^2 y_f}$$

$$u^* = \frac{u}{(m_1 + m_2 + m_3)y_f\omega_1^2}$$

reference. The shaped force input is also transmitted directly to the system as a feedforward signal to improve response, as indicated by the dotted line in Figure 4.20. The same controller is used regardless of reference input. These comparisons for the two cases being considered serve to illustrate the importance of carefully shaping the reference input to minimize residual vibration when the optimal regulator cannot do it alone.

4.4.2 Limited Closed-Loop Damping Ratio:

Even though optimal regulators are designed to actively damp out system vibration, they are limited in the amount of additional damping they can impose on the system modes. To illustrate this phenomenon, we will look at the response of a lightly-damped three-mass system (Fig. 4.21). The dimensionless parameters used for this system are defined in Table 4.2, where y_f is the final position and ω_1 is the undamped natural frequency of the first mode of vibration. The second mode is given in dimensionless form as ω_2/ω_1. Damping ratios for the first and second modes are ζ_1 and ζ_2, respectively. The transfer function relating the endpoint position y_e^*
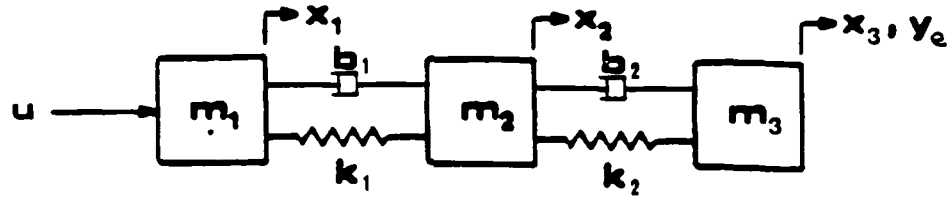
Figure 4.21: Damped Three-Mass System Model.

to the control effort u^* is given by:

$$\frac{y_e^*(s)}{u^*(s)} = \frac{(2\zeta_1 s + 1)\left[2\zeta_2\left(\frac{\omega_2}{\omega_1}\right)s + \left(\frac{\omega_2}{\omega_1}\right)^2\right]}{s^2(s^2 + 2\zeta_1 s + 1)\left[s^2 + 2\zeta_2\left(\frac{\omega_2}{\omega_1}\right)s + \left(\frac{\omega_2}{\omega_1}\right)^2\right]} \qquad (4.18)$$

An optimal state feedback regulator was designed for this system using a control weight $\rho = 1/49$. This weighting penalizes endpoint vibration more heavily than the control effort. System parameters were chosen so that $\omega_2/\omega_1 = 2$ and $\zeta_1 = \zeta_2 = 0.1$. Results when the square wave force profile generates the reference for a dimensionless move time $\omega_1 T_s/2\pi = 1.5$ are shown in Figure 4.22. The control effort u^* is shown in (a) and the endpoint acceleration $\ddot{y}_e^*$ in (b). Even though the first mode vibration is damped out quickly by the state feedback regulator, the second mode continues to oscillate for several cycles. This suggests that the optimal regulator is less effective at actively damping out the higher frequency. In fact, the damping ratio of the most lightly-damped closed-loop poles is only 0.15.

To explain why optimal regulators give lower closed-loop damping ratios for higher modes, we will look at the typical configuration of poles in optimally regulated systems. As the control weight ρ approaches zero, all the closed-loop poles which do not go toward the open-loop zeros will approach a Butterworth configuration in the left-half-plane [68]. In general, a lightly-damped n-mass system like that of Figure 4.21 will have $2n$ open-loop poles and $n - 1$ real zeros. Thus, n+1 closed-loop poles will approach the Butterworth configuration. Such a model has been shown to be a good representation of dynamic systems, like industrial robots, having transmission

Response to Integrated Square Wave Reference
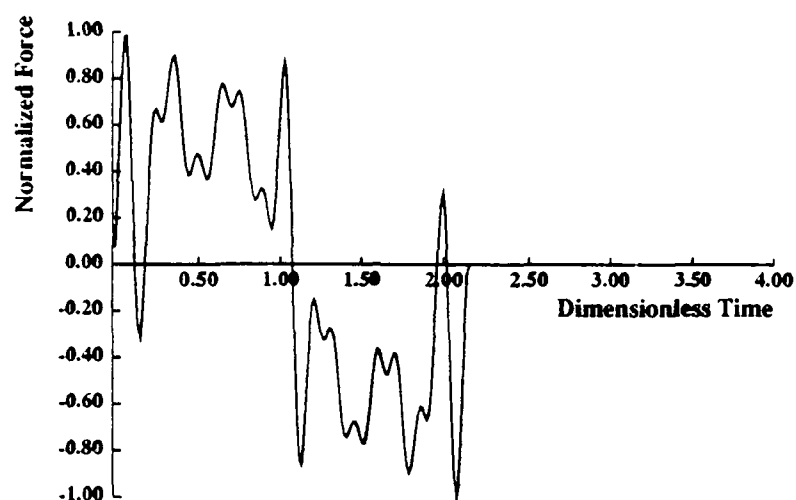
(a)

Response to Integrated Square Wave Reference
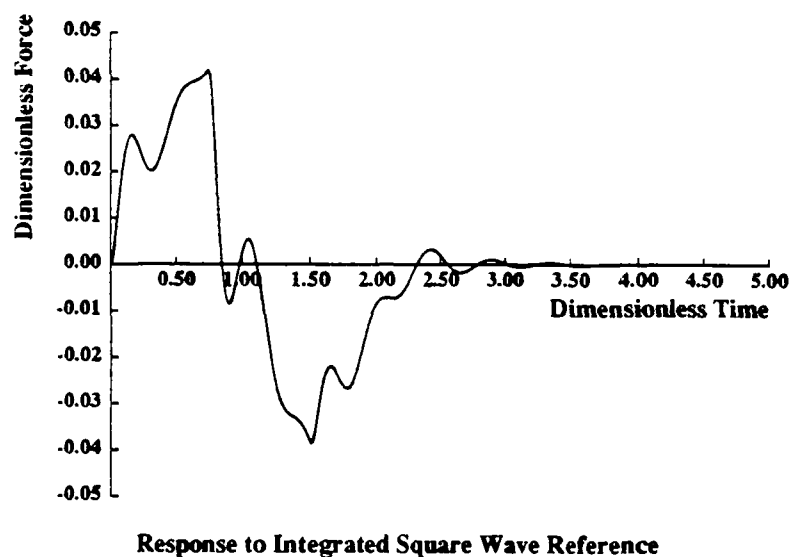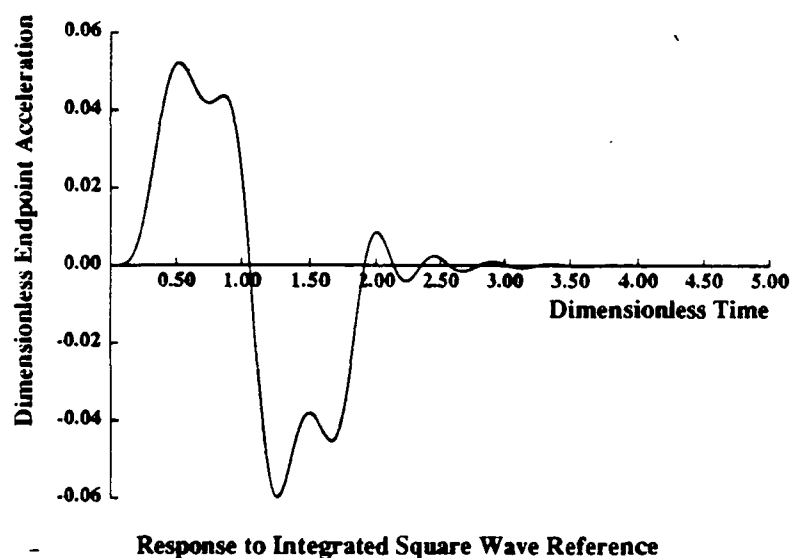
(b)

Figure 4.22: Optimal Regulator Response of Three-Mass System using Integrated Square Wave Reference for $\omega_1 T_s/2\pi = 1.5$: (a) Control Force (b) Acceleration Response.

compliance and structural flexibility [69]. The number of masses contained in the model will go up as more vibration modes are included. As the number of masses n increases, the closed-loop poles closest to the imaginary axis will become more and more lightly damped. For $n = 2$, the damping ratio is 0.5; for $n = 5$, it is only 0.26. Even with infinite control effort available ($\rho = 0$), these closed-loop poles cannot achieve higher damping ratios than those dictated by the Butterworth pole configuration.

Often, these ideal pole locations cannot be achieved in practice because of bandwidth limitations. Since the dynamics of real systems cannot be precisely known, some modeling error can be expected. Ignoring some of the higher natural frequencies in the system model may lead to instabilities unless control gains and hence bandwidth are reduced [36]. Some modeling errors can lead to a flip in the relative locations of open-loop poles and zeros which can also drive a system unstable [29]. Again, bandwidth must be reduced to guarantee stability. Under these circumstances, some of the higher frequencies will not be adequately suppressed by the optimal regulator and lightly damped residual vibration can be expected.

When we use a shaped ramped sinusoid force profile to generate the reference trajectory for the optimal regulator, residual vibration of the second mode can be reduced. The ramped sinusoid input function we used was constructed to minimize excitation energy at two frequencies: $\omega_1 T_s/2\pi = 1.5$ and $\omega_2 T_s/2\pi = 3$. This time function is shown in Figure 4.23(a), with its frequency spectrum in Figure 4.23(b). Response of the three-mass system to this reference input is shown in Figure 4.24. Notice that residual vibration has been minimized for both natural frequencies. Because an optimal regulator cannot always guarantee well-damped response, it is helpful to use shaped reference inputs to generate motions which do not excite the lightly-damped modes.

Ramped Sinusoid Input Function

(a)
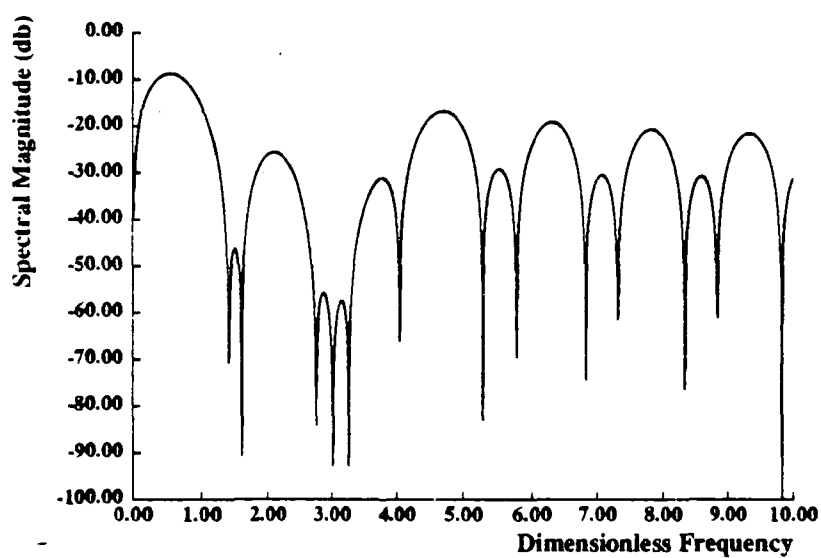
Frequency Spectrum of Ramped Sinusoid Input

(b)

Figure 4.23: Ramped Sinusoid Input Tuned to $\omega_1 T_s/2\pi = 1.5$ and $\omega_2 T_s/2\pi = 3.0$: (a) Time Function (b) Frequency Spectrum.

Response to Ramped Sinusoid Input

(a)
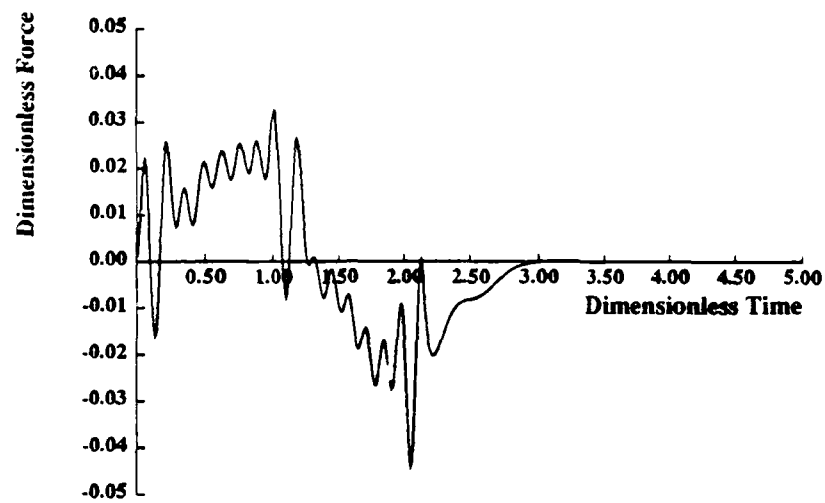
Response to Ramped Sinusoid Input

(b)

Figure 4.24: Optimal Regulator Response of Three-Mass System using Integrated Ramped Sinusoid Reference and Feedforward for $\omega_1 T_s/2\pi = 1.5$: (a) Control Force (b) Acceleration Response.

Figure 4.25: Two-Mass System Model Exhibiting Weakly Coupled Torsional and Translational Modes.

4.4.3 Nearly Unobservable Modes:

Another case in which optimal regulators fail to give adequate performance is in systems having nearly unobservable modes. This occurs when the sy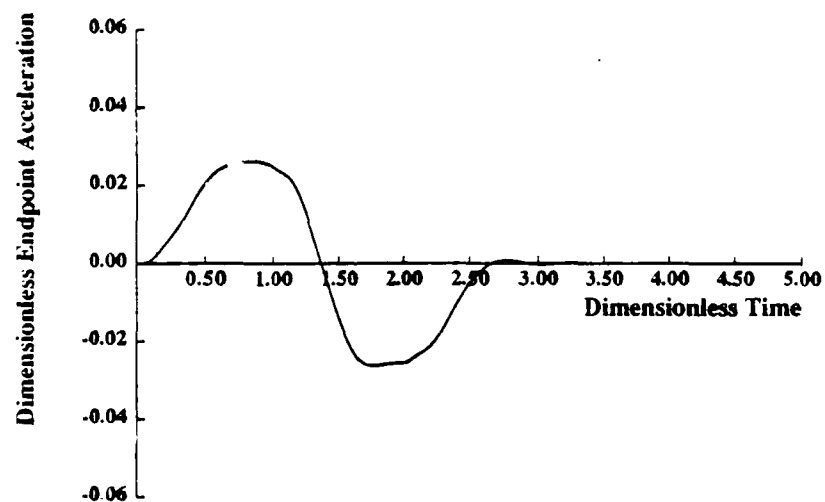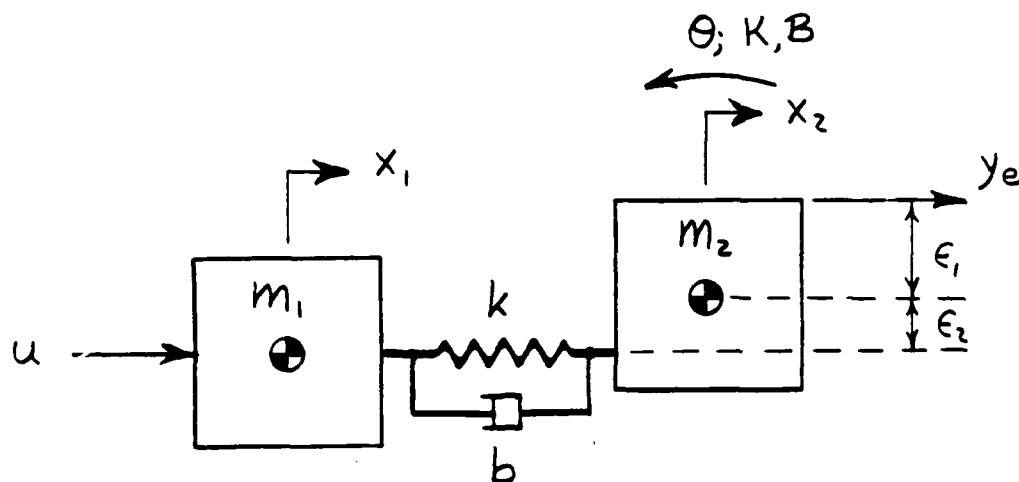stem consists of several subsystems that are only weakly coupled. A simple example is a Cartesian robot whose axes are not exactly orthogonal to one another. In that case, motion in an axis can excite vibration in the other axes. Such systems are characterized by transfer functions having open-loop pole and zero pairs that almost cancel. These poles cannot be adequately compensated using an optimal regulator.

A good system to illustrate this kind of behavior is shown in Figure 4.25. This system is basically a two-mass system but the second mass m_2 can exhibit rotation as well as translation. This rotation is resisted by a torsional spring K and damper B. Such a model may be used to represent a positioning axis riding on linear bearings, which have a certain finite stiffness. The endpoint position y_e will sense both the translation and the rotation of the second mass as measured at the edge a distance ϵ_1 from its center of mass. To accurately position this mass, the endpoint

Table 4.3

Definition of Dimensionless Parameters

$$t^* = \omega_1 t / 2\pi$$

$$y_e^* = \frac{y_e}{y_f}$$

$$\ddot{y}_e^* = \frac{\ddot{y}_e}{\omega_1^2 y_f}$$

$$u^* = \frac{u}{(m_1 + m_2) y_f \omega_1^2}$$

must undergo pure translation. That will be the goal of the optimal regulator.

Because any asymmetries in friction on opposite sides of mass m_2 will cause it to pivot, the line of action of the force transmitted through the spring k and damper b will be a certain distance ϵ_2 from the center of mass of m_2. For simplicity, mass m_2 will be assumed to be square, with sides of length $2\epsilon_1$. Thus, its mass moment of inertia I is given as

$$I = \frac{2}{3} m_2 \epsilon_1^2. \tag{4.19}$$

Dimensionless parameters can be defined as shown in Table 4.3. The desired final position y_f is used to normalize endpoint position y_e. The undamped natural frequency ω_1 corresponds to the frequency for the purely-translating two-mass system (Fig. 2.13). Another natural frequency ω_2 corresponds to torsional vibration of mass m_2:

$$\omega_2 = \sqrt{\frac{K}{I}}. \tag{4.20}$$

In dimensionless terms, this second mode frequency is given as ω_2/ω_1. Damping ratios of the first and second modes are ζ_1 and ζ_2. Additional dimensionless parameters used in this model are the ratios m_2/m_1 and ϵ_2/ϵ_1.

The transfer function relating the endpoint position y_e^* to the control effort u^* can be expressed as

$$\frac{y_e^*(s)}{u^*(s)} = \frac{0.17(s + 5.0)(s^2 + 0.02s + 4.7)}{s^2(s^2 + 0.2s + 1.0)(s^2 + 0.02s + 4.0)} \tag{4.21}$$

for parameter values $m_2 \cdot m_1 = 1$, $\epsilon_2/\epsilon_1 = 0.1$, $\omega_2/\omega_1 = 2$, and $\zeta_1 = \zeta_2 = 0.1$. Notice the presence of a lightly damped pair of zeros nearly canceling the lightly damped poles representing the second mode. The existence of these zeros near the vibrating poles is characteristic of systems having weakly coupled subsystems. In this case, the torsional mode is only weakly coupled to the remaining two-mass translating system.

An optimal regulator can be derived for this plant model and combined with a reference input to follow a specified trajectory. Control weight $\rho = 1/49$ was used to determine the state feedback gains. Rigid-body response to a square wave force was used as a reference trajectory (Fig. 4.20). Results for a dimensionless move time $\omega_1 T_s/2\pi = 1.5$ are shown in Figure 4.26, with control force u^* in (a) and endpoint acceleration $\ddot{y}_e^*$ in (b). The second mode continues to vibrate for a considerable time after the system reaches the desired position. In fact, the closed-loop damping ratio for this mode is only 0.03.

This response can again be explained by making reference to the closed-loop pole configurations of optimal regulators. As control weight approaches zero, some of the closed-loop poles approach the open-loop zeros. As the transfer function (4.21) makes clear, two of these poles will approach a pair of very lightly damped zeros, having damping ratio of 0.005. No matter how high the controller bandwidth is made (ρ small), this pair of poles will always dominate and give vibratory response.

When the reference trajectory is generated from a doubly-integrated ramped sinusoid input (Fig. 4.23) and a direct feedforward signal is added, then the response of Figure 4.27 results. The system undergoes the same move ($\omega_1 T_s/2\pi = 1.5$). Notice that this time the residual vibration has been eliminated, even though the same state feedback compensator was used.
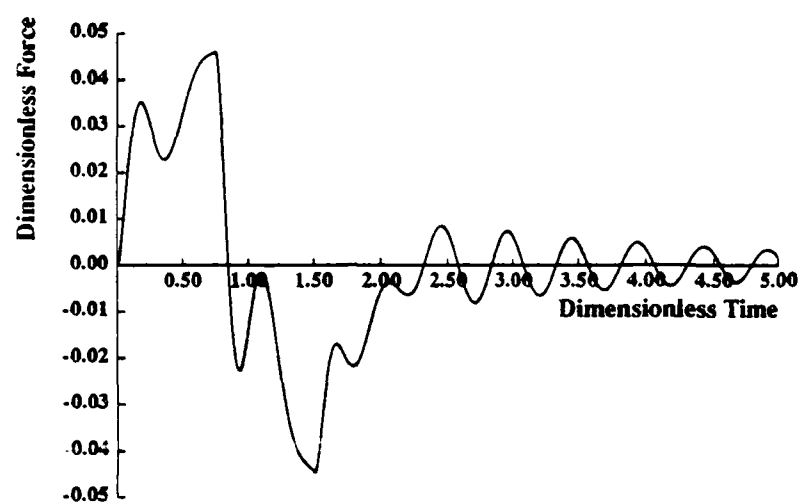
Response to Integrated Square Wave Reference

(a)
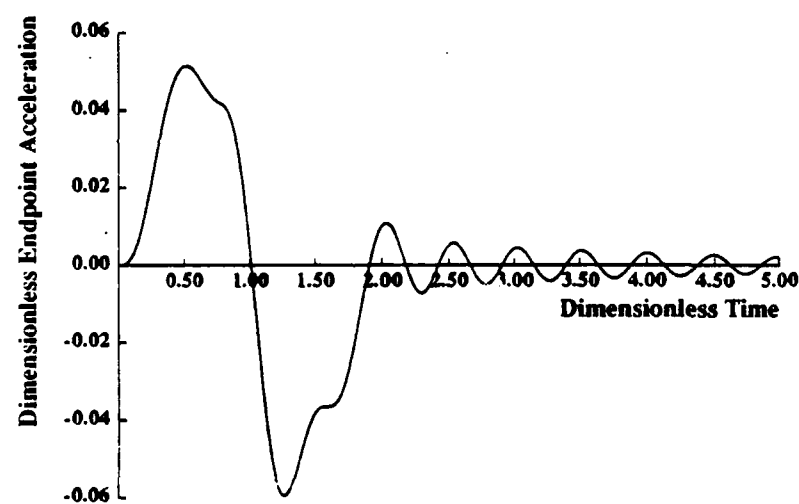
Response to Integrated Square Wave Reference

(b)

Figure 4.26: Optimal Regulator Response of Weakly-Coupled System using Integrated Square Wave Reference for $\omega_1 T_s/2\pi = 1.5$: (a) Control Force (b) Acceleration Response.

Response to Ramped Sinusoid Input

(a)
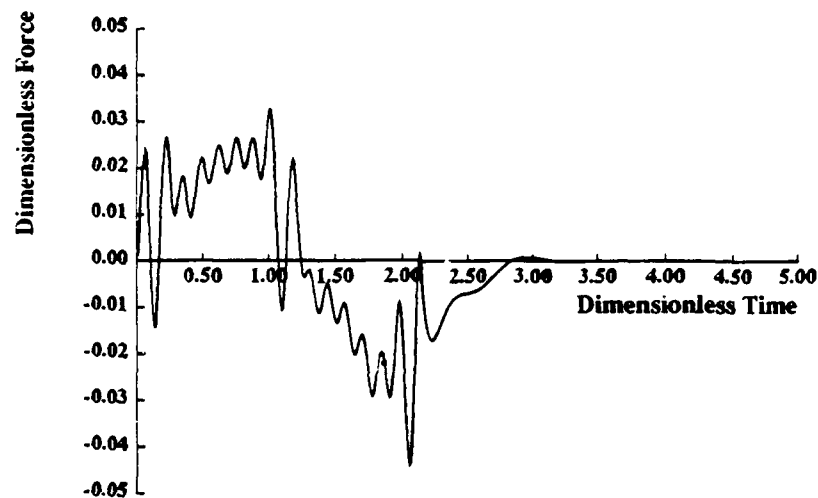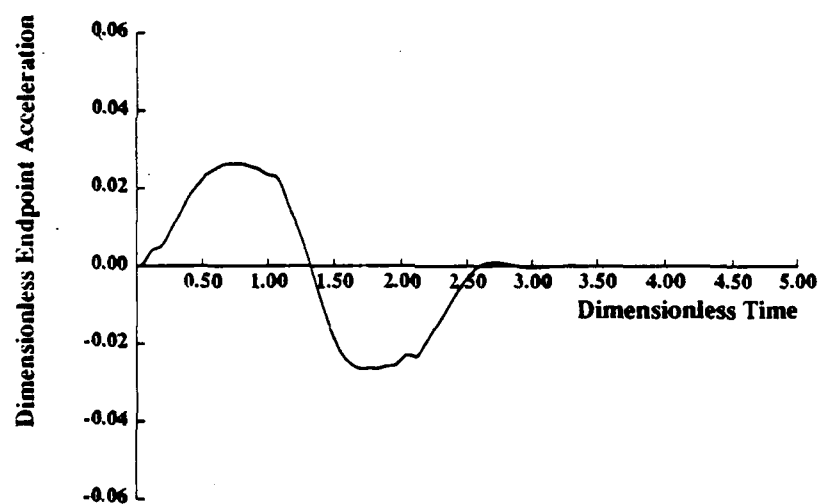
Response to Ramped Sinusoid Input

(b)

Figure 4.27: Optimal Regulator Response of Weakly-Coupled System using Integrated Ramped Sinusoid Reference and Feedforward for $\omega_1 T_s/2\pi = 1.5$: (a) Control Force (b) Acceleration Response.

These examples illustrate the advantage of using frequency-shaped reference inputs in order to improve the performance of state feedback control systems. When bandwidth limitations prevent adequate damping ratios of higher modes, or when nearly unobservable modes prevent effective compensation by optimal regulators, the use of shaped inputs can significantly reduce residual vibration.

4.5 Closure:

This chapter has presented two alternative methods of incorporating a shaped force input into a closed-loop system. The first technique uses a reference model of the open-loop system to impose the desired performance on the closed-loop system. With modeling errors, however, this control scheme can introduce closed-loop natural frequencies that will not be attenuated by force profiles tuned to the open-loop natural frequencies. Therefore, a second implementation was presented that tunes the shaped inputs to the closed-loop natural frequencies. A simple rigid-body model of the system generates a reference position profile from the shaped force. A simple PD compensator is used to illustrate the effectiveness with which shaped inputs alone can reduce system residual vibration. Then, several cases were presented for which even an optimal regulator provides inadequate performance. The use of shaped inputs in those cases helps provide good response with minimum residual vibration.

Shaped Inputs for Velocity-Limited Systems

5.1 Introduction: `

In generating force profiles up to this point, we have assumed that the systems to be controlled can always reach peak velocity. Since all these inputs resemble a single cycle of a square wave, the move consists of only acceleration and deceleration regions. No time is spent coasting at the peak velocity. If the system has a maximum allowable speed, the force input must be scaled down until the peak speed achieved during the move falls within the velocity limit. This can lead to unnecessarily long move times for longer moves. An alternative is to develop a new set of force profiles that allow motion at constant velocity and give velocity waveforms resembling a trapezoid. Such force profiles will be developed in this chapter.

Velocity limits can occur in physical systems for a number of reasons. Typically, peak motor velocity is limited by saturation in the amplifiers. With a limited supply voltage available to the amplifier, the motor can accelerate only up to a speed where this voltage just cancels the voltage drop across the winding resistance and the back emf voltage. A plot of motor velocity as a function of time for a typical amplifier
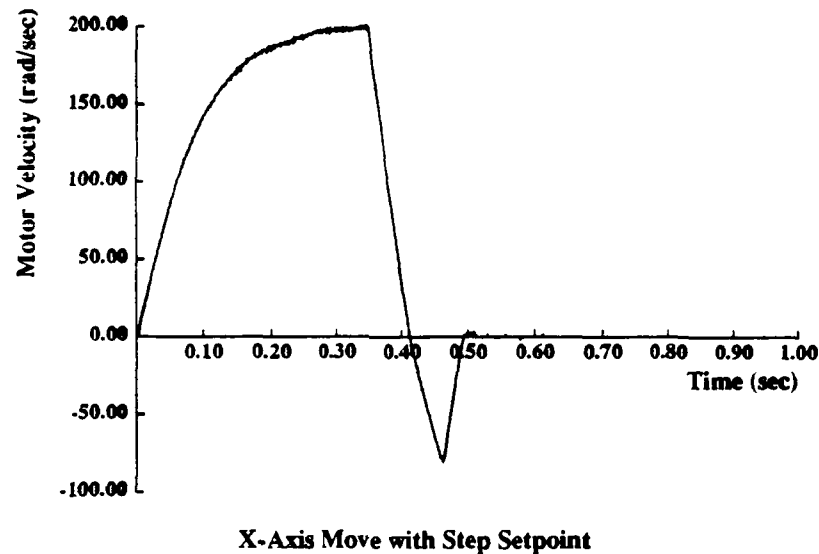
X-Axis Move with Step Setpoint

Figure 5.1: Motor Velocity for a Typical Saturating Amplifier.

giving full voltage output is shown in Figure 5.1. Notice that a velocity limit is reached gradually. Other possible reasons for limiting peak velocity are requirements on the speed with which balls can circulate in a lead screw or requirements on decelerating large inertial loads.

In this chapter, we will develop open-loop force profiles, analogous to the ramped sinusoid functions of Chapter 2, that accelerate a two-mass system to a specified velocity. These open-loop functions will be used directly to accelerate this system to peak velocity, and will then be incorporated into the closed-loop scheme presented in Chapter 4. Finally, a complete force profile will be constructed, consisting of acceleration, dwell, and deceleration regions, to achieve any desired position.

5.2 Development of Shaped Functions:

Typical systems with velocity limits approach peak velocity gradually. The acceleration during this period is constantly decreasing. Thus, the force or torque that

can be applied during acceleration is a maximum initially and then decreases. Since the exact nature of this allowed force variation with time depends on the type of amplifier being used, as well as other system characteristics, we decided against trying to model this time-varying force signal. We chose instead to approximate the open-loop force profile by assuming that the acceleration (and deceleration) are constant. This can be accomplished by using constant force during acceleration and deceleration. While the system is coasting at the peak velocity, the input force is zero. This is only true under ideal conditions when no damping to ground or friction is present. However, feedback control can be used to compensate for this effect.

The trapezoidal velocity waveform that results from the use of constant accelerating and decelerating force pulses is necessarily slower than the actual velocity profile if saturation is to be avoided. But acceleration and peak velocity can be adjusted to give a trapezoidal profile that optimally fits within the actual achievable profile. Details of this development are given in Chapter 6. Thus, even though a trapezoidal velocity waveform is not the best response that a particular system can achieve, it serves as a reasonably fast reference response that avoids saturation.

In order to produce a trapezoidal velocity profile having a constant velocity region where the speed remains constant, the force profile must consist of three regions: acceleration, dwell, and deceleration. Ideally, the acceleration and deceleration regions resemble rectangular pulses in order to optimally utilize the available force. However, with their large discontinuities, these pulses cause considerable vibration when applied to the system. Thus, a smooth version of a rectangular pulse is needed that has energy removed at the system natural frequency. This force profile will accelerate the system to peak velocity.

Such a smooth profile can be constructed from a versine (1−cosine) function, shown in Figure 5.2. Notice that there are no discontinuities in slope at the beginning and end. When higher harmonics of this function are added to the fundamental, a function resembling a rectangular pulse can be created. The coefficients of the
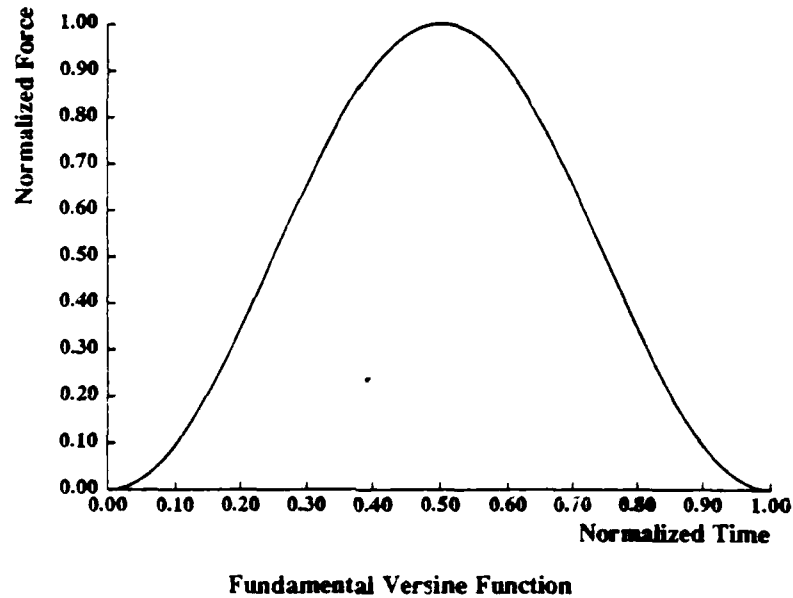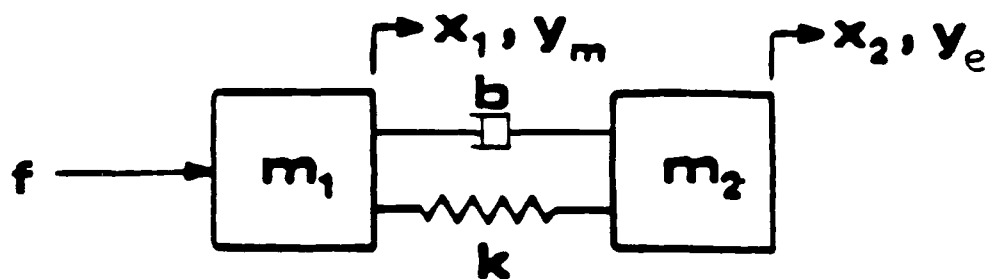
Fundamental Versine Function

Figure 5.2: Fundamental Versine Function.

harmonics can be chosen to minimize the energy of the resulting function at the system natural frequency. This requires that the frequency spectrum of the function be minimized at the natural frequency. This can be accomplished by performing an optimization in a manner analogous to that done for the ramped sinusoid functions of Chapter 2. Preliminary discussion of this development is soon to be published [70]. Shaped input functions will be constructed for a two-mass system as before (Fig. 5.3), having undamped natural frequency ω_n and dimensionless parameters as given in Table 5.1. The parameter v_p represents the peak velocity and T_R represents the time to move the equivalent rigid-body mass to peak velocity v_p using a rectangular pulse input having peak force F. As in Chapter 2, dimensionless parameters use the nominal natural frequency ω_N, while the actual natural frequency ω_A is represented by the ratio ω_A/ω_N. To simplify the derivation of the shaped versine inputs, an undamped system model will be assumed, which has a damping ratio ζ of zero.

In general, the input functions can be represented by the following series expan-

$$\frac{y_e^*}{f^*} = \frac{\left(\frac{\omega_A}{\omega_N}\right)^2}{s^2\left[s^2 + 2\zeta\left(\frac{\omega_A}{\omega_N}\right)s + \left(\frac{\omega_A}{\omega_N}\right)^2\right]}$$

Figure 5.3: Two-Mass System Model.

Table 5.1

Definition of Dimensionless Parameters

$$t^* = \omega_N t / 2\pi$$

$$y_m^* = \frac{\omega_N y_m}{v_p}$$

$$y_e^* = \frac{\omega_N y_e}{v_p}$$

$$\ddot{y}_e^* = \frac{\ddot{y}_e}{v_n \omega_N}$$

$$F^* = \frac{F}{(m_1 + m_2)v_p \omega_N} = \frac{1}{\omega_N T_R}$$

sion, where B_ℓ is the coefficient for each harmonic, and T_p represents the time for the versine response to reach peak velocity:

$$f(t) = \sum_{\ell=1}^{L} B_\ell \, \Phi_\ell^*(t) \tag{5.1}$$

$$\Phi_\ell^*(t) = 1 - \cos \frac{2\pi \ell t}{T_p} \tag{5.2}$$

$$\ell = 1, 2, 3, \dots \tag{5.3}$$

The goal is to choose appropriate values for B_ℓ that will minimize the time T_p and minimize the magnitude of the frequency spectrum over a range of frequencies surrounding the system resonant frequency ω_n.

To achieve this, we will combine these objectives into a single minimization problem to pick the coefficients B_ℓ. To minimize T_p, we will minimize the square of the difference between the versine series and a rectangular pulse. In addition, a second expression will be added to minimize the squared magnitude of the frequency spectrum F^* at several frequencies ω_i surrounding the system resonance. A weighting factor ρ determines relative weighting between these objectives. The overall objective function J represents the quantity to be minimized.

$$J = \frac{1}{T_p} \int_0^{T_p} [1 - f(t)]^2 dt + \rho \sum_{i=1}^{11} (\omega_i T_R)^2 |F^*(\omega_i T_p)|^2 \tag{5.4}$$

In this formulation, we have chosen 11 frequencies surrounding resonance to satisfy the spectral magnitude constraint. The upper and lower limits on frequency can be adjusted to give any desired frequency band. For a $\pm 10\%$ frequency range, the bounds on the frequency ω_i are $0.9\omega_n < \omega_i < 1.1\omega_n$.

The coefficients of the harmonics B_ℓ can be calculated by differentiating the objective function J with respect to B_r, where r represents a particular value of the index ℓ, and setting the result to zero. This gives an expression explicitly in terms of B_ℓ and $I'_{r\ell}$:

$$\sum_{\ell=1}^{L} B_\ell \, I'_{r\ell} = 1 \tag{5.5}$$

where

$$I'_{r\ell} = \left[I^{\bullet}_{r\ell} + \rho \, 4(2\pi)^4 \sum_{i=1}^{11} (\omega_i T_R)^2 \frac{\ell^2}{(2\pi\ell)^2 - (\omega_i T_p)^2} \frac{r^2}{(2\pi r)^2 - (\omega_i T_p)^2} \frac{\sin^2 \frac{\omega_i T_p}{2}}{(\omega_i T_p)^2} \right] \quad (5.6)$$

$$I^{\bullet}_{r\ell} = \begin{cases} 1 & r \neq \ell \\ 1.5 & r = \ell \end{cases} \quad (5.7)$$

If the time T_p is known then $I'_{r\ell}$ is known and the coefficients B_ℓ can be determined by simply solving the following set of linear equations, expressed in matrix form:

$$[I'_{r\ell}][B_\ell] = [1] \quad (5.8)$$

where $[1]$ is a vector of 1's. Unfortunately, T_p is not known until the coefficients B_ℓ are known. The dependence of T_p on B_ℓ is given by

$$T_p = \Gamma_V \, T_R \quad (5.9)$$

where

$$\Gamma_V = \frac{1}{\frac{1}{SF} \sum_{\ell=1}^{L} B_\ell}, \quad (5.10)$$

$$T_R = \frac{(m_1 - m_2)v_p}{F}. \quad (5.11)$$

SF is a scale factor which normalizes the peak of the function to 1. T_R represents the time to reach peak velocity v_p when the input is a rectangular pulse of magnitude F. Γ_V is a function of B_ℓ that ensures that the resulting input signal brings the system to the desired velocity. Since the versine functions cannot supply as much energy for the same peak force as the corresponding rectangular pulse, they will take slightly longer to reach peak velocity. This time penalty is represented by Γ_V.

Due to the inherent coupling of B_ℓ and Γ_V, an iteration scheme is necessary to correctly compute values for the coefficients B_ℓ. This iterative procedure is completely analogous to that for the ramped sinusoid functions of Chapter 2:

1. Determine $\omega_n T_R$ for given peak velocity and system parameters.

2. Guess a value of Γ_V. (Note that Γ_V is slightly greater than 1.)

3. Solve for B_ℓ by solving the matrix equation (5.8).

4. Normalize the versine series expansion by determining the value for the scale factor SF.

5. Calculate Γ_V using expression (5.10).

6. Use the new value of Γ_V to update B_ℓ.

7. Repeat until Γ_V converges to acceptable accuracy (error with respect to previous value is less than 10^{-5}).

Using the procedure outlined above, we can derive functions that satisfy our objectives. We used a total of $L = 15$ terms for computational efficiency while retaining enough parameters to achieve acceptable minimization. A good compromise between minimizing acceleration time T_p and minimizing spectral magnitude is achieved for a value of $\rho = 10$. Note that larger values of ρ will give lower spectral magnitudes and slightly longer acceleration times. Results for two nominal values of the dimensionless parameter $\omega_n T_R / 2\pi$ (7 and 10), minimizing spectral magnitudes at 11 frequencies extending $\pm 10\%$ around resonance, are shown in Figures 5.4 and 5.5. The time function is shown in (a) and the frequency spectrum is shown in (b). Notice that the spectral magnitudes for the entire range of frequencies extending $\pm 10\%$ about $\omega_n T_R$ have been significantly attenuated.

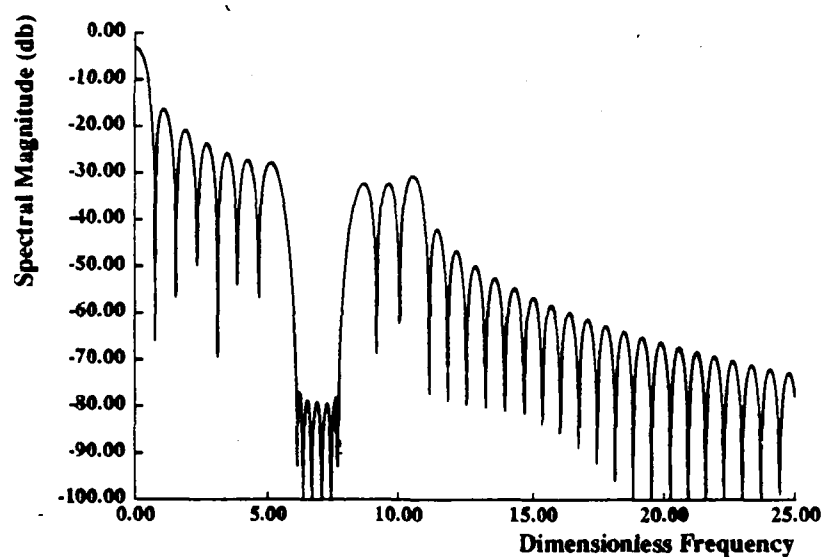## 5.3   Shaped Versine Inputs for Several Natural Frequencies:

The approach outlined in the previous section can also be extended to minimize excitation energy at several natural frequencies. The new objective function can be

Versine Input

(a)
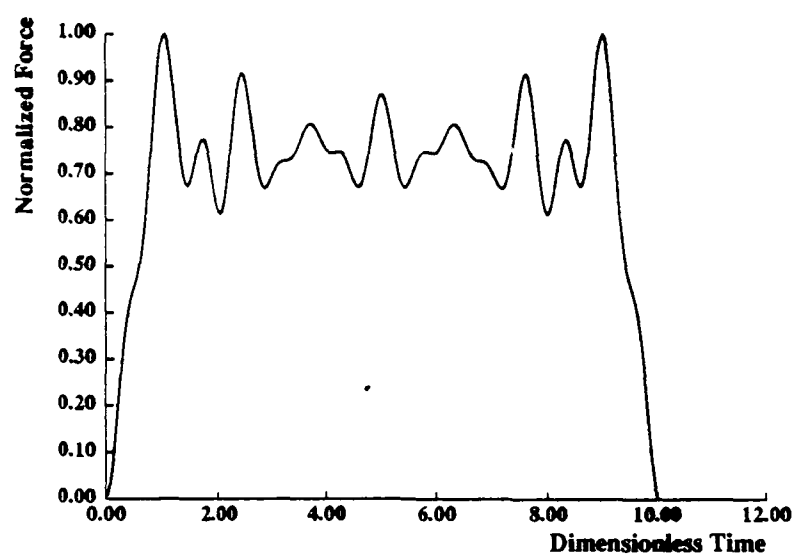
Frequency Spectrum of Versine Input

(b)

Figure 5.4: Versine Input Tuned to $\omega_n T_R/2\pi = 7 \pm 10\%$: (a) Time Function (b) Frequency Spectrum.

Versine Input
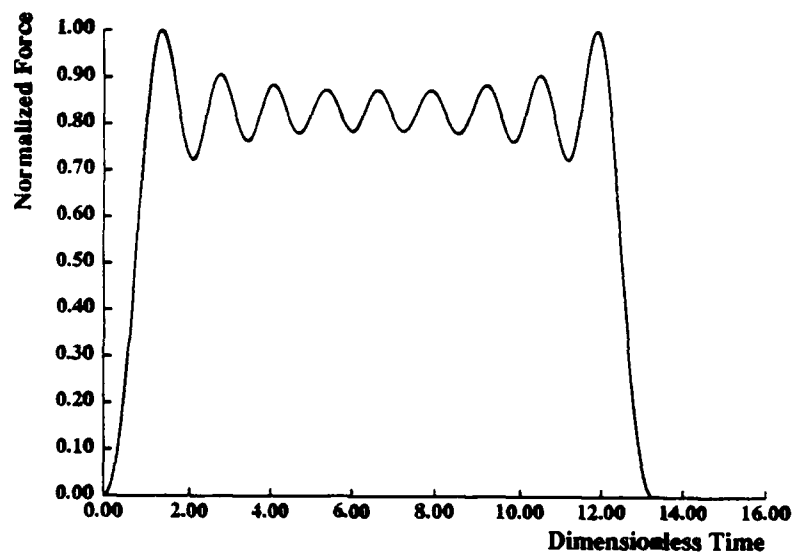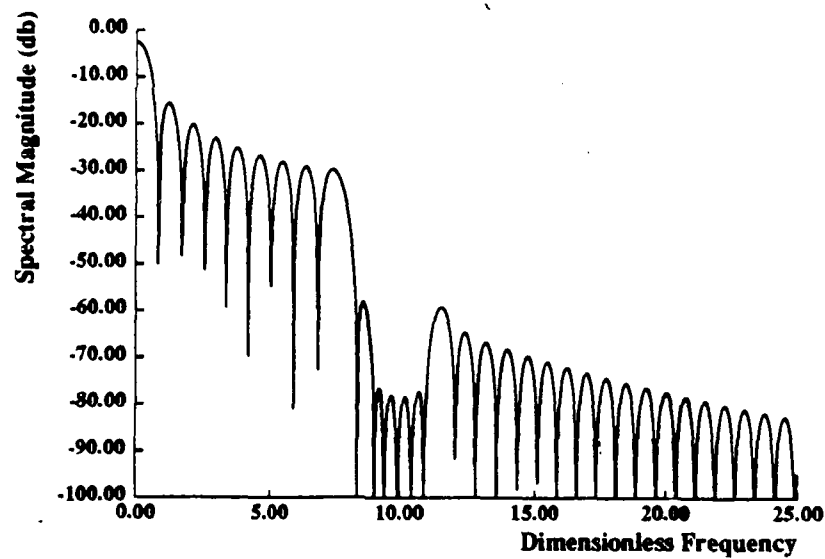
(a)

Frequency Spectrum of Versine Input

(b)

Figure 5.5: Versine Input Tuned to $\omega_n T_R/2\pi = 10 \pm 10\%$: (a) Time Function (b) Frequency Spectrum.

expressed as

$$J = \frac{1}{T_p} \int_0^{T_p} [1 - f(t)]^2 dt + \rho \sum_{i=1}^{11M} (\omega_i T_R)^2 |F^*(\omega_i T_p)|^2 \qquad (5.12)$$

where M is the total number of modes (natural frequencies) to attenuate, and ω_i is given by

$$(1 - p_m)\omega_m < \omega_i < (1 - p_m)\omega_m, \qquad i = m, \ldots, 11m \qquad (5.13)$$

where p_m represents the fraction of nominal frequency that determines the upper and lower bounds of the frequency band surrounding the nominal natural frequency ω_m for the mth mode.

When this minimization is carried out as before, a new set of coefficients are determined. A versine input attenuating three natural frequencies at $\omega_m T_s / 2\pi = 1.5$, 5, and 10 with 10% frequency bands is shown in Figure 5.6(a), with corresponding frequency spectrum in (b). Notice that all three frequencies have been attenuated as specified.

5.4 Shaped Versine Inputs for Lightly-Damped Systems:

In section 2.6 of Chapter 2, we presented results that showed the effect of inherent system damping on the residual acceleration amplitudes when the system is driven by a particular shaped input. We can now apply those results to the versine functions developed here. We will use the single-resonance model (Fig. 5.3) for simplicity.

The entire development follows exactly as in Chapter 2, except that the Fourier transform of the versine function is expressed as

$$F(\omega) = F_R(\omega) \epsilon^{-j \frac{\omega T_p}{2}} \qquad (5.14)$$

where

$$F_R(\omega) = 2 \frac{F T_p}{SF} \left| \sum_{\ell=1}^{L} \frac{B_\ell (2\pi \ell)^2 \sin \frac{\omega T_p}{2}}{\omega T_p [(2\pi \ell)^2 - (\omega T_p)^2]} \right|, \qquad (5.15)$$

Versine Input

(a)
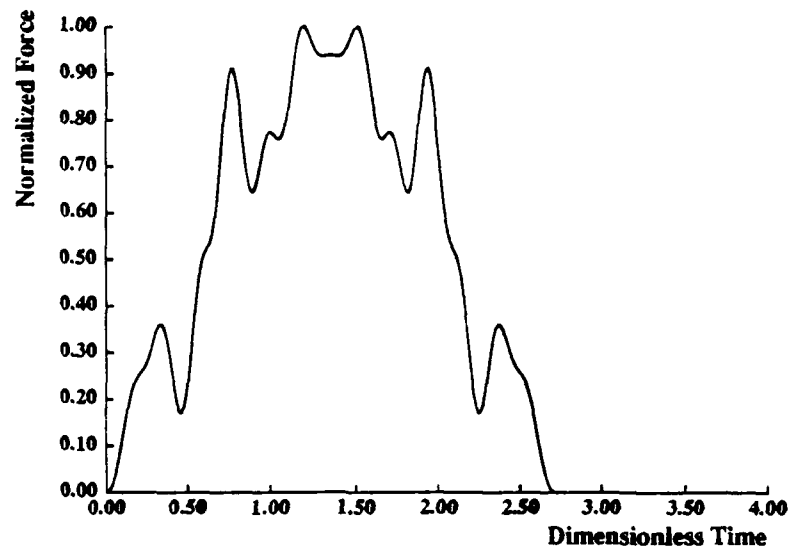
Frequency Spectrum of Versine Input

(b)

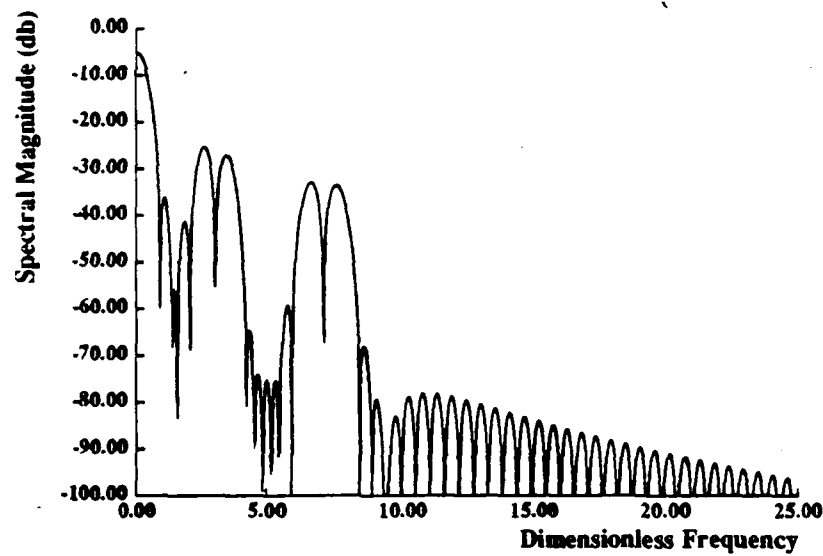Figure 5.6: Versine Input Tuned to $\omega_m T_R/2\pi = 1.5$, 5, and $10\pm\%$: (a) Time Function (b) Frequency Spectrum.

F is the peak force, and SF is a normalizing scale factor. This modifies the expression for the square of the residual acceleration amplitude to be in terms of $F_R(\omega)$ rather than $F_I(\omega)$ as in (2.38):

$$A^2 = \left(\frac{\omega_n}{m_1 + m_2}\right)^2 \frac{e^{-\zeta \omega_n T_p}}{1 - \zeta^2} F_R(\omega_n \sqrt{1 - \zeta^2} + j\zeta\omega_n) F_R(-\omega_n\sqrt{1 - \zeta^2} + j\zeta\omega_n). \quad (5.16)$$

When the expression for $F_R(\omega)$ is inserted into (5.16), the dimensionless residual acceleration amplitude can be expressed as

$$(A^*)^2 = \left(\frac{A}{F/(m_1 + m_2)}\right)^2 = 4\left(\frac{\omega_n T_p}{SF}\right)^2 \frac{e^{-\zeta\omega_n T_p}}{1 - \zeta^2}\left[\frac{s^2 ch^2 + c^2 sh^2}{(\omega_n T_p)^2}\right.$$

$$\left. \bullet \sum_{\ell=1}^{L}\sum_{r=1}^{L} \frac{B_\ell B_r (2\pi\ell)^2 (2\pi r)^2 [\phi(2\pi\ell)\phi(2\pi r) + 4\zeta^2(1 - \zeta^2)(\omega_n T_p)^4]}{[\phi(2\pi\ell)^2 + 4\zeta^2(1 - \zeta^2)(\omega_n T_p)^4][\phi(2\pi r)^2 + 4\zeta^2(1 - \zeta^2)(\omega_n T_p)^4]}\right] \quad (5.17)$$

where s, c, sh, and ch are defined as

$$s = \sin \omega_n \sqrt{1 - \zeta^2}\frac{T_p}{2} \quad (5.18)$$

$$c = \cos \omega_n \sqrt{1 - \zeta^2}\frac{T_p}{2} \quad (5.19)$$

$$sh = \sinh \zeta\frac{\omega_n T_p}{2} \quad (5.20)$$

$$ch = \cosh \zeta\frac{\omega_n T_p}{2} \quad (5.21)$$

and the functions $\phi(2\pi\ell)$ are defined as

$$(2\pi\ell)^2 - (1 - 2\zeta^2)(\omega_n T_p)^2. \quad (5.22)$$

Expression (5.17) gives the dimensionless peak residual amplitude for a versine input as a function of the dimensionless frequency ωT_p. Using the known value of Γ_V for a particular versine input, this functional dependence can also be expressed in terms of ωT_R.

Some typical plots showing this functional dependence for several different values of ζ with a versine input tuned to $\omega_n T_R/2\pi = 10$ are shown in Figures 5.7 to 5.9. For the case when $\zeta = 0$ (Figure 5.7), the plot of residual amplitude as a function

Figure 5.7: Residual Acceleration Amplitude as a Function of $\omega T_R/2\pi$ for Versine Input Tuned to $\omega_n T_R = 10 \pm 10\%$; $\zeta = 0.0$.

Figure 5.8: Residual Acceleration Amplitude as a Function of $\omega T_R/2\pi$ for Versine Input Tuned to $\omega_n T_R = 10 \pm 10\%$; $\zeta = 0.1$.
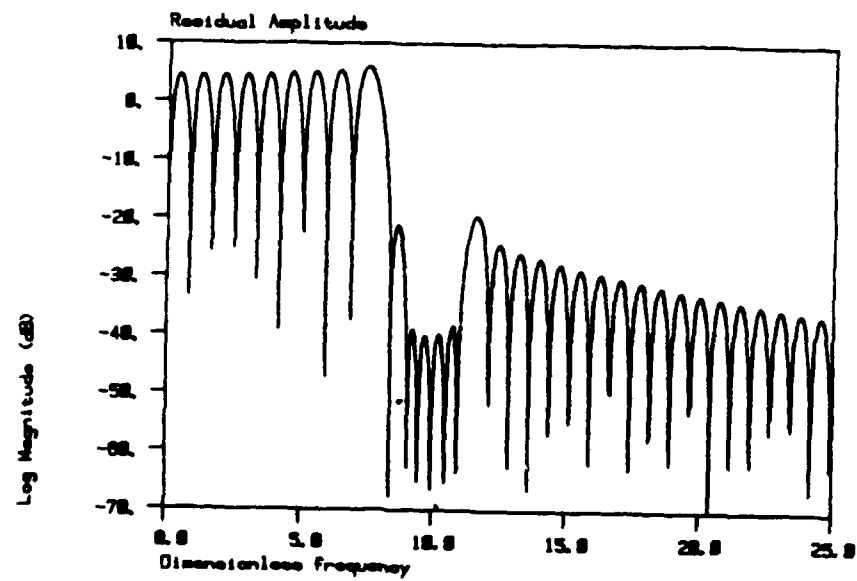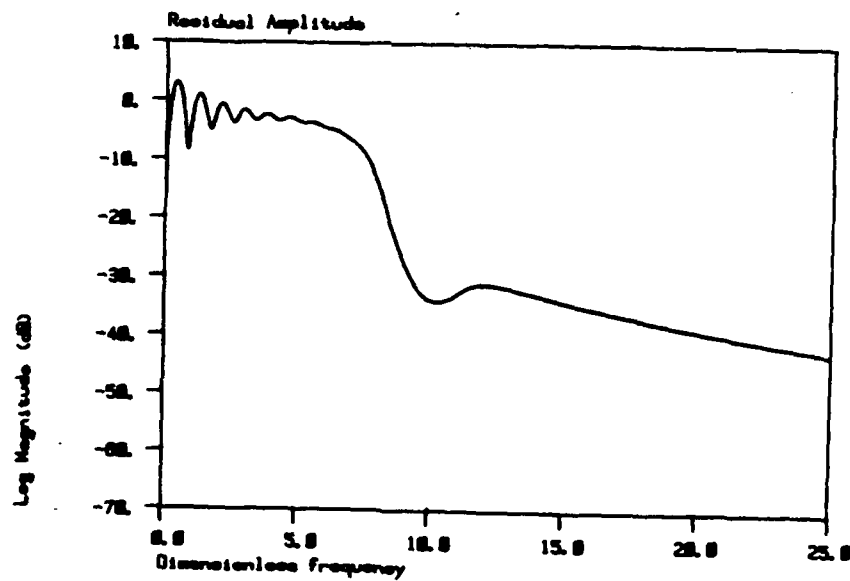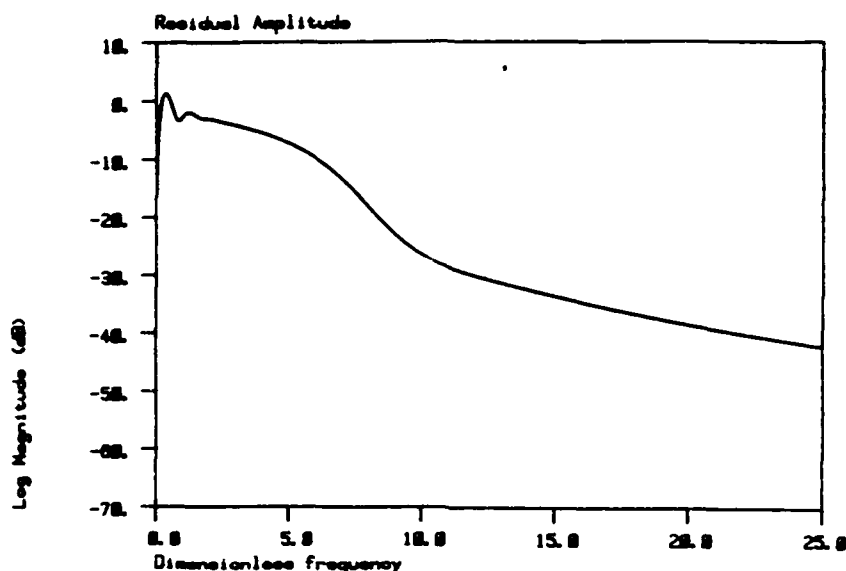
Figure 5.9: Residual Acceleration Amplitude as a Function of $\omega T_R/2\pi$ for Versine Input Tuned to $\omega_n T_R = 10 \pm 10\%$; $\zeta = 0.3$.

of frequency resembles the frequency spectrum of the versine input (Figure 5.5). It differs from the frequency spectrum because it represents $\omega_n T_R$ times the frequency spectrum. As ζ increases from $\zeta = 0.1$ in Figure 5.8 to $\zeta = 0.3$ in Figure 5.9, the residual acceleration function becomes smoother, the valleys rise and the peaks drop. In general, the range of frequencies over which good vibration attenuation is maintained is reduced as the damping ratio increases.

For lightly damped systems, the effect of damping is small enough that versine inputs with notched frequency spectra will work quite well. For more heavily damped systems, the expression (5.17) for residual acceleration could be inserted into the objective function J of (5.4) in place of the frequency spectrum. This would ensure small residual vibration over the specified frequency range.

5.5 Closed-Loop Simulation Results:

The force profiles that we have just developed are suitable for open-loop implementation, where force inputs can be directly specified. In closed-loop systems, however,

the force input is typically determined by the combination of a reference trajectory and several feedback signals. Thus. only by specifying a reference trajectory can the force input be affected.

We will again use the closed-loop control scheme proposed in Section 4.3 of Chapter 4. A damped two-mass system model is used as the plant (Fig. 4.2). Motor position and velocity are measured and fed back with gains k_1 and k_2 as shown in Figure 4.8. This represents a simple PD controller. The control input u^* is generated from a reference signal y_r^* and from the motor feedback position and velocity. An advantage of this control scheme is its stability robustness when system parameters change. Stability robustness improves when actuator and sensor are colocated at the motor.

The force profile used in this control scheme must be tuned to the closed-loop natural frequencies. For the PD feedback loop with $k_1 = k_2 = 4$. the dominant closed-loop natural frequency is 70% of the open-loop natural frequency. Thus, the versine force profile should be tuned to a natural frequency which is 70% of the open-loop natural frequency.

Once the proper force profile has been tuned to the closed-loop system, the corresponding reference trajectory can be determined. The reference trajectory y_r^* is generated by doubly integrating the force profile u_d^*. This generates a position reference signal which contains very little energy at the specified closed-loop natural frequency.

For a system model with parameter $\omega_N T_R / 2\pi = 10$, where ω_N represents the nominal open-loop natural frequency, the shaped input must be tuned to $\omega_C T_R / 2\pi = 7$, where ω_C corresponds to the closed-loop natural frequency. This force profile is shown in Figure 5.4(a). Using this force profile in the closed-loop control system leads to the simulation results shown in Figure 5.10. The actual control force u^* is shown in (a), while the endpoint acceleration of the mass distant from the motor is shown in (b). When the force ends near the dimensionless time of 15, the system
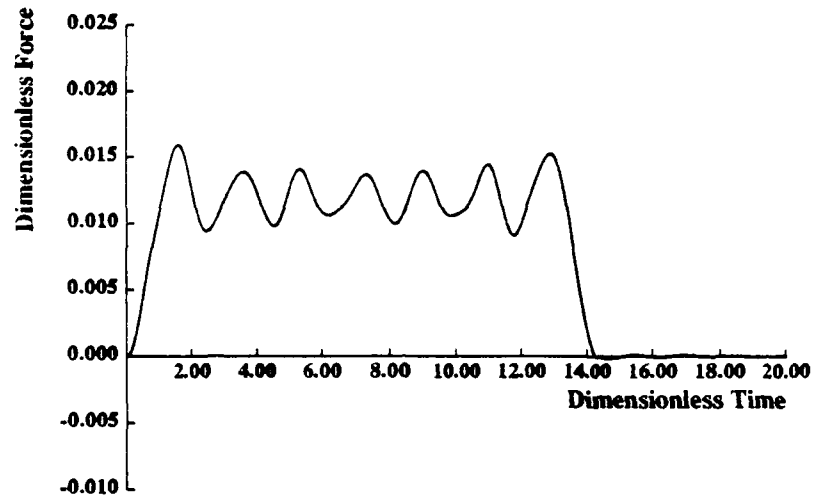
Nominal Closed-Loop Response to a Versine Input

(a)
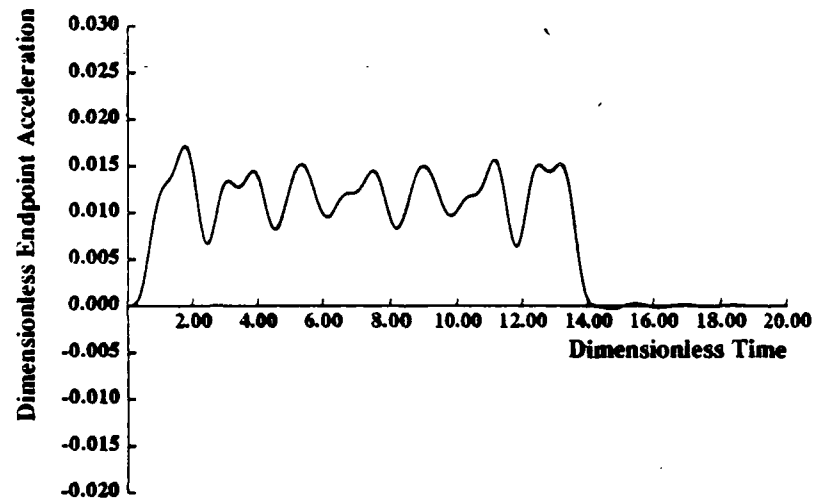
Nominal Closed-Loop Response to a Versine Input

(b)

Figure 5.10: Simulated Closed-Loop Response for Nominal System Accelerating to Peak Velocity with Versine Input; $\omega_N T_R/2\pi = 10$, $\omega_C T_R/2\pi = 7$, $\zeta = 0.1$: (a) Control Force (b) Endpoint Acceleration Response.

has reached peak velocity. As the acceleration signal indicates, the system achieves peak velocity with very little vibration remaining as it begins its constant velocity region.

The situation described above represents the case when the closed-loop natural frequency is known exactly. When the actual system frequency differs from the nominal natural frequency for which the inputs were constructed, the simulation response of Figure 5.11 results. In this case, the ratio of actual natural frequency to nominal natural frequency was assumed to be $\omega_A/\omega_N = 0.9$. Notice that the residual vibration has increased compared to that when no error in natural frequency exists. This is due to the effect of damping. However, the response is still quite good despite the error in natural frequency.

It is instructive to compare these results with the response obtained by simply using a rectangular pulse as the force profile. Simulation plots for that case are shown in Figure 5.12, again with control force in (a) and endpoint acceleration in (b). Notice that considerable vibration occurs when peak velocity is reached after 11 dimensionless time units, and this has not decayed to the level achieved by the shaped profile even after 20 dimensionless time units. Thus, the shaped versine profile achieves peak velocity with considerably less vibration than the rectangular pulse.

5.6 Development of Shaped Inputs to Reach a Specified Position:

So far in this chapter, shaped inputs have been developed in order to accelerate a vibrating system to peak velocity with minimum residual vibration. In order to arrive at a desired position, the system must also be brought from peak velocity to rest using a shaped decelerating force profile. This can be accomplished by using exactly the same force profile as for acceleration but with the opposite sign. The
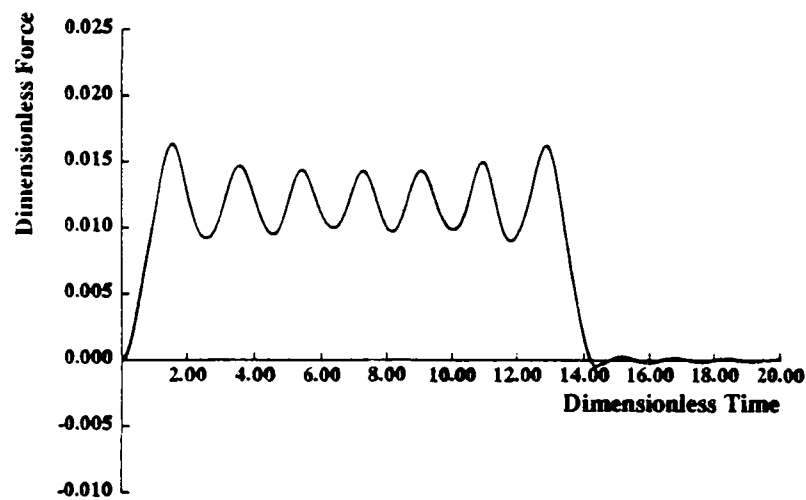
Actual Closed-Loop Response to a Versine Input

(a)
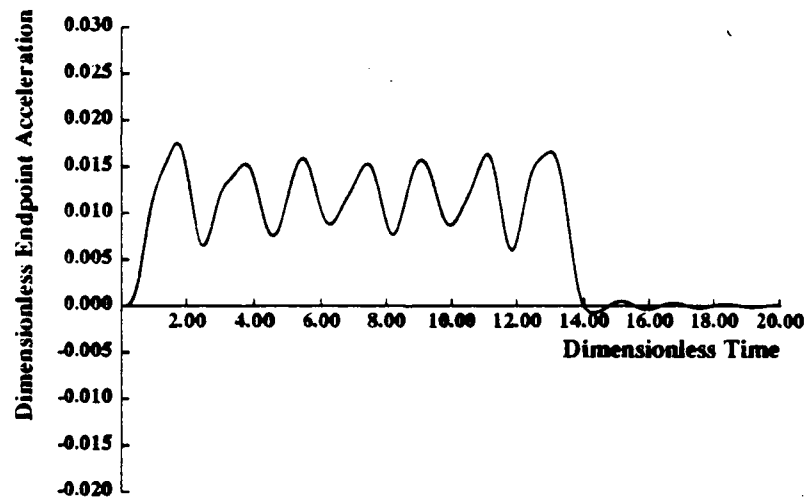
Actual Closed-Loop Response to a Versine Input

(b)

Figure 5.11: Simulated Closed-Loop Response for Actual System Accelerating to Peak Velocity with Versine Input; $\omega_N T_R/2\pi = 10$, $\omega_C T_R/2\pi = 7$, $\zeta = 0.1$, $\omega_A/\omega_N = 0.9$: (a) Control Force (b) Endpoint Acceleration Response.

Nominal Closed-Loop Response to a Rectangular Pulse Input

(a)

Nominal Closed-Loop Response to a Rectangular Pulse Input

(b)

Figure 5.12: Simulated Closed-Loop Response for Nominal System Accelerating to Peak Velocity with Rectangular Pulse Input; $\omega_N T_R/2\pi = 10$, $\omega_C T_R/2\pi = 7$, $\zeta = 0.1$: (a) Control Force (b) Endpoint Acceleration Response.

only remaining parameter to be determined is the time for which the system moves at peak velocity.

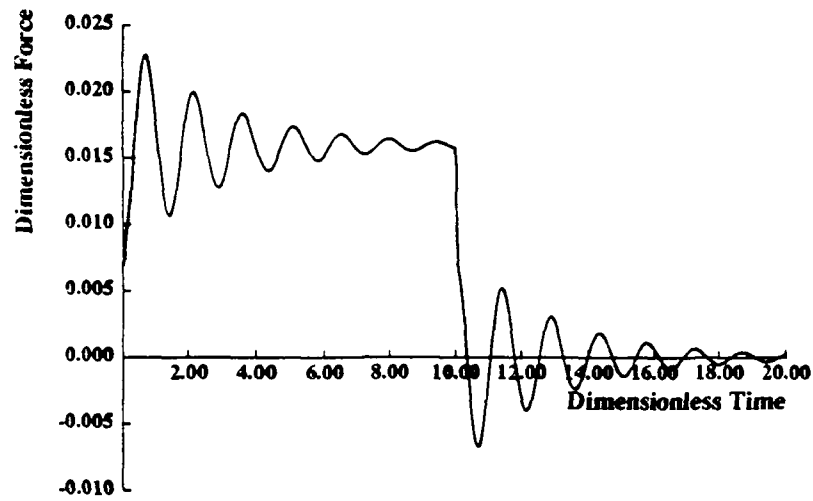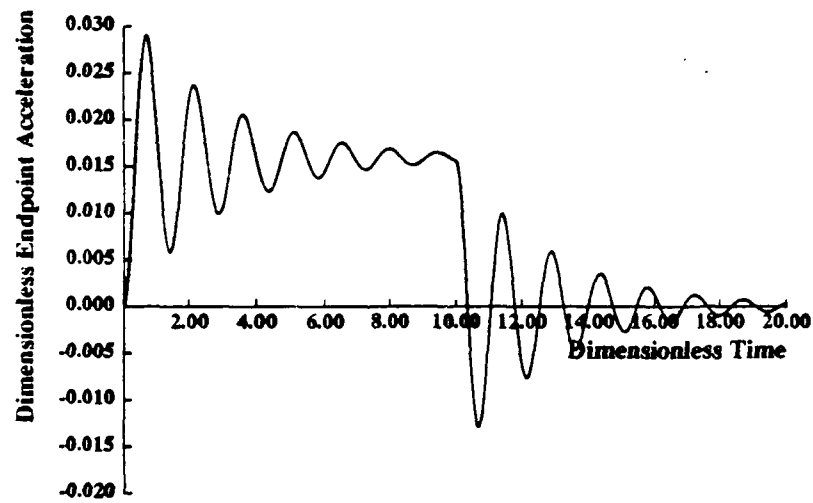In order to ensure that the system arrives at the desired final position y_f, the dwell time T_d at which the system moves at constant velocity v_p should be determined as follows:

$$T_d = \frac{y_f}{v_p} - T_p \qquad (5.23)$$

In dimensionless form, this can be rewritten as

$$\omega_N T_d = y_f^* - \omega_N T_p. \qquad (5.24)$$

A typical force profile, with the corresponding velocity profile and position trajectory is shown in Figure 5.13. Notice that the velocity resembles a trapezoidal profile.

For a dimensionless distance y_f^* giving a dwell time of $\omega_N T_d = \omega_N T_p$ for the versine input, the simulated nominal system response with PD feedback is as shown in Figure 5.14. Notice that the acceleration amplitude remains low after both the acceleration and the deceleration phases of the motion.

In comparison, the rectangular pulse input for the same distance y_f^* has a dwell time of $\omega_N T_d = y_f^* - \omega_N T_R$. This is longer than the dwell time for the versine input since the system accelerates and decelerates more rapidly with the rectangular pulse input. System response for the rectangular pulse input is shown in Figure 5.15. As before (Figure 5.12), there is considerably more vibration after acceleration and deceleration with the rectangular pulse input than with the versine input.

A comparison of move times shows that the rectangular pulse input is faster if the additional settling time is ignored. But this time advantage is lost by the additional time required for the vibration to settle. For longer moves, the versine time penalty becomes comparatively smaller because the longer acceleration time becomes a smaller fraction of total move time. This can be seen by expressing total
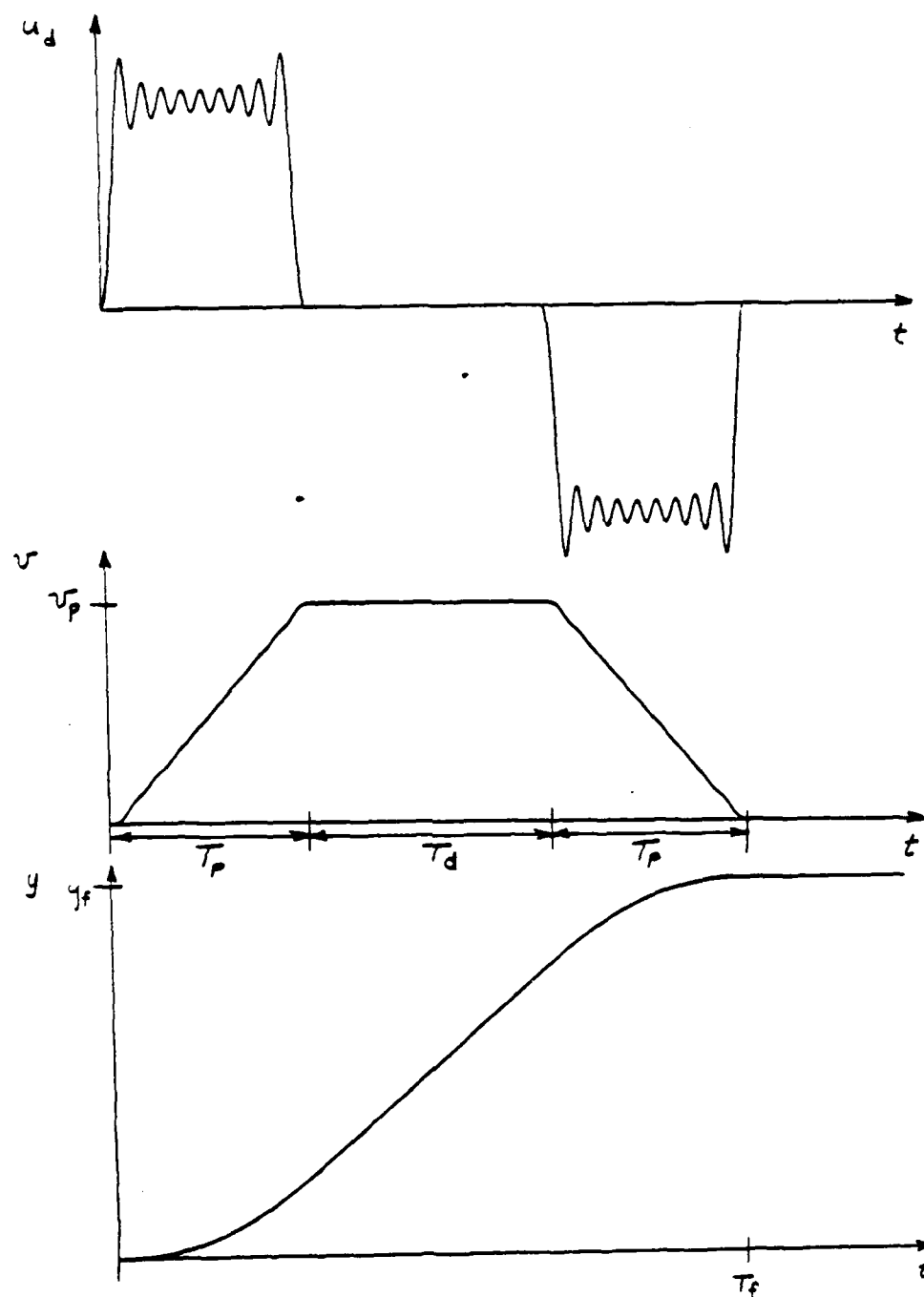
Figure 5.13: Force Profile, Velocity Profile, and Position Trajectory for a Versine Input to Reach a Specified Position.
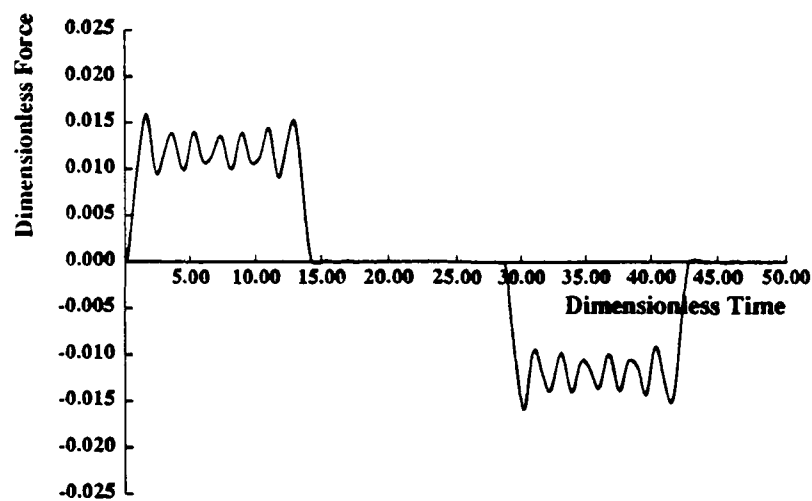
Versine Response to a Specified Position

(a)
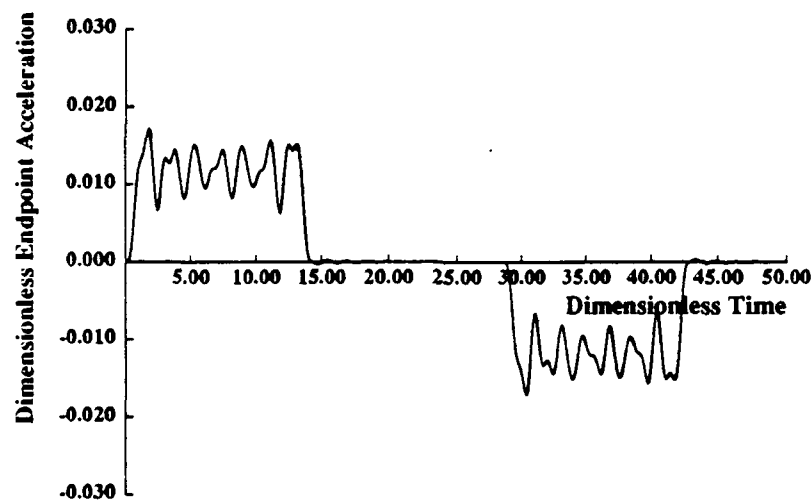
Versine Response to a Specified Position

(b)

Figure 5.14: Simulated Closed-Loop Response for Nominal System Moving a Specified Distance with Versine Input; $y_f^*/2\pi = 28.6$, $\omega_N T_R/2\pi = 10$, $\omega_C T_R/2\pi = 7$, $\zeta = 0.1$: (a) Control Force (b) Endpoint Acceleration Response.
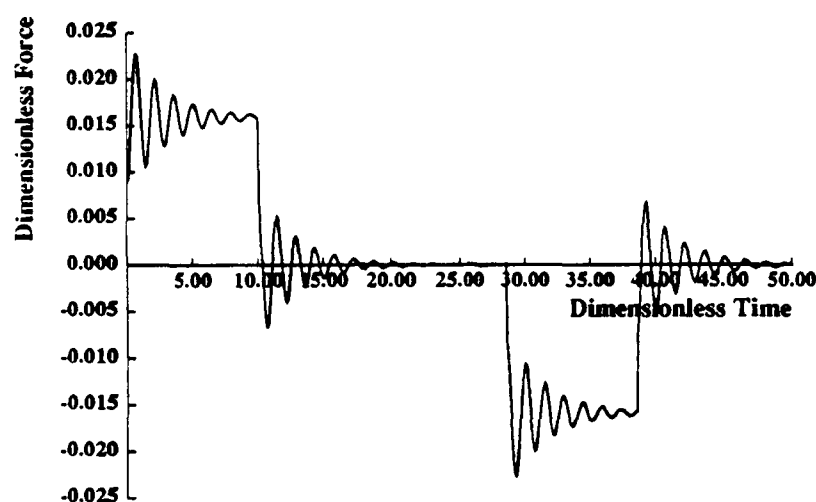
Rectangular Pulse Response to a Specified Position

(a)
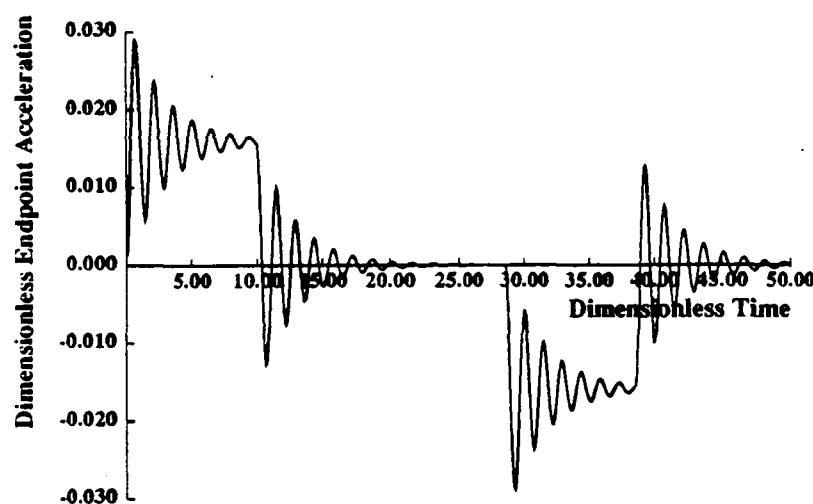
Rectangular Pulse Response to a Specified Position

(b)

Figure 5.15: Simulated Closed-Loop Response for Nominal System Moving a Specified Distance with Rectangular Pulse Input; $y_f^*/2\pi = 28.6$, $\omega_N T_R/2\pi = 10$, $\omega_C T_R/2\pi = 7$, $\zeta = 0.1$: (a) Control Force (b) Endpoint Acceleration Response.

move time as

$$\omega_N T_f = 2\omega_N T_p + \omega_N T_d = y_f^* + \omega_N T_p = y_f^* + \Gamma_V \omega_N T_R. \qquad (5.25)$$

The effect of $\Gamma_V > 1$ becomes smaller as the distance y_f^* increases. Thus, the time penalty in shaping the inputs becomes less important for longer moves.

An additional advantage of versine inputs is that for a given set of system parameters and peak velocity, only a single shaped function needs to be derived for all moves which are long enough to at least reach peak velocity. This can greatly simplify the computations needed to develop inputs for any desired position. In comparison, the ramped sinusoid inputs need to be rederived for each new position.

For distances which are short enough that the system cannot reach peak velocity, the ramped sinusoid inputs are preferred. This is because they only reduce vibration at the end of the move, while the versine inputs reduce vibration after both the acceleration and the deceleration phases. These more stringent constraints on the versine input generally increase the total move time compared to the ramped sinusoid input. Thus, ramped sinusoid inputs should be constructed for all moves which can just reach peak velocity. For all longer moves, the versine inputs should be used.

5.7   Closure:

This chapter has presented the development of a new set of functions that can be used for systems having a velocity limit. Shaped versine inputs can accelerate and decelerate the system with very little residual vibration. The total time to cover a specified distance is longer for these shaped inputs than for rectangular pulse inputs. But rectangular pulse inputs generate residual vibration that requires additional time to damp out. For longer moves, the time penalty associated with shaped versine inputs becomes less important. With moves long enough for the system to reach peak velocity, the versine input need only be constructed once and

only the dwell time must be altered to arrive at any desired position. For shorter moves, the ramped sinusoid functions of Chapter 2 must be determined for each desired move distance.

Modeling the MIT Cartesian Robot

6.1 Introduction:

Having presented a set of shaped force inputs and a control scheme in which they can be incorporated, we are now in a position to apply these inputs to a physical device – the MIT Cartesian Robot [71,72]. This chapter will develop a detailed model of the robot structure, actuators, and digitally-implemented control loop. Once this model has been verified by experimental results, it will be used to determine optimum parameters for the velocity profile generating a specified motion.

The MIT robot was designed for stiffness and speed. A schematic is shown in Figure 6.1. A Cartesian configuration was chosen in order to minimize coupling between axes and to simplify trajectory calculations. This arrangement also permits higher stiffnesses. The cantilevered top frame permits maximum access to the robot workspace. Structural members are constructed of steel box sections welded and bolted together. Moving elements are made of hollow aluminum weldments for maximum stiffness-to-weight ratio.

The moving elements – X,Y, and Z carriages – move on cam rollers stiffly

126
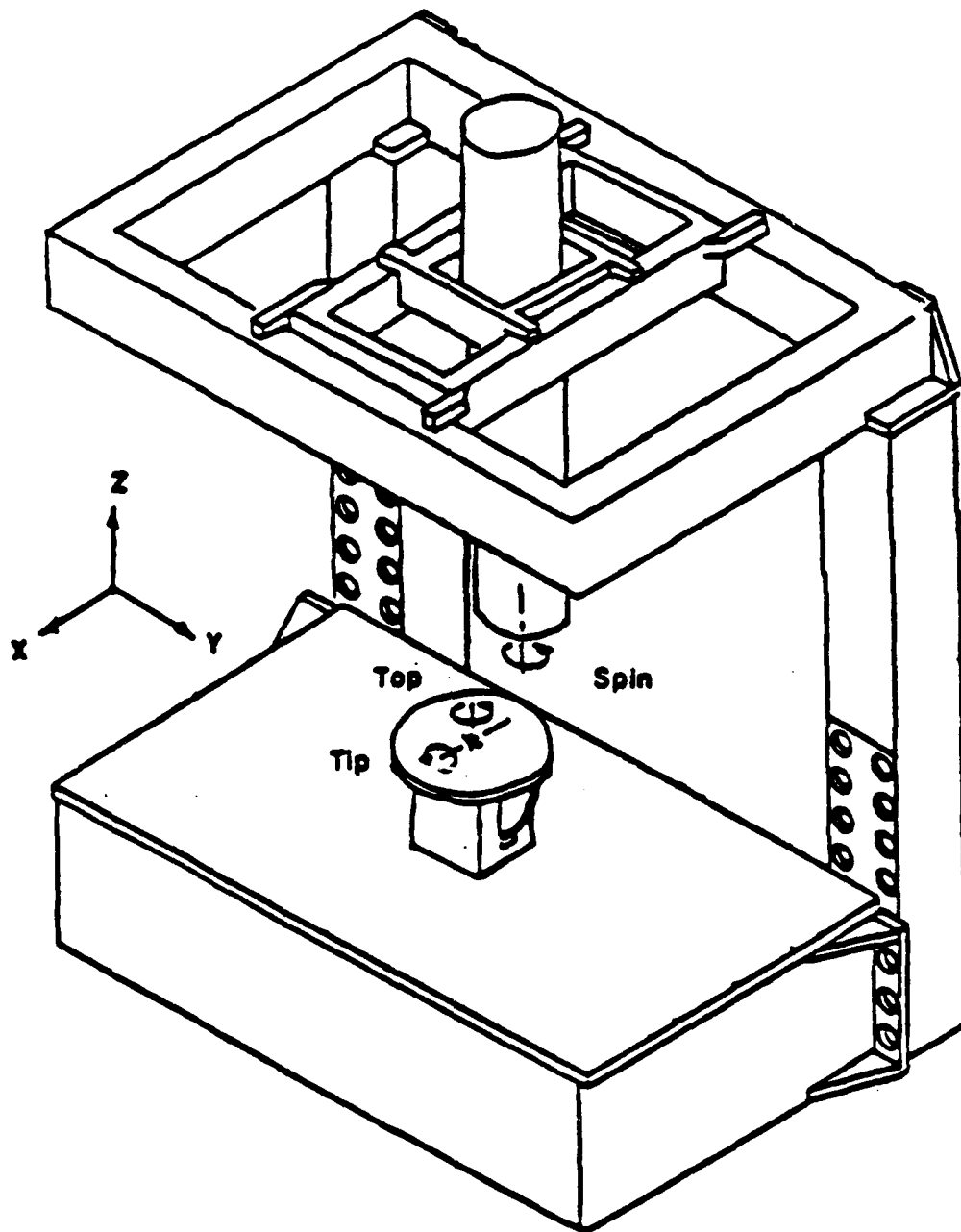
Figure 6.1: M.I.T. Cartesian Robot.
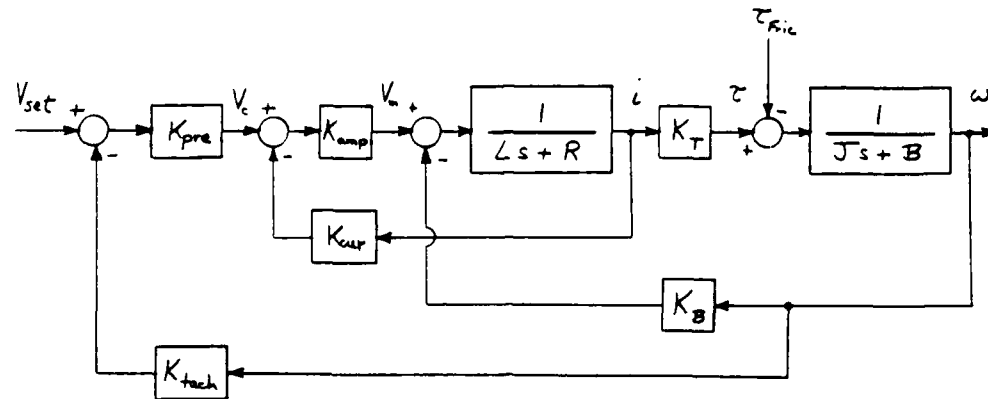
Figure 6.2: Block Diagram Model of Actuator.

preloaded against ground steel ways. Three Aerotech DC permanent magnet motors drive the axes. Ground ball screws convert motor rotation to translation of the X and Y carriages. The Z-axis uses a rack and pinion drive. Further details on the design and construction of the MIT robot can be found in Vaaler [71] and Podoloff [72].

Power for the Aerotech motors comes from an Automatix pulse-width-modulating amplifier which uses both current and tachometer feedback. Motor voltage is supplied by varying the pulse width of a 19.4 kHz pulse generator having a supply voltage of 150 volts. The inductance in the motor effectively filters this pulsing signal to generate smooth motion. Further details on the amplifier are contained in Nussbaum [73] and Drlik [74].

6.2 Actuator Model:

A block diagram model of the actuator can be developed by representing the dynamics of the amplifier and the DC motor. This model is shown in Figure 6.2. For the time being, the robot axis is treated simply as a rigid-body inertia, with viscous damping and friction.

The input to this model is a voltage command V_{set} which specifies the desired
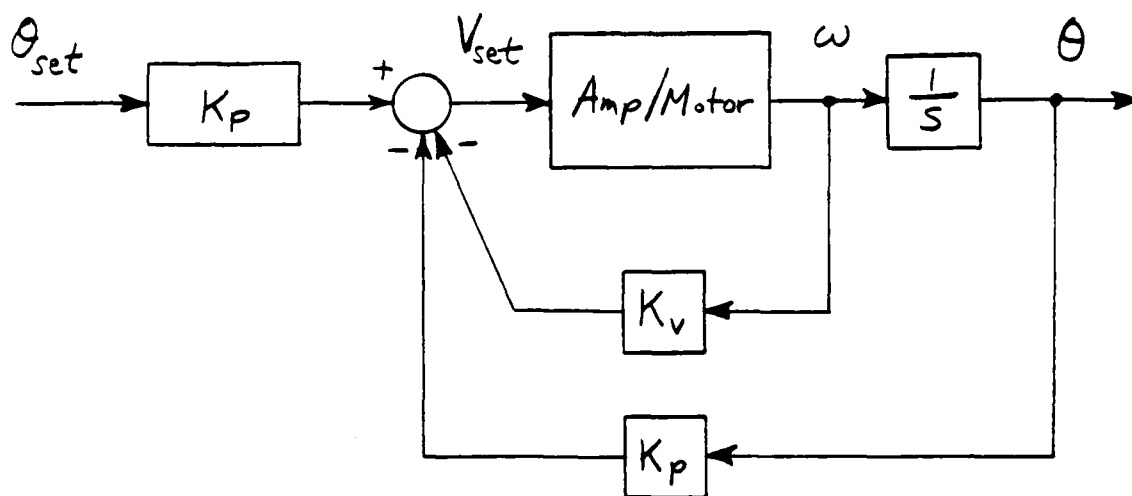
Figure 6.3: Block Diagram Model of Closed-Loop Controller.

velocity. This is compared with the tach velocity signal and amplified in the preamplifier section. This generates a current command V_c which is compared with the measured current signal to regulate the pulse width of the voltage signal V_m to the motor.

The motor model includes the effects of winding resistance R and inductance L. The motor generates a torque τ_m proportional to current i and develops a back emf voltage proportional to rotational velocity ω.

The transfer function relating the speed ω to the velocity command V_{set} can be expressed as

$$\frac{\omega(s)}{V_{set}(s)} = \frac{\frac{1}{JL} K_T K_{amp} K_{pre}}{s^2 + \left(\frac{R + K_{amp} K_{cur}}{L} + \frac{B}{J}\right) s + \frac{B(R + K_{amp} K_{cur}) + K_T(K_{amp} K_{pre} K_{tach} + K_B)}{JL}}. \quad (6.1)$$

Treating this actuator model as a single block to represent the hardware, a complete block diagram of the closed-loop position controller implemented in software is shown in Figure 6.3.

Computer control of the robot is achieved by a hierarchical software architecture. A PDP 11/23 minicomputer runs FORTH words that download commands to a set of Intel 8031 microprocessors, one for each axis. The PDP 11/23 is also connected to

a VAX 780 running in UNIX that can be used for generating complicated trajectory profiles and for plotting data. A detailed presentation of the computer controller can be found in Benjamin [75].

In the block diagram of Figure 6.3, the position measurement is obtained from an optical encoder mounted behind the tachometer on each motor. Velocity is calculated by dividing the difference in encoder counts by the sampling time interval. Each encoder generates 4000 counts per revolution and the servo loop runs at 1500 Hz so the velocity information obtained from these differences is quite satisfactory. Because of the limited resolution of the analog-to-digital converter, this differenced velocity is more accurate than the tachometer signal.

The proportional and derivative feedback gains are implemented in microcode on the microprocessors. Since motor position is obtained in encoder counts and the actual velocity command to the amplifiers is calculated as an equivalent 12-bit count to the digital-to-analog converter, the values for K_p and K_v used in the equivalent analog representation of Figure 6.3 differ from the digital counts K_{pd} and K_{vd} specified in the computer. The relationships between these two sets of parameters are given by:

$$K_p = K_{pd} K_{enc} K_{D/A} \tag{6.2}$$

$$K_v = K_{vd} K_{enc} K_{D/A} T_{samp} \tag{6.3}$$

where

$K_{enc} = 4000$ counts$/2\pi$ rad

$K_{D/A} = 10\text{V}/2047$ counts

$T_{samp} = 0.667$ msec.

The digital feedback gains used during actual tests were $K_{pd} = 0.9$ and $K_{vd} = 7.5$.

The response of the X-axis to a step change in position setpoint of 56.55 radians on the actual robot is shown in Figure 6.4. The velocity is shown in (a), the motor current in (b), the motor position in (c), and the motor velocity in (d). A number of signals saturate during this step response. The velocity command voltage saturates

X-Axis Move with Step Setpoint

(a)
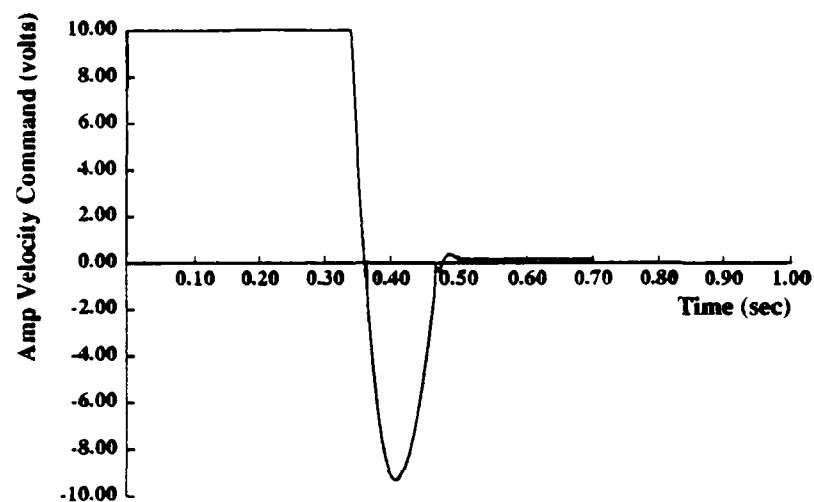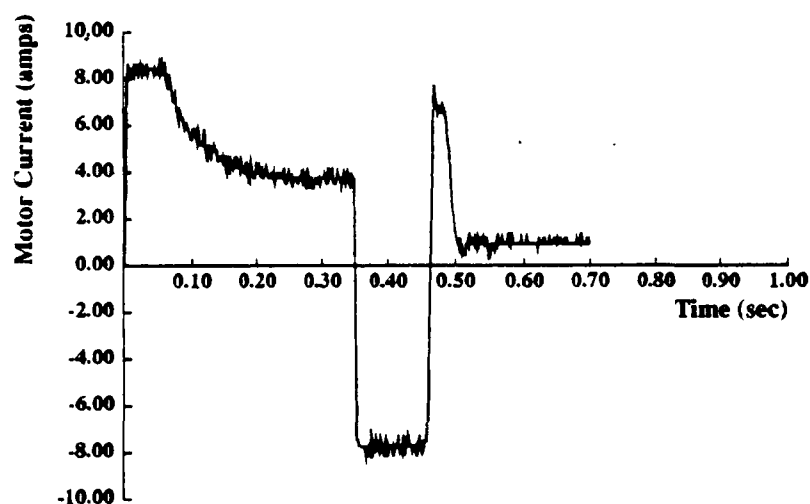
X-Axis Move with Step Setpoint

(b)

Figure 6.4: Actual X-Axis Response to 56.55 rad Step Setpoint: (a) Velocity Command (b) Motor Current.

X-Axis Move with Step Setpoint

(c)
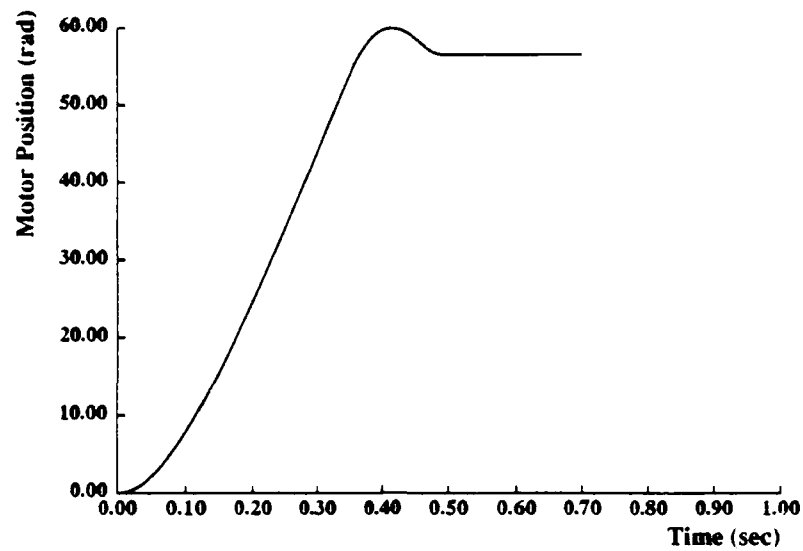
X-Axis Move with Step Setpoint

(d)

Figure 6.4: Actual X-Axis Response to 56.55 rad Step Setpoint: (c) Motor Position (d) Motor Velocity.

Table 6.1

Actuator Model Simulation Parameters

$K_{pre} = 4.3$	$K_{tach} = 0.024$ Volt $-$ sec/rad
$K_{amp} = 23.8$	$J_X = 2.053 \times 10^{-3}$ kg $-$ m^2
$K_{cur} = 0.333$	$J_Y = 2.780 \times 10^{-3}$ kg $-$ m^2
$L = 0.0158$ h	$B = 0.0055$ Nm $-$ sec
$R = 2 \Omega$	$\tau_{fric} = 0.7$ Nm
$K_T = 0.5$ Nm/amp	$K_p = 3.11$
$K_B = 0.5$ Volt $-$ sec/rad	$K_v = 0.04$

at ± 10 volts, the current command at ± 5.4 volts. Maximum motor voltage is 150 volts and the current saturates at 8 amps. This response served as the basis for evaluating the simulation model.

Parameters for the simulation model representing the robot under position control were determined from measurements and specifications. Values for these parameters are given in Table 6.1. Some of these values, in particular K_{amp} and K_v, had to be adjusted in order to make simulated transient response agree with the actual data of Figure 6.4.

When saturation is included in the robot simulation model, the simulated step response for the same 56.55 radian step is shown in Figure 6.5. Notice that the model captures the same dynamic behavior that the actual system exhibits. While the system is accelerating, motor voltage is saturated. As motor speed increases, so does the back emf voltage. More motor voltage goes into overcoming the back emf losses so that motor current begins to decrease. This reduces the rate of acceleration and eventually motor velocity reaches a maximum value near 200 rad/sec. The simulation model predicts this behavior quite well, and therefore will serve as a good testbed for trying out various inputs before implementing them on the actual

(a)
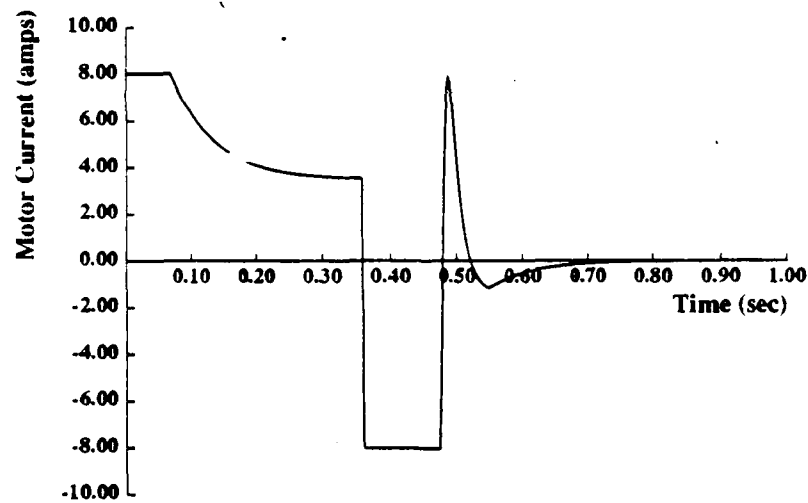
(b)

Figure 6.5: Simulated X-Axis Response to 56.55 rad Step Setpoint: (a) Velocity Command (b) Motor Current.
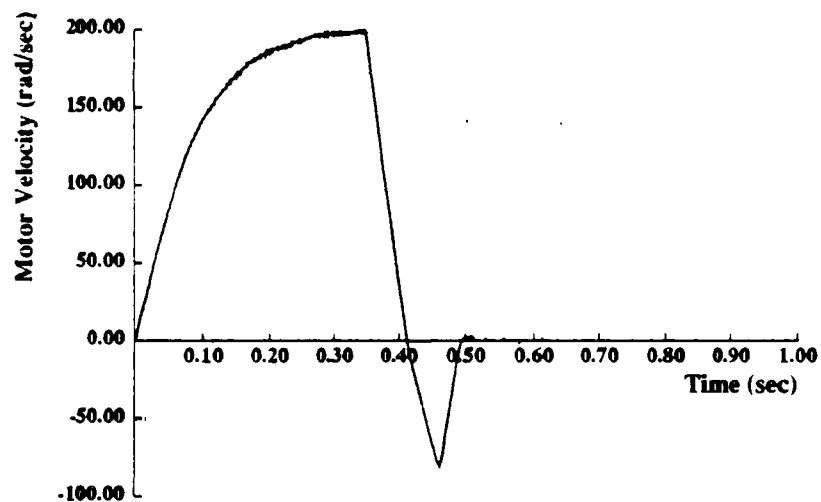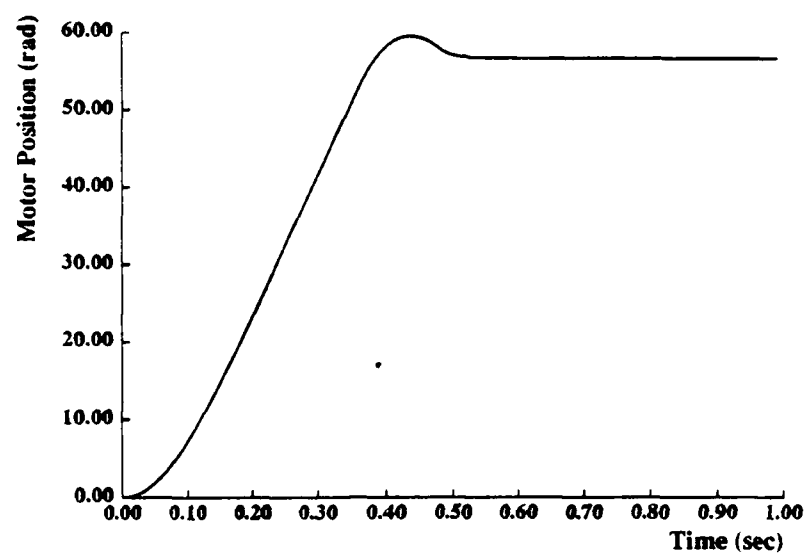
X-Axis Simulation with Step Setpoint

(c)
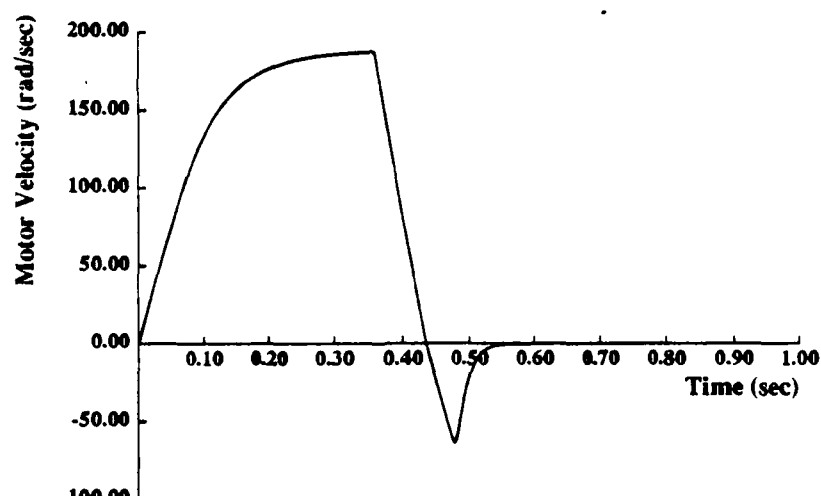
X-Axis Simulation with Step Setpoint

(d)

Figure 6.5: Simulated X-Axis Response to 56.55 rad Step Setpoint: (c) Motor Position (d) Motor Velocity.
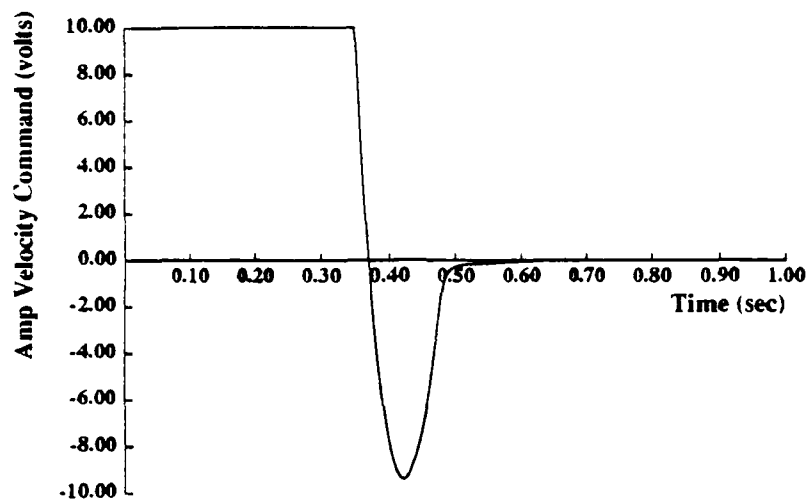
hardware.

6.3 Structural Resonance Model:

Before the simulation model can be used to predict the vibration response, it must be modified to include the structural resonance of the lowest mode of vibration. We will concentrate on those modes which have dominant motion in the X-direction.

Both open-loop and closed-loop determinations of the structural natural frequencies were made. These were based on the extensive work done by Garcia [61] to determine the mode shapes and frequencies of the MIT Robot. A piezoelectric accelerometer (B&K 4371) was mounted at the bottom of the Z-axis measuring in the positive X-direction. Open-loop measurements were performed using a Structural Dynamics Analyzer (HP 5423A). A random noise signal was used as a velocity command input directly to the X-axis amplifier. Acceleration was measured using the accelerometer and a charge amplifier (B&K 2651). The analyzer was used to determine the transfer function between random noise input and acceleration output. The magnitude of this transfer function is shown in Figure 6.6(a), for the X-axis located in front (−X) and the Y-axis midway in its total travel.

Closed-loop measurements with the proportional-derivative controller of Figure 6.3 were performed by moving the X-axis over a distance of 0.23 m (9 in.) corresponding to the step setpoint of 56.55 rad. The Y-axis was in the same position as before. The analyzer was used to record the residual acceleration signal after the final position was reached (in 0.5 sec.). The magnitude of the Fourier transform of this residual vibration is shown in Figure 6.6(b).

These two measurements indicate that modes with dominant X-direction occur at 12, 40, 51, 63, 70, 76, and 83 Hz. Most of these modes show up in both open-loop and closed-loop measurements. The 12 Hz mode in particular does not appear to change frequency despite the addition of the feedback controller. Since this mode dominates
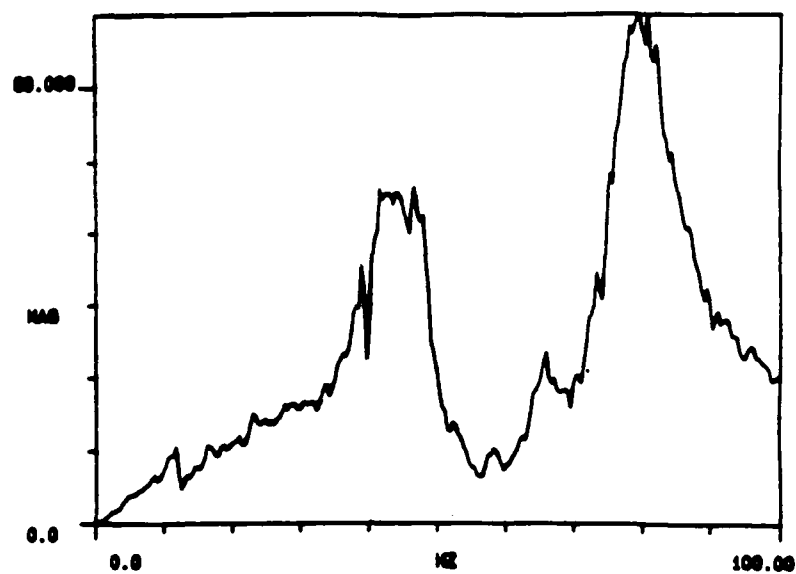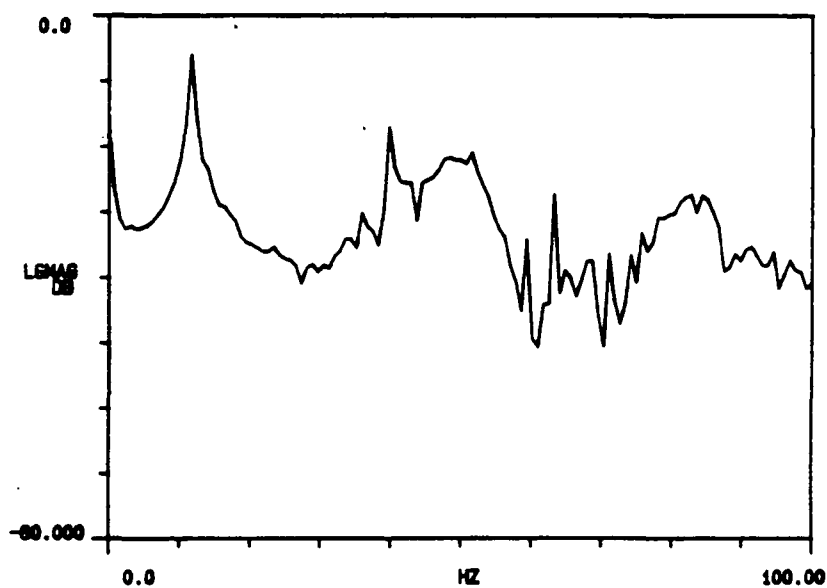
Figure 6.6: Robot Natural Frequencies: (a) Open-loop Transfer Function. (b) Frequency Spectrum of Closed-Loop Residual Response.
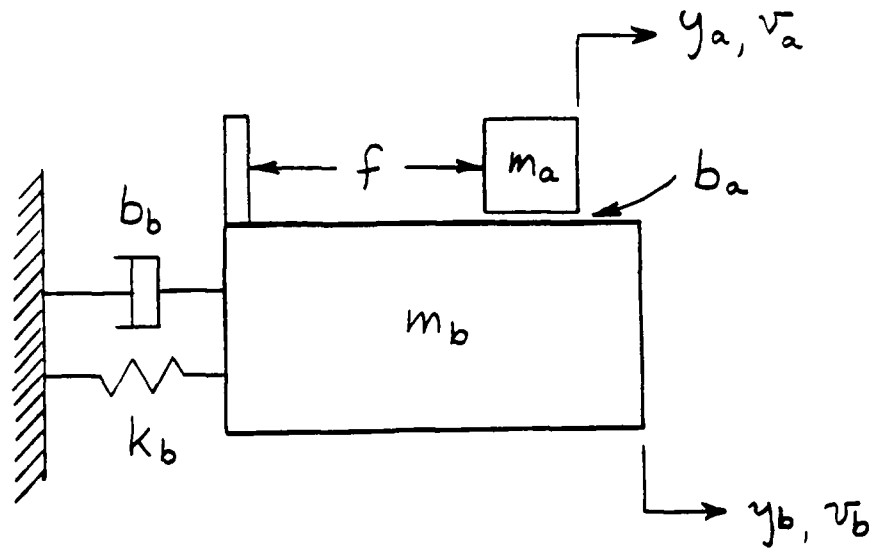
Figure 6.7: Resonant Model of First Mode of Robot.

the closed-loop residual vibration, we will use that frequency in a structural model of the robot. Concentrating on a single mode simplifies the modeling and still allows us to test the effectiveness of the shaped inputs on a realistic representation of an actual system.

The detailed modal analysis of the robot performed by Garcia [61] showed that the 12 Hz mode consists of the entire robot structure rocking back and forth on the floor in the X-direction. This requires a slightly different resonant model than the two-mass model used so far. This new model is represented in schematic form in Figure 6.7. The spring k_b and damper b_b represent the stiffness and dissipation of the floor, while m_b represents the mass of the nonmoving robot structure. Notice in particular the reaction force f due to the motor pushing against the base in order to move the axis m_a. Damping b_a and friction is assumed to exist between the moving axis and the nonmoving structure.

This resonant model can be inserted into the block diagram of Figure 6.2 with the addition of a transmission ratio r converting rotation to translation in the ball screw. The transfer function model to be inserted in place of the rigid-body model
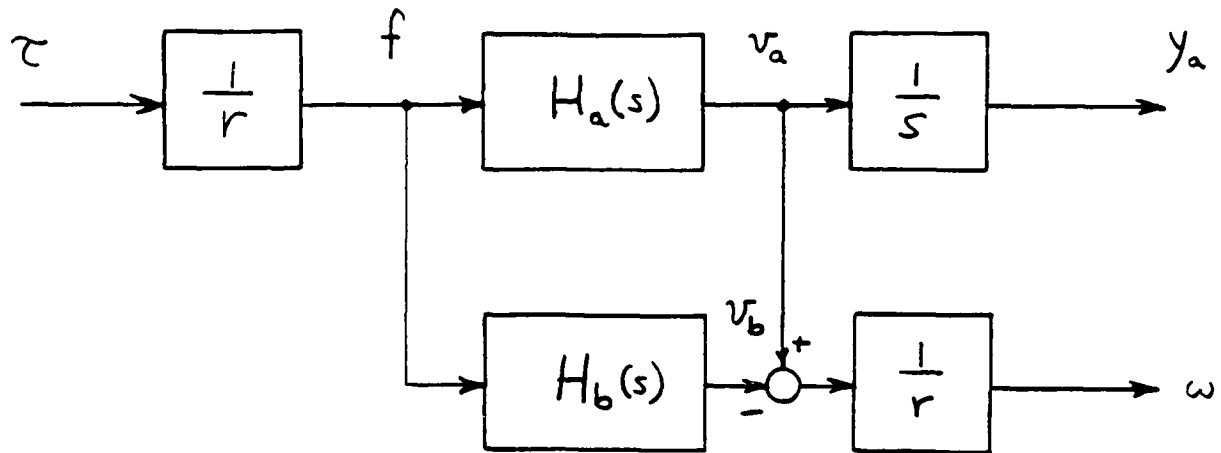
Figure 6.8: Block Diagram Model of Structural Resonance.

is shown in Figure 6.8, where

$$H_a(s) = \frac{v_a}{f} = \frac{\frac{1}{m_a}\left(s^2 + \frac{b_b}{m_b}s + \frac{k_b}{m_b}\right)}{s^3 + \left(\frac{b_a+b_b}{m_b} + \frac{b_a}{m_a}\right)s^2 + \left(\frac{b_a}{m_a}\frac{b_b}{m_b} + \frac{k_b}{m_b}\right)s + \frac{k_b}{m_b}\frac{b_a}{m_a}} \qquad (6.4)$$

and

$$H_b(s) = \frac{v_b}{f} = \frac{-\frac{1}{m_b}s^2}{s^3 + \left(\frac{b_a+b_b}{m_b} + \frac{b_a}{m_a}\right)s^2 + \left(\frac{b_a}{m_a}\frac{b_b}{m_b} + \frac{k_b}{m_b}\right)s + \frac{k_b}{m_b}\frac{b_a}{m_a}}. \qquad (6.5)$$

The measured motor velocity ω actually represents the relative velocity between the axis and the robot base. The acceleration as measured by the accelerometer is the absolute acceleration of the axis. Thus, the simulations give the second derivative of y_a as the accelerometer output. Values for the additional simulation parameters are given in Table 6.2.

Including the resonant model in the simulation gives the results shown in Figure 6.9 for a step setpoint of 56.55 rad. The motor current is given in (a) and the absolute acceleration of the axis in (b). This compares with the actual X-axis step response of Figure 6.10. The biggest difference in the responses is the oscillation of the current signal at the natural frequency in the simulation. This does not occur in the actual system response. This suggests that the encoder mounted on the motor
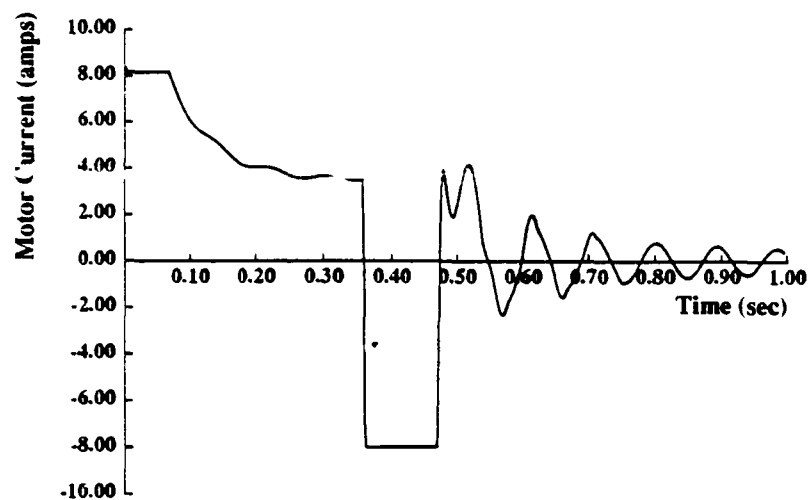
X-Axis Simulation with Step Setpoint

(a)
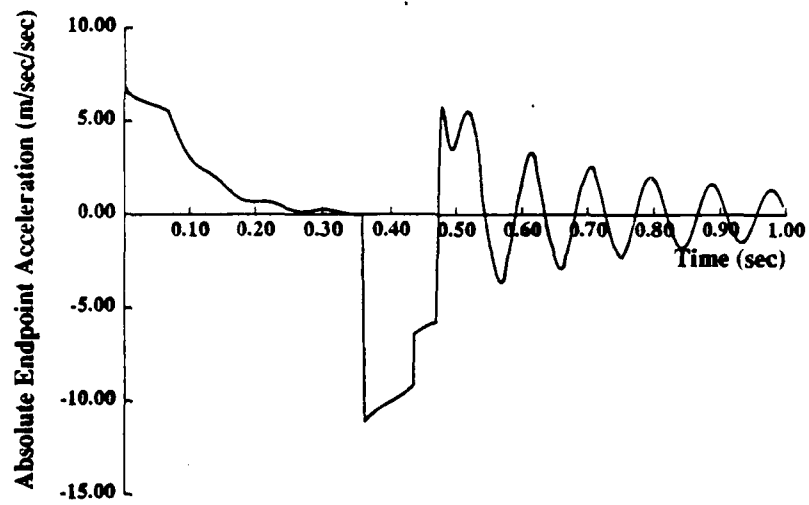
X-Axis Simulation with Step Setpoint

(b)

Figure 6.9: Simulated X-Axis Response to 56.55 rad Step Setpoint Including Structural Resonance: (a) Motor Current (b) Absolute Endpoint Acceleration.

X-Axis Move with Step Setpoint

(a)
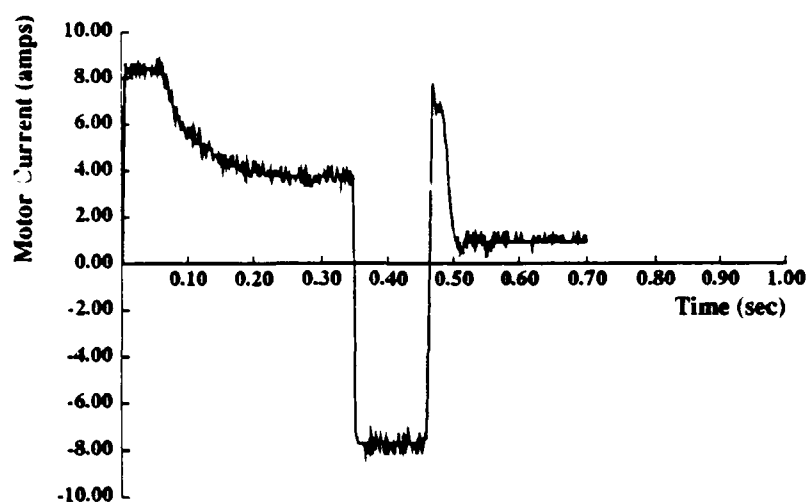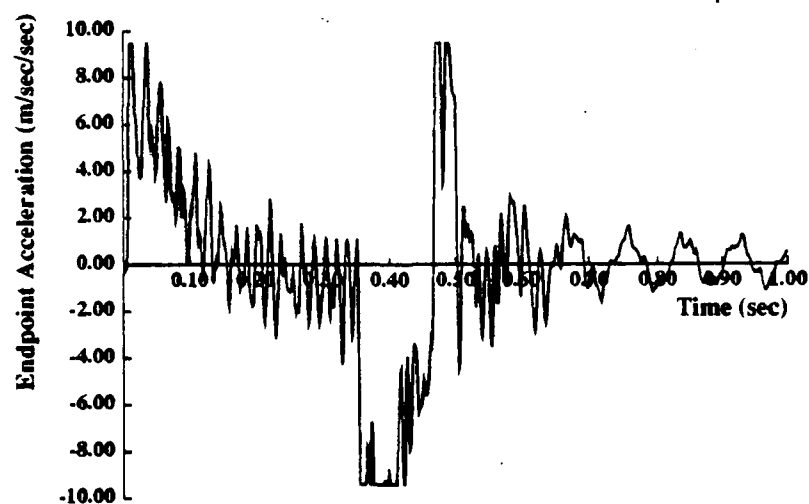
X-Axis Move with Step Setpoint

(b)

Figure 6.10: Actual X-Axis Response to 56.55 rad Step Setpoint: (a) Motor Current (b) Absolute Endpoint Acceleration.

Table 6.2

Resonant Model Simulation Parameters

$$r = 0.004 \text{ m/rad} \quad (1 \text{ inch/rev})$$
$$m_a = J/r^2 = 126 \text{ kg}$$
$$b_a = B/r^2 = 337 \text{ N} - \text{sec/m}$$
$$m_b = 500 \text{ kg}$$
$$b_b = 1546 \text{ N} - \text{sec/m}$$
$$k_b = 2.9875 \times 10^6 \text{ N/m}$$

cannot adequately measure the vibration of the structure for the controller to damp it out. This also explains why the open-loop and closed-loop natural frequencies are nearly the same. However, the resonant model is still useful in evaluating the performance of the system to the proposed shaped inputs.

6.4 The Effect of Actuator Saturation:

In order to test the versine inputs in the simulation model, the closed-loop controller of Figure 6.3 must be changed slightly. In this case, only the position reference is used as the signal to be followed. The velocity is simply compared with zero. However, in order to ensure good reference following, the velocity of the reference trajectory should be included. This arrangement is shown in Figure 6.11, with both θ_{set} and its time derivative being used as reference inputs.

The reference position trajectory θ_{set} is again determined by doubly integrating the shaped force (torque) profile through an inertia. Thus, $\theta_{set}(s) = \tau(s)/Js^2$. Since the velocity saturates near 200 rad/sec and the torque saturates near 4 Nm (8 amps), the torque profile must be chosen to remain within these limits. Because the shaped inputs are constructed assuming no friction or damping to ground, additional
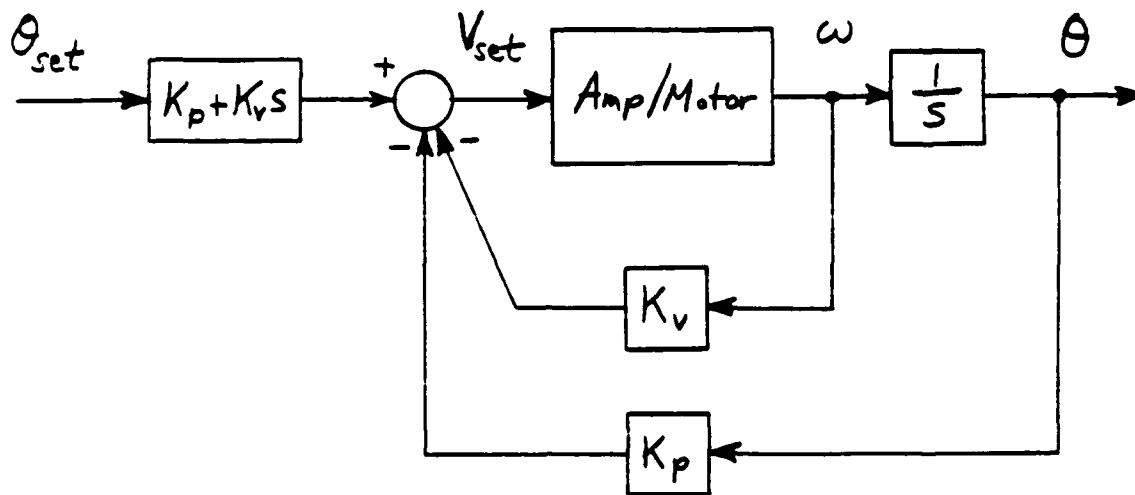
Figure 6.11: Closed-Loop Controller Including Reference Velocity.

torque must be available beyond the maximum torque used in the shaped profile. This can be accomplished by using a maximum torque τ_r for the shaped input of 2.9 Nm and a peak velocity ω_p of 189 rad/sec. For these values, the dimensionless parameter $\omega_n T_R/2\pi = (\omega_n/2\pi)J\omega_p/\tau_r$ for the 12 Hz mode has a value of 1.44. The shaped torque profile tuned to this parameter is shown in Figure 6.12 along with its simulated response. The reference velocity trajectory specified by the torque waveform of Figure 6.12(a) is shown in Figure 6.12(b). Simulated motor current, motor velocity, and endpoint acceleration are shown in Figure 6.12(c), (d), and (e). A considerable amount of vibration remains despite the use of a shaped versine input.

A comparison of the desired and actual velocity profiles will help explain this response. As Figures 6.12 (b) and (d) make clear, the actual simulated velocity cannot keep up with the reference velocity profile. Even though the system does finally reach the desired peak velocity, it does so more slowly than specified. A look at the current waveform of Figure 6.12(c) shows a noticeable drop-off in current in exactly the same region where velocity begins to lag behind. This current saturation was
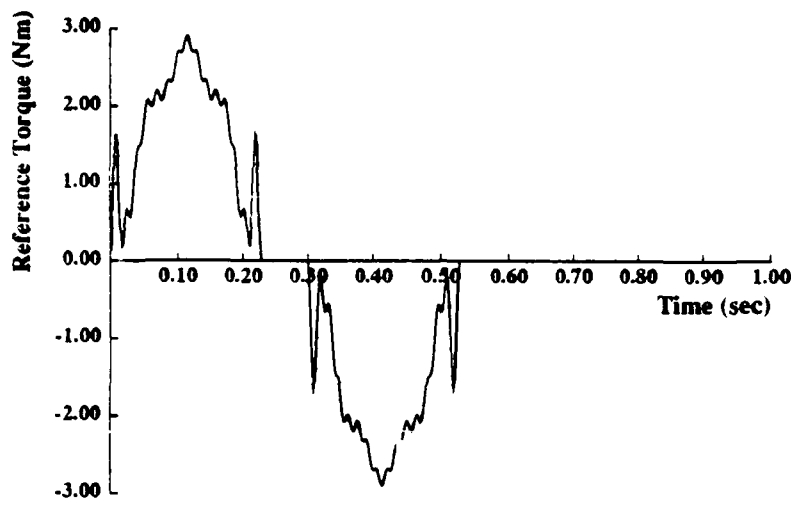
X-Axis Simulation with Versine Input

(a)

Figure 6.12: Simulated X-Axis Response to Versine Input with $\tau_r = 2.9$ Nm and $\omega_p = 189$ rad/sec: (a) Reference Torque Waveform.

also observed for the step response of Figures 6.4 and 6.5. Basically, the saturation in the amplifier prevents the system from following the specified input waveform. As a result, the response behaves differently from the desired response and leads to residual vibration.

This test highlights the importance of specifying an input waveform which will not cause the amplifier to saturate. Once saturation does take place, some residual vibration is to be expected even when properly shaped inputs have been specified.

X-Axis Simulation with Versine Input

(b)
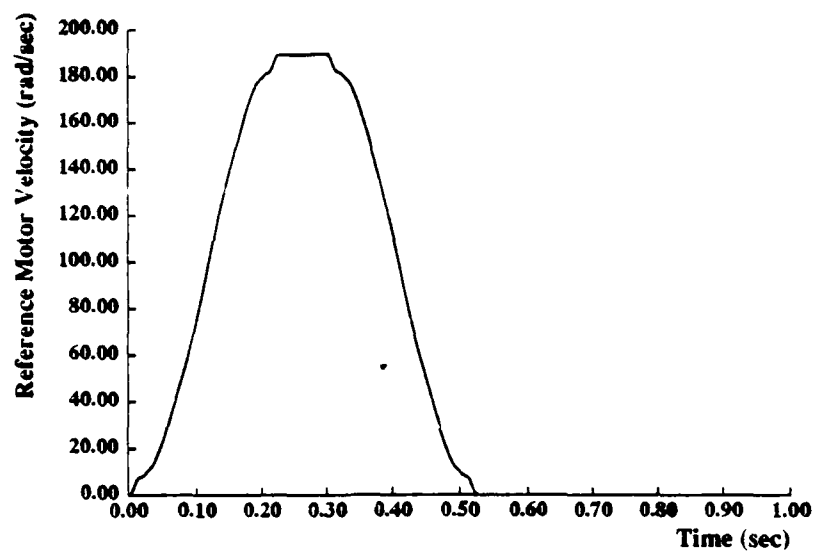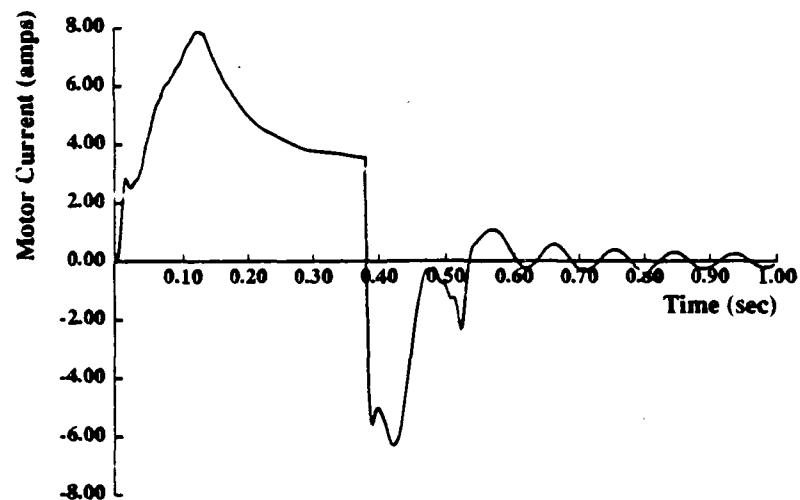
X-Axis Simulation with Versine Input

(c)

Figure 6.12: Simulated X-Axis Response to Versine Input with $\tau_r = 2.9$ Nm and $\omega_p = 189$ rad/sec: (b) Reference Velocity Trajectory (c) Motor Current.

X-Axis Simulation with Versine Input

(d)

X-Axis Simulation with Versine Input

(e)

Figure 6.12: Simulated X-Axis Response to Versine Input with $\tau_r = 2.9$ Nm and $\omega_p = 189$ rad/sec: (d) Motor Velocity (e) Endpoint Acceleration.

6.5 Development of Nonsaturating Velocity Profiles:

As the previous section makes clear. amplifier saturation may prevent the shaped inputs from minimizing residual vibration. Even though the current waveform never exceeds 8 amps. it still saturates when sufficient motor velocity is reached. A new velocity profile must therefore be developed that takes this velocity-dependent saturation into account.

The parameters of the velocity profile that are to be determined are acceleration and peak velocity. The acceleration is proportional to the peak amplitude of the shaped torque profile used. There are two different saturation phenomena that should be avoided. First. the maximum specified current should never exceed 8 amps. Second, the specified current should never exceed the level that is achievable with increasing back emf losses.

Incorporating these constraints into a determination of velocity profile parameters requires some assumptions on the shape of the reference input torque waveform. This reference input ignores friction so its peak torque level must be low enough that when the controller calls for extra torque to compensate for damping and friction, the total torque will be within saturation levels. Since viscous damping torque is proportional to velocity, we must determine the correspondence between torque and velocity at the critical points when either reference torque or velocity are at maximum values. Since the reference torque profile is a complicated function of time that also depends on the parameters for which it was tuned, relating torque and velocity analytically can be difficult. Instead. we will make some conservative assumptions that should apply for all inputs to be considered. We will assume that the reference torque near maximum velocity ω_p is $1/2$ of its peak value τ_r and that the peak reference torque occurs for a velocity as high as $2\omega_p/3$.

Keeping these assumptions in mind, we will proceed by specifying the constraints

on the reference torque in order to avoid amplifier saturation. With current saturating at 8 amps, the peak motor torque that can be generated is 4 Nm. Thus, peak reference torque plus the torque required to overcome friction and damping must never exceed this value:

$$\tau_r + \frac{2}{3}B\omega_p + \tau_{fric} \leq 4 \text{ Nm} \tag{6.6}$$

In addition, the torque required at maximum velocity should not exceed the limit imposed by back emf losses. This current limit occurs as a result of the saturation of the current command V_c. Steady-state current i can be expressed in terms of V_c and ω from Figure 6.2 as follows:

$$i = \frac{K_{amp}V_c - K_B\omega}{R + K_{amp}K_{cur}} \tag{6.7}$$

Thus, the second torque constraint at peak velocity ω_p is given by

$$\frac{1}{2}\tau_r + B\omega_p + \tau_{fric} \leq K_T \left[\frac{K_{amp}V_c - K_B\omega_p}{R + K_{amp}K_{cur}} \right]. \tag{6.8}$$

These constraints can be expressed in terms of a linearized acceleration α, defined as

$$\alpha = \omega_p / T_p \tag{6.9}$$

where T_p is the time required for the versine input to reach peak velocity ω_p. Peak reference torque τ_r is related to this acceleration by the expression:

$$\tau_r = \Gamma_V J \alpha. \tag{6.10}$$

where Γ_V is the time-scale factor associated with the versine input defined by (5.10). Thus, the constraint expressed by (6.8) using the equality establishes a relationship between α and ω_p that will just avoid current saturation. This relationship can be rewritten as

$$\alpha = c_1 - c_2\omega_p \tag{6.11}$$

where c_1 and c_2 are constants resulting from the substitution of (6.10) into (6.8).

To determine the best values of α and ω_p for fastest response without saturation, we will try to minimize the total move time T_f given by

$$T_f = 2T_p + \frac{\theta - \omega_p T_p}{\omega_p} = \frac{\theta}{\omega_p} + T_p \tag{6.12}$$

where θ is the desired angular displacement. Our goal is to express T_f in terms of θ and ω_p only, and then to determine that velocity which minimizes T_f for a given θ. This can be done by expressing T_p as ω_p/α from (6.9) and substituting for α from (6.11). The result is the time T_f expressed as a function of ω_p. For $\theta = 56.55$ rad, this function is plotted in Figure 6.13(a). A value of 1.75 was assumed for Γ_V to represent a typical versine function. With the help of expressions (6.10) and (6.11), T_f can also be plotted as a function of τ_r, as shown in Figure 6.13(b). The constraint of (6.6) was included in these figures to ensure that the 4 Nm saturation torque is not exceeded. This limit causes the discontinuities in these curves.

For the rotation of 56.55 rad, minimum T_f occurs for a peak velocity of roughly 145 rad/sec and a peak reference torque of about 2.75 Nm. Since the shaped torque profile calls for half peak torque at a speed just below peak velocity rather than at peak velocity as was assumed in this development, we will use the parameters $\omega_p = 150$ rad/sec and $\tau_r = 2.75$ Nm to generate versine inputs for the rotation of 56.55 radians. This corresponds to an axis velocity of 0.6 m/s (2.0 ft/s) and an accelerating force of 688 N (155 lbf). For larger moves, the same approach can be used. In general, as move distance increases, more time is spent at peak velocity. Thus, the peak torque which will minimize move time will be lower and peak velocity will be higher to minimize the time spent at constant velocity.

For the parameters selected, the versine input for the single-resonance model of Figure 6.7 gives the simulated response shown in Figure 6.14. Notice that this time the residual vibration, shown in Fig. 6.14(e), has indeed been eliminated, in part because the amplifier current no longer saturates.

With these values for τ_r and ω_p and the known X-axis inertia, the value for $T_R = J\omega_p/\tau_r$ becomes 0.112 sec. We can now determine an appropriate versine
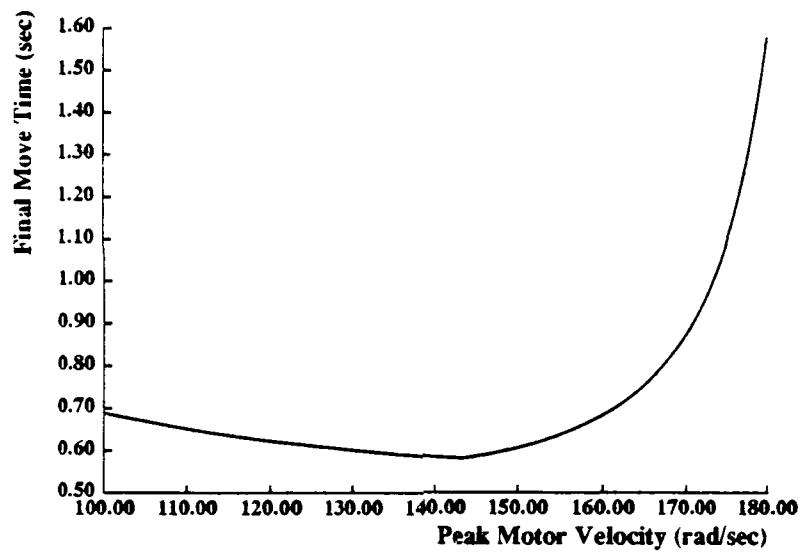
Function to Determine Velocity Profile Parameters

(a)
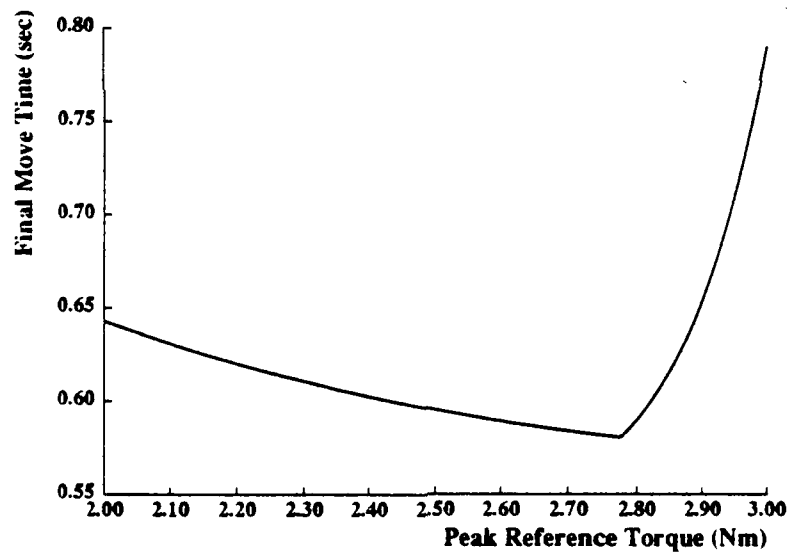
Function to Determine Velocity Profile Parameters

(b)

Figure 6.13: Total Move Time for a Rotation of 56.55 rad as a Function of: (a) Peak Velocity ω_p, and (b) Peak Reference Torque τ_r.
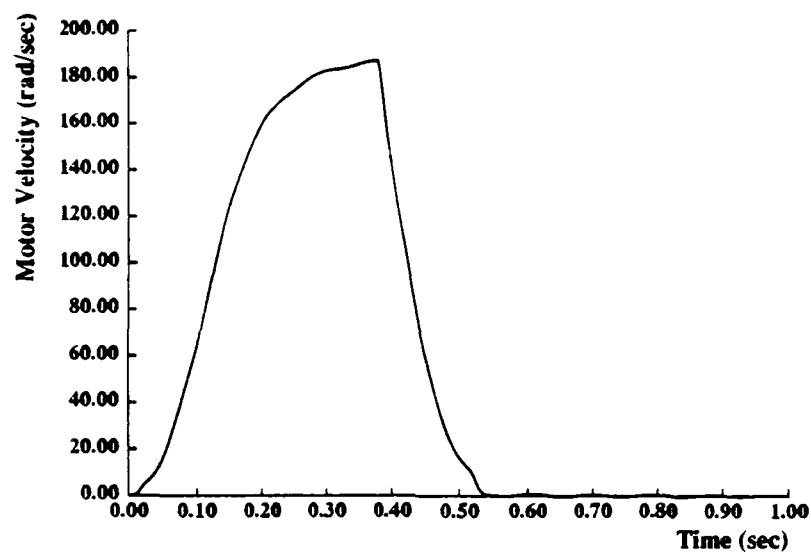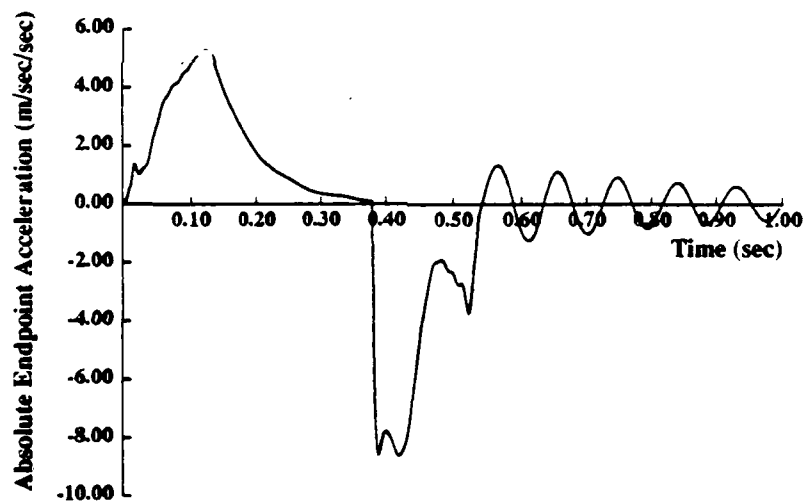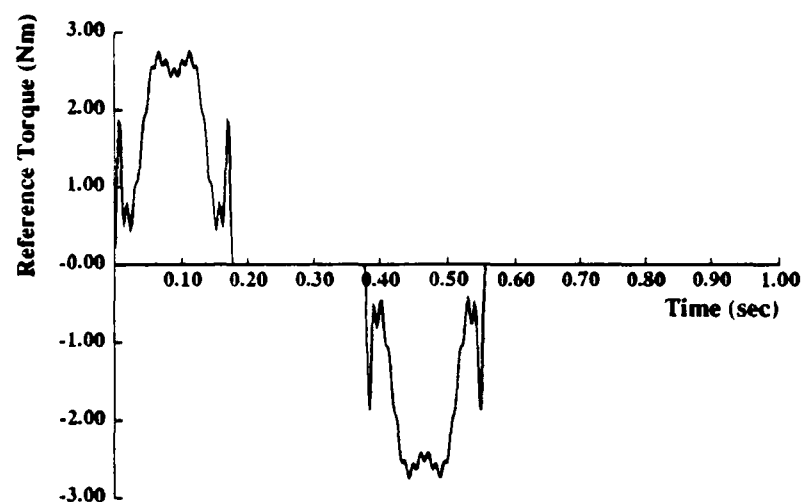
X-Axis Simulation with Versine Input

(a)

Figure 6.14: Simulated X-Axis Response to Versine Input with $\tau_r = 2.75$ Nm and $\omega_p = 150$ rad/sec: (a) Reference Torque Waveform.

input using this time value to normalize the natural frequencies for the actual robot. This input profile is constructed to minimize spectral magnitude at four frequencies (12, 40, 70, and 84 Hz), with a $\pm 20\%$ band about 12 Hz and $\pm 10\%$ band about the others. Such a shaped input is shown in Figure 6.15(a), with its frequency spectrum in (b). This input was used to perform tests on the robot which are discussed in Chapter 7.

6.6 Closure:

This chapter developed a detailed model of the MIT Cartesian Robot in preparation for performing experiments. This model includes the effects of actuator saturation and the first structural resonance of the robot. Simulation results with the versine input indicate the importance of avoiding current saturation to ensure that resid-

X-Axis Simulation with Versine Input

(b)
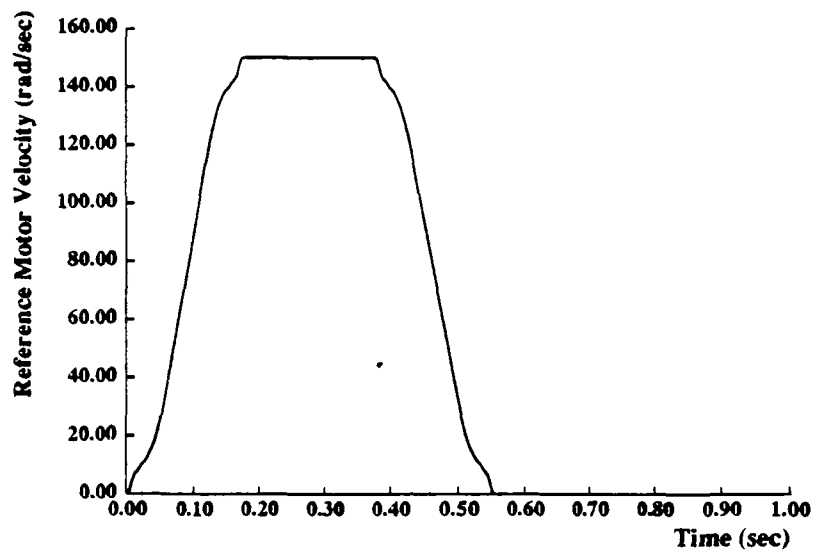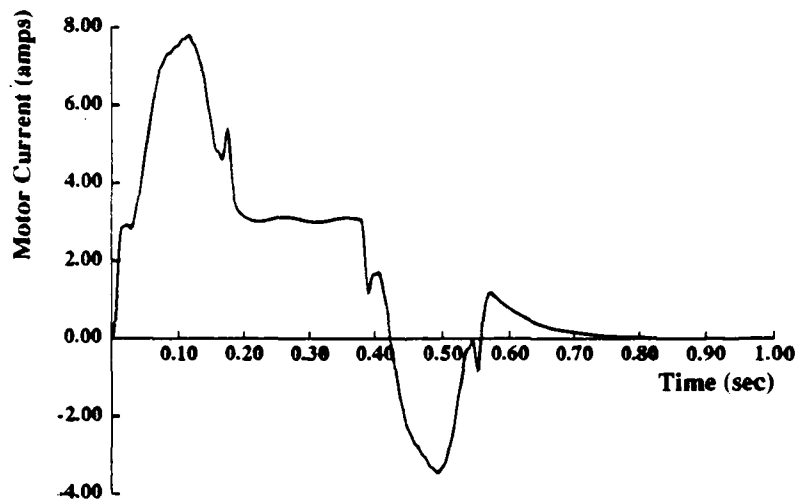
X-Axis Simulation with Versine Input

(c)

Figure 6.14: Simulated X-Axis Response to Versine Input with $\tau_r = 2.75$ Nm and $\omega_p = 150$ rad/sec: (b) Reference Velocity Trajectory (c) Motor Current.

X-Axis Simulation with Versine Input

(d)
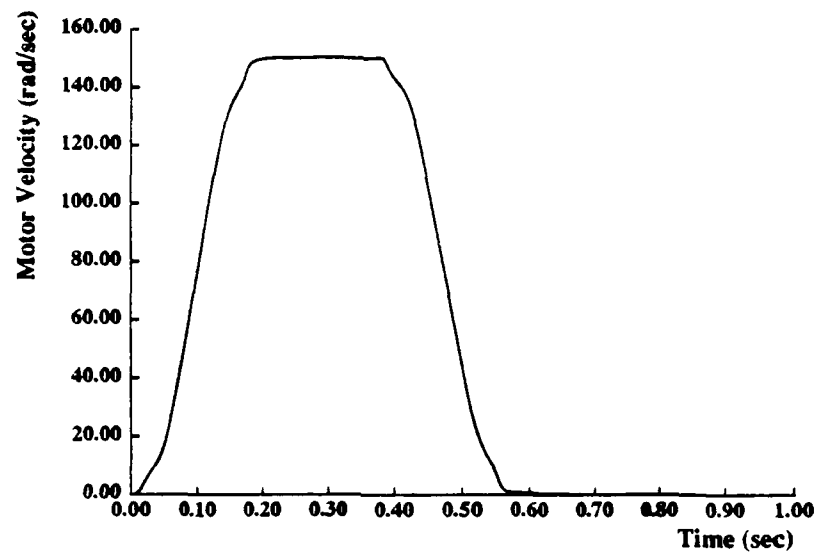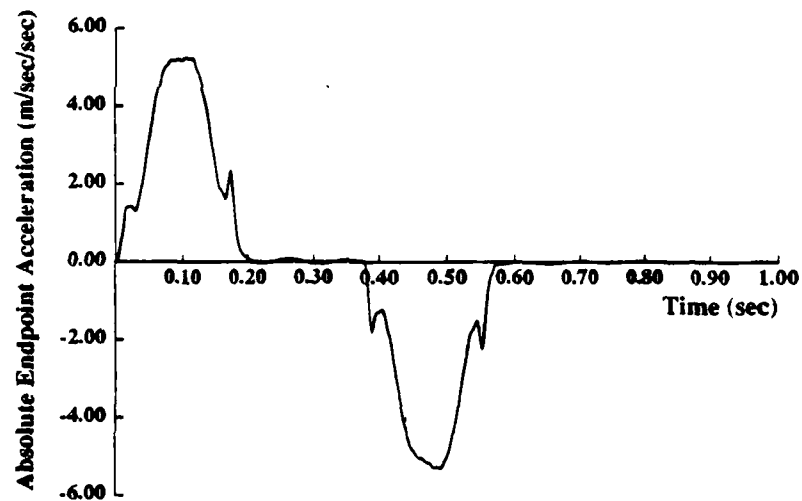
X-Axis Simulation with Versine Input

(e)

Figure 6.14: Simulated X-Axis Response to Versine Input with $\tau_r = 2.75$ Nm and $\omega_p = 150$ rad/sec: (d) Motor Velocity (e) Endpoint Acceleration.

Versine Input

(a)
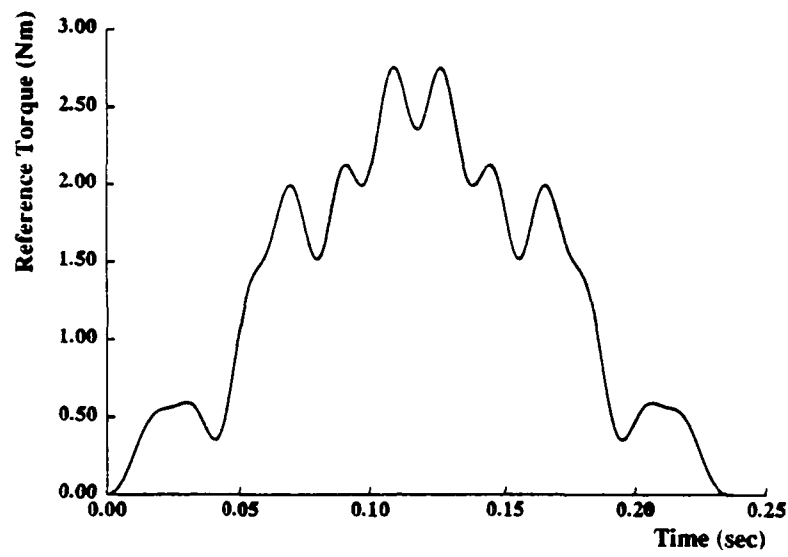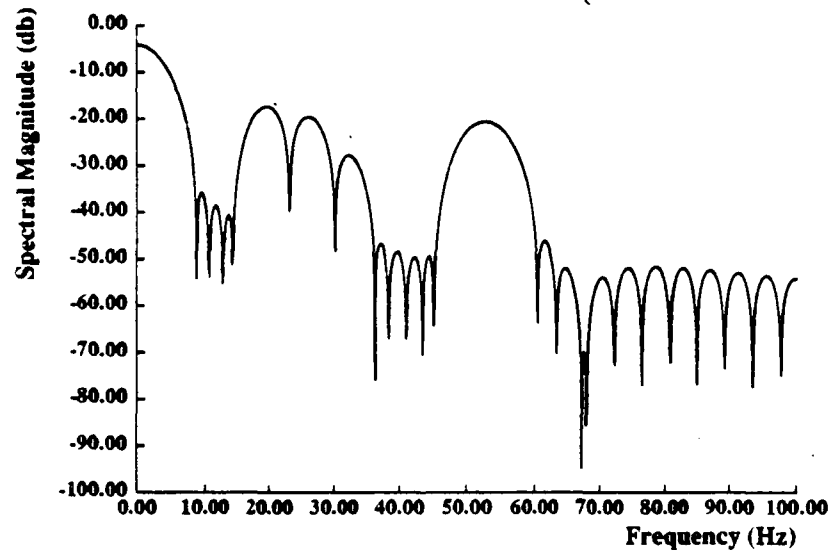
Frequency Spectrum of Versine Input

(b)

Figure 6.15: Versine Input Tuned to 12, 40, 70, and 84 Hz for $\tau_r = 2.75$ Nm and $\omega_p = 150$ rad/sec: (a) Time Function (b) Frequency Spectrum.

ual vibration is indeed minimized. Parameters for the velocity profile were then determined which avoid current saturation and still generate fast motion. These parameters were used to construct a versine input to run the X-axis on the actual robot. Experimental results are discussed in the next chapter.

Experimental Results

7.1   Introduction:

This chapter will present experimental results for the MIT Cartesian Robot using the versine input developed in Chapter 6. These responses will be compared with the step response and the response to a rectangular pulse input. Robustness to variation in natural frequency will be illustrated by performing tests on the X-axis for several different positions of the Y-axis. The effect of modal coupling between axes will be illustrated by generating motion in Y and measuring vibrations in X. An advantage of the shaped versine input is its ability to avoid the excitation of any specified natural frequency, including modes that vibrate in directions orthogonal to the motion and cannot be measured.

7.2   Microprocessor Implementation:

Before presenting experimental results, we will describe the implementation of time-varying setpoints in the control microprocessors. Since the reference signal used by the controller presented in Section 4.3 of Chapter 4 is generated by doubly integrating the shaped force profile, it represents a continuously-varying function

of time. The controller as configured by Benjamin [75] takes a constant setpoint as reference to be followed. This generates a step response but does not allow the implementation of time-varying setpoints. Thus, some of the software for the microprocessors must be changed.

Since the microprocessors are connected to a VAX computer (see Figure 7.1), the time-varying setpoints could be stored in the VAX and sent to the microprocessors at each time step, or stored directly in the microprocessors. Because the VAX and the micros run on different internal clocks, the setpoints are stored directly in the micros to ensure that the correct setpoint is synchronized with the servo time step. Thus, before each move, a file of setpoints is downloaded to memory in the micros. These setpoints are generated by doubly integrating the desired force profile.

To read these setpoints sequentially, using a different memory location at each time step, the framework program that controls the operation of the micros must be modified. The new code, in Intel 8031 assembly language, is given in Appendix C. At the start of the move, the beginning memory location is read. Then, each new time step increments the memory location to read the next setpoint, and so on. A control bit is used to signal the micros to use a time-varying setpoint, rather than the constant step setpoint.

In order to introduce both the position reference and the velocity reference as called for by the controller of Chapter 4, the derivative of the sequence of position setpoints must be obtained. This is easily accomplished by computing the difference in reference setpoints in each time step. This difference is then compared with the actual differenced velocity and the resulting velocity error and position reference are used in the PD servo loop as originally configured by Benjamin.
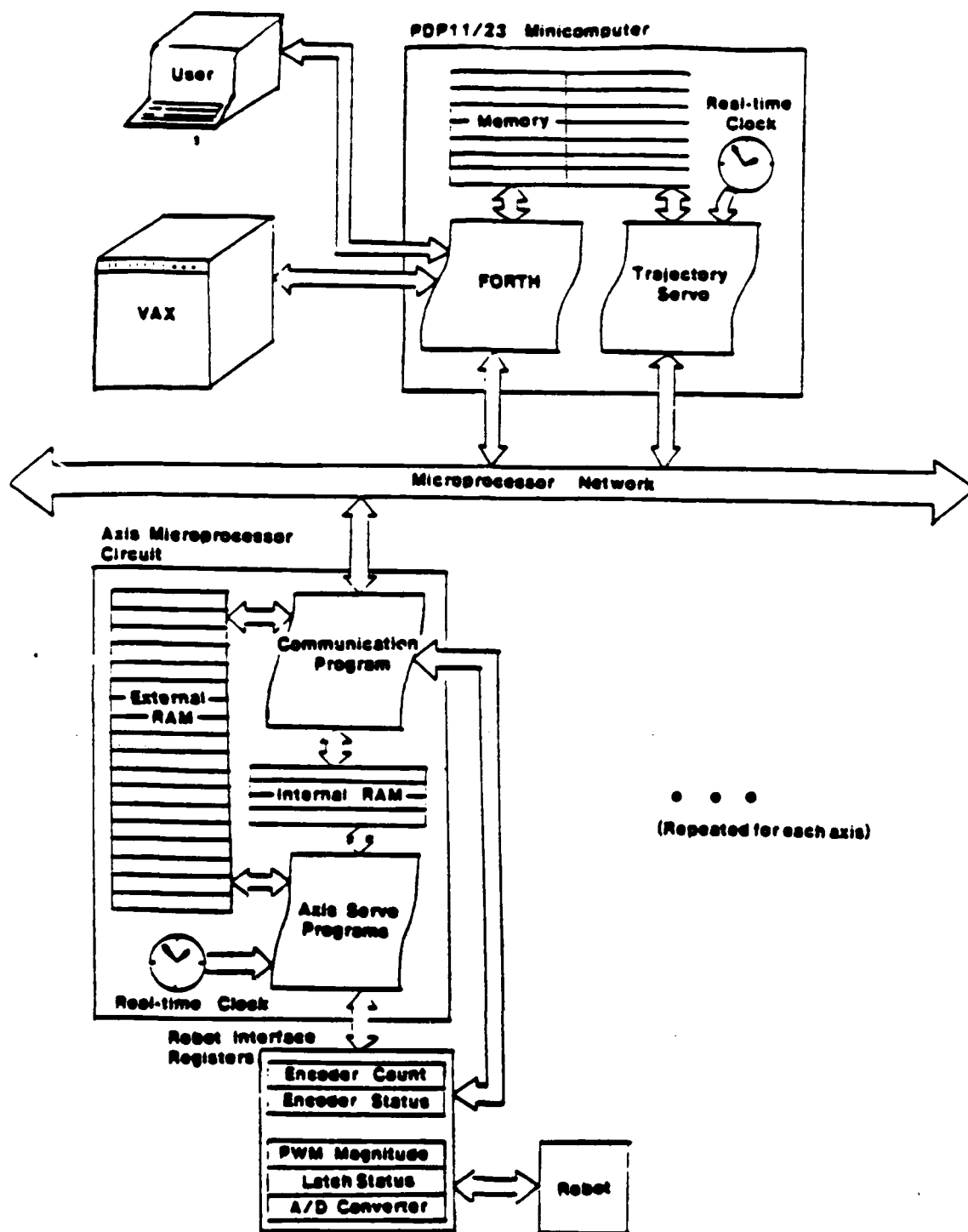
Figure 7.1: Schematic of Hierarchical Controller Architecture.

7.3 Experimental Setup:

In all of the tests performed, the acceleration was measured in the X-direction. A B&K 4371 accelerometer was mounted at the bottom of the Z-axis facing the $+$X-direction. The accelerometer signal was conditioned by a B&K 2651 charge amplifier, giving an output of 0.1 volt for 1 g (10 m/s^2) of acceleration. Garcia's work suggests that accelerations on the order of 1 g are to be expected in the transient response. Since the analog-to-digital (A/D) converter which sends this data to the microprocessors for storage has a range of ± 10 V, the accelerometer signal must be amplified. Therefore, an Analog Devices AD521 chip was configured into an instrumentation amplifier with a gain of 105.

All data taken for each move was stored on the micros during the motion and then transferred to the VAX for analysis and plotting. This data was stored in the same block of memory as that containing the setpoints, writing over the setpoints used for the previous time step. In order to ensure that this data does not write over any setpoints which are yet to be used, data was only taken every other servo time step, at a rate of 750 Hz.

In order to avoid aliasing of the acceleration signal when sampled at 750 Hz, it has to be filtered before entering the A/D converter. To retain fidelity of the vibration signal up to 100 Hz but effectively remove any frequency components above the Nyquist frequency of 375 Hz, an Ithaco model 4112 low-pass filter was used. Its cut-off frequency was set at 160 Hz to sufficiently attenuate the signal at 375 Hz.

Because of the limited memory on board the micros, the acceleration signal was stored on the Y-axis micro, while the current signal measured by the amplifier was stored on the X-axis micro, along with the encoder position and the amp velocity command signal for the X-axis.

The residual acceleration signal and its frequency spectrum were measured using an HP 5423A Structural Dynamics Analyzer. The accelerometer output was sent to

both the analyzer and the micro A D converter. The analyzer was triggered as soon as motion began, with a sufficient time delay to start taking the measurement only when motion had stopped. In this way, only the residual vibration was measured.

Before acceptable data could be obtained, an additional change had to be made in the amplifiers. Initial tests using a nonsaturating reference input showed considerable current oscillation during the constant velocity portion of the move. This oscillation did not occur for the saturating step input. Perhaps saturation precluded this oscillation because the current signal was kept at its extreme value.

Since the current oscillation during the constant velocity phase is also picked up by the accelerometer, it tends to degrade the performance. Further tests indicated that this oscillation has nothing to do with the input being used. In fact, the preamp gains were originally chosen for maximum servo stiffness without going unstable (Drlik [74]). Thus, the amplifiers were only marginally stable. To solve this problem, resistor R100 which sets the preamp gain was removed from the X-axis amplifier. Likewise, resister R83 was removed from the Y-axis amplifier. (These resistors are identified in schematics given by Nussbaum [73]). Replacing the resistors reduces the inner loop servo stiffness of the amplifier and greatly improves the current signal at constant velocity.

The FORTH commands used to generate motion for the experimental tests are summarized in Appendix B. These FORTH words are defined in Appendix D. Once the robot had completed its motion and data had been stored, the data was copied from the micros to the VAX. There, the numbers were converted into appropriate units and plotted. These results are described in the next section.

7.4   Experimental Tests on X-Axis:

With the Y-axis in the middle of its workspace, the X-axis was moved from zero to 0.23 m (9 in.) in the +X-direction. Three types of reference inputs were used: a step,

an integrated rectangular pulse input, and an integrated versine input. By doubly integrating the rectangular pulse input and the versine input, a smooth reference profile is achieved that the system can follow. Total motor rotation during this move was 56.55 rad. The results for a step reference input are shown in Figure 7.2, those for the integrated rectangular pulse input in Figure 7.3, and those for the integrated versine input in Figure 7.4. In each case, the current signal is shown in (a), the motor position in (b), the motor velocity in (c), and the endpoint acceleration in (d). The current signal is nonzero even when the axis has reached its destination because of stiction in the moving elements.

The step response reaches the final position most quickly but also generates the most residual vibration. The shaped versine force input with reference torque $\tau_r = 2.75$ Nm and peak velocity $\omega_p = 150$ rad/sec takes about 20% longer, but it generates much lower residual vibration.

The rectangular pulse force input used here to generate a smooth reference profile for comparison with the versine response was selected to have the same move time as the versine input. Its peak torque therefore is less than 2.75 Nm. The reason for choosing this input, rather than a pulse of equivalent peak torque, is that the parameters τ_r and ω_p chosen for the versine do not prevent saturation for the rectangular pulse input. Saturation occurs because the reference acceleration for the rectangular pulse is much higher than for the versine input. Since saturation tends to increase residual vibration, the rectangular pulse peak torque was scaled down to 1.31 Nm to make total move time equal to that of the versine input. As the results of Figure 7.3 show, the use of a smooth reference input based on a rectangular pulse helps compared to the step input, but it still generates more residual vibration than the versine input.

The frequency spectrum of the residual vibration resulting from the three different inputs are shown in Figures 7.5, 7.6, and 7.7. Notice that the integrated versine reference reduces the vibration of the 12 Hz mode by 20 db compared to the

X-Axis Move with Step Setpoint

(a)
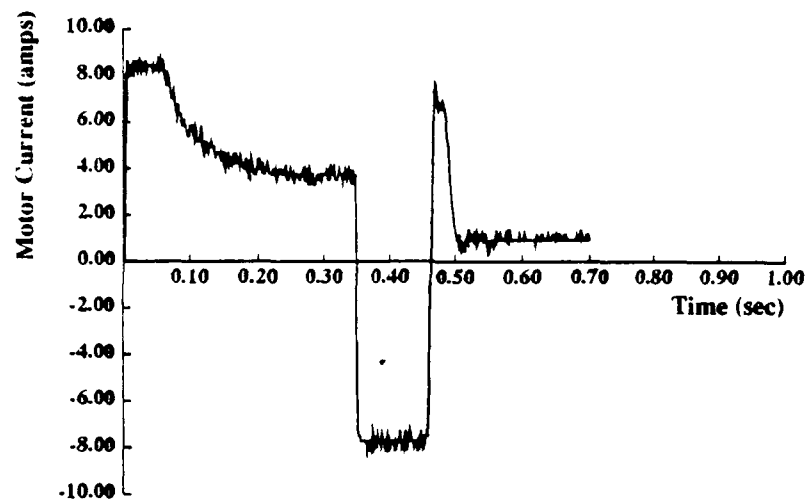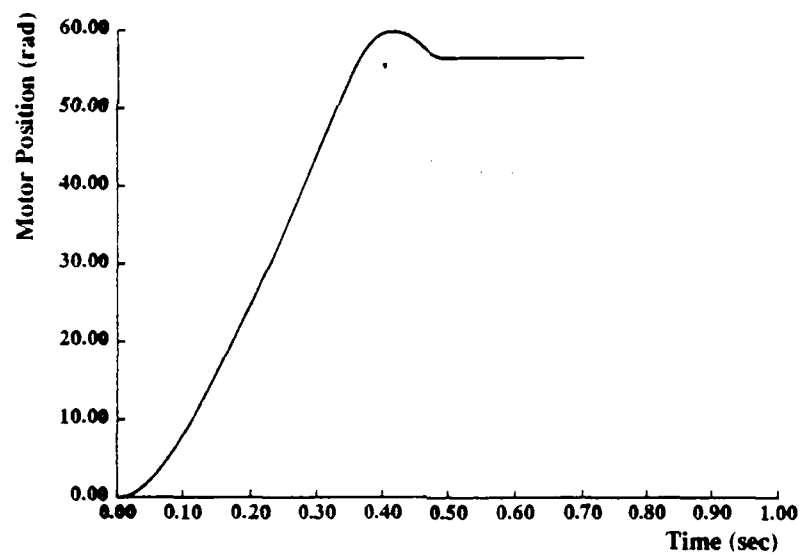
X-Axis Move with Step Setpoint

(b)

Figure 7.2: X-Axis Response to a Step Input of 0.23 m: (a) Motor Current (b) Motor Position.

X-Axis Move with Step Setpoint

(c)
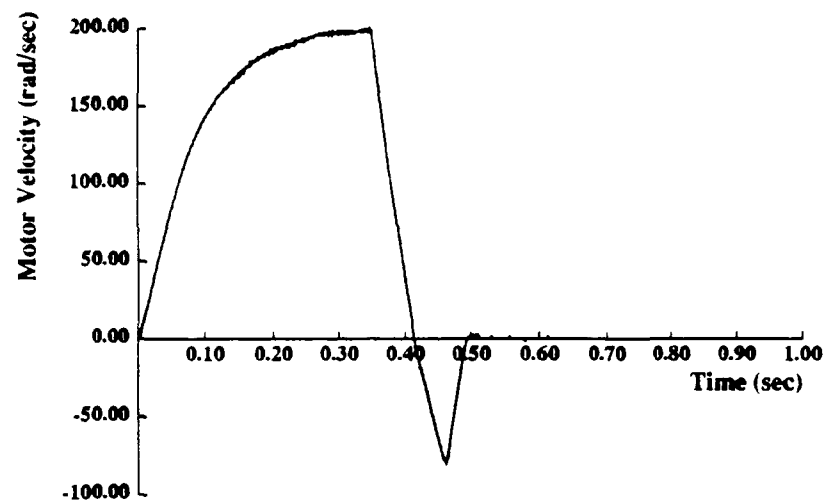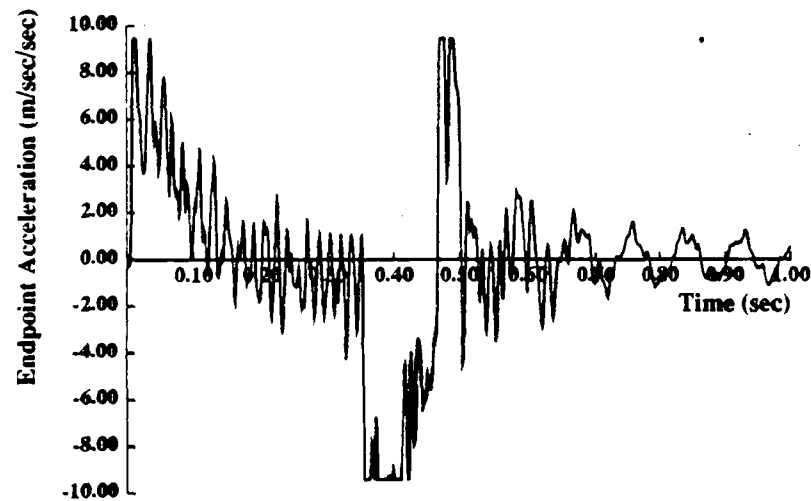
X-Axis Move with Step Setpoint

(d)

Figure 7.2: X-Axis Response to a Step Input of 0.23 m: (c) Motor Velocity (d) Endpoint Acceleration.
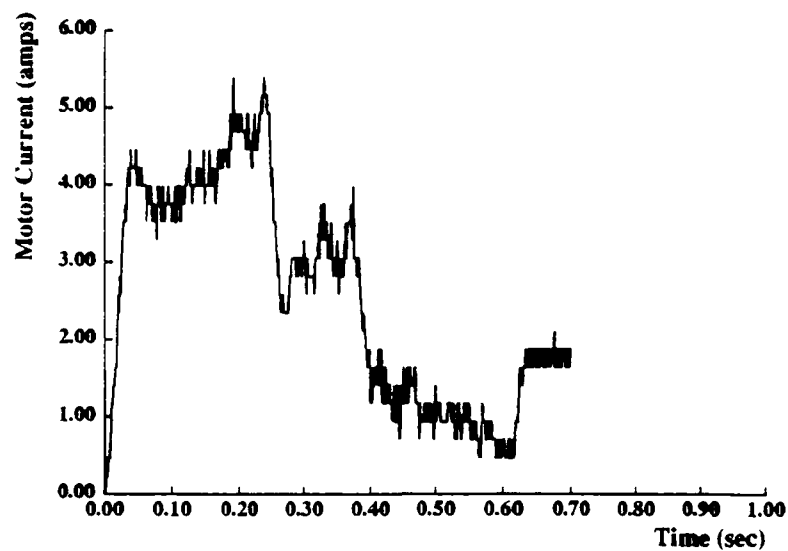
X-Axis Move with Rectangular Pulse Input

(a)
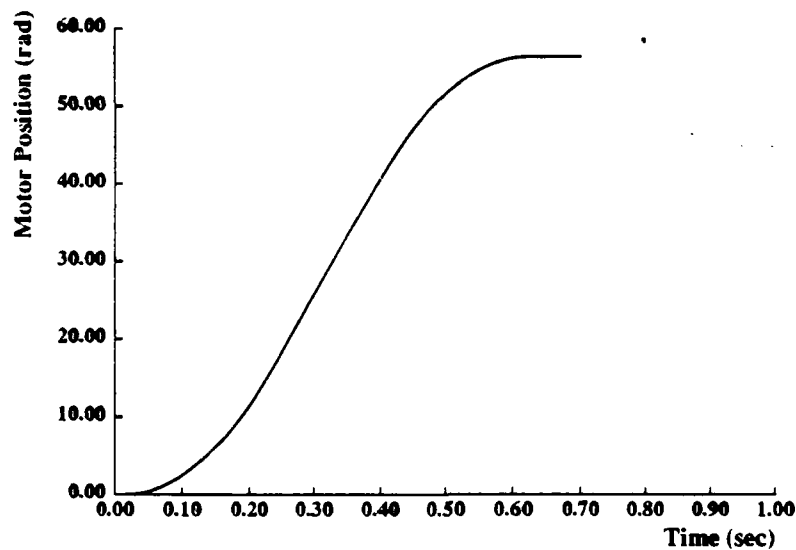
X-Axis Move with Rectangular Pulse Input

(b)

Figure 7.3: X-Axis Response to a Rectangular Pulse Input for a 0.23 m Move with $\tau_r = 1.31$ Nm and $\omega_p = 150$ rad/sec: (a) Motor Current (b) Motor Position.
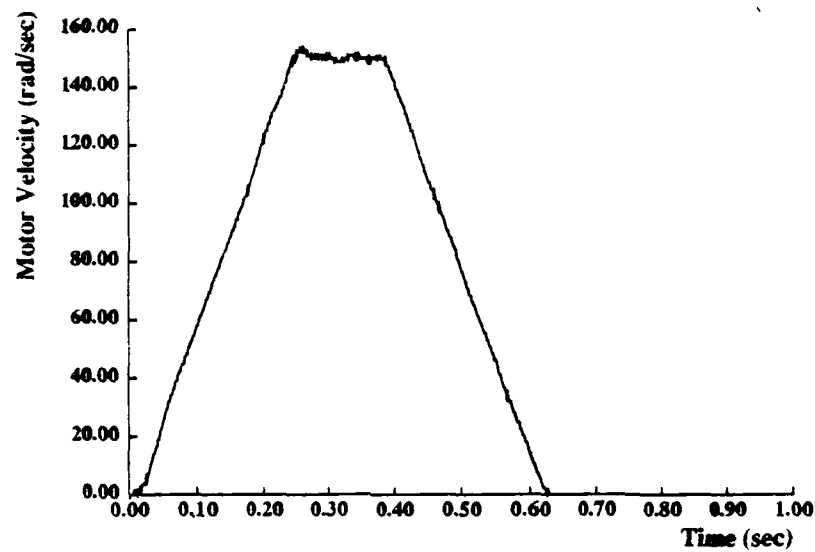
X-Axis Move with Rectangular Pulse Input

(c)
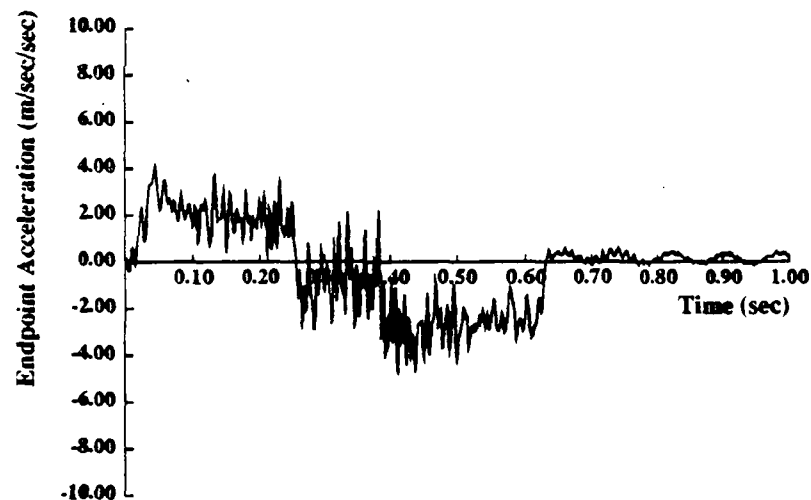
X-Axis Move with Rectangular Pulse Input

(d)

Figure 7.3: X-Axis Response to a Rectangular Pulse Input for a 0.23 m Move with $\tau_r = 1.31$ Nm and $\omega_p = 150$ rad/sec: (c) Motor Velocity (d) Endpoint Acceleration.
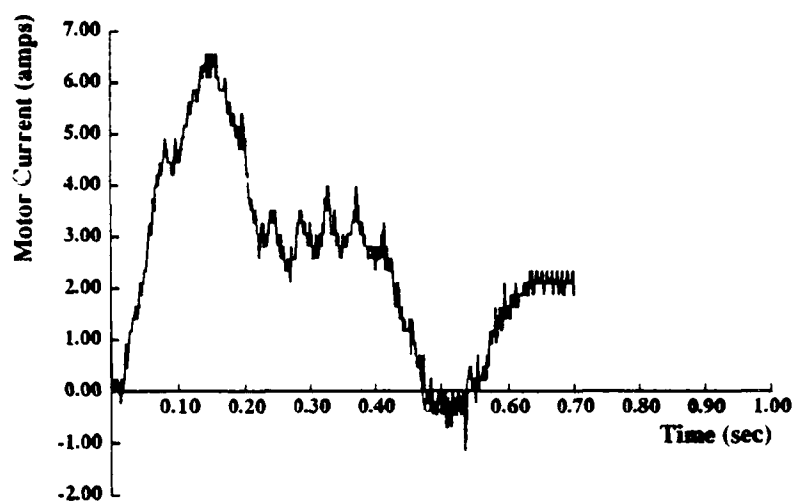
X-Axis Move with Versine Input

(a)
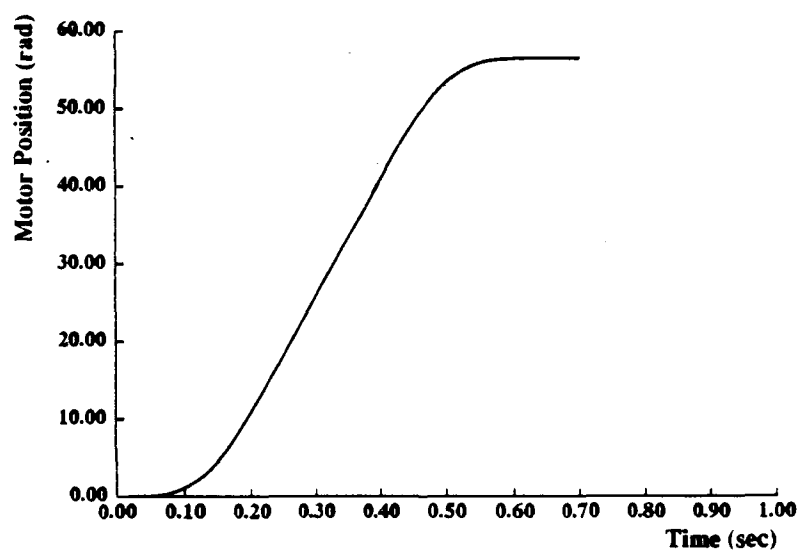
X-Axis Move with Versine Input

(b)

Figure 7.4: X-Axis Response to a Versine Input for a 0.23 m Move with $\tau_r = 2.75$ Nm and $\omega_p = 150$ rad/sec: (a) Motor Current (b) Motor Position.
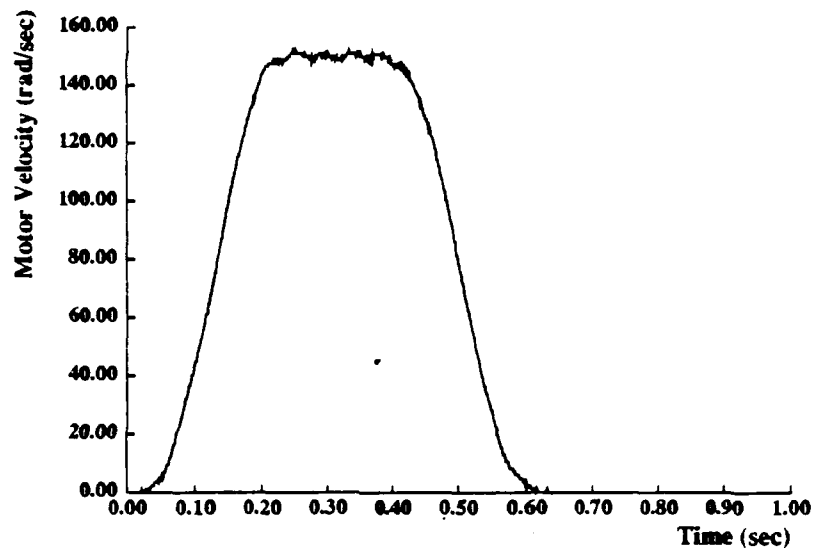
X-Axis Move with Versine Input

(c)
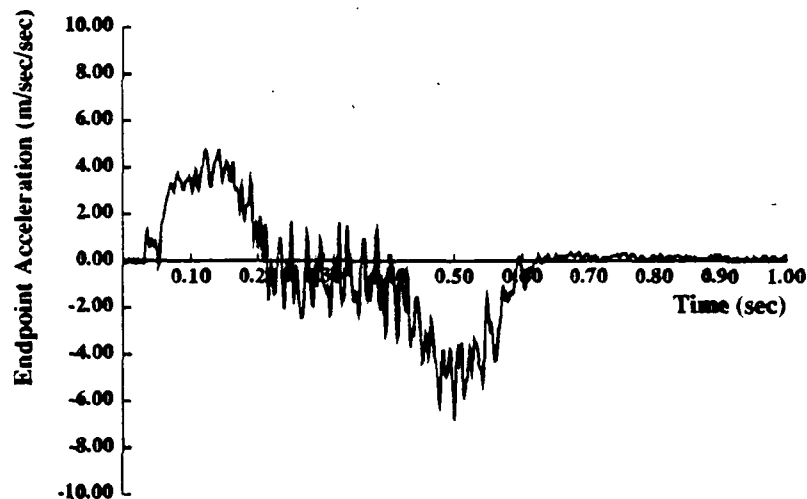
X-Axis Move with Versine Input

(d)

Figure 7.4: X-Axis Response to a Versine Input for a 0.23 m Move with $\tau_r = 2.75$ Nm and $\omega_p = 150$ rad/sec: (c) Motor Velocity (d) Endpoint Acceleration.
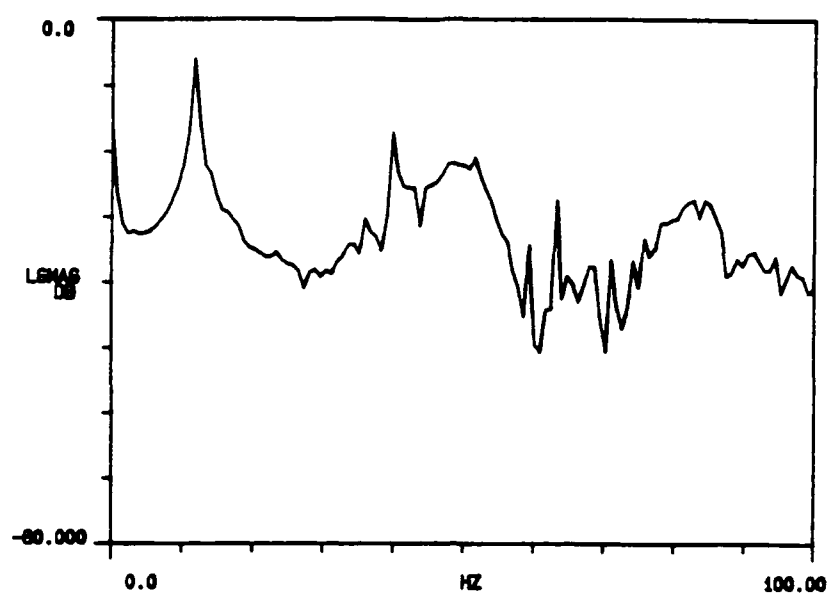
Figure 7.5: Frequency Spectrum of Residual Vibration for Step Input.
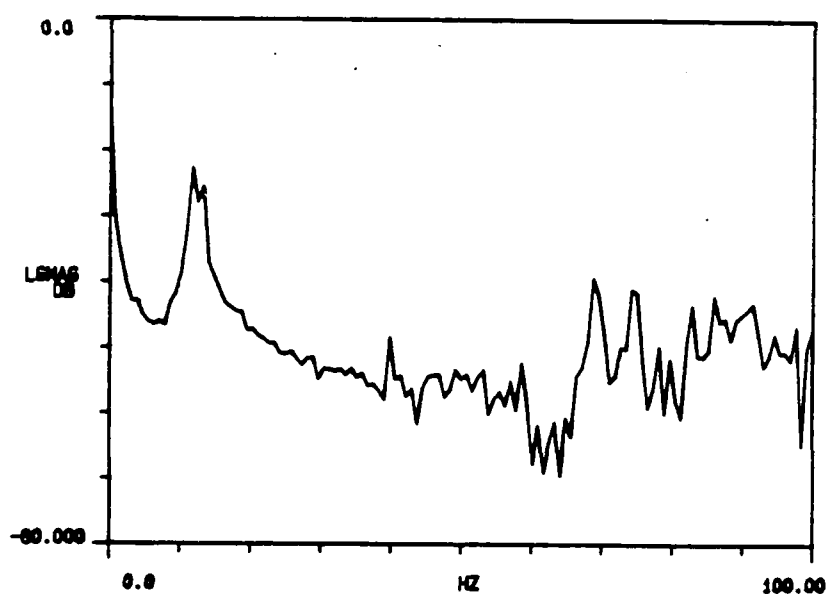
Figure 7.6: Frequency Spectrum of Residual Vibration for Rectangular Pulse Input.
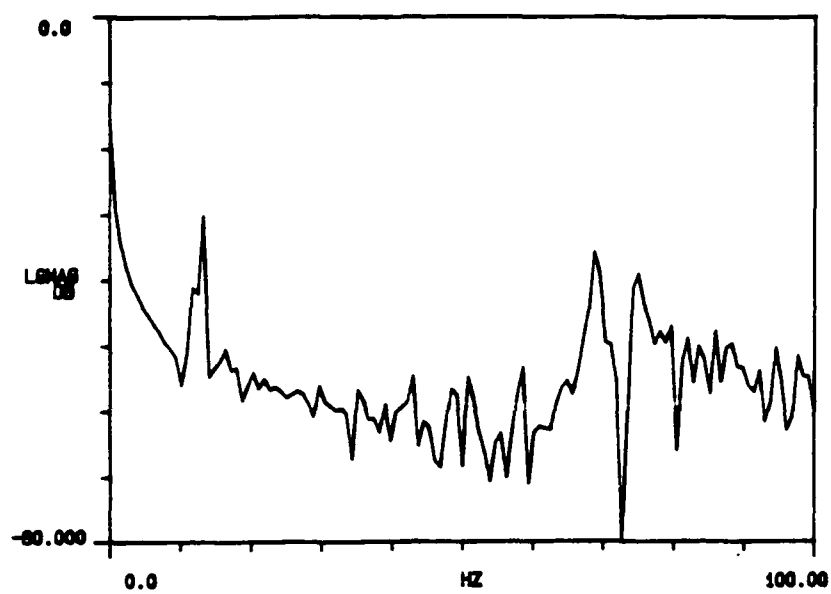
Figure 7.7: Frequency Spectrum of Residual Vibration for Versine Input.
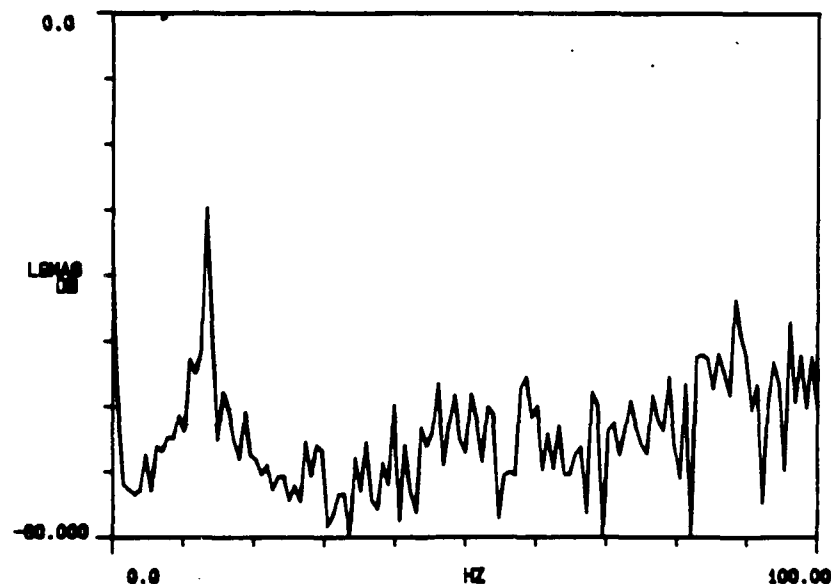
Figure 7.8: Frequency Spectrum of Vibration Due to Ambient Noise.

Table 7.1

Residual Endpoint Motion (mm)

Step Reference :	0.230
Rectangular Pulse Reference :	0.028
Versine Reference :	0.014

step reference and by 8 db compared to the integrated rectangular pulse reference. Further attenuation of the 12 Hz mode is impossible since the ambient noise in the building generates the remaining excitation. Figure 7.8 shows the frequency spectrum of the robot excited only by ambient noise. Notice that the peak at 12 Hz is at −30 db, the same level as that for the versine input.

The versine reference also reduces the residual vibration at 40 Hz, compared with either the step or the rectangular pulse reference. However, modes at 68 Hz and 75 Hz remain despite the low excitation energy which the versine function has at these frequencies. Perhaps some excitation energy from lower frequencies is exciting these higher modes due to some nonlinearities in the robot structure. Regardless of their origin, these modes contribute only 0.5 micron to the residual amplitude. A comparison of the residual vibration at the endpoint measured in mm (rather than acceleration units) for the three inputs is shown in Table 7.1. These values were determined by doubly integrating the acceleration amplitudes. If we assume that a single frequency at 12 Hz dominates, then the amplitude of the endpoint position oscillations can be approximated by dividing the acceleration amplitudes by the square of the frequency.

7.5   Robustness to Variation in Natural Frequency:

Garcia [61] determined that the robot modes with dominant X-direction change natural frequency by 10% depending on the location of the Y-axis. Therefore, tests were performed with the Y-axis in the extreme left (Y = 0) and extreme right (+Y) positions to see this shift in natural frequency and to determine whether the same versine input will work equally well for all cases.

Results for X-axis motion with the Y-axis to the left are shown in Figures 7.9 to 7.11. and with the Y-axis to the right are shown in Figures 7.12 to 7.14. The same three reference inputs are used as before. The acceleration signal is shown in (a) and the frequency spectrum of the residual vibration in (b). The two different step responses show a shift in the first natural frequency from 11.5 Hz when the Y-axis is to the left to 13 Hz when the Y-axis is to the right. Despite this variation in natural frequency of roughly 10%, the same versine input effectively reduces the residual vibration at that mode in both cases. In fact, the attenuation is the same as it was previously for the Y-axis in the middle, the position for which the waveform was originally specified.

One additional phenomenon shows up in the frequency spectrum when the Y-axis is to the right. For that configuration, an additional mode at 33 Hz appears that did not appear when Y was in the middle. The mode shapes measured by Garcia [61] indicate that the 33 Hz mode consists of the top frame twisting about the middle (Figure 7.15). Therefore, this mode is difficult to detect in X when Y is in the middle, but rather easy to detect when Y is to the right. A new versine input can be developed which reduces the energy at 33 Hz. This new time function is shown in Figure 7.16(a), with its spectrum in (b). The response of the X-axis to this input with the Y-axis to the right is shown in Figure 7.17. Notice that the residual vibration at 33 Hz is reduced by 8 db when the input is filtered at that frequency.
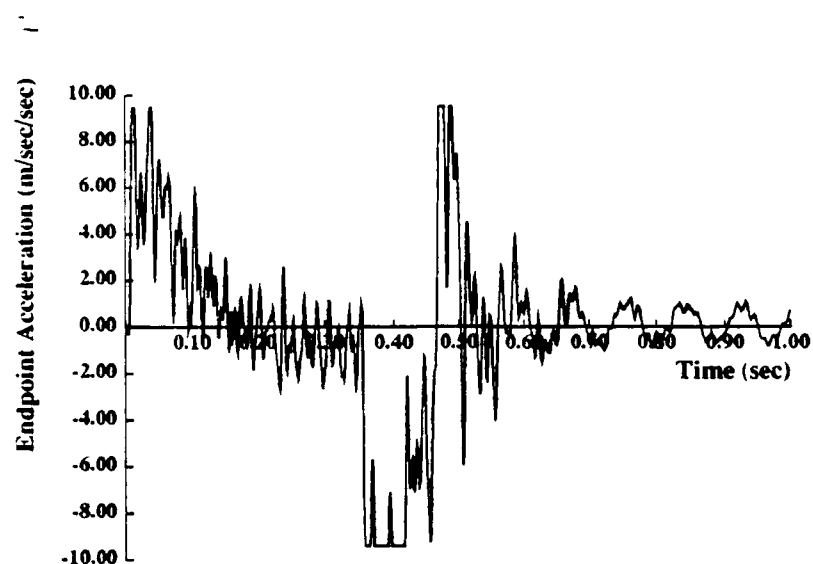
X-Axis Move with Step Setpoint (Y Left)

(a)
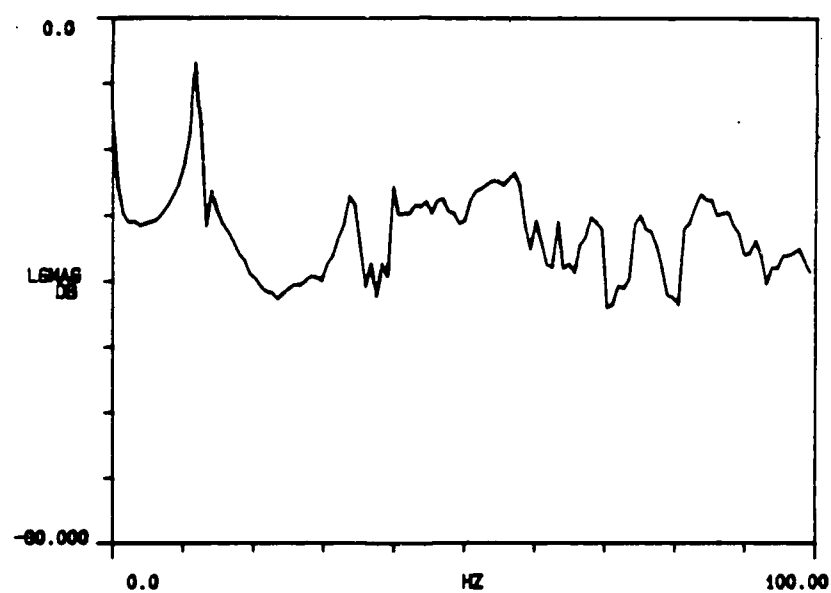
(b)

Figure 7.9: X-Axis Response to a Step Input of 0.23 m; Y-Axis Left: (a) Endpoint Acceleration (b) Frequency Spectrum of Residual Vibration.
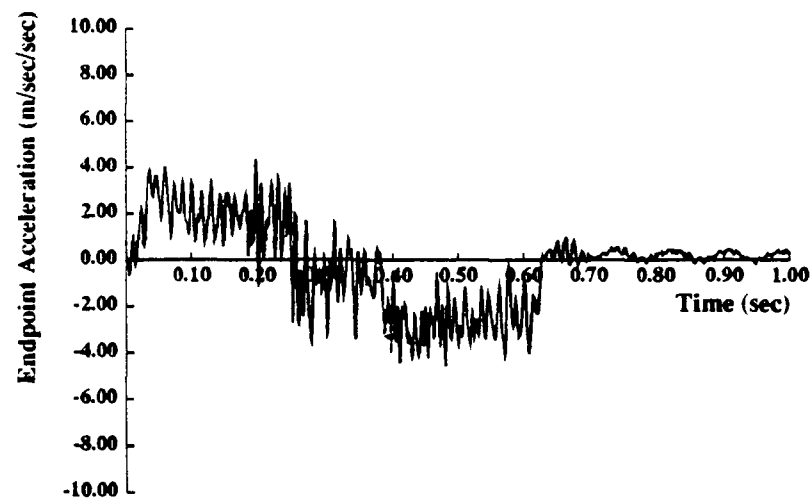
X-Axis Move with Rectangular Pulse Input (Y Left)

(a)
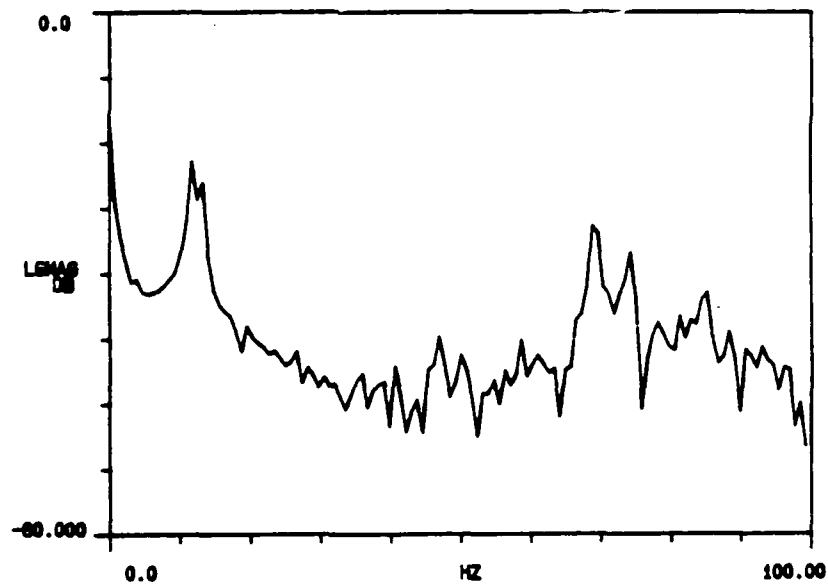
(b)

Figure 7.10: X-Axis Response to a Rectangular Pulse Input for a 0.23 m Move; Y-Axis Left: (a) Endpoint Acceleration (b) Frequency Spectrum of Residual Vibration.
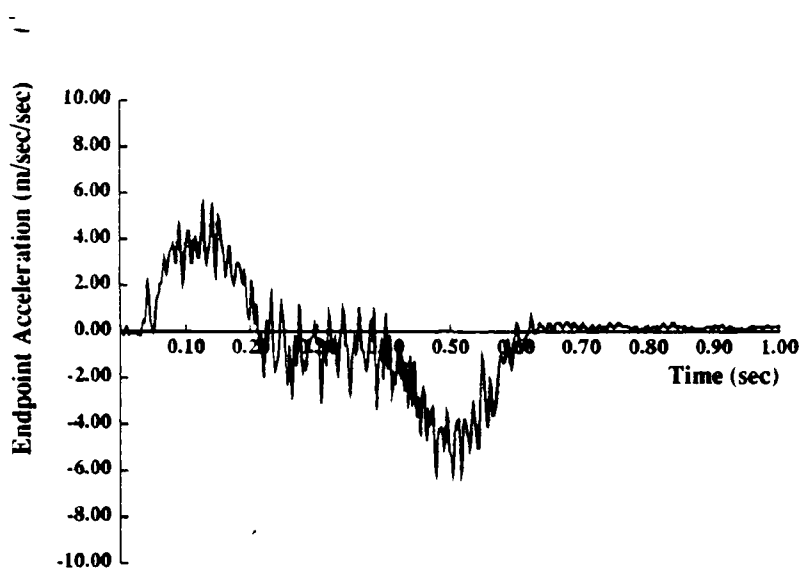
X-Axis Move with Versine Input (Y Left)

(a)
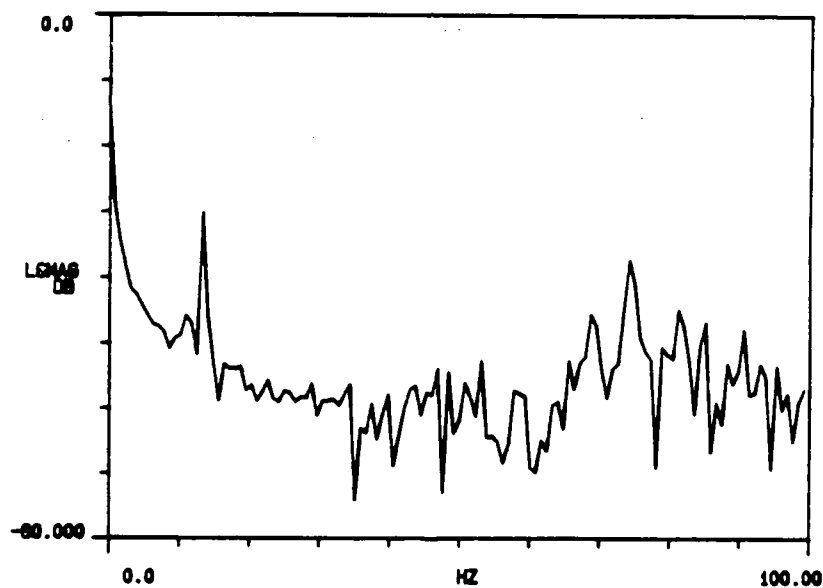
(b)

Figure 7.11: X-Axis Response to a Versine Input for a 0.23 m Move; Y-Axis Left: (a) Endpoint Acceleration (b) Frequency Spectrum of Residual Vibration.
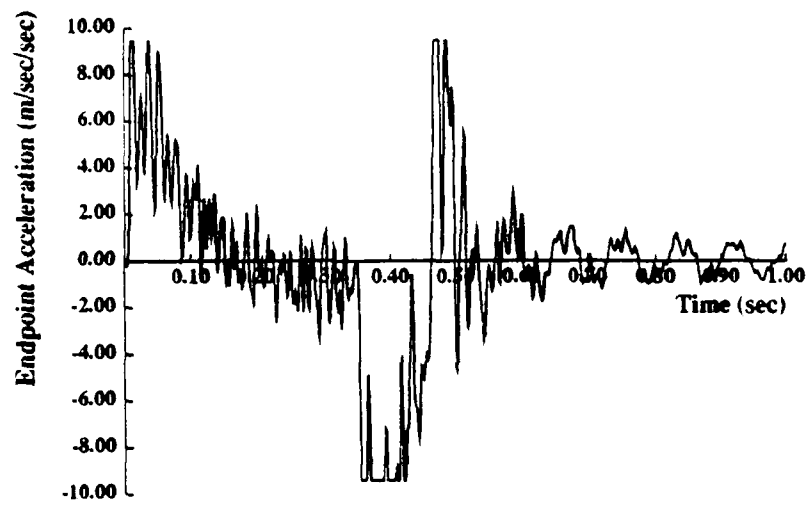
X-Axis Move with Step Setpoint (Y Right)

(a)
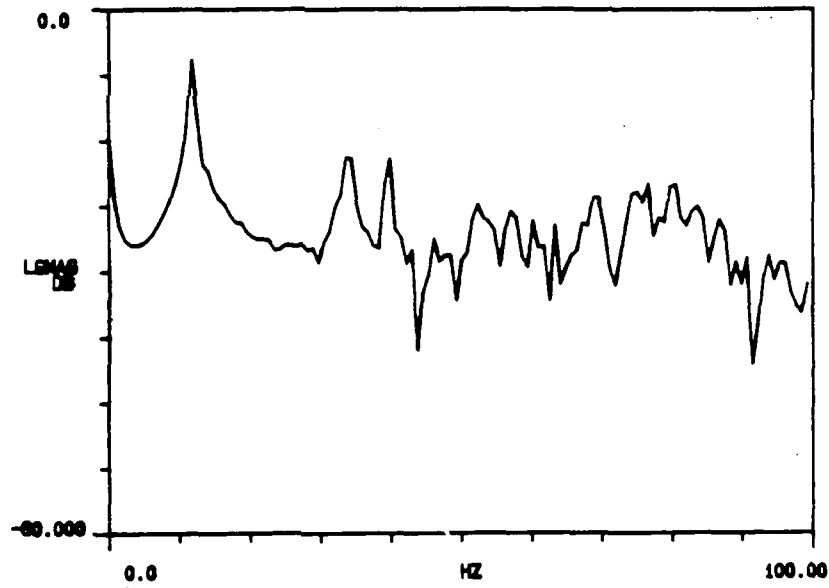
(b)

Figure 7.12: X-Axis Response to a Step Input of 0.23 m; Y-Axis Right: (a) Endpoint Acceleration (b) Frequency Spectrum of Residual Vibration.
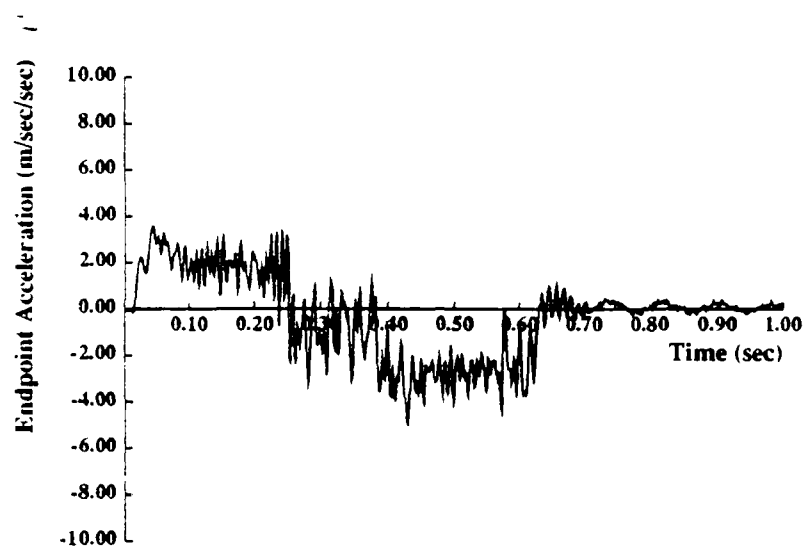
X-Axis Move with Rectangular Pulse Input (Y Right)

(a)
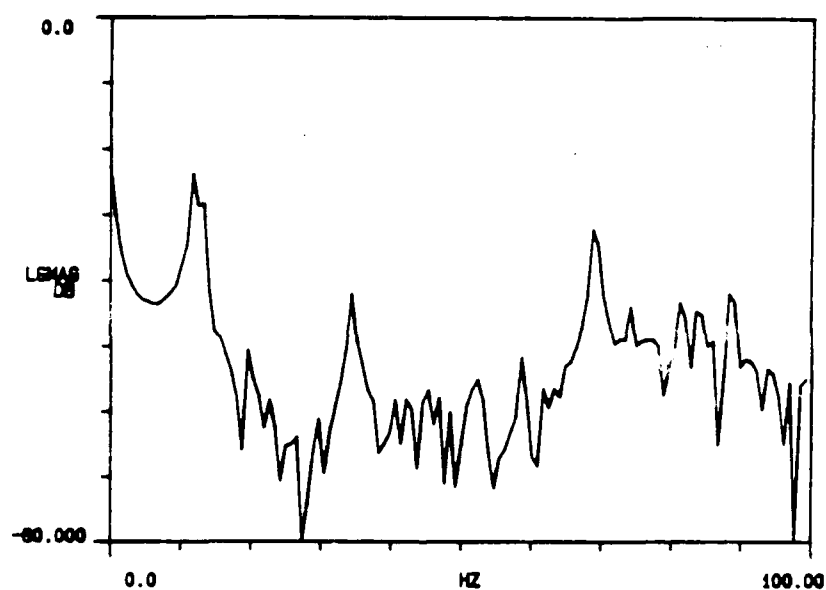
(b)

Figure 7.13: X-Axis Response to a Rectangular Pulse Input for a 0.23 m Move; Y-Axis Right: (a) Endpoint Acceleration (b) Frequency Spectrum of Residual Vibration.
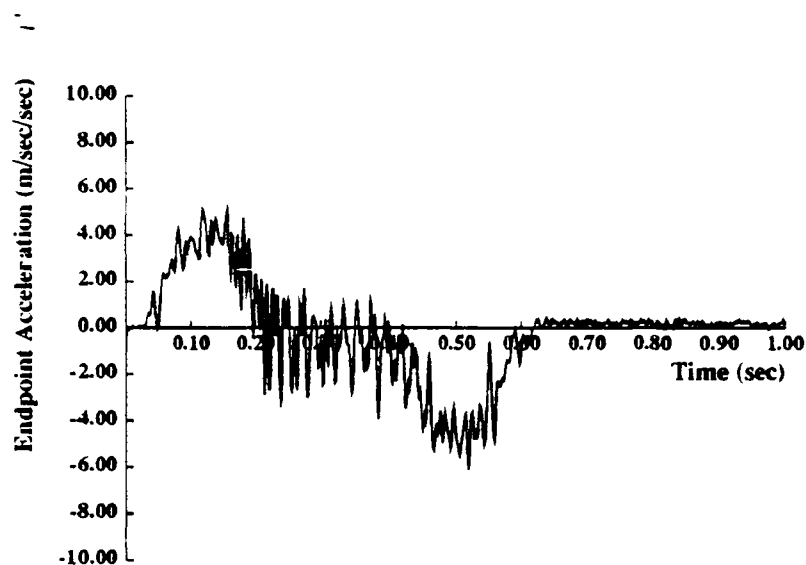
X-Axis Move with Versine Input (Y Right)

(a)
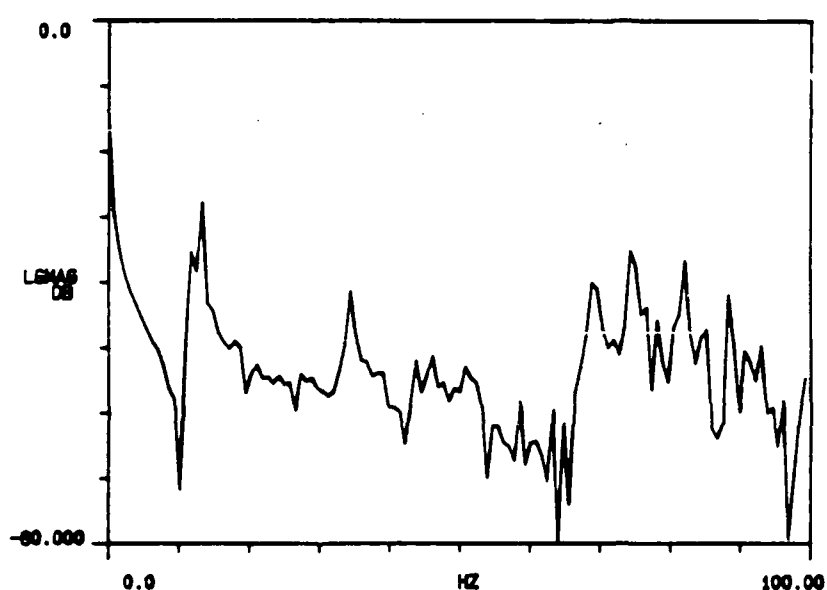
(b)

Figure 7.14: X-Axis Response to a Versine Input for a 0.23 m Move; Y-Axis Right: (a) Endpoint Acceleration (b) Frequency Spectrum of Residual Vibration.
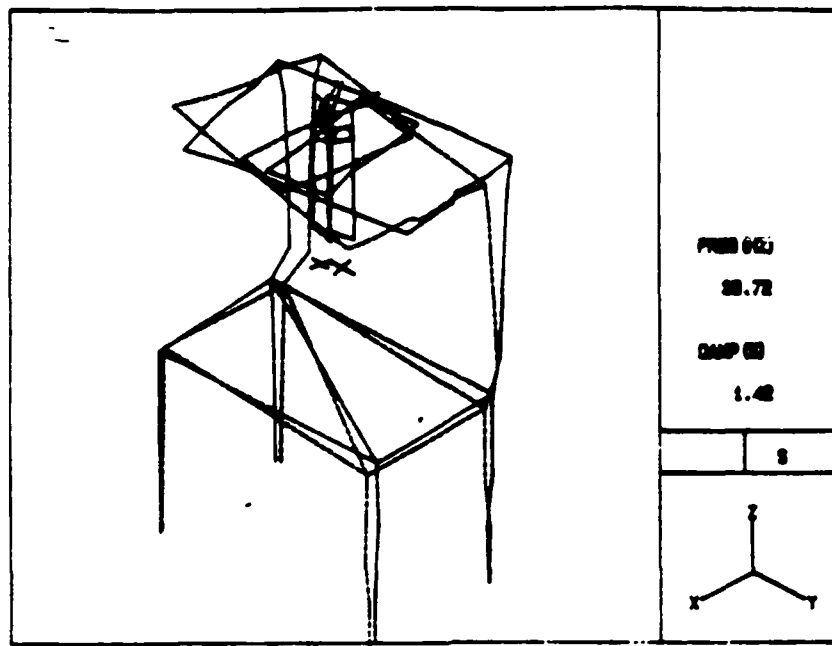
Figure 7.15: Measured Mode Shape for 33 Hz.

7.6 Modal Coupling Between Axes:

The 33 Hz mode in which the top frame twists involves motion in both the X and Y directions when Y is to the right ($+$Y). Thus. motion in Y is likely to excite this mode and hence cause vibration in the X-direction. Without a detailed three-dimensional model of the robot, this mode would be very difficult to damp out using a conventional modal controller for Y-motion. However, running the Y-axis with the versine input which attenuates this particular frequency ensures that no excitation occurs in the X-direction.

Experimental results for vibration in X when the Y-axis is moved a distance of 0.20 m (8 in.) using a step, rectangular pulse. and the versine reference of Fig. 7.16 are shown in Figures 7.18. 7.19. and 7.20. These reference inputs have been constructed for a Y-axis inertia of 2.78×10^{-3} kg-m^2. Motion took place in the rightmost part of the workspace. The step response shows considerable excitation of the 33 Hz mode in X from the motion in Y. However, the versine input effectively

Versine Input Filtering 33 Hz Mode

(a)
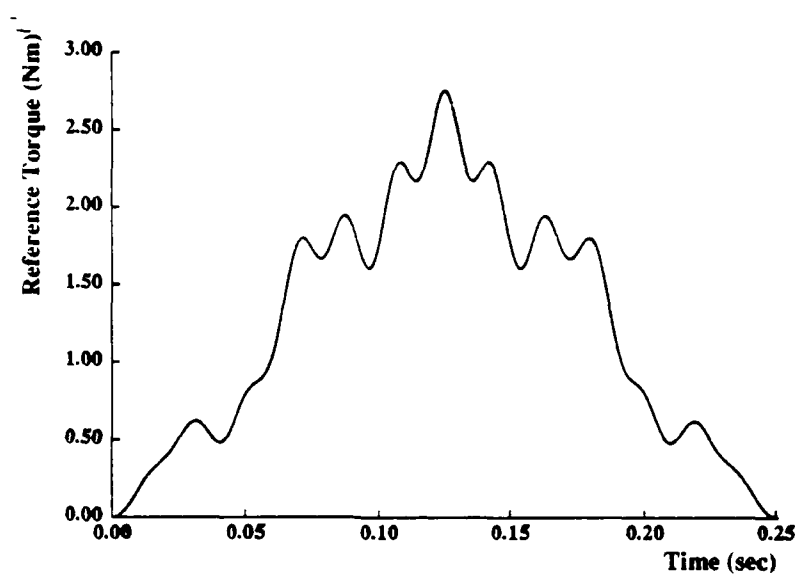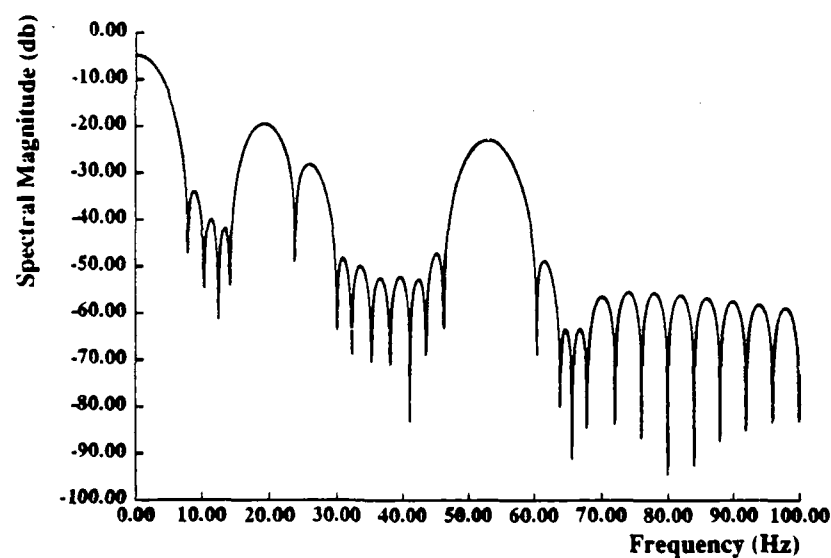
Frequency Spectrum of Versine Input

(b)

Figure 7.16: Versine Input tuned to 12, 33, 40, 70, and 84 Hz for $\tau_r = 2.75$ Nm and $\omega_p = 150$ rad/sec: (a) Time Function (b) Frequency Spectrum.
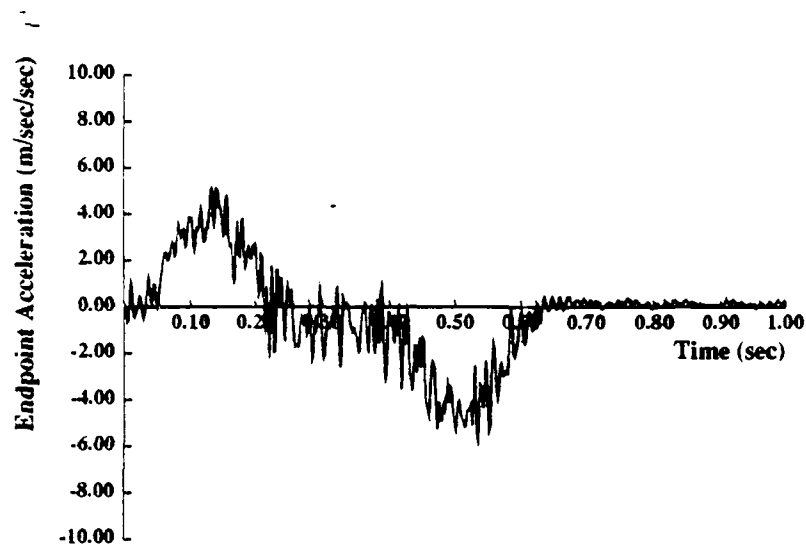
X-Axis Move with Versine Input Filtering 33 Hz (Y Right)

(a)
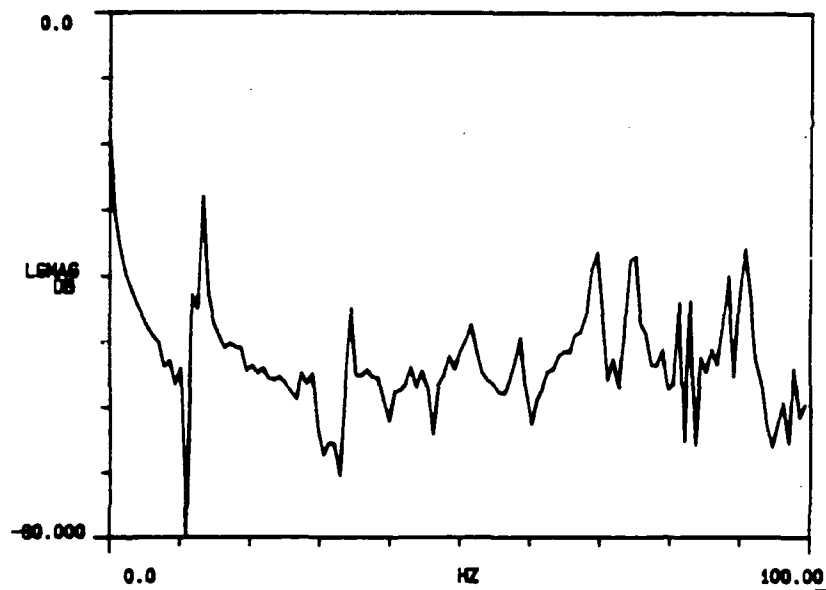
(b)

Figure 7.17: X-Axis Response to a Versine Input for a 0.23 m Move with 33 Hz Mode Filtered; Y-Axis Right: (a) Endpoint Acceleration (b) Frequency Spectrum of Residual Vibration.
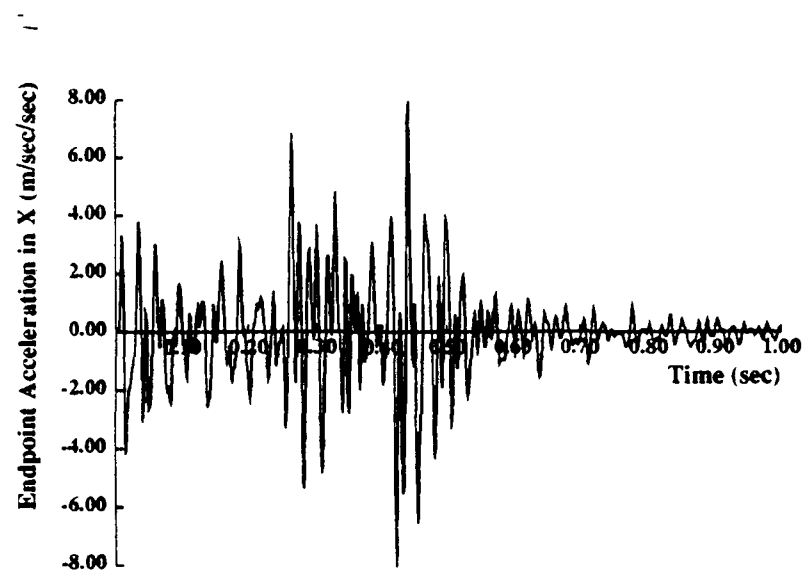
Y-Axis Move with Step Setpoint

(a)
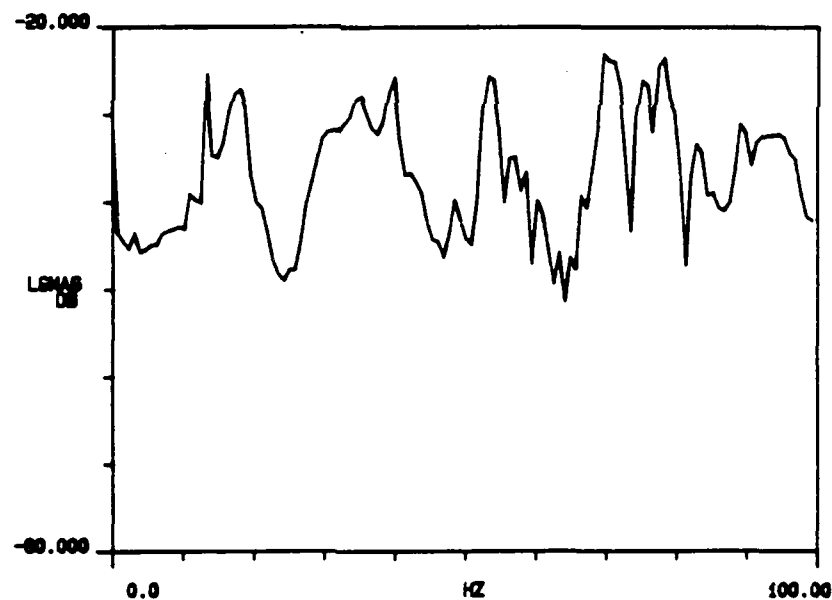
(b)

Figure 7.18: X-Axis Response to Y-Axis Motion of 0.2 m using a Step Input: (a) Endpoint Acceleration in X (b) Frequency Spectrum of Residual Vibration in X.
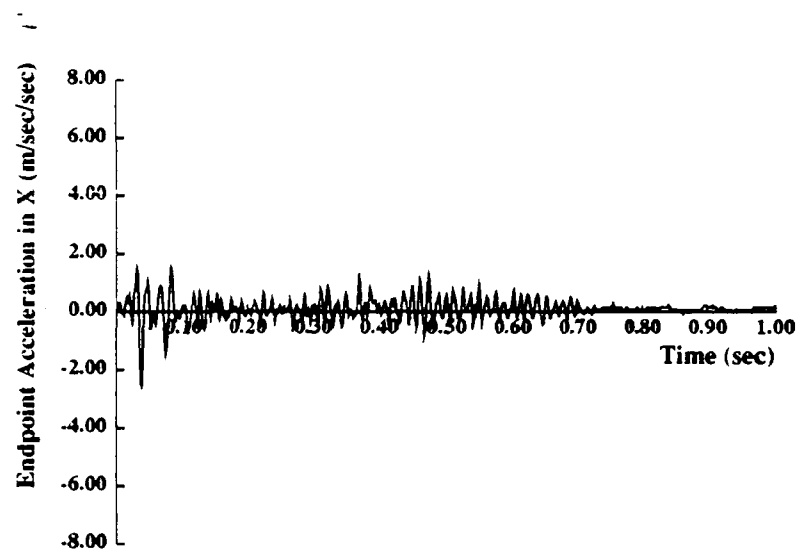
Y-Axis Move with Rectangular Pulse Input

(a)
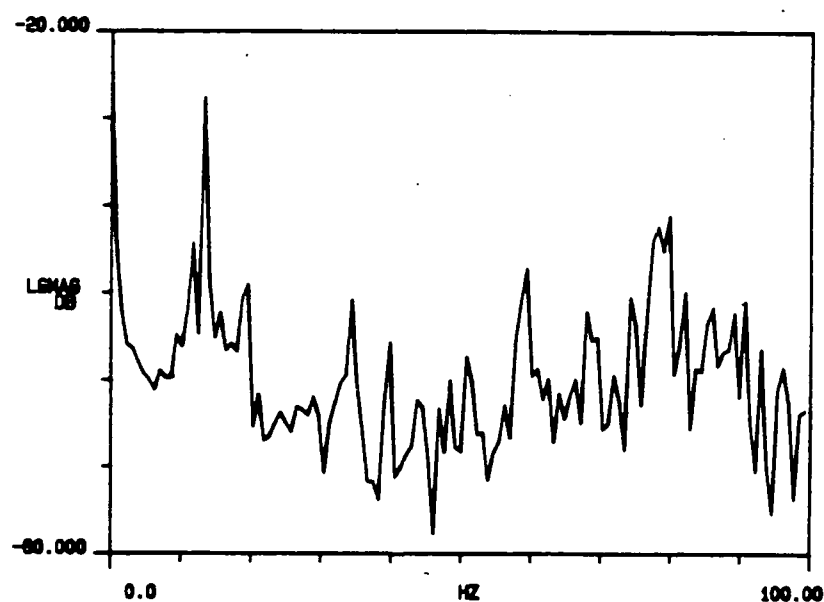
(b)

Figure 7.19: X-Axis Response to Y-Axis Motion of 0.2 m using a Rectangular Pulse Input: (a) Endpoint Acceleration in X (b) Frequency Spectrum of Residual Vibration in X.
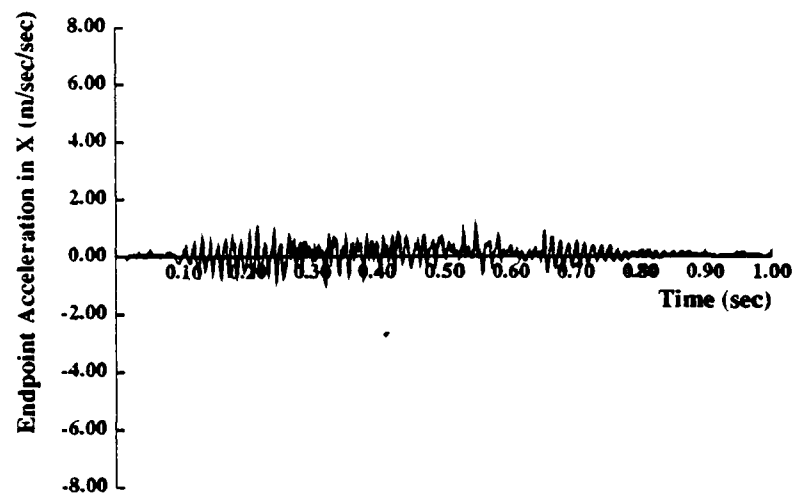
Y-Axis Move with Versine Input

(a)
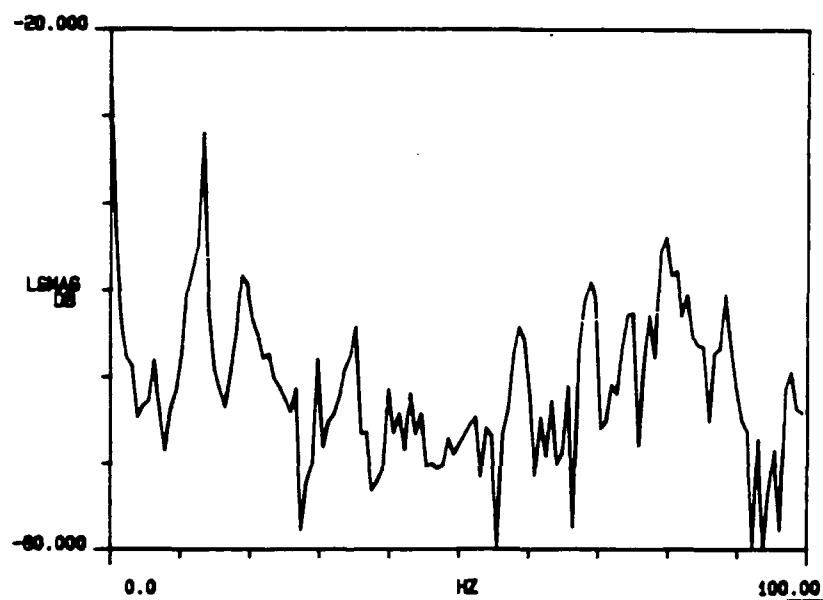
(b)

Figure 7.20: X-Axis Response to Y-Axis Motion of 0.2 m using a Versine Input: (a) Endpoint Acceleration in X (b) Frequency Spectrum of Residual Vibration in X.

reduces excitation of this mode by 8 db. Thus, even when the vibration cannot be measured in the axis of motion, the shaped inputs can avoid excitation of vibration occurring in orthogonal directions to the motion.

7.7 Time-Varying Natural Frequencies:

If both the X and Y axes are moved using the versine inputs, then the variation in Y-position will continuously alter the natural frequencies which would be measured statically at each succeeding Y-position. Such a test would determine whether the shaped inputs can reduce residual vibration for dynamically varying natural frequencies. The acceleration in the X-direction when moving the X-axis a distance of 0.23 m (9 in.) and the Y-axis a distance of 0.20 m (8 in.) is shown in Figure 7.21. The residual vibration at 12 Hz has again been reduced to the ambient level of −30 db as before. Thus despite the dynamic variation in resonant characteristics during the move, the versine input is still capable of attenuating the residual vibration.

7.8 Discussion:

The shaped versine reference inputs were tested on the MIT Cartesian Robot to determine how effective they are at reducing residual vibration under actual conditions. When moving in a single direction, the versine input is capable of bringing the residual vibration down to the level existing only with ambient noise. This holds true even when the location of the Y-axis is changed and the natural frequencies vary.

Running the X-axis for different static positions of the Y-axis gives the same attenuation of residual vibration. And when both axes are moved simultaneously, causing a dynamic variation in natural frequencies, residual vibration still remains low. Finally, for modes which can be excited by motion in an axis orthogonal to the dominant vibration, the use of shaped inputs can significantly reduce such
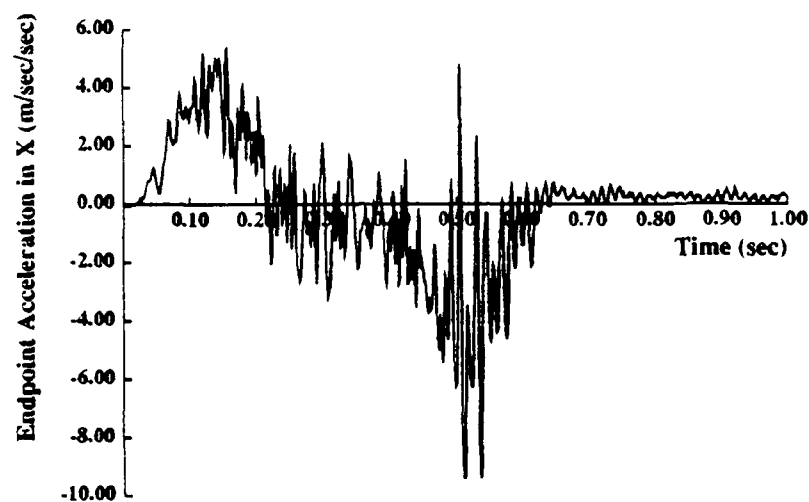
Combined X and Y Moves with Versine Inputs

(a)
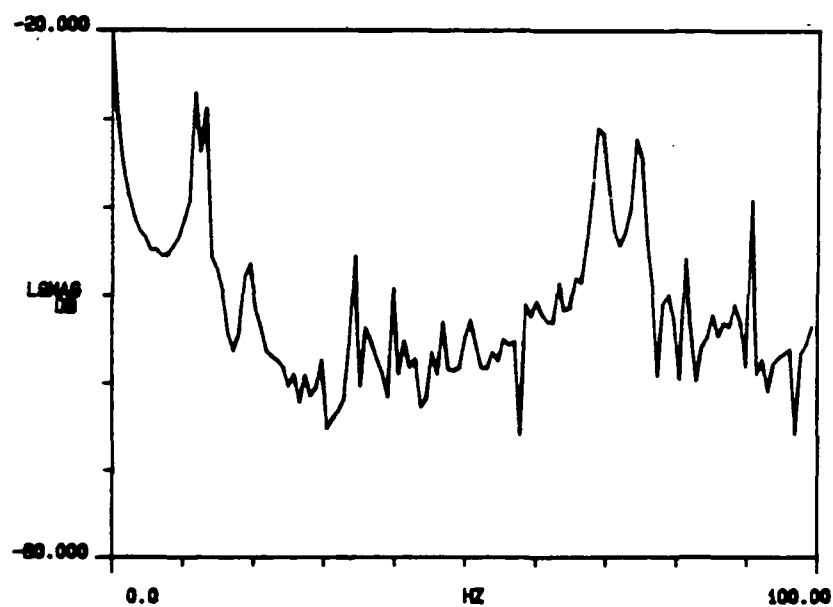
(b)

Figure 7.21: Combined X-Axis and Y-Axis Motion using Versine Inputs: (a) Endpoint Acceleration in X (b) Frequency Spectrum of Residual Vibration in X.

excitation.

Conclusions and Future Work

8.1   Conclusions:

Experimental tests done on the MIT Cartesian Robot indicate the effectiveness of shaping inputs to generate motion with minimum residual vibration. Such inputs allow the use of a simple PD controller to achieve accurate position without the need for complex controllers to damp out vibration during motion. However, this technique does not preclude the use of a more sophisticated controller to suppress vibration. The shaped inputs will always improve the residual vibration response generated by the motion, especially in cases when optimal regulators cannot provide adequate vibration suppression.

This approach is especially effective when dealing with complex three-dimensional structures with mode shapes in directions other than the motion direction. For such systems, the modes in the non-motion direction are only weakly coupled to the dynamics in the motion direction. As a result, these modes cannot be sufficiently compensated, and they will exhibit considerable off-axis vibration if lightly damped. These vibrations can be reduced during motion using shaped reference inputs tuned to the off-axis natural frequencies.

Shaped force inputs were developed as sums of ramped sinusoid harmonics by

187

picking the coefficients to minimize excitation over a range of natural frequencies. This allows for uncertainties in the determination of the natural frequencies and dynamic variation in natural frequency during motion. An additional set of inputs was developed using versine inputs to permit motion of constant speed for systems which are velocity-limited.

Shaped inputs were constructed on the assumption that the system to be controlled has no damping or friction. This simplifies the determination of coefficients for these functions. The presence of modal damping does reduce the effectiveness of the inputs but only near the limits of the frequency band where spectral energy has been minimized. This effect can be ignored for lightly-damped systems.

The presence of friction can easily be compensated for when these shaped force inputs are incorporated into a closed-loop feedback system. All that is required is that the shaped force profile be converted into a shaped position reference by double integration. The feedback loop compensates for friction without altering the vibration-reducing properties of the shaped inputs.

Despite these advantages, there are a number of drawbacks to this method. While conventional controllers only require a step reference, these inputs require a series of time-varying reference setpoints which must be recomputed for each move distance. This is not a problem, since trajectory controllers already compute appropriate trajectories to achieve a desired move. But it does increase the computational and storage requirements of the controller.

A more severe disadvantage is the requirement that the actuator never saturate during the motion. In order to ensure that residual vibration is minimized, the actual response must closely follow the response called for by the shaped reference input. If the actuator saturates. actual response lags behind and more residual vibration occurs. To ensure that no saturation occurs, the forces used for the motion must be reduced until the entire force profile fits within the saturation limits. This significantly increases the time needed to complete the move using shaped inputs

rather than a step reference. However, settling time due to residual vibration has been greatly reduced.

8.2   Future Work:

Several additional studies are motivated by this work. First of all, it would be useful to investigate the use of shaped inputs for large variations in natural frequency. such as occur when the robot configuration changes significantly (e.g. PUMA Robot) or when picking up a heavy workpiece.

A new set of inputs could be developed that compute coefficients to take into account modal damping for moderately-damped systems.

An entirely new set of functions could be developed that are based on more realistic assumptions about the allowable force profile. The actual motor torque for a typical amplifier saturates as a function of velocity rather than saturating at a constant limit. It would be useful to use more complicated saturation profiles than a square wave or a rectangular pulse in developing shaped inputs resembling these profiles. Such inputs could also be constructed to include the effects of friction and damping to ground. This would ensure that these inputs lead to actual torque profiles which maximally utilize the available torque without saturating.

Because feedback plays an important role in determining the actual torque profile. it would be interesting to evaluate the effect of this feedback. If the feedback signal introduces energy at natural frequencies which have been filtered out of the shaped input, then considerably more residual vibration will occur. It would be useful to study the interaction between feedback and the shaped inputs and determine whether different feedback compensators would improve performance. Perhaps the use of acceleration feedback, either from the motor or from an accelerometer mounted at the end point, would improve feedback compensation.

It would also be useful to evaluate the effect of actuator bandwidth on the

residual vibration attenuation of shaped inputs used in closed-loop systems.

These additional studies would answer further questions concerning the use of shaped inputs for generating motion in physical systems. These inputs have already been shown to reduce residual vibration for motion of a Cartesian Robot. With additional studies, inputs shaped to achieve minimum residual vibration and minimum move time may become an important element to control the vibration of actual dynamic systems.

Bibliography

[1] Nurre, G. S., Ryan R. S., Scofield, H. N., and Sims, J. L., "Dynamics and Control of Large Space Structures," AIAA *Journal of Guidance and Control*, Vol. 7, No. 5, Sept.-Oct. 1984, pp. 514-526.

[2] Bryson, Arthur E., Jr., "New Concepts in Control Theory, 1959-1984," AIAA *Journal of Guidance, Control, and Dynamics*, Vol. 8, No. 4, July-Aug. 1985, pp. 417-425.

[3] Seltzer, Sherman M., "Active Control of Flexible Space Structures," *Guidance and Control* 1980, Volume 42, Advances in the Astronautical Sciences, Rocky Mountain Guidance and Control Conference, 1980, pp. 477-489.

[4] Croopnick, S. R., Lin, Y. H., and Strunce, R. R., "A Survey of Automatic Control Techniques for Large Space Structures," *Proceedings of the 8th IFAC Symposium on Automatic Control in Space*, Oxford, England, July 1979, pp. 275-284.

[5] Joshi, S. M., and Groom, N. J., "Controller Design Approaches for Large Space Structures Using LQG Control Theory," *Proceedings of the Second VPI&SU/AIAA Symposium on Dynamics and Control of Large Flexible Spacecraft*, Blacksburg, Va., June 1979, pp. 35-50.

[6] Meirovitch, L., and Öz, H., "An Assessment of Methods for the Control of Large Space Structures," *Proceedings of the 1979 Joint Automatic Control Conference*, Denver, CO, June 1979, pp. 34-41.

[7] Aspinwall, D. M., "Acceleration Profiles for Minimizing Residual Response," ASME *Journal of Dynamic Systems, Measurement, and Control*, Vol. 102, No. 1, Mar. 1980, pp. 3-6.

[8] Swigert, C. J., "Shaped Torque Techniques," *Journal of Guidance and Control*, Vol. 3, No. 5, Sept.-Oct. 1980, pp. 460-467.

[9] Farrenkopf, R. L., "Optimal Open-Loop Maneuver Profiles for Flexible Spacecraft," AIAA *Journal of Guidance and Control*, Vol. 2, No. 6, Nov.-Dec. 1979, pp. 491-498.

[10] Turner, J. D., and Junkins, J. L., "Optimal Large-Angle Single-Axis Rotational Maneuvers of Flexible Spacecraft," AIAA *Journal of Guidance and Control*, Vol. 3, No. 6, Nov.-Dec. 1980, pp. 578-585.

[11] Turner, James D., and Chun, Hon M., "Optimal Distributed Control of a Flexible Spacecraft During a Large-Angle Maneuver," AIAA *Journal of Guidance, Control, and Dynamics*, Vol. 7, No. 3, May-June 1984, pp. 257-264.

[12] Alfriend, K. T., and Longman, R. W., "Rotational Maneuvers of Large Flexible Spacecraft," *Guidance and Control* 1980, Volume 42, Advances in the Astronautical Sciences, Rocky Mountain Guidance and Control Conference, 1980, pp. 453-475.

[13] Lisowski, Ronald J., and Hale, Arthur L., "Optimal Design for Single Axis Rotational Maneuvers of a Flexible Structure," *The Journal of the Astronautical Sciences*, Vol. 33, No. 2, Apr.-June 1985, pp. 179-196.

[14] Makino, H., et al., "Research and Development of the SCARA Robot," *Proceedings of the 4th International Conference cn Production Engineering*, Tokyo, 1980, pp. 885-890.

[15] Sehitoglu, H., and Aristizabal, J. H., "Design of a Trajectory Controller for Industrial Robots Using Bang-Bang and Cycloidal Motion Profiles," *Robotics: Theory and Applications*, ASME Winter Annual Meeting, Anaheim, CA, Dec. 1986, pp. 169-175.

[16] Smith, Otto J. M., *Feedback Control Systems*, McGraw-Hill Book Co., Inc., New York, 1958, pp. 331-345.

[17] Singer, Neil C., "Residual Vibration Reduction in Computer Controlled Machines," PhD Thesis, Department of Mechanical Engineering, Massachusetts Institute of Technology.

[18] Breakwell, J. A., "Optimal Feedback Slewing of Flexible Spacecraft," AIAA *Journal of Guidance and Control*, Vol. 4, No. 5, Sept.-Oct. 1981, pp. 472-479.

[19] Juang, Jer-Nan, Turner, James D., and Chun, Hon M., "Closed-Form Solutions for Feedback Control with Terminal Constraints," AIAA *Journal of Guidance, Control, and Dynamics*, Vol. 8, No. 1, Jan.-Feb. 1985, pp. 39-43.

[20] Chun, Hon M., Turner, James D., and Juang, Jer-Nan, "Disturbance-Accomodating Tracking Maneuvers of Flexible Spacecraft," *The Journal of the Astronautical Sciences*, Vol. 33, No. 2, Apr.–June 1985, pp. 197–216.

[21] Juang, J-N, Horta, L. G., and Robertshaw, H. H., "A Slewing Control Experiment for Flexible Structures," *Proceedings of the Fifth VPI&SU/AIAA Symposium on Dynamics and Control of Large Structures*, Blacksburg, Va., June 1985, pp. 547–570.

[22] Dougherty, H., Tompetrini, K., Levinthal, J., and Nurre, G., "Space Telescope Pointing Control System," *AIAA Journal of Guidance, Control, and Dynamics*, Vol. 5, No. 4, July–Aug. 1982, pp. 403–409.

[23] Dougherty, H., Rodoni, C., Rodden, J., and Tompetrini, K., "Space Telescope Pointing Control," *Astrodynamics 1983*, Volume 54, Part I, Advances in the Astronautical Sciences, Proceedings of the Conference, Lake Placid, NY, Aug. 1983, pp. 619–630.

[24] Hughes, P. C. and Abdel-Rahman, T. M., "Stability of Proportional-Plus-Derivative-Plus-Integral Control of Flexible Spacecraft," *AIAA Journal of Guidance and Control*, Vol. 2, No. 6, Nov.–Dec. 1979, pp. 499–503.

[25] Baruh, H., and Silverberg, L. M., "Implementation Problems Associated with Simultaneous Maneuver and Vibration Suppression of Flexible Spacecraft," *Proceedings of the Fifth VPI&SU/AIAA Symposium on Dynamics and Control of Large Structures*, Blacksburg, Va., June 1985, pp. 585–599.

[26] Meirovitch, L., Van Landingham, H. F., and Öz, H., "Distributed Control of Spinning Flexible Spacecraft," *Proceedings of the First VPI&SU/AIAA Symposium on Dynamics and Control of Large Flexible Spacecraft*, Blacksburg, Va., June 1977, pp. 249–269.

[27] Balas, M., "Modal Control of Certain Flexible Dynamic Systems," *SIAM Journal of Control Optimization*, Vol. 16, No. 3, May 1978, pp. 450–462.

[28] Henrichfreise, Hermann, Moritz, Wolfgang, and Siemensmeyer, Hubert, "Control of a Light, Elastic Manipulation Device," *Proceedings of the Conference on Applied Motion Control*, Minneapolis, MN, June 1987.

[29] Cannon, Robert H., Jr., and Rosenthal, Dan E., "Experiments in Control of Flexible Structures with Noncolocated Sensors and Actuators," *AIAA Journal of Guidance and Control*, Vol. 7, No. 5, Sept.–Oct. 1984, pp. 546–553.

[30] Cannon, R. H., Jr., and Schmitz, E., "Initial Experiments on the End-Point Control of a Flexible One-Link Robot," *The International Journal of Robotics Research*, Vol. 3, No. 3, Fall 1984, pp. 62–75.

[31] Hollars, Michael G., and Cannon, Robert H., Jr., "Initial Experiments on the End-Point Control of a Two-Link Manipulator with Flexible Tendons," presented at the Winter Annual Meeting of ASME, Miami Beach, Florida, November 1985.

[32] Alberts, T. E., Hastings. G. G., Book. W. J., Jr., and Dickerson, S. L., "Experiments in Optimal Control of a Flexible Arm with Passive Damping," *Proceedings of the Fifth VPI&SU/AIAA Symposium on Dynamics and Control of Large Structures*, Blacksburg, Va., June 1985, pp. 423–435.

[33] Silverberg, L. M., "Uniform Damping Control of Spacecraft." *Proceedings of the Fifth VPI&SU/AIAA Symposium on Dynamics and Control of Large Structures*, Blacksburg, Va., June 1985, pp. 145–161.

[34] Burke, Shawn E., and Hubbard, James E., Jr., "Active Vibration Control of a Simply Supported Beam Using a Spatially Distributed Actuator," IEEE *Control Systems Magazine*, Vol. 7, No. 4, Aug. 1987, pp. 25–30.

[35] Finzi, A. Ercoli, Lanz, M., and Mantegazza, P., "Active Structural Control with Decentralized and Colocated Control Units," *Proceedings of the Fifth VPI&SU/AIAA Symposium on Dynamics and Control of Large Structures*, Blacksburg, Va., June 1985, pp. 487–501.

[36] Nesline, F. William, and Zarchan, Paul, "Why Modern Controllers Can Go Unstable in Practice," AIAA *Journal of Guidance, Control, and Dynamics*, Vol. 7, No. 4, July–Aug. 1984, pp. 495–500.

[37] Kosut, Robert, L., Salzwedel, Horst, and Emami-Naeini, Abbas, "Robust Control of Flexible Spacecraft," AIAA *Journal of Guidance, Control, and Dynamics*, Vol. 6, No. 2, Mar.–Apr. 1983, pp. 104–111.

[38] Arbel, Ami, and Gupta, N. K., "Robust Colocated Control for Large Flexible Space Structures," AIAA *Journal of Guidance, Control, and Dynamics*, Vol. 4, No. 5, Sept.–Oct. 1981, pp. 480–486.

[39] Balas, M. J., "Feedback Control of Flexible Systems," IEEE *Transactions on Automatic Control*, Vol. AC-23, No. 4, Aug. 1978, pp. 673–679.

[40] Radcliffe, C. J., and Mote, C. D., Jr., "Identification and Control of Rotating Disk Vibration," ASME *Journal of Dynamic Systems. Measurement. and Control*, Vol. 105, No. 1, Mar. 1983, pp. 39–45.

[41] Gupta, N. K., "Frequency-Shaped Cost Functionals: Extension of Linear-Quadratic-Gaussian Design Methods," AIAA *Journal of Guidance and Control*, Vol. 3, No. 6, Nov.–Dec. 1980, pp. 529–535.

[42] Gupta, N. K., Lyons, M. G., Aubrun, J.-N., and Margulies, G., "Frequency-Shaping Methods in Large Space Structures Control", AIAA Guidance and Control Conference, Albuquerque, New Mexico, Aug. 1981.

[43] Balas, M. J., "Enhanced Modal Control of Flexible Structures Via Innovations Feedthrough," *Proceedings of the Second VPI&SU/AIAA Symposium on Dynamics and Control of Large Flexible Spacecraft*, Blacksburg, Va., June 1979, pp. 677–700.

[44] Lin, J. G., Hegg., D. R., Lin, Y. H., and Keat, J. E., "Output Feedback Control of Large Space Structures: An Investigation of Four Design Methods," *Proceedings of the Second VPI&SU/AIAA Symposium on Dynamics and Control of Large Flexible Spacecraft*, Blacksburg, Va., June 1979, pp. 1–18.

[45] Sesak, J. R., Likins, P. W., and Coradetti, T., "Flexible Spacecraft Control by Model Error Sensitivity Suppression," *Proceedings of the Second VPI&SU/AIAA Symposium on Dynamics and Control of Large Flexible Spacecraft*, Blacksburg, Va., June 1979, pp. 349–368.

[46] Dorato, Peter, "A Historical Review of Robust Control," IEEE *Control Systems Magazine*, Vol. 7, No. 2, April 1987, pp. 44–47.

[47] Yamada, I. and Nakagawa, M., "Reduction of Residual Vibrations in Positioning Control Mechanism," ASME *Journal of Vibration, Acoustics, Stress, and Reliability in Design*, Vol. 107, No. 1, Jan. 1985, pp. 47–52.

[48] Calico, R. A., and Moore, S., "The Effects of Structural Perturbations on Modal Suppression," *Proceedings of the Fifth VPI&SU/AIAA Symposium on Dynamics and Control of Large Structures*, Blacksburg, Va., June 1985, pp. 341–351.

[49] Ih, Che-Hang Charles, Wang, S. J., and Leondes, C. T., "An Investigation of Adaptive Control Techniques for Space Stations," *Proceedings of the 1985 Joint Automatic Control Conference*, Boston, MA, June 1985, pp. 81–94.

[50] Bar-Kana, I., Kaufman, H., and Balas, M., "Model Reference Adaptive Control of Large Structural Systems," AIAA *Journal of Guidance, Control, and Dynamics*, Vol. 6, No. 2, Mar.–Apr. 1983, pp. 112–118.

[51] Dubowsky, S., and DesForges, D. T., "The Application of Model-Referenced Adaptive Control to Robotic Manipulators," *Proceedings of the 1979 Joint Automatic Control Conference*, Denver, CO, June 1979, pp. 507–513.

[52] Johnson, C. R., Jr., "Approaches to Adaptive Digital Control Focusing on the Second Order Modal Descriptions of Large, Flexible Spacecraft Dynamics," *Proceedings of the Second VPI&SU/AIAA Symposium on Dynamics and Control of Large Flexible Spacecraft*, Blacksburg, Va., June 1979, pp. 301–315.

[53] Benhabib, R. J., Iwens, R. P.. and Jackson, R. L., "Active Vibration Control of a Flat Plate Using Model Reference Adaptive Techniques." *Proceedings of the Second VPI&SU/AIAA Symposium on Dynamics and Control of Large Flexible Spacecraft.* Blacksburg, Va.. June 1979, pp. 317–329.

[54] Potter, J. E.. and Ginter. S. D.. "A New Concept in Adaptive Structural Control," *Proceedings of the Second VPI&SU/AIAA Symposium on Dynamics and Control of Large Flexible Spacecraft,* Blacksburg, Va., June 1979, pp. 331–348.

[55] Meckl. Peter H.. "Minimizing Residual Vibration of a Linear System Using Appropriately Shaped Forcing Functions." SM Thesis, Department of Mechanical Engineering, Massachusetts Institute of Technology, June 1984.

[56] Meckl. P. H. and Seering, W. P., "Active Damping in a Three-Axis Robotic Manipulator." ASME *Journal of Vibration, Acoustics, Stress, and Reliability in Design,* Vol. 107, No. 1, Jan. 1985, pp. 38–46.

[57] Meckl. P. H.. and Seering, W. P., "Minimizing Residual Vibration for Point-to-Point Motion." ASME *Journal of Vibration, Acoustics, Stress, and Reliability in Design,* Vol. 107, No. 4, Oct. 1985, pp. 378–382.

[58] Meckl. P. H., and Seering, W. P., "Reducing Residual Vibration in Systems with Time-Varying Resonances," *Proceedings of the 1987 IEEE International Conference on Robotics and Automation,* Raleigh, N. C., March–April 1987, pp. 1690–1695.

[59] Meckl. Peter H.. and Seering, Warren P., "Reducing Residual Vibration in Systems with Uncertain Resonances," IEEE *Control Systems Magazine,* Vol. 8, No. 1, Feb. 1988.

[60] Papoulis, Athanasios, *The Fourier Integral and its Applications.* McGraw-Hill, New York, 1962, pp. 172–173.

[61] Garcia Reynoso, Alfonso, "Structural Dynamics Model of a Cartesian Robot." ScD Thesis, Department of Mechanical Engineering, Massachusetts Institute of Technology, Oct. 1985.

[62] Singer, Neil C., "Using Acausal Shaping Techniques to Reduce Manipulator Vibration." *Proceedings of the 1988 IEEE International Conference on Robotics and Automation,* Philadelphia, PA, April 1988.

[63] Meckl. P. H.. and Seering, W. P., "Feedforward Control Techniques to Achieve Fast Settling Time in Robots", *Proceedings of the 1986 Joint Automatic Control Conference.* Seattle, WA, June 1986, pp. 1913–1918.

[64] An, Chae H., Atkeson, Christopher G., and Hollerbach, John M., "Experimental Determination of the Effect of Feedforward Control on Trajectory Tracking Errors," *Proceedings of the 1986 IEEE International Conference on Robotics and Automation*, San Francisco, CA, April 1986, pp. 55–60.

[65] Bryson, A. E., Jr., "Some Connections Between Modern and Classical Control Concepts," ASME *Journal of Dynamic Systems, Measurement, and Control*, Vol. 101, June 1979, pp. 91–98.

[66] Larson, V., and Likins, P., "An Application of Modern Control Theory to an Elastic Spacecraft," *Proceedings of the Symposium on Dynamics and Control of Non-Rigid Spacecraft*, Frascati, Italy, May 1976, pp. 221–226.

[67] Martin, Gary Don, and Bryson, Arthur E., Jr., "Attitude Control of a Flexible Spacecraft," AIAA *Conference on Guidance and Control*, Palo Alto, CA, August 1978, pp. 281–287.

[68] Kwakernaak, Huibert, and Sivan, Raphael, *Linear Optimal Control Systems*, John Wiley & Sons, Inc., New York, 1972, pp. 281–297.

[69] Good, M. C., Sweet, L. M., and Strobel, K. L., "Dynamic Models for Control System Design of Integrated Robot and Drive Systems," *Journal of Dynamic Systems, Measurement, and Control*, Vol. 107, No. 1, March 1985, pp. 53–59.

[70] Meckl, Peter H., and Seering, Warren P., "Controlling Velocity-Limited Systems to Reduce Residual Vibration," *Proceedings of the 1988 IEEE International Conference on Robotics and Automation*, Philadelphia, PA, April 1988.

[71] Vaaler, E., and Seering, W. P., "Design of a Cartesian Robot," *Proceedings of Robotics and Manufacturing Automation Symposium*, ASME, November 1985, pp. 163–168.

[72] Podoloff, Robert Michael, "Accuracy Considerations for the M.I.T. Cartesian Assembly Robot," SM Thesis, Department of Mechanical Engineering, Massachusetts Institute of Technology, May 1984.

[73] Nussbaum, Michael, AI Documents #ER-GN-11, #ER-RB-09, #EDM-RB-02, Automatix, Inc., Billerica, MA, 1984.

[74] Drlik, Gary J., "Dynamic Performance Enhancement of the M.I.T. Precision Assembly Robot," SB Thesis, Department of Mechanical Engineering, Massachusetts Institute of Technology, May 1985.

[75] Benjamin, Michael H., "Design and Analysis of a Control System for the M.I.T. Precision Assembly Robot," SM Thesis, Department of Mechanical Engineering, Massachusetts Institute of Technology, January 1985.

Frequency Spectrum of Bang-Bang Function

<div align="right">Appendix A</div>

Chapter 2 presented a direct relationship between residual acceleration amplitude of a two-mass system and the frequency spectrum of the input forcing function used to generate the motion. Since this result applies for any input function, it should also apply to the bang-bang function developed in my Master's Thesis [55]. The bang-bang function is a generalization of a square wave forcing function that always produces peak force and switches between positive and negative levels a given number of times. This input function is known to give time-optimal response.

For the undamped two-mass system model of Figure 2.3, the appropriate bang-bang function consists of three switches, as shown in Figure A.1. The first and third switches, occurring at times t_1 and t_3 respectively, are symmetric about the second switch at t_2, which happens halfway into the move. The input is turned off at the final time T_f. The switch times t_1, t_2, and t_3 satisfy the following expressions:

$$1 - 2\cos\omega_n t_1 + 2\cos\omega_n t_2 - 2\cos\omega_n t_3 + \cos\omega_n T_f = 0 \tag{A.1}$$

$$t_2 = T_f/2 \tag{A.2}$$

$$t_3 = T_f - t_1 \tag{A.3}$$

<div align="center">198</div>
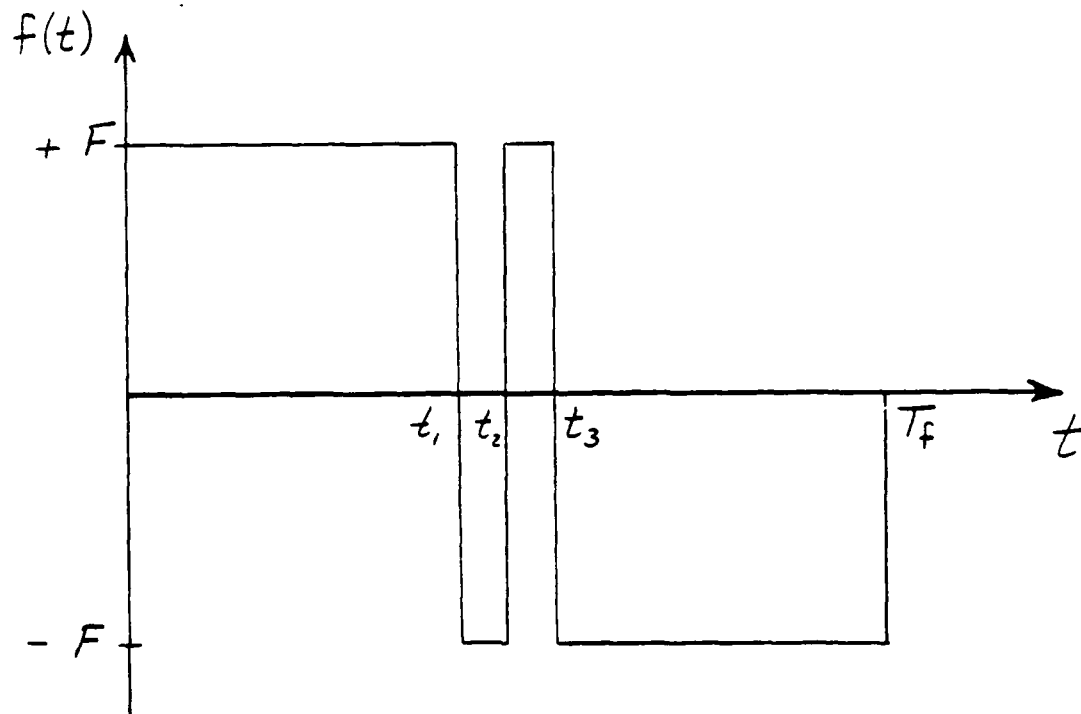
Figure A.1: Three-Switch Bang-Bang Forcing Function.

Making the appropriate substitutions, (A.1) can be simplified to

$$2 \left[\cos \frac{\omega_n T_f}{2} - 2 \cos \omega_n \left(\frac{T_f}{2} - t_1 \right) + 1 \right] = 0. \qquad (A.4)$$

This expression must be satisfied by t_1 and T_f in order to ensure zero residual vibration for the two-mass system.

The frequency spectrum of the three-switch bang-bang function can be determined by taking the Fourier transform as follows:

$$F(\omega) = \int_0^{T_f} f(t) e^{-j\omega t} dt \qquad (A.5)$$

When the required integration is performed, the frequency spectrum can be represented as

$$|F(\omega)| = \frac{2F}{\omega} \left| \cos \frac{\omega T_f}{2} - 2 \cos \omega \left(\frac{T_f}{2} - t_1 \right) + 1 \right|. \qquad (A.6)$$

At the frequency corresponding to the system natural frequency ω_n, spectral mag-

nitude is given by

$$|F(\omega_n)| = \frac{2F}{\omega_n} \left| \cos \frac{\omega_n T_f}{2} - 2 \cos \omega_n \left(\frac{T_f}{2} - t_1 \right) + 1 \right|. \qquad (A.7)$$

Substituting the expression (A.4) into (A.7) gives the final result:

$$|F(\omega_n)| = 0 \qquad (A.8)$$

Thus, the bang-bang function developed to eliminate residual vibration can be shown to have a frequency spectrum having no energy at the natural frequency. This is consistent with the relationship (2.13) derived in Chapter 2.

Since the bang-bang function contains no spectral energy at the system natural frequency, we might conclude that this input never excites the system at its natural frequency. However, the sharp transitions in the forcing function suggest that many frequencies are excited by this input, including the system natural frequency. In fact what is happening is that the input does excite the natural frequency in the first half of the move and then totally reverses the phase of the excited vibration in the second half of the move to bring the system to rest when the function is over.

To prove this assertion, we will look at the frequency spectrum of the first and second half of the bang-bang function separately. The Fourier transform for the first half of the move is given by

$$F_1(\omega) = \int_0^{T_f/2} f(t) e^{-j\omega t} dt = \frac{F}{j\omega} \left[e^{j\omega \frac{T_f}{2}} - 2 e^{j\omega \left(\frac{T_f}{2} - t_1 \right)} + 1 \right] e^{-j\omega \frac{T_f}{2}}. \qquad (A.9)$$

The Fourier transform for the second half of the move is given by

$$F_2(\omega) = \int_{T_f/2}^{T_f} f(t) e^{-j\omega t} dt = \frac{F}{j\omega} \left[1 - 2 e^{-j\omega \left(\frac{T_f}{2} - t_1 \right)} + e^{-j\omega \frac{T_f}{2}} \right] e^{-j\omega \frac{T_f}{2}}. \qquad (A.10)$$

Since the frequency spectrum depends only on the magnitude of expressions (A.9) and (A.10), we will restrict attention to the bracketed quantities. These can be shown to have the same magnitude and opposite phase. Thus, whatever energy is present in the input at the natural frequency during the first half of the move is

removed in the second half. This leaves the system without residual vibration when final position is reached.

Even though the bang-bang function produces no residual vibration, it does so only because the input is precisely phased to cancel in the second half any vibration generated in the first half. Thus, the vibration in the second half must have exactly the opposite phase to that of the vibration in the first half. If there is any error in the natural frequency for which this input was tuned, cancellation will be unsuccessful and residual vibration will result.

Commands to Generate Robot Motion

Many of the FORTH commands necessary to move the robot were defined by Benjamin [75]. Several additional commands were written in order to allow the servo routines to follow time-varying reference setpoints.

The servo control loops run in the 8031 microprocessors at a 1500 Hz update rate. At each pass through the loop, various memory registers are checked to determine subsequent action. Calibration, data-taking, and control output are specified by setting appropriate bits in these memory registers using the corresponding FORTH words.

The commands used to conduct experiments can be divided into three groups: initialization, motion, and data-storage. The initialization section sets up the microprocessors, allocates data storage, stores setpoints, and zeros the axis position. The motion section actually generates the motion. The data-storage section transfers data from the micros to the VAX for processing and plotting.

A typical sequence of commands to generate X-axis response to a versine reference input would be given as follows:

202

Initialization:

PREP*

XAXIS

900 E-3 PGAIN

2 T_MULTIPLIER !

9806 E_ADDR !

INIT_DATA_VARS

YAXIS

8156 E_ADDR !

INIT_DATA_VARS

XAXIS

SET_LOAD /U/MECKL/DATA/VERS1.DAT

SET_LOAD /U/MECKL/DATA/VERS2.DAT

START_CAL INFO

(move axis to zero position)

Motion:

(lift red stop button)

GO*

XAXIS

DATA_&_MOVE*

Data-storage:

XAXIS DATA_TO_VAX X.DAT

YAXIS DATA_TO_VAX X-ACC.DAT

Most of the commands for initialization were developed by Benjamin [75] and are defined there. PREP* initializes the X and Y-axis microprocessors and downloads the servo routines from the VAX. The subsequent commands stiffen the position gain and allocate memory for data-taking. The SET_LOAD command (as defined in

Appendix D) downloads the setpoints given at each servo time step from files on the VAX and stores them in successive memory locations on the microprocessor. START_CAL INFO alerts the servo routine to look for the calibration micro-switch to set. As the X-axis is manually moved in a negative direction, the position in encoder counts will appear on the terminal display. After the calibration micro-switch has been reached, the position count will zero out, and the axis will be at its zero position.

To generate motion, all limit switches must be cleared and the red stop button must be released. Once this has been done, GO* activates the servo routines to enable the amplifiers and generate a voltage command output. The command DATA_&_MOVE* (defined in Appendix D) tells the servos to look at successive memory locations for setpoints and sets up data-taking. Position, current, and amplifier command data are stored in the X-axis microprocessor, while acceleration data is stored in the Y-axis micro. In order to generate a simple step response, the command DATA_&_MOVE* would be replaced by 36000. DATA_&_SET* to generate a 36000 count move while taking data.

The data-storage commands simply take the data stored on each microprocessor and transfer them to do unit conversions and to generate graphic plots.

Microprocessor Assembly Code

Appendix C

The 8031 microprocessors which run each axis are programmed with three distinct pieces of software. In addition, routines have been burned into PROMs residing on the micro cards to facilitate communication and interrupts.

The three software programs are written in 8031 assembly language and consist of a framework program, servo loops, and mathematical routines. The servo loops (LOOPS.ASS) and mathematical routines (MATH.ASS) have been retained as developed by Benjamin [75] without changes. The framework program establishes the sequence of events during each servo clock cycle. A revised version of this program (FRAMESET.ASS) was written to allow for time-varying position setpoints.

A copy of the assembly code for FRAMESET.ASS is given on subsequent pages. A majority of this program remains unchanged from the framework program FRAME.ASS written by Benjamin. Two additional sections were added to permit time-varying setpoints. Section 3 checks whether time-varying setpoints are called for and if so fetches the setpoint value from the appropriate memory location. This memory address is incremented during each pass through the framework routine.

Section 3 also determines the change in setpoint from the previous pass. This is a discrete representation of reference velocity. Section 4 then determines the difference between this reference velocity and the measured velocity to generate a

```
;   **********************************************************
;   *                                                        *
;   *         Micro-Processor Based Control Program          *
;   *                   Mike Benjamin                        *
;   *                                                        *
;   **********************************************************
;
;   *** modified by Peter Meckl, 11-5-87 ***
;
;         reads time-varying setpoints if so enabled
;         (located at Starting Address of Data Block+3
;         and following); Data Rate must be 2 or more
;
;         uses velocity error (rather than merely
;         measured velocity) in PD loop
;
;         changed 'jnb acc.7' to 'jnc' in data-taking routine
;         to ensure that it stops at right address
;
;   *** modified by FGM, 3-31-86 ***
;
;         saves Force data rather than Setpoint data
;
;         ignores trouble, encoder overrun bit.
;
; Pre-Defined Registers (all numbers base 8)
; Reg 40: Bit 0 - Jump to RAM bit set by START com'nd in communications program
; Reg 41: Bit 0 - Enable Bit - Set to enable out put to amplifiers
;         Bit 1 - Calibrate Bit - Indicates Calibration Routine should be run
;         Bit 2 - Calibration Indicator - Set by this program to indicate that
;                 axis was calibrated.
;         Bit 3 - Amplifier Select Bit - Set for use with Automatix Amps
;                 Cleared for use with MIT amps
;
; Reg 44: Bit 0 - Enable data taking
;         Bit 1 - Set externally to save Position Data
;         Bit 2 - Set externally to save A/D Data
;         Bit 3 - Set externally to Save Output Data
;         Bit 4 - Set by this program to indicate full data buffer
;                 - cleared by PDP-11
;         Bit 5 - Set by program to indicate data taking in progress
;                 - cleared by program
;         Bit 6 - Set to enable time-varying setpoint
;                 - Cleared by program at the end of the move
;         Bit 7 - Set by this program to indicate that move with time-varying
;                 setpoints is in progress
;                 - Cleared by program
; Reg 45: Data Rate - Data is saved every N-th time through control loop
; Reg 46: Starting Address of Data Block  - low byte
; Reg 47:                                  - high byte
; Reg 50: Ending Address of Data Block - low byte
; Reg 51:                              - high byte
; Reg 52: Current Address of Data  - low byte
; Reg 53:                          - high byte
;
; Reg 54: Sampling Time - low byte
; Reg 55:               - high byte
; Reg 56: Address of Servo Routine - low byte
; Reg 57:                          - high byte
;
; Reg 60,61,62: Current position of axis (Reg 60 is least significant)
; Reg 63,64,65: Current Setpoint for axis
;
; Reg 66,67: Two's Compliment integer representation of OUTPUT value for
;            amplifiers - Loaded by Servo Subroutine
; Reg 70: Used by servo subroutine to calculate output in micro-notation
```

```
; Reg 71 - 122: Scratch pad for servo routines
; Reg 74,75,76: Must be Loaded with the Speed for use in the Servo subroutine
; Reg 114: Current Address of Setpoint - low byte
; Reg 115;                              - high byte
; Reg 116,117,120: Change in Setpoint in micro-notation
; Reg 121,122: Must remain unused to avoid conflict with velocity transitions
;              when using above registers (114-120) -- (see loopsvel.ass)
; Reg 123, 124, 125, 126, and 127 Scratch pad for add and multiply routines
; Reg 130 - 177: Stack Registers
;
;
; *** MAIN SERVO FRAMEWORK PROGRAM ***
; This code runs on a timed interrupt basis and is responsible for
;        Reading Encoder and updating position counts
;        Loading Time-varying Setpoints - if so enabled
;        Checking for calibration pulse - if we are in calibration mode
;        Checking Limit Switches and Enable Bit
;        Calling Servo Subroutine
;        Taking Data
;        Outputing values to PWM amplifiers
;                                             -mhb
;
 = 10000                                 ;TIMER 0 interrupt routine at 10000
;
; Section 1: push items onto stack and restart timer.
;
     clr  tcon.4                        ;stop timer 0 for a moment
     push psw                          ;store things away
     push dpl
     push dph
     push acc
     setb psw.3                        ;select register bank 1
     mov  th0,55                       ;load starting counts
     mov  tl0,54
     setb tcon.4                       ;restart timer 0
;
; Section 2: Read current Position and update high bytes of count
;
     mov  dptr,#154000                 ;address of force d/a
     movx @dptr,a                      ;start convert
     mov  76,#1                        ; initialize sign/exp byte of speed
     mov  74,#0                        ; init lmb of speed to zero
;
     mov  dptr,#140000                 ; address of encoder count
     mov  r0,#60
     mov  r5,#0                        ;initialize high byte of change
     movx a,@dptr                      ;fetch current encoder reading
     clr  c
     subb a,@r0                        ;New-reading - Old-reading = Low-change
     mov  r4,a                         ;r4 = low-change
     mov  75,a                         ; speed-hmb = low-change
;
     jnb  acc.7,pos                    ;jump ahead if positive change
     mov  r5,#377                      ;set High-change = -1
     mov  76,#201                      ;change sign of speed
     clr  c
     clr  a
     subb a,75                         ;take abs value of change for speed
     mov  75,a                         ;store as the hmb of speed
;
pos  mov  a,@r0
     clr  c
     addc a,r4                         ;New-reading = Low-change + Old-reading
     mov  @r0,a                        ;Stash new reading
     inc  r0
```

```
        mov a,@r0                       ;fetch old-high-reading
        addc a,r5                       ;New-high-reading
                                        ;   = old-high + high-change
        mov @r0,a                       ;stash new-high-reading
        inc r0
        mov a,@r0                       ;fetch old-very-high-reading
        addc a,r5                       ;New-very-high
                                        ;   = old-very-high + high-change
        mov @r0,a                       ;stash new-very-high-reading
;
; Section 3: Load current setpoint and determine change in setpoint by
;            looking at lowest byte change
;
        push dpl                        ;save pointer address to encoder count
        push dph
        jnb  44.6,cal                   ;skip this if no time-varying setpoint
        jb   44.7,read                  ;move is in progress - skip on
        mov dph,47                      ;load in starting addr. of data block
        mov dpl,46
        inc dptr                        ;first setpoint located at S_ADDR+3
        inc dptr
        inc dptr
        mov 115,dph                     ;store starting addr. of setpoints
        mov 114,dpl
        setb 44.7                       ;set indicator that move is in progress
;
read mov 120,#1                         ;initialize sign/exp byte of change
        mov 116,#0          .           ;init lmb of change to zero
        mov dph,115                     ;load setpoint data pointer
        mov dpl,114
        movx a,@dptr                    ;read low byte of new setpoint (lb)
        mov r6,a                        ;temporarily store new setpoint lb
        mov r0,#63                      ;point to low byte of current setpoint
        clr c
        subb a,@r0                      ;New-reading - Old-reading = Low-change
;
        cjne a,#177,neof                ;skip if more setpoints coming
        clr 44.7                        ;end-of-setpoint-file reached (a=177)
        clr 44.6                        ;use same setpoint from now on
        sjmp cal
;
neof mov 117,a                          ;store as hmb of change = Low-change
        jnb  acc.7,plus                 ;jump ahead if positive change
        mov 120,#201                    ;reverse sign of setpoint change
        clr c
        clr a
        subb a,117                      ;take abs value of change
        mov 117,a                       ;store as hmb of change
;
plus mov a,r6                           ;stash new setpoint low byte
        mov @r0,a
        inc dptr
        movx a,@dptr                    ;fetch medium byte of new setpoint
        inc r0
        mov @r0,a                       ;stash medium byte of new setpoint
        inc dptr
        movx a,@dptr                    ;fetch high byte of new setpoint
        inc r0
        mov @r0,a                       ;stash high byte of new setpoint
        inc dptr
        mov 115,dph                     ;store pointer to next setpoint
        mov 114,dpl
;
; Section 4: Determine velocity error as position change - setpoint change to
;            conform to PD controller convention
;
```

```
        xrl 120,#200                    ;change sign of setpoint velocity term
        mov r0,#74                      ;point to position change
        mov r1,#116                     ;point to -setpoint change
        lcall add2                      ;add -> @74 = @74 - @120
;
cal     pop dph                         ;restore encoder count addr. pointer
        pop dpl
;
; Section 5: Calibrate Axis if required
;
        inc dph                         ;inc dph once to access enc status
        jnb  41.1,bb                    ;bit 41.1 indicates that we are in
                                        ;       calibration mode
        jb  41.2,bb                     ;bit 41.2 indicates we are calibrated
        movx a,@dptr                    ;fetch encoder status
        anl a,#17                       ;check for calib & A & B & Zero pulse
        cjne a,#13,bb                   ;if not at calibration pt skip ahead
        dec dph                         ;set dptr to encoder count register
        mov a,#0                        ;accum = 0
        movx @dptr,a                    ;clear count
        inc dph                         ;restore dptr
        mov r0,#60                      ;r0 = pointer to position & setpt blk
        clr a
zap     mov @r0,a
        inc r0
        cjne r0,#66,zap                 ;jump back to clear more if necessary
        setb  41.2                      ;set  to indicate calibration occured!
;
;
; Section 6: Initialize Output to zero and check for shut down conditions
;
bb      clr a
        mov 67,a                        ; Reg 67,66 = 0
        mov 66,a
        jb 41.0,lim                     ; bit 41.0 is enable
        sjmp out                        ; if not enabled - jump to output
;
; check for limit switches or encoder overrun.
;
lim     movx a,@dptr                    ; fetch encoder status
        anl a,#60                       ;check for overrun flag or limit trip
        jz cont                         ;if none are set keep going!!
        clr 41.0                        ; clear enable bit
        sjmp out                        ;if some have been tripped - BAIL OUT
;
; Section 7: Jump to servo Routine
;
cont    acall load                      ; load subroutine loads addresses
        lcall servo                     ; actual address for servo provided by
                                        ; load subroutine from Reg 56 & 57
;
; Section 8: Data taking
;
        jb  44.5,dt0                    ;we are currently taking data - skip on
        jb  44.4,out                    ; data buffer is full - move on
        jnb  44.0,out                   ; not taking data at present
;
        mov r3,#1                       ; Start taking Data - Initialize things
        mov 53,47                       ; load in starting addr. of data block
        mov 52,46
        setb  44.5                      ;set indicator
;
dt0     djnz r3,out                     ; r3 is countdown for when to take data
;
; all tests have been passed - time to take data
        mov r3,45                       ; initialize r3
```

```
        mov dph,53                      ; load data pointer
        mov dpl,52
        jnb  44.1,dt1                   ; are we saving position data?
        mov a,60                        ; get position from registers 60 & 61
        movx @dptr,a                    ; stash
        inc dptr
        mov a,61
        movx @dptr,a
        inc dptr
;
dt1  jnb  44.2,dt2                       ; are we saving A/D data?
        push dpl
        push dph                        ; save dptr
        mov dptr,#154000                ; addr of A/D data
        movx a,@dptr                    ; fetch A/D reading
        pop dph
        pop dpl                         ; restore
        movx @dptr,a                    ; stash
        inc dptr
        mov a,#0                        ; high byte is zero
        movx @dptr,a
        inc dptr
;
dt2  jnb  44.3,dt3                       ; are we saving output data?
        mov a,66                        ; get output from registers 66 & 67
        movx @dptr,a                    ; stash
        inc dptr
        mov a,67              .
        movx @dptr,a
        inc dptr
;
dt3  mov 53,dph                         ; store away data pointer
        mov 52,dpl
        mov a,51                        ; is data buffer full?
        clr c
        subb a,53                       ; subtract high bytes of data addresses
        jnz out                         ; data not full
        clr c
        mov a,50
        subb a,52                       ; subtract low bytes
        subb a,#1                       ; subtract an extra 1
        jnc out                         ; positive answer - keep going
;
; data block is full - stop data taking
        mov 51,53                       ; update end of data block markers
        mov 50,52
        setb  44.4                      ; raise flag
        clr  44.5                       ;lower flag
;
; Section 9: Output to Motor
;
out     jb 41.3,aout                    jump if we are using Automatix Amps
        clr a
        mov r2,#0                       initialize for disabled amp
        jnb 41.0,put                    if we are not enabled jump ahead
        mov r2,#1                       set for forward motion
        mov a,67
        jnb acc.7,pos1                  test sign
neg1    mov r2,#3                       negative output
        clr c
        clr a
        subb a,66                       change sign
        sjmp put
pos1    mov a,66
put     mov dptr,#152000                address of PWM Mag for MIT amps
        movx @dptr,a                    output magnitude
```

```
        mov a,r2
        mov dptr,#150000          address of PWM status
        movx @dptr,a              output status & direction bits
        sjmp popr
;
; The following command causes initialization to occur at original location
; but gives extra room to finish framework program.
;
 = 10600
        sjmp init
;
aout    mov r2,#0                 ' initialize enable command to zero
        jnb 41.0,apos             jump if we aren't enabled
        inc r2                    r2 used later for status byte
apos    mov dptr,#152000          dptr = base address of latch card's d/a
        mov a,66
        movx @dptr,a              output lowest four bits
        inc dpl                   incriment pointer
        swap a                    swap nibbles
        movx @dptr,a              output mid 4 bits
        inc dpl                   incriment pointer
        mov a,67
        xrl a,#10                 compliment bit-11 to change into right
                                  ;format for d/a
        movx @dptr,a              output high 4 bits
        inc dpl                   increment pointer
        movx @dptr,a              output to latch convertion
        mov dptr,#150000          dptr = address of enable register
        mov a,r2
        movx @dptr,a              output enable bit
;
; Section 8: Pop Stack and return from interrupt
;
popr    pop acc
        pop dph
        pop dpl
        pop psw                   ; leave things as they were found
        reti
;
 servo nop                       ; bogus label to fill in lcall
                                  ;        instruction
;
;
; Subroutine LOAD - moves the address of the suervo subroutine to the end
;        of the two bytes directly following the lcall instruction.
;        This allows changing the subroutines by writing the address of the new
;        servo routine into locations 56 & 57 of internal RAM.
;
 load pop dph                     ; get program counter address
                                  ;         from stack
        pop dpl                   ; and load into data pointer
        inc sp
        inc sp
        inc dptr
        mov a,57                  ; fetch high byte of servo rotine addr.
        movx @dptr,a              ; store jump to address
        inc dptr
        mov a,56                  ; fetch low byte
        movx @dptr,a
        ret
;
; Initialization Section - this program is run only once
;        at the start of operation
;
 = 10700                          ;this code goes at micro-addr 10700
init clr  40.0                    ;clear jump to ram flag
```

```
        mov tmod,#1                     ;configure timer zero in mode 1
        mov 55,#375                     ; initialize servo rate registers for
        mov 54,#164                     ;  1.5 kHz sampling
        mov th0,55                      ;load starting counts
        mov tl0,54
        setb tcon.4                     ;start up timer 0
        mov iec,#203                    ;enable comm. and timer interrupts
        mov ipc,#2                      ; set priority of servo loop high
        mov a,#316
        anl 44,a                        ; clear start data and data full bits
        mov 112,#377                    ; Initialize amplifier Max.
        mov 113,#7
;
wait jnb  40.0,wait                     ; check  which is startup flag
        clr  40.0                       ; leave cleared before jumping to RAM
        push psw
        anl psw,#347                    ; select register bank 0
        mov dpl,r0                      ; load data pointer
        mov dph,r1
        pop psw
        clr a
        jmp @a+dptr                     ;jmp to ram
;
; The following label is purely for the assembler to check that the above
; code fits before memory location 11000.
;
= 11000
        nop

; The following bogus label is so that the assembler will know where the
;   math services are.
= 12000
add2 nop
;
```

FORTH Commands

The FORTH language operates as a hierarchy of definitions, in which more complex words are built up from simpler words. These definitions are stored in a dictionary when compiled, which resides on the PDP 11/23. Most of the FORTH words needed to run the experiments were already contained in this dictionary. Additional words were defined in a file on the VAX called /u/meckl/forth/data-send.fth and were added to the dictionary on the PDP 11/23 using the FORTH command:

```
INTERPRET_VAX_FILE /U/MECKL/FORTH/DATA-SEND.FTH
```

The following glossary of FORTH words describes what each command does and specifies the input and output for each word. FORTH operates on a stack, so input and output is specified by the expressions surrounded by parentheses and separated by a double hyphen. The first expression represents the input to be placed on the stack, while the second expression represents the output returned from the stack. One or both of these may be absent.

DATA_TO_VAX (FILENAME --)

> reads data from the microprocessor specified by **MN** and transfers it to the file **FILENAME** on the VAX.

214

VAX_TO_MICRO (FILENAME --)

transfers the contents of FILENAME on the VAX to the microprocessor specified by **MN**.

SET_LOAD (FILENAME --)

transfers a sequence of setpoints from **FILENAME** on the VAX to the microprocessor specified by **MN** starting at an actual memory location given at the start of the file.

ENABLE_MOVE (--)

signals the framework routine for microprocessor specified by **MN** to start servoing to setpoints from successive memory locations.

DATA_&_MOVE (--)

starts servoing to setpoints from successive memory locations for micro specified by **MN** while taking data for position, A/D input, and amplifier command.

DATA_&_MOVE* (--)

does **DATA_&_MOVE** for axis specified by MN while reading A/D data on other axis micro without moving that axis.

DATA_&_MOVE (--)**

does **DATA_&_MOVE** for X-axis and servos to setpoints from successive memory locations in Y-axis micro while reading A D data on that axis.

DATA_&_SET* (DOUBLE INTEGER --)

signals the framework routine for microprocessor specified by MN to start following setpoint given by DOUBLE INTEGER while reading data for position, A/D input, and amplifier command from the moving axis, and A D input only from the other axis micro without moving that axis.